RÉPUBLIQUE FRANÇAISE
Liberté Égalité Fraternité

Université de Toulouse

Doctorat de l'Université de Toulouse

préparé à l'INSA Toulouse

Aperçu de la fonctionnalisation du graphène pour le développement de nouveaux dispositifs 2D

Thèse présentée et soutenue, le 24 octobre 2025 par

Tom FOURNIER

École doctorale
SDM - SCIENCES DE LA MATIERE - Toulouse

Spécialité
Nanophysique

Unité de recherche
CEMES - Centre d'Elaboration de Matériaux et d'Etudes Structurales

Thèse dirigée par
Pascal PUECH et Benjamin LASSAGNE

Composition du jury
M. Stéphane BERCIAUD, Rapporteur, Institut de Physique et Chimie des Matériaux de Strasbourg (IPCMS) - Université de Strasbourg
M. Bernard HUMBERT, Rapporteur, Institut des matériaux de Nantes (IMN) - Université de Nantes
Mme Rozenn LE-PARC, Examinatrice, Laboratoire Charles Coulomb (L2C) - Université de Montpellier
Mme Nedjma BENDIAB, Examinatrice, Institut Néel - Université Grenoble Alpes
M. Alfonso SAN MIGUEL, Examinateur, Institut Lumière Matière - Université Lyon 1
M. Xavier MARIE, Examinateur, Laboratoire de Physique et Chimie des nano-objets (LPCNO) - Institut national des sciences appliquées (INSA)
M. Pascal PUECH, Directeur de thèse, Centre d'élaboration des matériaux et d'études structurales (CEMES) - Université de Toulouse
M. Benjamin LASSAGNE, Co-directeur de thèse, Laboratoire de Physique et Chimie des nano-objets (LPCNO) - Institut national des sciences appliquées (INSA)

Membres invités
M. Fabrice Piazza, PUCMM

Insight into the functionalization of graphene for the development of novel 2D devices

Remerciements

En premier lieu, je tiens à remercier très sincèrement chacun des membres du jury d'avoir accepté d'évaluer mes travaux de thèse et d'avoir fait l'effort de se déplacer (ou de se connecter à distance) pour ma soutenance. J'ai particulièrement apprécié nos échanges lors des questions, qui ont été pour moi très enrichissants et m'ont permis de prendre davantage de recul sur mon sujet de thèse. J'espère que nos chemins se croiseront à nouveau, afin d'avoir d'autres occasions d'échanger sur diverses thématiques liées au Raman, au graphène, à la physique des matériaux 2D, ou encore sur bien d'autres sujets passionnants sur lesquels j'ai beaucoup à apprendre de leur expertise. Plus particulièrement, je remercie Stéphane Berciaud et Bernard Humbert pour avoir rapporté mes travaux de thèse ; Rozenn Le-Parc, Nedjma Bendiab et Alfonso San Miguel pour les avoir examinés ; et enfin Xavier Marie pour avoir examiné ma thèse et présidé le jury de soutenance. Je remercie aussi Emmanuel Flahaut et Nedjma Bendiab pour avoir fait partie de mon comité de suivi individuel.

De toute évidence, je remercie mes encadrants, Pascal Puech et Benjamin Lassagne, pour une multitude de raisons. Tout d'abord, je les remercie de m'avoir donné la chance de faire cette thèse, d'avoir cru en moi, et de m'avoir fait confiance durant ces trois années. Ensuite, je les remercie de m'avoir accompagné tout au long de ces trois ans de thèse, en m'aiguillant et en me transmettant leurs connaissances ainsi que leur expérience pour me permettre de réussir. Je les remercie également pour l'aide précieuse qu'ils m'ont apportée lors de la rédaction de ce manuscrit et de la préparation de la soutenance. Enfin, je les remercie pour leur soutien et leurs conseils lorsqu'il a s'agit de rechercher un post-doc. Et plus largement, je les remercie pour leur amitié. J'espère fortement que nous resterons en contact. Individuellement, je remercie Pascal Puech pour m'avoir donné l'occasion de voyager en me finançant des séjours en République Dominicaine, au Danemark et en France ; et je remercie Benjamin Lassagne d'avoir été un excellent enseignant lors de mes études à l'INSA Toulouse et de m'avoir recruté en stage de fin d'études d'ingénieur.

Ensuite, je remercie Fabrice Piazza, Marc Dubois et Liv Hornekaer pour m'avoir accueilli au sein de leurs laboratoires respectifs. Tout particulièrement, un grand merci à Fabrice Piazza pour son accueil chaleureux lors de mes séjours en République Dominicaine, son aide précieuse pour trouver un logement et son amitié. Je suis très reconnaissant envers lui pour m'avoir invité à plusieurs reprises et m'avoir fait visiter son beau pays. Je le remercie également pour avoir consacré du temps à l'hydrogénation des échantillons et pour m'avoir formé sur l'utilisation du réacteur à filaments chauds. J'ai également fortement apprécié nos nombreuses discussions scientifiques au cours desquelles j'ai beaucoup appris. Au sein de son laboratoire, j'ai pu échanger avec Kelvin Cruz et Germercy Paredes que je remercie également pour leur amitié et leurs nombreuses aides lors de mes séjours en République Dominicaine. En particulier, je remercie Kelvin Cruz pour son soutien technique et scientifique et pour m'avoir fait découvrir des spécialités culinaires locales et je remercie Germercy Paredes de m'avoir invité à passer une journée dans sa famille en province. Je n'oublierai jamais ces moments. Côté Danemark, je remercie John Thrower, ingénieur de recherche au sein de l'équipe de Liv Hornekaer, pour m'avoir accueilli au sein du laboratoire et avoir consacré du temps à tenter d'hydrogéner mes échantillons. Un grand merci également à Marc Dubois pour avoir consacré du temps à la fluoration de mes échantillons et pour m'avoir invité à participer à une séance de travaux pratiques sur la spectroscopie par résonance magnétique nucléaire.

Je remercie également tous les membres de l'ANR GLADIATOR avec qui j'ai eu l'occasion de travailler et d'échanger durant ces trois ans de thèse, jusqu'à même rédiger des articles : Marc Monthioux, Iann Gerber, Samir El Madaoudi, Cédric Crespos, Jean-Marc Leyssale, Felana Andriambelaza et Germercy Paredes.

Un grand merci à tous mes collègues et amis du CEMES et du LPCNO avec qui j'ai passé d'excellents moments tout au long de ma thèse. Côté CEMES, je remercie particulièrement Sébastien Moyano pour m'avoir formé et fourni son soutien technique pour l'utilisation des différents spectromètres Raman, Jean-Marie Poumirol pour m'avoir formé à l'utilisation du TERS, Robin Cours pour m'avoir formé sur l'utilisation du MEB, Elie Rouchy pour m'avoir montré comment transférer du graphène CVD sur un substrat le plus proprement possible, et Sébastien Pinaud ainsi que Justine Harmel pour l'aide qu'ils m'ont fourni sur certaines manipes en salle blanche. Enfin, un grand merci à tous les doctorants et post-doctorants avec qui j'ai passé de très bons moments au laboratoire et en dehors, notamment Elie Rouchy, Marine Resano, Salomé Trillot, Quentin Gromoff, Anais Fondet, Loic Grossetete, Agathe Duclos, Hassan Lamsaadi et Afnan Al Saati. Côté LPCNO, je remercie en particulier Lionel Petit (« *le mentor* »), qui m'a formé sur toutes les étapes de fabrication des échantillons ainsi que sur les mesures de transport. C'est quelqu'un à qui je dois beaucoup car il a su être très pédagogue et très patient à mon égard lorsque j'étais en stage de fin d'études, et il a toujours été là pour m'aider lorsque j'en avais besoin. J'ai surtout beaucoup appris à ces côtés lors de nos nombreuses discussions scientifiques. C'est quelqu'un de passionné et doté d'une grande culture scientifique dans de nombreux domaines liés à la physique. Plus largement, je remercie Lionel pour son amitié durant toutes ces années. Je remercie aussi tous ceux avec qui j'ai eu le plaisir de partager le bureau : Abraao Cefas Torres Dias, Maryam Sadeghiyan, Danny Gweha et Kosseila Air-Oukaci. Je remercie tout particulièrement Abbraao et Maryam pour leur amitié et les nombreuses aides qu'ils m'ont apportées. Je remercie aussi Cédric Robert et Delphine Lagarde pour avoir réalisé des spectres de photoluminescence sur l'un de mes échantillons, ainsi que Maxime Mauguet pour son soutien technique. Enfin, un grand merci à tous les doctorants et post-doctorants avec qui j'ai passé de très bons moments au laboratoire et en dehors, notamment Lionel Petit, Ilona Lecerf, Marion Luu, Bastien Sanglard, Marie-Hélène Pietraru, Abraao Cefas Torres Dias, Maryam Sadeghiyan, Jules Fraunié, Dorian Beret, Kerwan Morin, Sébastien Roux, Louka Hemmen, Tilly Guyot, Cora Crunteanu-Stanescu, Gaëtan Petit et Adrien Delpoux.

Je remercie chaleureusement ma famille pour son soutien, son encouragement ainsi que son amour qu'elle m'a apportés depuis ma naissance et jusqu'à maintenant, notamment pendant mes études, ce qui m'a permis de devenir la personne que je suis aujourd'hui. Mes parents, mes grands-parents, ainsi que mon petit frère Robin ont toujours été là pour moi et je leur serai éternellement reconnaissant. Je n'aurais pas pu accomplir tout cela sans eux.

Je tiens tout particulièrement à remercier de tout cœur ma bien-aimée Mathilde pour m'avoir donné tout son amour et son soutien moral durant ma dernière année de thèse, et pour faire aujourd'hui la folie de me suivre jusqu'à Grenoble, ville où je pars pour réaliser mon post-doc. Elle a été d'une grande aide pour moi, en particulier durant la rédaction du manuscrit et la préparation de la soutenance, et je lui en serai éternellement reconnaissant. Un grand merci également à toute sa famille, particulièrement ses parents, pour toute l'aide et le soutien qu'ils m'ont apportés, ainsi que pour leur accueil chaleureux que je n'oublierai jamais. Vous êtes ma deuxième famille.

Enfin, un énorme merci à l'ensemble de mes amis qui m'ont soutenu durant toutes ces années, notamment mes amis du CEMES et du LPCNO que j'ai cités plus haut. Parmi eux, je tiens tout particulièrement à remercier Jules Fraunié, Marion Luu, Dorian Beret, Kerwan Morin, Sébastien Roux et Louka Hemmen ; nos débats gênants, nos ivresses (merci Henry Westons) et nos parties de Diplomatie vont me manquer. Un grand merci aussi à mes amis de l'INSA avec qui j'ai passé des moments inoubliables durant toutes mes années d'études et de doctorat : Hugo Kerreneur, Julien Touchais, William Sablé, Guillaume Buissière, Mathilde Ibled, Martin Loncle, Yohan Simard, Eva Minot, Léa Diani, Sarah Lawpois, Clément Liorit, Hugo Cortes, Léo Bourdon, Nidish Burton, Lucile Miloche, François Lepetit Aimon, Marvyn Panetier, Eléonore Gaich, Santiago Sanchez, Sherife Dergici, Leïla Payet et Léa Choury. Une mention spéciale est faite à mes deux colocataires, Hugo Kerreneur et Julien Touchais, pour leur soutien au quotidien. Je tiens aussi à

remercier Hanna Bacave pour son aide précieuse le jour de ma soutenance. Enfin, je souhaite terminer ces remerciements en honorant mes plus vieux amis, ceux du lycée, avec qui j'ai tissé des liens très étroits et qui m'ont toujours soutenu et encouragé dans mes projets : Maxime Guillaume, Alexis Neveu, Kélian Parisse, David Morin, Gabriel Patarin et Nicolas Plottu. Je les remercie particulièrement d'avoir parcouru tous ces kilomètres pour être présents le jour de ma soutenance. C'est un très beau geste d'amitié que je n'oublierai jamais.

Table of contents

Remerciements iv
Introduction 1
Chapter 1 Interest in controlling carbon hybridization in graphene 4
1.1 Role of carbon hybridization on structural and electronic properties 4
1.1.1 Carbon hybridization 4
1.1.2 sp^3 vs sp^2 carbon hybridization in crystals 4
1.2 Graphene 7
1.2.1 Definition 7
1.2.2 Crystalline structure 7
1.2.3 Electronic structure 8
1.2.4 Graphene based 2D electronic devices 10
1.3 Chemically induced sp^3-hybridization in graphene for 2D devices application 10
1.3.1 Diamond-like 2D film 10
1.3.2 Functionalized graphene 11
Chapter 2 Samples Fabrication 14
2.1 Graphene on Si/SiO_2 substrate 14
2.1.1 Mechanical exfoliation of HOPG on Si/SiO_2 substrate 14
2.1.2 Substrate effect on optical contrast 15
2.1.3 Microfabrication of graphene devices on Si/SiO_2 20
2.2 Graphene on ultra-flat Au <111> substrate 25
2.2.1 Ultra-flat gold 25
2.2.2 Mechanical exfoliation of HOPG on gold substrate 26
2.2.3 Polymer-assisted transfer of CVD-grown graphene layer 27
Chapter 3 Experimental techniques for graphene hydrogenation and fluorination 30
3.1 Graphene hydrogenation 30
3.1.1 Plasma hydrogenation 30
3.1.2 Hot Filament Chemical Vapor Deposition (HFCVD) 32
3.1.3 Hydrogen beam under ultra-high vacuum 36
3.1.4 Patterned hydrogenation 39
3.2 Graphene fluorination 41
3.2.1 Gas phase fluorination 41
3.2.2 Patterned fluorination 45
Chapter 4 Characterization techniques 48
4.1 Raman spectroscopy in graphene 48

4.1.1 Raman scattering 48
4.1.2 Raman scattering in graphene 53
4.1.2.2 Substrate effect on Raman signal intensity 62
4.1.3 Experimental set-up 69
4.2 Atomic Force Microscopy (AFM) 70
4.2.1 Basic Principle (Contact mode) 70
4.2.2 Tapping mode 72
4.2.3 Experimental details 73
4.3 Tip Enhanced Raman spectroscopy (TERS) 75
4.3.1 Basic concept 75
4.3.1.1 Raman signal enhancement and nanoscale resolution 75
4.3.1.2 Tip-sample interactions 76
4.3.2 C-H and C-F vibrational modes 77
4.4 Electrical transport measurement 79
4.4.1 Electronic properties of pristine graphene 79
4.4.1.1 Electric field effect 79
4.4.1.2 Magnetic field effect 85
4.4.2 Electronic properties of functionalized graphene 87
4.4.3 Measurement set-up 89
4.4.3.1 Ambient conditions measurement with probe station 89
4.4.3.2 Low-pressure and low temperature measurements with a physical properties measurement system (PPMS) 91
Chapter 5 Raman model to quantify the sp^3/sp^2 ratio in functionalized graphene 92
5.1 Empirical point-defects model based on ion-bombardment 92
5.1.1 Description and limits of the model 92
5.1.2 Correction of the model's equation 94
5.1.3 Challenges related to model calibration 96
5.1.4 Failure in model adaptation to functionalized graphene 97
5.2 Non-empirical model based on quantum chemistry calculations 98
5.2.1 Description of the sp^3-type point-defect 98
5.2.2 Equations of the model 99
5.2.3 Input parameters 101
5.2.4 Results and discussion 104
Chapter 6 Results and analysis of hydrogenated graphene 110
6.1 Experimental parameters 110

6.2 Raman spectroscopy 111
6.2.1 Raman features of hydrogenated graphene 111
6.2.2 Raman analysis of hydrogen thermal stability 113
6.3 Atomic Force Microscopy 119
6.4 Tip-enhanced Raman spectroscopy 124
6.5 Perspectives: Patterned hydrogenation enabled by electron beam irradiation 125
Chapter 7 Results and analysis of fluorinated graphene 128
7.1 Experimental parameters 128
7.2 Raman spectroscopy 128
7.3 Atomic Force Microscopy 131
7.4 Tip-enhanced Raman spectroscopy 133
7.5 Electrical transport measurements 134
7.5.1 Devices 134
7.5.2 Measurements 135
7.5.3 Perspectives 144
Conclusion & Perspectives 146
References 150
Résumé en français 158
Introduction & Contexte 158
1 Fabrication des échantillons 159
1.1 Exfoliation mécanique 159
1.2 Microfabrication de dispositifs en graphene sur Si/SiO_2 160
1.3 Méthode de transfert humide assistée par polymères 161
2 Description des techniques utilisées pour l'hydrogénation et la fluoration 162
2.1 Hydrogénation 162
2.1.1 Procédé à filaments chauds 162
2.1.2 Hydrogénation locale par faisceau d'électrons 163
2.2 Fluoration 163
3 Techniques de characterisation 163
3.1 Spectroscopie Raman dans le graphène 163
3.2 Rôle du substrat interférentiel 165
3.3 Setup expérimental 166
3.4 Microscopie à force atomique 167
3.5 Spectroscopie Raman amplifiée par effet de pointe (TERS) 167
3.6 Mesures de transport électrique 168

3.6.1 Propriétés électroniques du graphène fonctionnalisé 168
3.6.2 Mesures 169
4 Modèle Raman pour quantifier le ratio sp^2/sp^3 dans le graphène fonctionnalisé 169
5 Résultats et analyse du graphène hydrogéné 172
5.1 Spectroscopie Raman 172
5.1.1 Caractéristique Raman du graphène hydrogéné 172
5.1.2 Etude Raman de la stabilité thermique de l'hydrogène 174
5.2 Microscopie à force atomique 177
5.3 Raman amplifié par effet de pointe 178
5.4 Perspectives : hydrogénation locale par faisceau d'électrons 179
6 Résultats et analyse des échantillons fluorés 180
6.1 Spectroscopie Raman 180
6.2 Microscopie à force atomique 182
6.3 Spectroscopie Raman amplifiée par effet de pointe (TERS) 183
6.4 Mesures de transport électrique 183
Conclusion 187

Introduction

The large family of Van der Waals materials, i.e., stacks of layers maintained together by van der Waals interactions, covers a large panel of crystalline compounds with many different electronic properties. For instance, hexagonal boron nitride (h-BN) is a very good electrical insulator with a bandgap in the ultraviolet range [1], whereas graphite has metallic properties due to its zero-energy gap [2]. Some other compounds are semiconductors, such as the transition metal dichalcogenides (TMDs), covering energy gaps from the infrared to the visible range [1]. Moreover, due to their weak interlayer interactions, these materials can be exfoliated to obtain two-dimensional (2D) crystals, referred to as "2D materials", with electronic band structures different than their bulk equivalents. In 2004, two researchers from Manchester, A. K. Geim and K. S. Novoselov, were the first to evidence an atomically thin carbon layer, called *graphene*, obtained by mechanical exfoliation of a bulk graphite crystal [3]. In addition to being two-dimensional, graphene differs from graphite by its electronic band structure, which has a linear energy dispersion in the vicinity of some specific high symmetry points of the Brillouin's zone. Consequently, electrons and holes in graphene mimic massless Dirac Fermions. Their mobility can be much larger than in graphite, reaching values up to 180 000 $cm^2V^{-1}s^{-1}$ [4]. These electronic properties can be used in many applications, such as highly sensitive magnetic sensors [5] or high-frequency transistors [6]. However, due to its zero-energy gap, graphene transistors have a very low on/off ratio [7], which is unsuitable for digital electronic applications. To overcome this issue, several approaches to induce a bandgap in graphene were reported in the literature. For instance, it was demonstrated that, in graphene nanoribbons, confinement effects lead to wave-vector discretization, opening a bandgap tunable by the ribbon width [8,9]. Another approach consists of chemically switching carbon atom hybridization from sp^2 to sp^3 by covalently bonding adatoms. Hydrogenation [10-14] and fluorination [15-17] are the most common techniques for this purpose. In the ideal case, where each carbon is covalently bonded to a hydrogen or a fluorine atom, the respective materials are referred to as *graphane* or *fluorographane*, with energy gaps above 3 eV [18,19]. For uncompleted hydrogenation or fluorination, the value of the bandgap is driven by the hydrogen or fluorine coverage rate [20,21]. Additionally, the reversibility of these processes was demonstrated several times in the literature [11-14,21-24]. Hence, a fine control of the functionalization and defunctionalization processes should allow for chemically tuning graphene electronic properties. However, this cannot be achieved without using adapted characterization techniques, nor by drawing hasty conclusions from experiments. That involves combining Raman spectroscopy with electrical transport measurements and microscopy techniques, for instance, which is not always done in the literature. Although this PhD was first motivated by the bandgap opening in graphene via hydrogenation to fabricate 2D sp^2/sp^3 planar heterostructures for applications in nanoelectronics, it turned to different horizons when realizing the challenges related to both the synthesis and the characterization. Thus, this experimental work focuses on one-sided hydrogenation and fluorination of graphene layers supported by Si/SiO_2 or gold wafers, from the sample fabrication to their characterization. The preparation of the graphene samples, as well as their characterization, was entirely carried out at CEMES and LPCNO. The samples were mostly characterized in Raman spectroscopy, but some were also analyzed in atomic force microscopy (AFM), tip-enhanced Raman spectroscopy (TERS), and electrical transport measurements. Concerning hydrogenation and fluorination, these processes were carried out in collaboration with two specialists: Prof. Fabrice Piazza from the PUCMM at Santiago de los Caballeros (Dominican Republic) and Prof. Marc Dubois from the University of Clermont-Ferrand (France). During this PhD, I had the opportunity to spend a few months at the PUCMM and a few days at

the University of Clermont-Ferrand.

This report is divided into seven chapters. The first chapter of this manuscript introduces the impact of carbon hybridization on the structural and electronic properties of carbon crystals, in particular by comparing the case of graphite (sp^2 hybridization) and diamond (sp^3 hybridization), as well as their respective two-dimensional equivalents, graphene and 2D-diamond. The case of partially functionalized graphene, which is the intermediate state between pristine graphene and 2D-diamond, is also introduced, as well as its interest for graphene-based electronic devices.

The second chapter deals with the preparation of the graphene samples before undergoing hydrogenation or fluorination. The substrates' characteristics are presented, in particular, the role of the oxide thickness for the Si/SiO_2 substrates, which is a key parameter for identifying monolayer graphene. The different protocols used to prepare graphene layers supported by Si/SiO_2 and ultra-flat gold substrates are detailed, including the mechanical exfoliation of highly oriented pyrolytic graphite (HOPG) and the transfer of CVD-grown graphene from copper foil to gold substrates. Additionally, the microfabrication protocol employed to fabricate graphene devices on Si/SiO_2 substrates is detailed step by step.

The third chapter deals with the different processes used in this work to hydrogenate and fluorinate the samples, and compares them with other commonly used techniques reported in the literature. Simultaneously, some important results from the literature are presented. Since both hydrogenation and fluorination were mostly performed by collaborators, the idea is rather to give an overview of the different techniques and their experimental challenges, rather than giving a detailed description of the synthesis mechanisms.

The fourth chapter gives a global description of the different characterization techniques employed to analyse the properties of both pristine and functionalized graphene samples: (i) Raman spectroscopy, (ii) AFM, (iii) TERS, and (iv) electrical transport measurements. The accent is placed on Raman spectroscopy, which is the main technique used in this work.

The fifth chapter is focused on Raman spectroscopy, as it describes a model developed during this PhD to determine quantitatively the concentration of sp^3-hybridized carbon in functionalized graphene from the analysis of the Raman spectrum. The model is compared with a widely used law from the literature, which was found to be erroneous and non-adapted to functionalization.

The sixth chapter summarizes the major results extracted from the characterization of hydrogenated graphene supported by a Si/SiO_2 substrate. It includes the Raman analysis of some relevant samples, as well as the Raman study of hydrogen stability under thermal annealing and laser irradiation. Some AFM images are analysed to complete the Raman analysis, thereby pointing out an undesired mechanism happening during hydrogenation for some experimental conditions. In addition, this chapter briefly evokes some first post-hydrogenation TERS measurements performed on CVD-grown graphene transferred on a gold substrate.

The last chapter provides a summary of the characterization of fluorinated graphene supported by a Si/SiO_2 substrate. It includes the Raman analysis of all the samples, and is completed by the AFM images of some samples. This chapter also reports the data analysis of the electrical transport measurements performed on

a few fluorinated graphene devices. Finally, some early post-fluorination TERS measurements, carried out on graphene exfoliated on gold substrates, are presented.

Chapter 1 Interest in controlling carbon hybridization in graphene

1.1 Role of carbon hybridization on structural and electronic properties

1.1.1 Carbon hybridization

Carbon is the element with atomic number 6, represented by the letter C, and is one of the most common elements in the universe. It appears in many different molecules (such as CH_4 and CO_2) and materials (including polymers, diamond, and graphite) and is fundamental to all known life forms. Its versatility stems from its electronic structure ($1s^2\ 2s^2\ 2p^2$). In molecules and materials, the 2s and 2p orbitals are hybridized into sp, sp^2, or sp^3 orbitals (**Figure 1.1**) to lower the energy.

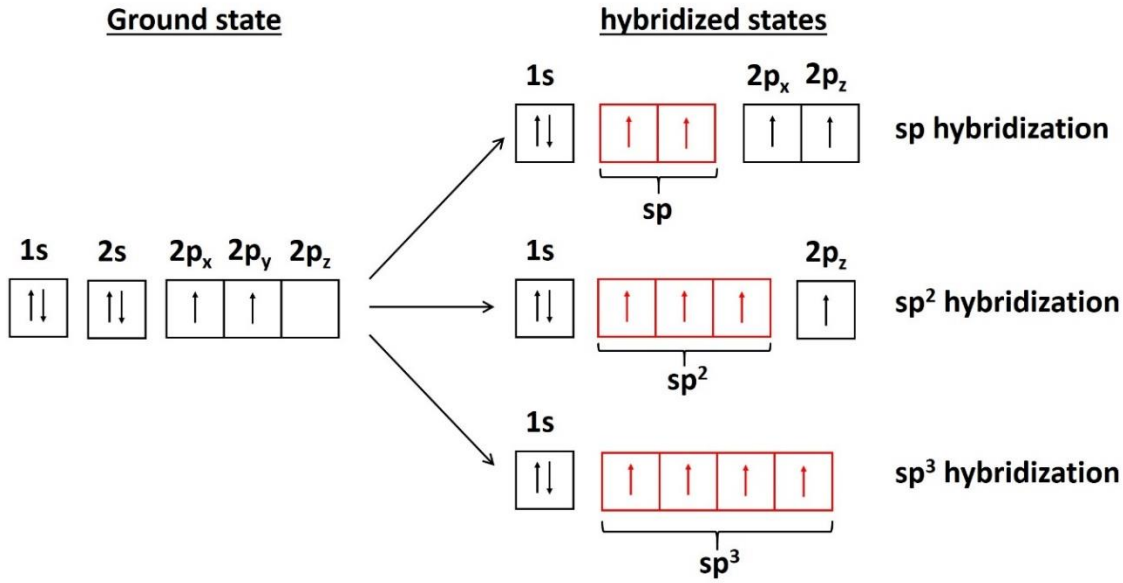


Figure 1.1: Different hybridizations of Carbon

1.1.2 sp^3 vs sp^2 carbon hybridization in crystals

1.1.2.1 Diamond: a sp^3 carbon crystal

In diamond, carbon atoms are tetravalent and arranged in a diamond structure, which corresponds to a face-centred cubic lattice with a basis composed of two carbon atoms (**Figure 1.2a**). Atomic orbitals are sp^3 hybridized, forming strong covalent bonds (called σ bonds) separated by an angle of 109°.

Diamond crystals can be found in their natural state (metastable) or can be synthesized in laboratories by chemical vapor deposition (CVD), a growth technique used to deposit crystalline thin films on substrates. It allows the growth of large areas but results in polycrystalline films due to a high number of nucleation

points. CVD involves a chemical reaction in the gas phase containing the needed chemical elements and some reactants. In the case of diamond, the gas phase is usually composed of CH_4 and H_2 [26].

In terms of electronic properties, diamond is classified as an electrical insulator due to the presence of a large energy gap in its electronic band structure. The theoretical value for this gap determined by the empirical pseudopotential method is about 5.4 eV [27] (**Figure 1.2b**), which is in good agreement with the experimental value obtained with optical absorption measurements.

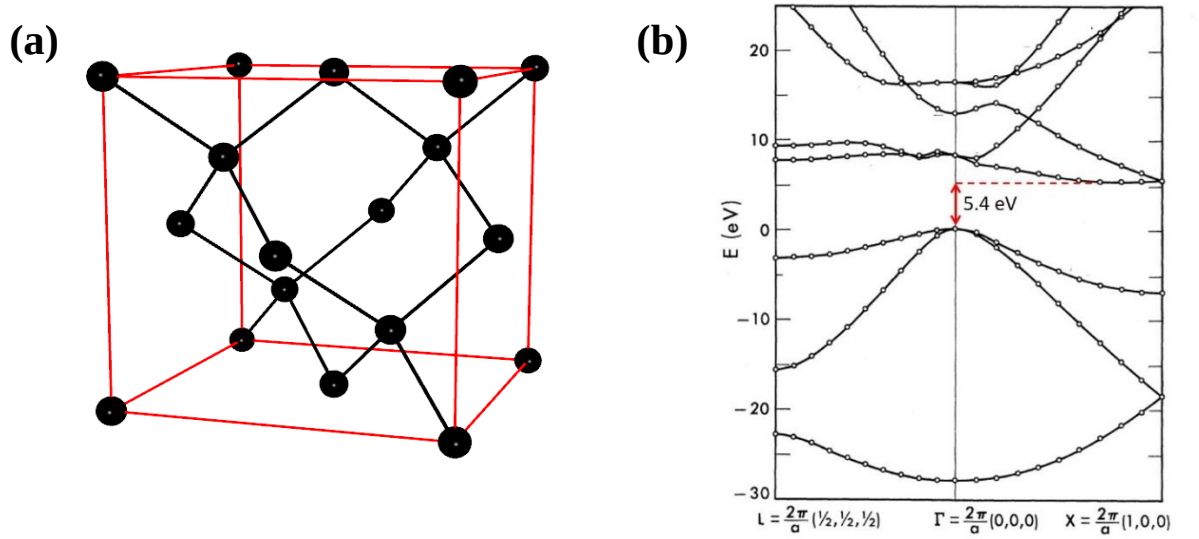


Figure 1.2: (a) Crystalline and (b) electronic band structure of diamond. In (a), black segments are covalent bonds between carbon atoms (black spheres), and the red cube represents the volume of the unit cell. (b) is adapted from [27] and the indirect bandgap is indicated by the red arrow.

1.1.2.2 Graphite: a sp^2 carbon crystal

In graphite, carbon atoms are trivalent and arranged in a hexagonal lattice with a carbon-carbon distance of 0.142 nm [28], forming a stack of multiple layers separated by 0.335 nm [28] (**Figure 1.3a**). Carbon atoms are sp^2 hybridized, meaning they have three in-plane sp^2 orbitals forming σ bonds separated by an angle of 120° and one out-of-plane $2p_z$ orbital forming a delocalized π state contributing to interlayer interactions (i.e., van der Waals forces) and electrical conduction. A single layer is referred to as *graphene* (see **1.2**).

Layers are not perfectly superposed but laterally shifted along a specific vector by a distance equal to the carbon-carbon bond length. There are different forms of graphite, distinguished by their stacking shift order (AB or ABC). **Figure 1.3** illustrates both Bernal (AB) and rhombohedral (ABC) stacking.

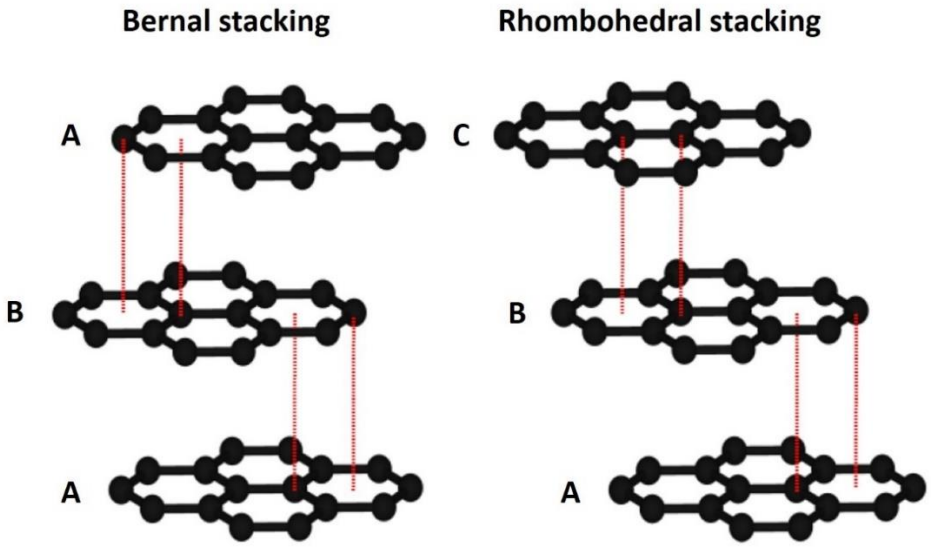


Figure 1.3: Bernal (AB) and rhombohedral (ABC) stacking in graphite, adapted from [29].

Graphite crystals can be found in a natural state or can be synthesized, as is the case with pyrolytic graphite grown by vapor deposition of hydrocarbons at high temperature (2100-2500°C) [30]. Some thermal treatments are usually added in order to increase the purity and the orientation degree. Highly oriented pyrolytic graphite (HOPG) is obtained by hot pressing at 2800-3000°C, followed by annealing under pressure at 3400-3600°C, which improves the layers' alignment, resulting in a high orientation degree along the c-axis [30].

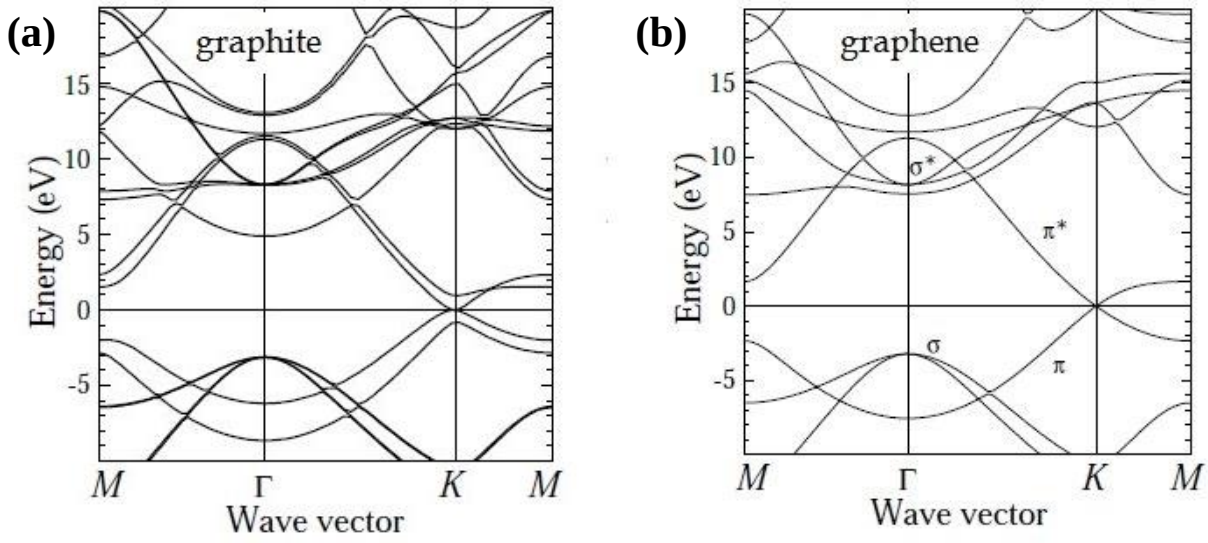


Figure 1.4: Electronic band structures of (a) graphite and (b) graphene, from [31].

In terms of electronic properties, graphite is a qualified of electrical conductor, due to the absence of an energy gap in its electronic band structure [2] (**Figure 1.4a**). Due to the sheet staking structure, the electrical conduction occurs mostly in the plane where the charge carrier's mobility measured by electrical transport measurements at room temperature can reach values up to 15 000 $cm^2 V^{-1} s^{-1}$ [3].

1.2 Graphene

1.2.1 Definition

Graphene is a two-dimensional (2D) carbon sheet corresponding to a single layer of graphite. Carbon atoms are sp^2 hybridized and form a honeycomb structure. It belongs to the family of Van der Waals materials like graphite, boron nitride, and transition metal dichalcogenides (TMDCs). Since van der Waals materials are characterized by weak interlayer interactions, it is relatively easy to separate the different layers and obtain atomically thin films qualified as 2D materials. The first result reporting the evidence of a graphene layer obtained by exfoliation of a graphite bulk crystal was published by A. K. Geim and K. S. Novoselov in 2004 [3]. The two scientists from Manchester were then granted a Nobel prize in 2010.

1.2.2 Crystalline structure

Graphene's hexagonal lattice can be decomposed into two inequivalent sublattices (**Figure 1.5a**). The crystalline structure is defined in real space by two lattice vectors $\vec{a}_1$ and $\vec{a}_2$ of coordinates:

$$\vec{a}_1 = \frac{a_{cc}}{2}\begin{vmatrix} 3 \\ \sqrt{3} \\ 0 \end{vmatrix} \qquad \text{(eq. 1.1a)}$$

$$\vec{a}_1 = \frac{a_{cc}}{2}\begin{vmatrix} 3 \\ -\sqrt{3} \\ 0 \end{vmatrix} \qquad \text{(eq. 1.1b)}$$

Where a_{cc} represents the carbon-carbon bond length equal to 0.142 nm (like in graphite). The reciprocal lattice is defined in k-space by the vectors $\vec{a}_1^*$ and $\vec{a}_2^*$ of coordinates:

$$\vec{a}_1^* = \frac{2\pi}{\|\vec{a}_1.(\vec{a}_2 \wedge \vec{e}_z)\|}\vec{a}_2 \wedge \vec{e}_z = \frac{2\pi}{3a_{cc}}\begin{vmatrix} 1 \\ \sqrt{3} \\ 0 \end{vmatrix} \qquad \text{(eq. 1.2a)}$$

$$\vec{a}_2^* = \frac{2\pi}{\|\vec{a}_1.(\vec{a}_2 \wedge \vec{e}_z)\|}\vec{e}_z \wedge \vec{a}_1 = \frac{2\pi}{3a_{cc}}\begin{vmatrix} 1 \\ -\sqrt{3} \\ 0 \end{vmatrix} \qquad \text{(eq. 1.2b)}$$

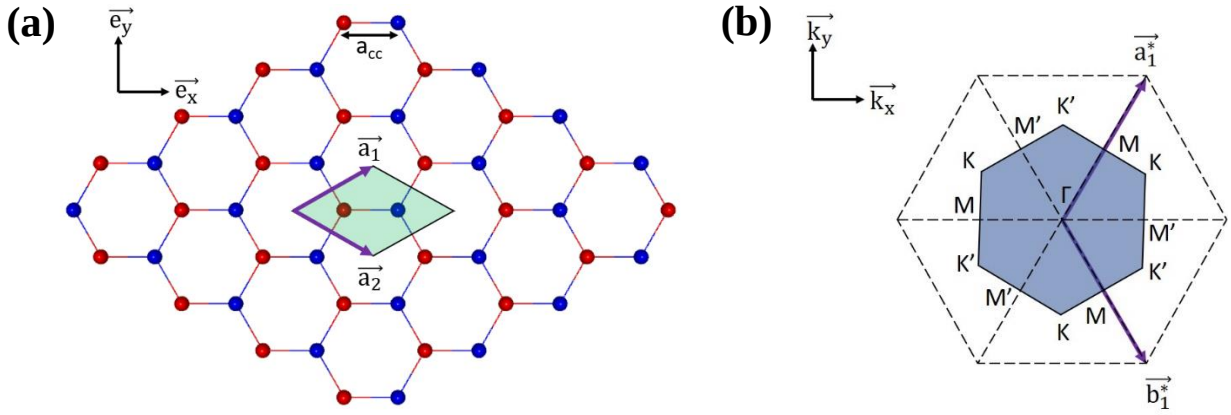


Figure 1.5: Graphene's (a) direct and (b) reciprocal lattices. The green area in (a) is the unit cell, and the blue area in (b) is the 1st Brillouin zone.

The blue hexagonal surface in **Figure 1.5b** corresponds to the Wigner-Seitz cell of the reciprocal lattice, also called 1st Brillouin zone. The centre of the hexagon is referred to as the Γ point, the corners are named K or K' points, and the middle of the hexagon's sides are the M or M' points.

1.2.3 Electronic structure

The electronic band structure given in **Figure 1.4b** shows that the valence and the conduction bands are in contact at the corners of the 1st Brillouin zone (K and K'), meaning that graphene is a semi-metal like graphite. The energy dispersion of the π and π* states (**Figure 1.6**) can be derived with the tight-binding model considering only first-neighbour interactions, which gives:

$$E(\vec{k}) = \pm|V_\pi|\sqrt{1 + 4cos\left(k_x\frac{3a_{cc}}{2}\right)cos\left(k_y\frac{\sqrt{3}a_{cc}}{2}\right) + 4\cos^2\left(k_y\frac{\sqrt{3}a_{cc}}{2}\right)} \qquad \text{(eq. 1.3)}$$

Where $V_\pi = \langle\varphi_a|\hat{H}|\varphi_b\rangle$ is the interaction term between first neighbours. The limited development at the vicinity of K and K' points ($k = K^{(\prime)} \pm \delta k$) gives:

$$E(k) = \pm\hbar v_f \delta k = \hbar v_f\sqrt{\delta k_x^2 + \delta k_y^2} \qquad \text{(eq. 1.4)}$$

Where ħ is the Planck constant divided by 2π and $v_f = V_\pi\frac{3a_{cc}}{2\hbar} = 1{,}0 \times 10^6\ \text{m}.s^{-1}$ [32] is the electron Fermi velocity in graphene.

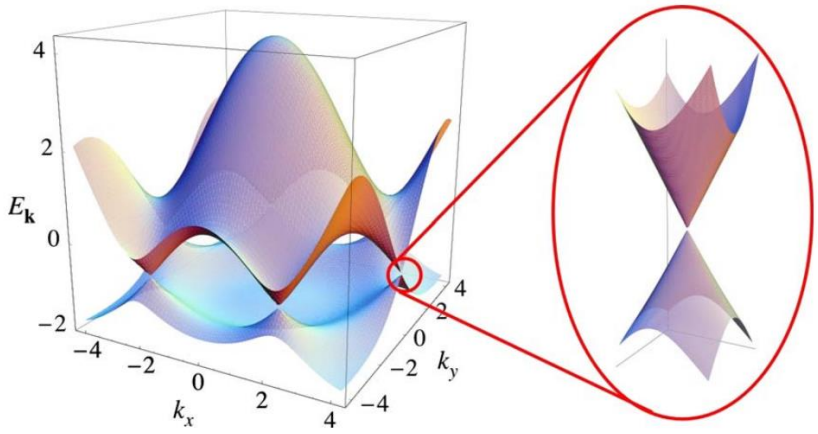


Figure 1.6: Energy dispersion of graphene's π and π* states, from [33], with a close-up on the Dirac cone at zone corners.

This linear energy dispersion is quite particular in condensed matter physics and gives some interesting properties to charge carriers in graphene. In many materials, the energy dispersion is parabolic and can be given by:

$$E(k) = \pm\frac{\hbar^2 k^2}{2m^*} \qquad \text{(eq. 1.5)}$$

The parameter $m^* = \left(\frac{1}{\hbar^2}\frac{\partial^2 E_{\pm}(k)}{\partial k^2}\right)^{-1}$ is the effective mass taken here as equal for holes and electrons for the sake of simplicity. Thus, the effective mass of charge carriers in graphene is null:

$$m^* = \frac{1}{\hbar^2}\frac{\partial^2(\pm\hbar v_f k)}{\partial k^2} = 0 \qquad \text{(eq. 1.6)}$$

Regarding this property, the analogy with photons comes easily if v_f is taken as an effective "speed of light". It suggests that holes and electrons mimic relativistic particles by their interaction with the periodic potential of graphene's honeycomb lattice. This low-energy region (|E| < 1eV) is known as the *Dirac cone* for its conical shape and the fact that charge carriers behave as quasiparticles described by the Dirac equation. These quasiparticles are called *massless Dirac Fermions* and can be seen either by electrons with a rest mass equal to zero or neutrinos with an electrical charge [32].

The symmetry of the Dirac cone between valence and conduction bands means that, for low energy values, the density of states in the valence and conduction bands is equivalent. Moreover, due to the conical shape of the energy dispersion, this region is characterized by a low density of states. It comes out that when the Fermi level is close to the charge neutrality point (Dirac point), the densities of holes and electrons are equal, and the electrical current is driven by the two charge carriers. It results in graphene being

fundamentally ambipolar.

1.2.4 Graphene based 2D electronic devices

The peculiar energy dispersion of graphene, along with the symmetry of the wave function, makes electrons in graphene very mobile. Value of carrier's mobility up to 180 000 $cm^2V^{-1}s^{-1}$ has been measured at room temperature [4], which is much more than other 2D materials such as monolayers of transition metal dichalcogenides (TMDCs) [7]. This property is an important asset for developing graphene-based electronic devices. However, the zero-gap band structure is a limiting factor. Since there is no activation barrier for charge carriers' diffusion, the maximal resistivity is limited, and the on/off ratio is very low compared to semiconductors. The on/off ratio (ρ_{max}/ρ_{min}) is generally around 5 (see **Chapter 4**), much less than TMDCs (10^8 for MOS_2) [7]. For this reason, graphene is not suitable for digital electronic applications but is much more interesting for sensors [5] and HF transistors [6].

Finally, a major challenge in the fabrication of graphene-based electronic devices is to be able to control locally the resistivity of a monolayer. The idea of having a graphene layer patterned with some resistive areas would correspond to planar conductor/insulator heterostructures, and that could be very promising for various applications in electronics or in biology (**Figure 1.9**).

1.3 Chemically induced sp^3-hybridization in graphene for 2D devices application

1.3.1 Diamond-like 2D film

In **1.1.2**, the electronic properties of graphite and diamond were compared, showing that carbon can be either an electrical conductor (graphite) or an insulator (diamond) depending on its hybridization. Those materials are bulk crystals, but graphite can exist in two dimensions in the form of graphene. Diamond does not exist in two dimensions, but diamond-like 2D films can be synthesized by converting graphene's carbon atoms' hybridization from sp^2 to sp^3. This can be done by covalently bonding an additional atom to each carbon. Hydrogen and fluorine radicals are interesting candidates because both have one non-bonded electron (H: $1s^1$ and F: $1s^2\ 2s^2\ 2p^5$). The full hydrogenation of a graphene layer leads to the formation of a 2D diamond-like hydrocarbon film called *graphane* (**Figure 1.7**). Previous theoretical studies predicted a stable relaxation of the crystalline structure in the *cis* configuration, which means that hydrogens are placed on different sides of the layer depending on the sublattice they belong to [18]. The carbon-hydrogen bond length is about 0.11 nm, and the carbon-carbon distance is increased by 0.01 nm compared to graphene [18]. The associated electronic band structure reveals a direct energy gap of 3.42 eV at the Γ point [18]. Similarly, a 2D diamond-like fluorocarbon film can be synthesized by fluorination.

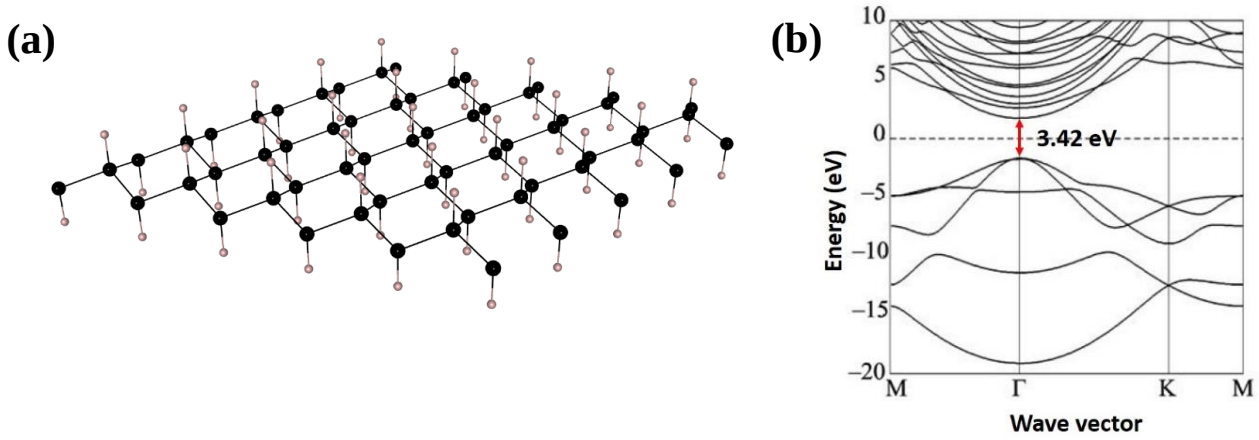


Figure 1.7: (a) crystalline structure and (b) electronic band structure of graphane, adapted from [18], with a red arrow to indicate the direct energy gap.

1.3.2 Functionalized graphene

Although graphane was predicted to be stable by Chernozatonskii *et al* [18], there are no studies in the literature reporting convincing proofs of its experimental synthesis. Moreover, graphane synthesis needs to be done from a free-standing graphene layer, which is not very helpful for electronic devices. In general, graphene is hydrogenated or fluorinated on a substrate, which means that hydrogen only has access to one side of the monolayer. In this case, the structure cannot relax similarly to graphane, except if carbon atoms can be covalently bonded to the substrate (possible for Iridium substrates, for example, [20]). A previous work reporting the calculation of the electronic density of states for various fluorine coverages shows that the energy gap increases with the fluorine concentration [21] (**Figure 1.8**).

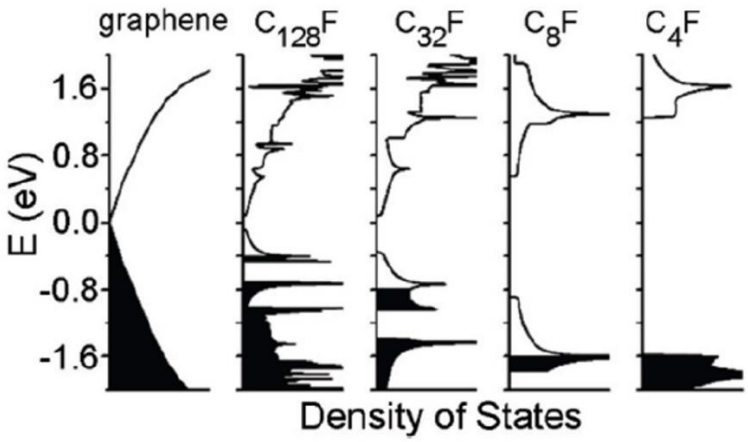


Figure 1.8: Electronic density of states of graphene and fluorinated graphene with different fluorine concentrations, from [21].

It means that, with a well-developed process, it is not only possible to open a gap in graphene's electronic band structure, but additionally, the value of this gap can be controlled by the hydrogen or fluorine concentration. Moreover, hydrogen (and possibly fluorine) can be partially or totally removed from a

graphene layer by thermal annealing under inert atmosphere [22]. Thus, graphene's conductivity can be controllably modified by hydrogenation or fluorination and restored by thermal treatment [12], making graphene a versatile material for 2D devices applications. Using a mask, it is possible to pattern a graphene layer with fully or partially sp^3 (resistive) areas, and such planar sp^2/sp^3 heterostructures can take the form of 2D transistors with a tunable on/off ratio or 2D electrodes for biological applications for example (**Figure 1.9**).

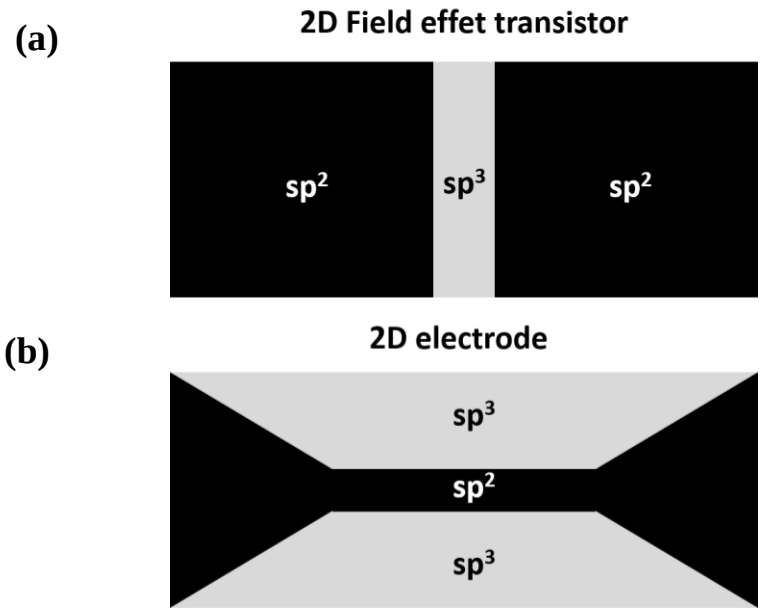


Figure 1.9: Examples of sp^2/sp^3 heterostructures for (a) electronic and (b) biological applications.

Chapter 2 Samples Fabrication

2.1 Graphene on Si/SiO_2 substrate

2.1.1 Mechanical exfoliation of HOPG on Si/SiO_2 substrate

Highly oriented pyrolytic graphite (HOPG) is a synthesized graphite characterized by a high alignment degree of the layers [30]. Due to weak interlayer interactions (vdW), the separation of one or several layers from the bulk crystal, called "exfoliation", can be performed. Different exfoliation methods are reported in the literature, including mechanical and thermal exfoliation [34]. The method used by A. K. Geim and K. S. Novoselov to obtain graphite thin films and monolayers is the "scotch-tape" technique, a mechanical exfoliation process consisting of peeling graphite with an adhesive tape. The same technique was used in the framework of this PhD to extract graphite thin films from a bulk HOPG crystal purchased from the company HQ graphene (**Figure 2.1a**). The method consists of putting a piece of adhesive tape in contact with the surface of the HOPG crystal (perpendicularly to the c-axis) and removing it. Normally, it is unnecessary to press the tape from behind if the adhesion is sufficient. A widely used tape for this purpose is the *magic tape* from Scotch, which was used for this work. Usually, the HOPG transferred to the tape is quite thick and appears dark (**Figure 2.1b**). A few more exfoliations are needed until a clear and homogeneous area is achieved. This can be done either with the help of another adhesive tape or simply by folding several times the same tape on itself (**Figure 2.1b**).

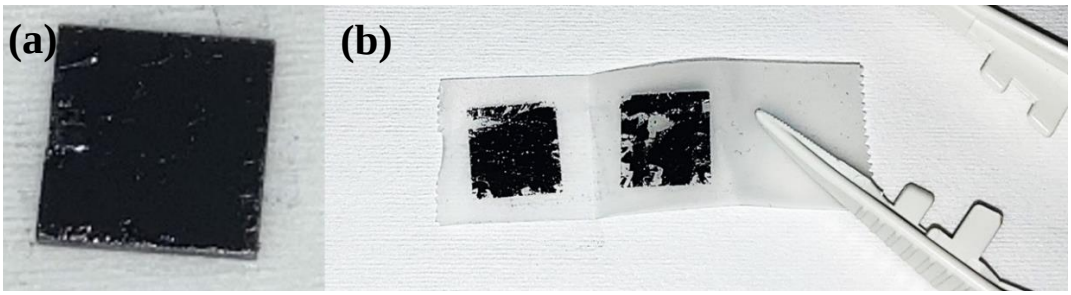


Figure 2.1: (a) HOPG bulk crystal and (b) exfoliated HOPG on adhesive tape.

The next step is to transfer the exfoliated HOPG onto a substrate. Here, Si/SiO_2 was selected for the following reasons:

(i) It can be used as an interferential substrate that allows for to recognition of graphene monolayers from the optical contrast (see details in **2.1.2**).
(ii) Since the doped Si is a conductor and the SiO_2 is an insulator, the substrate can be used to electrostatically control the charge density in graphene, which is primordial for electrical charge transport measurements (**Chapter 4**).

The transfer is done by putting the area of interest (i.e., clear and homogeneous) in contact with the surface of the substrate and pressing strongly with a finger at the back of the tape for approximately 30 seconds. After withdrawing the tape, due to vdW interactions between SiO_2 and graphite, one or several layers are

peeled off from graphite and stay on the substrate in the form of "flakes" (**Figure 2.2**).

In general, the substrate is previously cleaned with acetone and 2-propanol (IPA) in an ultrasonic bath for 5 minutes each to get rid of potential residues on the surface. This chemical cleaning is usually completed by a plasma treatment of the surface to make it free of remaining organic molecules. The process consists of placing the substrate inside a vacuum chamber ($10^{-6} < P < 10^{-5}$ mBar) and exposing it for 300 s to an oxygen plasma created by a constant O_2 flow of 25 sccm inside a 13.56 MHz radiofrequency (RF) field of 5 W. The created oxygen ions react with organic molecules adsorbed on the SiO_2 surface. The plasma-treated SiO_2 surface, terminated by charged silanol groups, has strong interactions with graphite, which has a significant effect on the transfer [31]. In particular, plasma cleaning allows for getting more flakes and usually larger monolayers (**Figure 2.2**). However, due to the hydrophilic nature of plasma-treated SiO_2 [35], exfoliation needs to be done directly after surface treatment (within a few seconds) to avoid having too much trapped water between graphene and SiO_2.

Although oxygen plasma treatment of SiO_2 allows for improving exfoliation, it affects the residual charge carrier density in the transferred graphene layer, which can complicate electrical transport measurements.

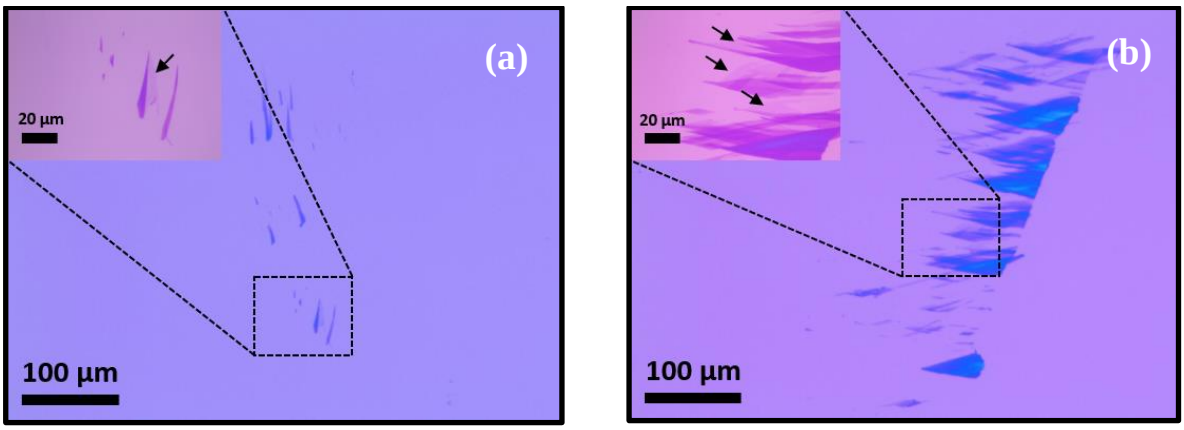


Figure 2.2: Optical image of graphite thin flakes deposited on (a) Si/SiO2 substrate and (b) plasma-cleaned Si/SiO2 substrate. The insets are higher magnification images of the framed areas, and the black arrows point at the position of monolayer graphene flakes.

2.1.2 Substrate effect on optical contrast

One of the interests in transferring exfoliated HOPG onto Si/SiO_2 substrates is to localize the different flakes and identify the number of layers from the optical contrast. The light interactions with the substrate can be used to enhance the electric field at the surface, maximizing the contrast and making graphene visible with an optical microscope [36]. However, the nature and the thickness of the substrate are determining parameters and need to be correctly selected to allow for distinguishing optically an atomic layer from the substrate. Those parameters can be optimized by numerical calculations of the optical contrast as a function of both the incident wavelength and the substrate thickness. For this purpose, the transfer matrix formalism can be used. This mathematical formalism allows us to define any optical system (even complex) by a transfer matrix T, such as:

$$\begin{pmatrix} A_1 \\ B_1 \end{pmatrix} = T \begin{pmatrix} A_2 \\ B_2 \end{pmatrix} = \begin{pmatrix} T_{11} & T_{12} \\ T_{21} & T_{22} \end{pmatrix} \begin{pmatrix} A_2 \\ B_2 \end{pmatrix} \quad \text{(eq. 2.1)}$$

Where A_1 and A_2 refer to a wave propagating forward, while B_1 and B_2 refer to a wave propagating backward (**Figure 2.3**). In the present case, there is only one light source (the lamp of the microscope) positioned on the "SiO_2 side" of the substrate. The amplitude of this incident wave is represented by A_1 and, for the sake of simplicity, can be normalized ($A_1 = 1$) without affecting the results of the calculations. A_2 and B_1 represent the total amplitude of the transmitted and reflected waves (respectively), and B_2 corresponds in this case to the wave reflected at the back of the sample after having propagated across its entire thickness. Here, since the sample thickness (~1 mm) is much larger than the wavelength of the propagating wave (400-800 nm) and silicon has a non-zero k index (imaginary part of the optical index) in this wavelength range, the propagating wave is sufficiently attenuated to consider B_2 equal to zero. As a consequence, **eq. 2.1** becomes:

$$\begin{pmatrix} 1 \\ B_1 \end{pmatrix} = \begin{pmatrix} T_{11} & T_{12} \\ T_{21} & T_{22} \end{pmatrix} \begin{pmatrix} A_2 \\ 0 \end{pmatrix} = \begin{pmatrix} T_{11}A_2 \\ T_{21}A_2 \end{pmatrix} \quad \text{(eq. 2.2)}$$

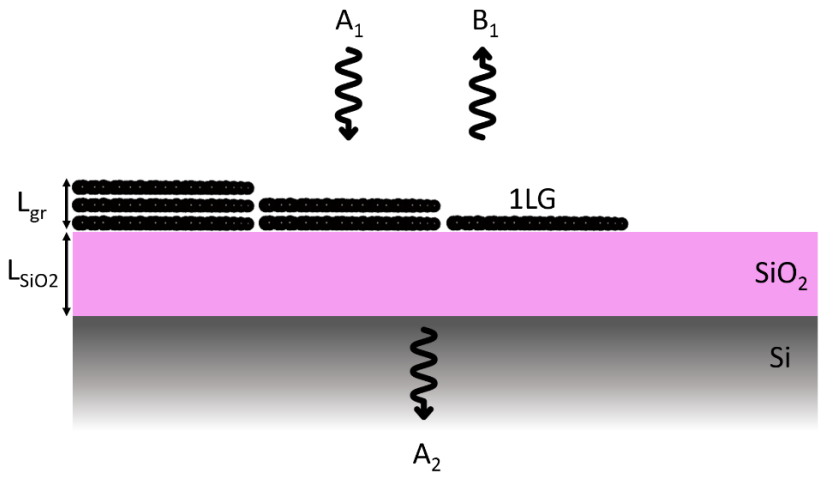


Figure 2.3: Schematic representation of a Si/SiO_2 substrate with various numbers (from 1 to 3) of graphene layers at the surface. The incident, reflected, and transmitted waves, respectively associated with the amplitudes A_1, B_1, and A_2, are represented by sinusoidal arrows.

It comes out that the normalized amplitude of the reflected wave is given by:

$$B_1 = \frac{T_{21}}{T_{11}} \quad \text{(eq. 2.3)}$$

The solution is only dependent on the T_{11} and T_{21} coefficients of the transfer matrix, which can be expressed as the matrixial product of all propagation and interface matrices of the optical system. The case considered here deals with a single-layer graphene on a Si/SiO_2 substrate. As a consequence, the transfer matrix T can

be written as:

$$T = \underbrace{T_{\tilde{n}_{air},\tilde{n}_{gr}}}_{\substack{air/gr.\\ interface}} \underbrace{T_{L_{gr},\tilde{n}_{gr}}}_{\substack{propag.\\ in\ gr.}} \underbrace{T_{\tilde{n}_{gr},\tilde{n}_{SiO2}}}_{\substack{gr./SiO_2\\ interface}} \underbrace{T_{L_{SiO_2},\tilde{n}_{SiO2}}}_{\substack{propag.\\ in\ SiO_2}} \underbrace{T_{L_{SiO_2},\tilde{n}_{SiO2}}}_{\substack{SiO_2/Si\\ interface}} \quad \text{(eq. 2.4)}$$

The transfer matrix for free propagation across a distance L in a medium of optical index $\tilde{n}(\lambda) = n(\lambda) + ik(\lambda)$ is given by:

$$T_{L,\tilde{n}} = \begin{pmatrix} e^{-i2\pi L\tilde{n}(\lambda)/\lambda} & 0 \\ 0 & e^{-i2\pi L\tilde{n}(\lambda)/\lambda} \end{pmatrix} \quad \text{(eq. 2.5)}$$

The real and imaginary parts of the optical index are plotted in **Figure 2.4** for Si, SiO_2 and graphene in the visible range.

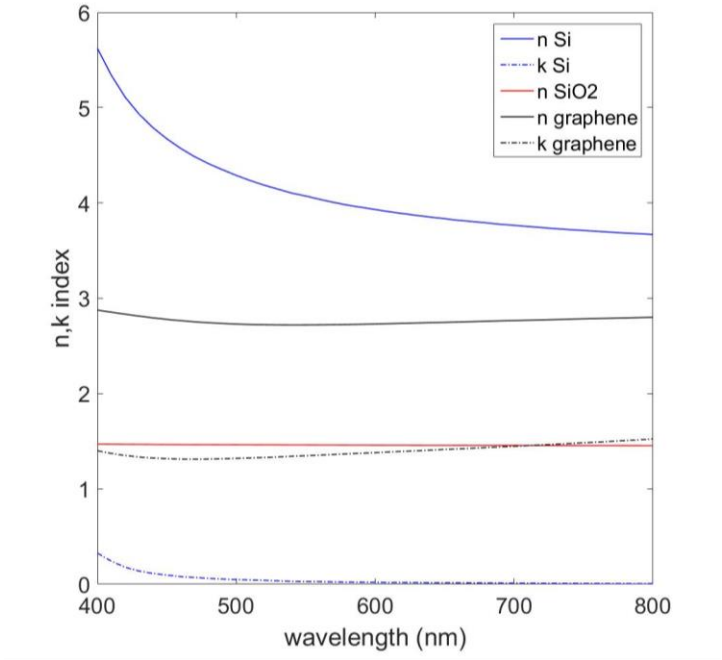


Figure 2.4: Plot of the real (n) and imaginary (k) components of the optical index in the visible range (400-800 nm) for Si, SiO2 and graphene. Data extracted from https://refractiveindex.info.

The transfer matrix for an interface between two media of optical indexes $\tilde{n}_1(\lambda)$ and $\tilde{n}_2(\lambda)$ is given by:

$$T_{\tilde{n}_1,\tilde{n}_2} = \frac{1}{t_{12}(\lambda)} \begin{pmatrix} 1 & r_{12}(\lambda) \\ r_{12}(\lambda) & 1 \end{pmatrix} \quad \text{(eq. 2.6)}$$

where the Fresnel coefficients $r_{12}(\lambda)$ and $t_{12}(\lambda)$ are wavelength dependent and correspond respectively to the

reflection and transmission coefficients for propagation from the medium of index $\tilde{n}_1(\lambda)$ to the one of index $\tilde{n}_2(\lambda)$. The reflection (respectively transmission) coefficient is defined as the amplitude ratio between the reflected (respectively transmitted) and incident electric field. Those coefficients are only dependent on the optical index $\tilde{n}_1$ and $\tilde{n}_2$, and their value can be approximated to [37]:

$$r_{12}(\lambda) = \frac{\widetilde{n_1}(\lambda) - \widetilde{n_2}(\lambda)}{\widetilde{n_1}(\lambda) + \widetilde{n_2}(\lambda)} \qquad \text{(eq. 2.8a)}$$

$$t_{12} = \frac{2\widetilde{n_1}(\lambda)}{\widetilde{n_1}(\lambda) + \widetilde{n_2}(\lambda)} \qquad \text{(eq. 2.9b)}$$

The Fresnel coefficients are not independent and must respect the following relationship:

$$r_{12}{}^{*} r_{12} + t_{12}{}^{*} t_{12} = 1 \qquad \text{(eq. 2.7)}$$

Finally, in the present case, the coefficients of the total transfer matrix T are variables depending on the wavelength, the SiO_2 thickness, and the number of graphene layers.

The optical contrast (C) can be defined as the relative difference between the reflected light intensity $B_1{}^{*}B_1$ with (I) and without (I_0) graphene on top of SiO_2:

$$C(\lambda, L_{SiO2}, N) = \frac{|I_0(\lambda, L_{SiO2}) - I(\lambda, L_{SiO2}, N)|}{I_0(\lambda, L_{SiO2})} \qquad \text{(eq. 2.7)}$$

Where L_{SiO2} is the SiO_2 thickness and N is the number of graphene layers.

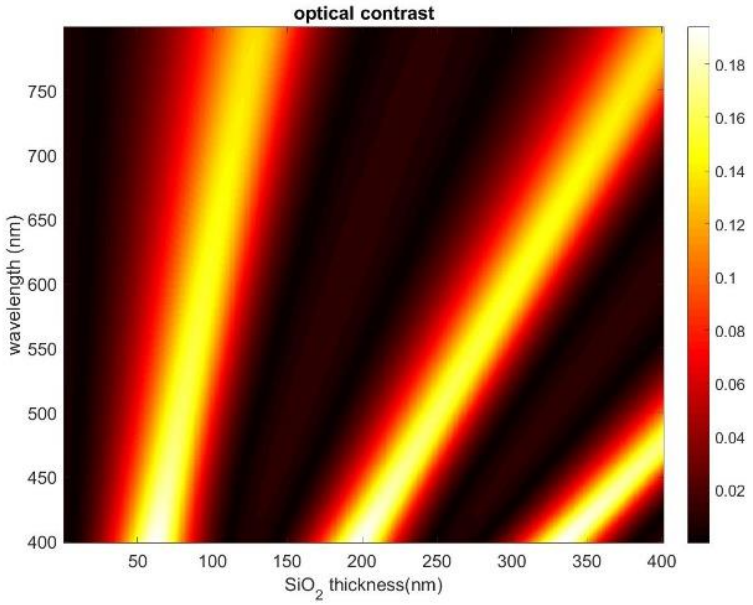


Figure 2.5: Map of the theoretical optical contrast of a graphene monolayer on Si/SiO_2 as a function of both the illumination wavelength and the SiO_2 thickness.

The map presented in **Figure 2.5** shows the optical contrast oscillation for one graphene layer on SiO_2, witnessing the strong effect of the interferential substrate and the importance of the oxide thickness to make graphene visible. For instance, graphene is invisible (i.e., $C \approx 0$) on a 20 nm SiO_2 substrate but is perfectly distinguishable if the SiO2 thickness is about 70 nm ($6\ \% < C < 18\ \%$). At the lab, most of the silicon wafers are ordered with an oxide thickness of 285 nm.

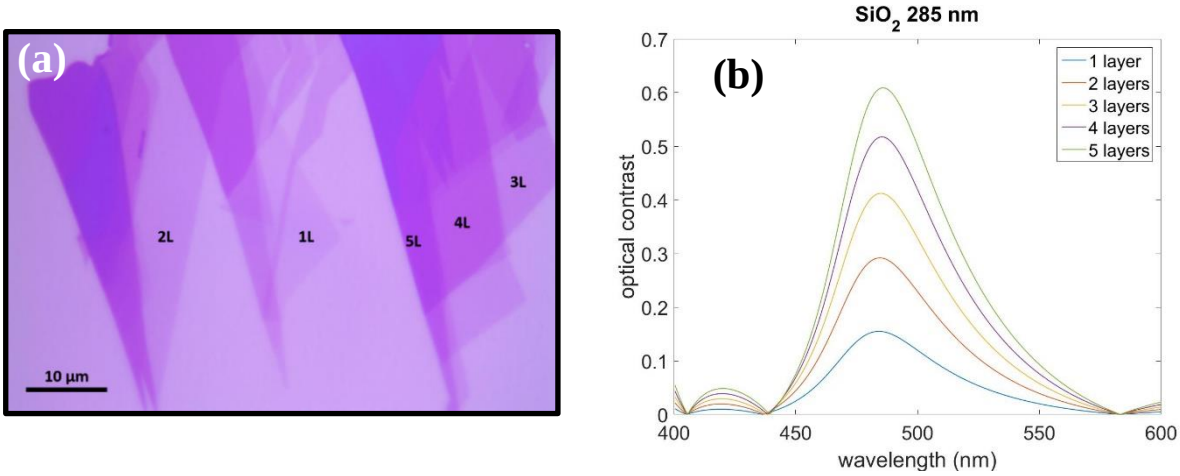


Figure 2.6: (a) Optical image of several graphene flakes deposited on a Si/SiO_2 substrate with an oxide thickness of 285 nm, presenting different contrasted areas corresponding to different numbers of layers. (b) Plot of the theoretical optical contrast for a SiO_2 thickness of 285 nm and various numbers (from 1 to 5) of graphene layers as a function of the wavelength.

Figure 2.6b reports a plot of the optical contrast corresponding to this thickness for different numbers of

graphene layers. It shows a significantly high contrast in a large range of the visible spectrum (500-700 nm) with a maximum at 570 nm. The contrast difference between different numbers of layers in this spectral region allows us to distinguish optically the change in reflectivity induced by a difference of one atomic layer (0.335 nm). In particular, there is a clear difference in contrast between a monolayer and a bilayer. **Figure 2.6a** shows an optical image of different numbers of graphene layers on a 285 nm SiO_2 substrate.

2.1.3 Microfabrication of graphene devices on Si/SiO_2

2.1.3.1 Global description of the protocol

Probing graphene's electronic transport properties requires several microfabrication steps to go from a graphene flake on SiO_2 (**Figure 2.7a**) to a patterned sample with electrical contacts and chosen geometry and dimensions (**Figure 2.7c**). In this work, HOPG was directly exfoliated on Si/SiO_2 substrates with an oxide thickness of 285 nm and patterned with L-shaped Cr/Au alignment marks distinguished by alphanumerical numbers. Then, since the resistance is dependent on geometric parameters of the sample, the graphene flake needs to be locally etched to define the geometry of the device and extract intrinsic parameters such as the conductivity, the mobility, and the residual charge carrier density (see **Chapter 4**). In general, the sample takes the form of a "Hall bar" that corresponds to a longitudinal channel crossed by several transversal channels (see **Figure 2.7b**). It allows to do 4-probe measurements to overcome the contact resistance and, particularly, to perform Hall measurements and determine both longitudinal and transverse resistance (see **Chapter 4**). Finally, microelectrodes are fabricated to connect the different channels to measure device properties. In the framework of this PhD, Hall bars with either 2 or 3 transversal channels were fabricated, involving respectively 6 or 8 electrodes per sample (see **Figure 2.7c**).

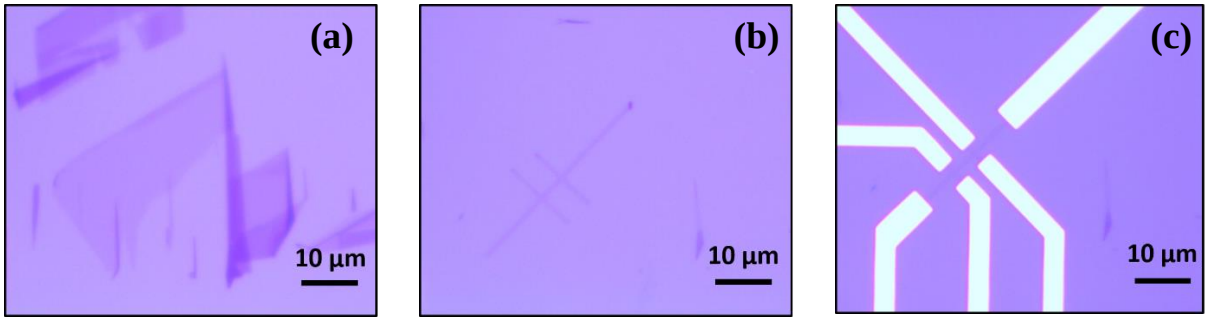


Figure 2.7: Optical images of a graphene flake on Si/SiO_2 (285 nm) (a) as exfoliated, (b) patterned and (c) connected with microelectrodes.

The fabrication of a graphene Hall bar from a graphene flake is achieved by sequentially performing the following steps:

1. Deposition of one layer of electron-sensitive resist (step 1 in **Figure 2.8**).
2. Electron beam lithography (step 2 in **Figure 2.8**).
3. Resist Development (step 3 in **Figure 2.8**).
4. Plasma etching (step 4 in **Figure 2.8**).
5. Resist removal (step 5 in **Figure 2.8**).

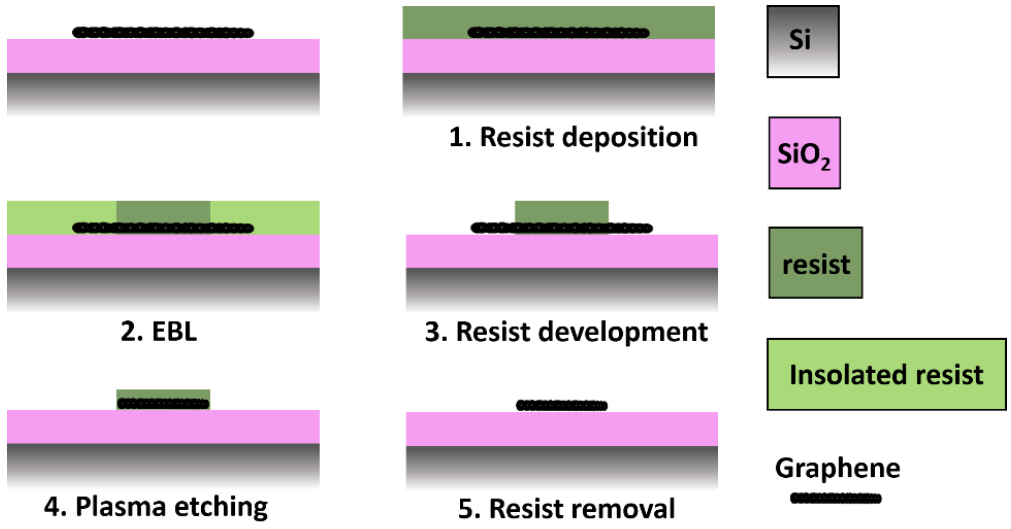


Figure 2.8: Schematic representation of the different steps of a graphene Hall bar fabrication from a graphene layer on Si/SiO_2.

The accurate positioning of microelectrodes is achieved by sequentially performing the following steps:

1. Deposition of three layers of electron-sensitive resist (step 1 in **Figure 2.9**)
2. Electron beam lithography (step 2 in **Figure 2.9**)
3. Resist Development (step 3 in **Figure 2.9**)
4. Metallization (step 4 in **Figure 2.9**)
5. Resist lift-off (step 5 in **Figure 2.9**)

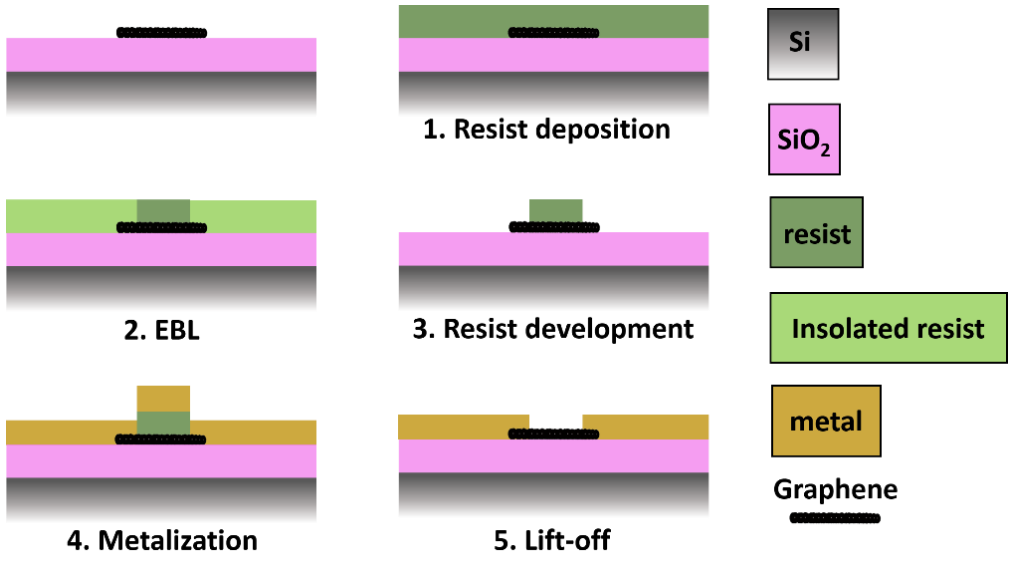


Figure 2.9: Schematic representation of the different steps of microelectrodes fabrication and positioning around a graphene Hall bar on Si/SiO_2.

2.1.3.2 Resist deposition

Thin layers of polymethyl methacrylate (PMMA), a positive electro-sensitive resist used for e-beam lithography (EBL), were deposited on top of the SiO_2 surface by spin-coating. Samples were previously placed in acetone and IPA baths (5 minutes each) for cleaning and then annealed at 170°C for approximately 3 minutes on a hot plate to remove water that can affect the adhesion of the resist. Then, a droplet of PMMA diluted in anisole was placed on top of the sample and was spread out by rotation at 3000 rounds per minute (rpm) for 45 s. Anisole was then evaporated by annealing at 170°C for 1 min, resulting in a homogeneous PMMA thin film on top of the SiO_2 surface. The deposit thickness at this rotation speed is dependent on the polymer's viscosity and the solid content in the solvent anisole [38]. At LPCNO, we have two different types of PMMA differentiated by their polymerization degree:

- PMMA 950k A2 (molecular weight: 950 kg/mol; solid content: 2%)
- PMMA 495k A3 (molecular weight: 495 kg/mol; solid content: 3%)

The estimated layer thickness after spinning at 3000 rpm for 45 s is about 75 nm for PMMA 950k A2 and 100 nm for PMMA 495k A3.

One layer of PMMA 950k A2 was deposited for the first mask (i.e., for etching), whereas the second one (i.e., for metallization) was composed of two layers of PMMA 495k A3 below 1 layer of PMMA 950k A2 (**Figure 2.10**) to obtain an inverse profile after development (**Figure 2.12**). Since the bottom layers have a smaller molecular weight, they are more soluble than the upper layer and, consequently, are overdeveloped by the developer. This profile is very important for the lift-off (see **2.1.3.8**).

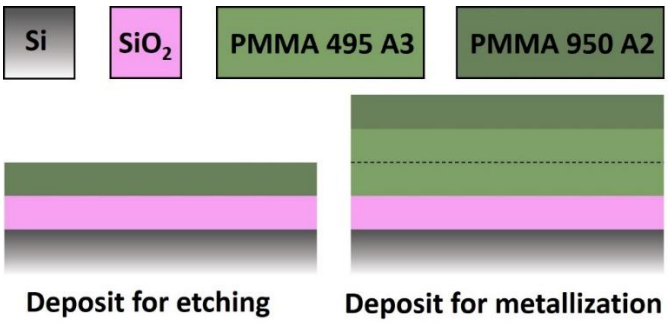


Figure 2.10: Comparison between the resist deposit for etching and metallization

2.1.3.3 Electron beam lithography

Electron beam lithography (EBL) consists of drawing a custom pattern on a resist layer with an electron beam. The surface of the sample is previously covered with an electron-sensitive resist layer and, with the help of a scanning electron microscope (SEM), a given electron dose is injected in the areas where the resist needs to be kept or removed, depending on whether it is a negative or positive resist, respectively. A negative resist is strengthened when exposed to the electron beam, whereas a positive resist is weakened. In general, a negative resist is used if a major part of the resist layer needs to be removed, whereas in the opposite case, a positive resist is more adapted. The interest in using electrons instead of photons, as is the case for laser lithography, is to enable drawing very small patterns due to a smaller spot size and a smaller

diffraction limit ($\lambda_{electron} < \lambda_{laser}$). EBL resolution is mainly limited by electron scattering and proximity effects that are dependent on the couple resist/substrate. For PMMA, which has a positive character, the resolution limit lies below 10 nm [39].

In the framework of this PhD, EBL was used to create masks for either etching or metallization (**Figure 2.11**). All lithography sessions were carried out according to the following protocol:

(1) Beam parameters setting (performed away from the area of interest): Acceleration voltage (V_{AC}), beam current (I), working distance (WD). Typical beam parameters are: V_{AC} = 15 kV, I = 100 pA, and WD = 10 mm.
(2) Focus, astigmatism correction, and beam alignment (performed away from the area of interest).
(3) Mechanical alignment (performed away from the area of interest): Origin correction, angular correction, and 3-point correction. The alignment was performed using the alignment marks on the substrate.
(4) Scan setting: calculation of the minimal step and dwell time to provide a given electron dose (usually 220 µC/cm²). Most of the time, the step was around 20 nm.
(5) Electronic alignment (performed inside the area of interest): Fine alignment using electron detection.
(6) Scan: Electron beam scan of the area of interest with respect to a graphical design provided in the form of a Graphic Design System (GDS) file.

2.1.3.4 Resist development

The resist development consists of dissolving the positive (respectively negative) resist on the irradiated (respectively non-irradiated) areas. Since PMMA is a positive resist, it becomes more soluble after being exposed to electrons. The solvent used for development is called "a developer". A good developer for PMMA is the methyl isobutyl ketone (MIBK). In this work, MIBK diluted in IPA (1:3) was used as a developer. The resist was first developed for 30 s and then rinsed in IPA for 30 s to remove the MIBK and stop the reaction. Since the irradiated areas are more soluble, they go off quicker than the non-irradiated ones. This selective reaction allows for obtaining a mask (**Figure 2.11**).

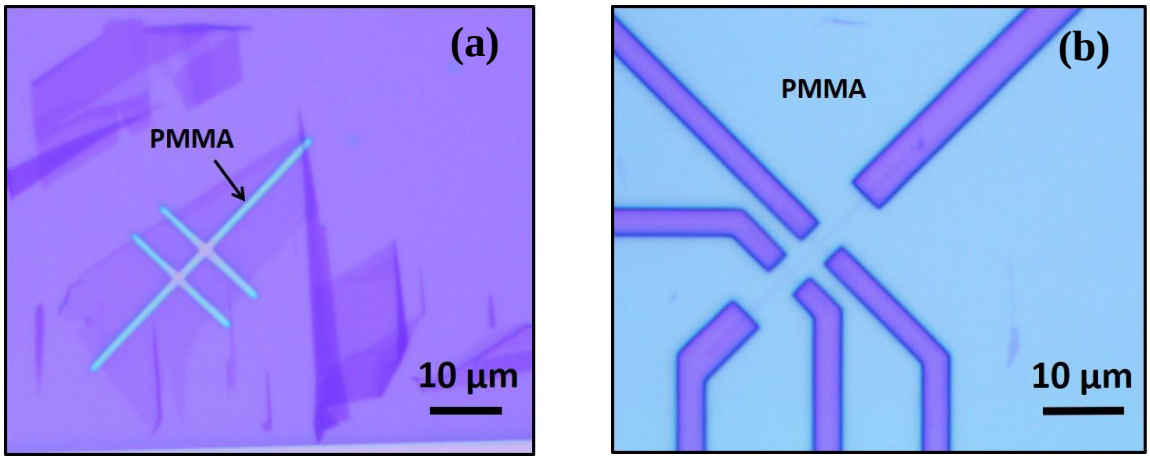


Figure 2.11: Optical images of a mask for (a) etching and (b) metallization.

2.1.3.5 Plasma etching

The monolayer and few-layer graphene on the non-masked area can be removed by plasma etching, also known as reactive ion etching (RIE). The plasma (ionic gas) is created by stripping electrons from gas molecules with a radiofrequency (RF) electric field. In addition, a bias voltage is applied between the sample and the chamber body, inducing an electric field to accelerate the ionized molecules toward the sample's surface. In this work, the recipe used to etch graphene involved a gas mixture composed of argon and oxygen injected with constant flows of 16 sccm and 8 sccm, respectively. The species were ionized by a 5W RF power for 20s. The process was iterated several times (between 4 and 8) until the non-masked monolayer and few-layer graphene areas were completely etched.

2.1.3.6 Resist removal

Since PMMA is soluble in acetone, samples were placed in an acetone bath for approximately 10-15 minutes and then in an IPA bath for approximately 5-10 minutes to remove acetone residues.

2.1.3.7 Metallization

The electrodes were made of a metallic layer of 30 nm: 5 nm of chromium below 25 nm of gold. The interest of using gold for electrical contacts is due to its good electrical conductivity and its inert properties that prevent oxidation. Chromium was used to guarantee a good adhesion to the substrate, which is not the case for gold.

Chromium and gold were deposited by Joule's effect evaporation under high vacuum (~10^{-8} torr). This process consists of heating a tungsten crucible containing one of these metals by injecting a high electrical current. Chromium evaporates around 350 A and gold around 250 A. The low pressure inside the chamber allows metallic atoms to evaporate directly before being deposited on the sample placed a few decimetres above the crucible. A quartz balance is positioned between the crucible and the sample to measure the deposition rate. The current is constantly adjusted during the process to keep the deposition rate at approximately 0.2 nm/s.

2.1.3.8 Resist lift-off

The resist removal is more complex here because PMMA is covered by the Cr/Au deposit. A specific resist profile is required to allow the solvent to penetrate below the Cr/Au layer (see **Figure 2.12**) and allow the resist lift-off. This last step consists of placing the sample in acetone at 60°C for approximately 15-20 minutes and, if needed, spraying the sample with the help of a syringe. Then, the sample is washed with IPA for approximately 5 minutes.

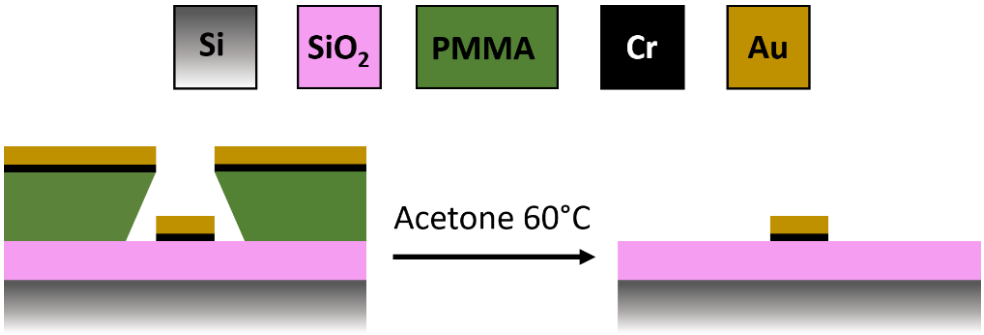


Figure 2.12: Schematic representation of the lift-off process after metallization, showing the inverse resist profile.

2.2 Graphene on ultra-flat Au <111> substrate

2.2.1 Ultra-flat gold

The interest in transferring graphene onto a gold substrate is the possibility of performing optical characterization at the nanoscale, such as tip-enhanced Raman spectroscopy (TERS). This kind of substrate is also commonly used by one of our collaborators, Kathleen Gough from the University of Manitoba (Winnipeg, Canada), for scanning near-field optical microscopy (SNOM). In the framework of this PhD, TERS can provide evidence of the presence of chemisorbed hydrogen or fluorine atoms on specific nanoscale regions of graphene's surface. More details concerning this characterization technique will be given in **Chapter 4**. However, since TERS is a technique based on surface plasmon excitation [40], a gold (or silver) substrate is required to optimize the Raman signal enhancement. Moreover, to avoid damaging the tip, a substrate with low surface roughness is preferable. For these reasons, transferring graphene layers onto ultra-flat gold substrates was required.

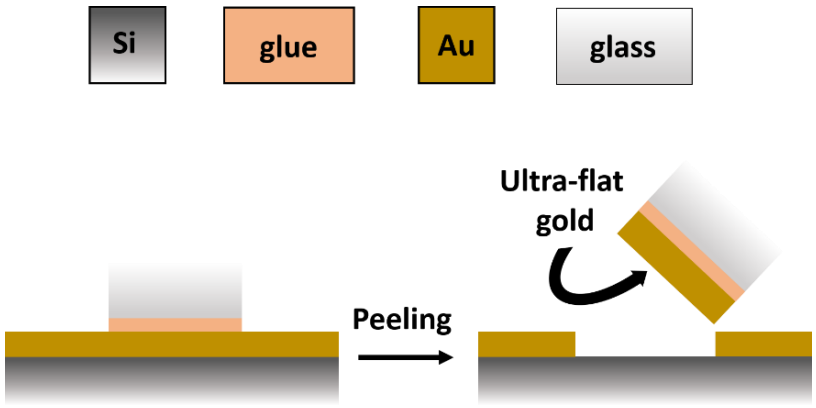


Figure 2.13: Schematic representation of the peeling process of a glass substrate glued onto a Si/Au substrate to obtain an ultra-flat gold surface.

Ultra-flat Au <111> substrates were purchased from Platypus Technologies. The company provides polished silicon wafers with a 100 nm gold (Au <111>) layer deposited on top of 1×1 cm glass chips glued to it. When peeling a glass chip from the substrate, the gold layer below is separated from the silicon wafer

(**Figure 2.13**). Silicon polishing before gold deposition makes the Si/Au interface perfectly flat and, since the entire gold layer is detached, the gold surface is as flat as the silicon surface. The company ensures a root mean square (RMS) roughness of 3.6 Å, significantly lower compared to the as-deposited gold layer (17.3 Å).

2.2.2 Mechanical exfoliation of HOPG on gold substrate

HOPG was mechanically exfoliated on gold substrates with the scotch tape technique described in **2.1.1**, but without plasma treatment. However, contrary to Si/SiO_2, the optical contrast of graphene monolayers on gold is quite low due to the absence of electric field enhancement by interference effect. That constitutes a real challenge to identifying monolayer flakes on the gold surface. To overcome this issue, the following procedure was intended:

(1) Exfoliation of HOPG on a Si/SiO_2 substrate to identify the monolayer flakes by optical contrast, taking pictures with different magnifications to determine their locations relative to few-layer graphene flakes having higher optical contrast on gold.
(2) Transfer of the graphene monolayer and neighbouring few-layer flakes from the Si/SiO_2 to the gold substrate using the hot pick-up technique [41], a transfer method based on the temperature dependence of adhesion forces between polymers and vdW materials. A polycarbonate film was used in this case.
(3) Polycarbonate removal with chloroform.

Unfortunately, chloroform appeared to strongly damage the gold substrate by dissolving the glue layer at the interface between glass and gold (see **Figure 2.13**). For this reason, this procedure was abandoned, and HOPG was just directly exfoliated on gold. The low optical contrast made the identification of monolayers challenging, but not impossible. A trick consists of scanning the sample with a low magnification microscope objective (×10, for example) to localize few-layer flakes and then observing the neighbourhood of these flakes with a high magnification microscope objective (×50, for example). It is quite common to find monolayer regions in the vicinity of few-layer areas. The less contrasted regions (see **Figure 2.14**) are likely to be monolayer flakes, which must constantly be confirmed by Raman spectroscopy.

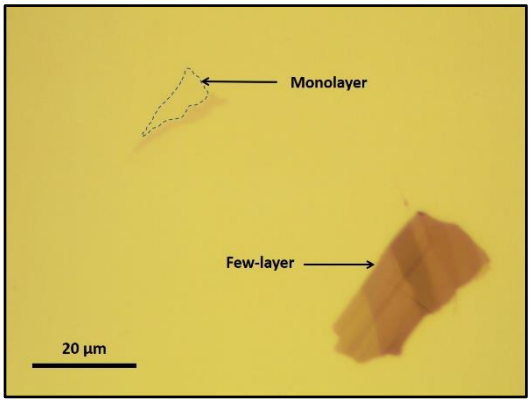


Figure 2.14: Optical image of a monolayer and a few-layer graphene flake on a ultra-flat gold substrate captured with a ×50 magnification microscope objective.

2.2.3 Polymer-assisted transfer of CVD-grown graphene layer

Since gold is a metal, it is difficult to see the change in reflectivity between the substrate and a graphene layer because there is no electric field enhancement induced by interferential effect. As a consequence, performing exfoliation directly on gold is not recommended since it is very difficult to localize optically the transferred monolayer graphene flakes. To overcome this issue, the transfer of large-area graphene layers was realized. CVD-grown polycrystalline graphene films on copper foils were purchased from Graphenea and transferred from copper to ultra-flat gold substrates. The company announces that the copper foil thickness is about 18 µm and more than 95% of the surface is covered with a polycrystalline graphene layer characterized by an average grain size of about 20 µm. Many different protocols were intended to successfully perform the transfer, but none of them really ended in a perfectly clean and flat graphene layer on gold. Most of the time, the transferred graphene was either ripped and wrinkled or contaminated by polymer residues. Several results from the literature reported very impressive quality transfer [42-45], particularly the paraffin-assisted transfer method [45], but they could not be reproduced during this PhD. Nonetheless, this section provides details concerning the most used protocol in this work, which is the polymer-assisted wet transfer. It consists of using a polymer (usually PMMA) thin film as a sacrificial layer to transfer graphene from its copper foil to a target substrate (**Figure 2.15**).

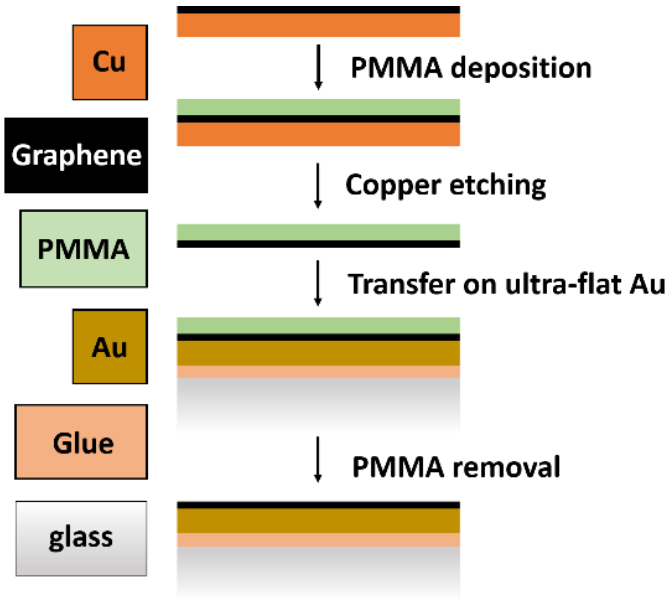


Figure 2.14: PMMA-assisted transfer of CVD-grown graphene from copper foil to ultra-flat gold substrate.

The protocol consists of the following steps:

(1) A thin layer of PMMA 950k A2 is deposited by spin-coating on one side of the graphene/copper foil (the side containing the CVD grown graphene layer).
(2) The foil is placed at the surface of an etchant in a way that has copper at the bottom and PMMA at the top. The etchant is an aqueous solution of ammonium persulfate prepared by dilution at a concentration of 10% in deionized (DI) water. The 18 µm of copper is usually etched within approximately 1h. After copper removal, the graphene/PMMA film remains at the surface and can be localized by eye due to the partial reflection of light on the transparent PMMA film.

(3) To limit the presence of ammonium persulfate on graphene, a rinsing step is required. However, it is concretely very difficult to transfer the graphene/PMMA film without folding it. To overcome this issue, the ammonium persulfate solution was diluted several times with DI water to decrease the concentration.

(4) The graphene/PMMA layer is transferred from the aqueous solution to the ultra-flat gold substrate. Two different methods have been used within this work:

(i) **Vertical fishing method (Figure 2.16a):** The graphene/PMMA film is fished from by the ultra-flat gold substrate by steeping it vertically in the solution and slowly moving it until it touches the film. Then the substrate is slowly removed from the solution, and the film spreads over its surface as the substrate rises.

(ii) **Scotch tape method (Figure 2.16b):** Before copper removal, a piece of adhesive tape is pasted on the PMMA film to keep a rigid film once copper is gone. Then, the scotch tape containing the PMMA/graphene film can be gently transferred to the ultra-flat gold substrate with a tweezer. Pressing on the tape with a finger after deposition helps to have good contact between the graphene and the substrate. It is recommended to heat the substrate at approximately 100°C during the transfer to limit the presence of water on the surface. For the same reason, blowing nitrogen on graphene before transfer can help remove water, thereby improving the quality of the graphene/gold interface.

(5) Water is moved away from the sample by spin-drying at a velocity of 2500 rpm for 45 s.

(6) The sample is placed on a hot plate at 100°C for 20 minutes to remove remaining water.

(7) The PMMA film is removed in acetone at 50°C for approximately 30 minutes, and the sample is washed in IPA for 5 minutes.

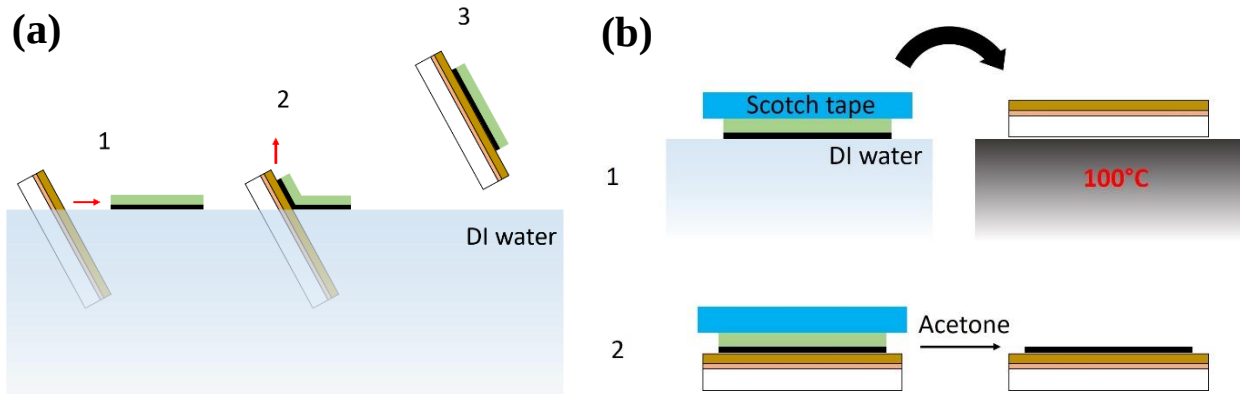


Figure 2.16: Schemes of (a) the vertical fishing technique and(b) the scotch-tape technique.

Chapter 3 Experimental techniques for graphene hydrogenation and fluorination

3.1 Graphene hydrogenation

3.1.1 Plasma hydrogenation

The high reactivity of hydrogen ions has been widely used to hydrogenate graphene, and many sources from the literature report successful results [12,24,46]. Plasma hydrogenation is usually performed in a Reactive Ion Etching (RIE) chamber [46] (**Figure 3.1**) or a Plasma-Enhanced Chemical Vapor Deposition (PECVD) reactor [24]. Those systems allow ionization of species and stabilize a homogeneous plasma state during long time-scales. In general, the gas mixture is composed of dihydrogen (H_2) and argon (Ar) and, due to their close ionization energy values (E_{H_2} = 15.76 eV and E_{Ar} = 15.42 eV) [46], the induced plasma is composed of ions from both species. Ar^+ ions are likely to create vacancies in graphene [47], meaning that structural damages are expected with this kind of plasma. The dominant hydrogen radicals are H_3^+ and, with lower concentration H_2^+ and H^+ [46].

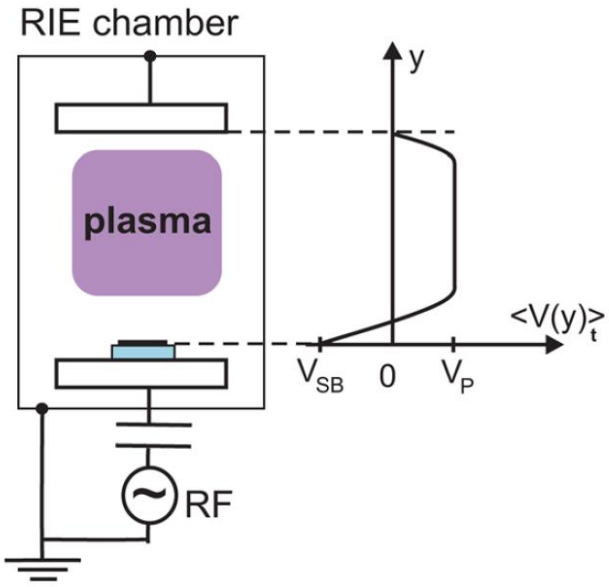


Figure 3.1: Schematic representation of the RIE chamber used in [46].

In 2009, Elias *et al* [12] were the first to demonstrate successful graphene hydrogenation by exposing graphene samples for 2 hours to 0.1 mbar of a DC hydrogen-argon plasma (10% of hydrogen). They even claimed to have successfully synthetized *graphane*, which corresponds to a fully hydrogenated graphene layer with hydrogen attached on both sides (see **Chapter 1**). However, regarding the corresponding Raman spectra (**Figure 3.2**), a significant proportion of sp^2-hybridized carbon remains after hydrogenation. Details concerning Raman spectroscopy in graphene will be given in the next chapter. For now, the most important

is to know that the G band corresponding to a Raman shift of ~1580 cm^{-1} characterizes the presence of sp^2-hybridized carbon whereas the D band corresponding to a Raman shift of ~1340 cm^{-1} reveals the presence of defects. Authors also demonstrated the reversibility of hydrogenation by partially recovering graphene after thermal annealing at 450°C for 24 hours under Ar atmosphere, as demonstrated by Raman spectroscopy (**Figure 3.2**).

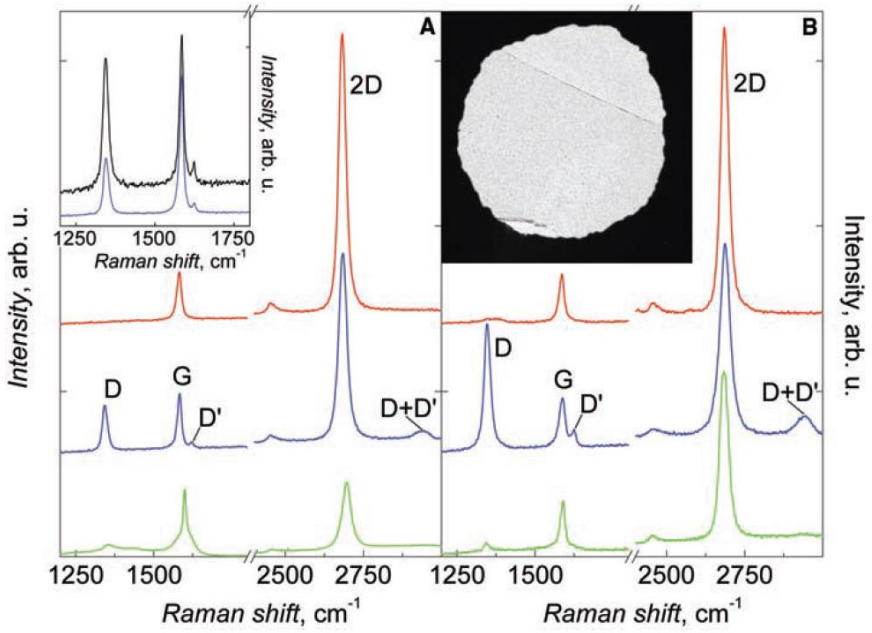


Figure 3.2: Raman spectra of pristine (red), hydrogenated (blue), and recovered (green) graphene (a) on Si/SiO_2 substrate and (b) on a TEM grid; from [12]. The left inset compares Raman spectra of one-sided (Graphene on SiO2) and double-sided (free-standing graphene on TEM grid) hydrogenated graphene. The right inset is a TEM image of a free-standing graphene membrane.

Luo *et al* [24] successfully hydrogenated graphene Si/SiO_2 substrate using a PECVD reactor. Samples were exposed to a hydrogen RF plasma of 10 W using a RF excitation of 13.56 MHz. The H_2 pressure in the reactor was about 1 torr. Then, graphene was almost perfectly recovered by vacuum annealing at 500°C for 30 minutes, as evidenced by Raman spectroscopy (**Figure 3.3**). However, the non-negligible intensity of the G band (**Figure 3.3**) before annealing demonstrates that a significant sp^2 surface fraction remains after exposure to the hydrogen plasma, meaning the hydrogenation is not complete.

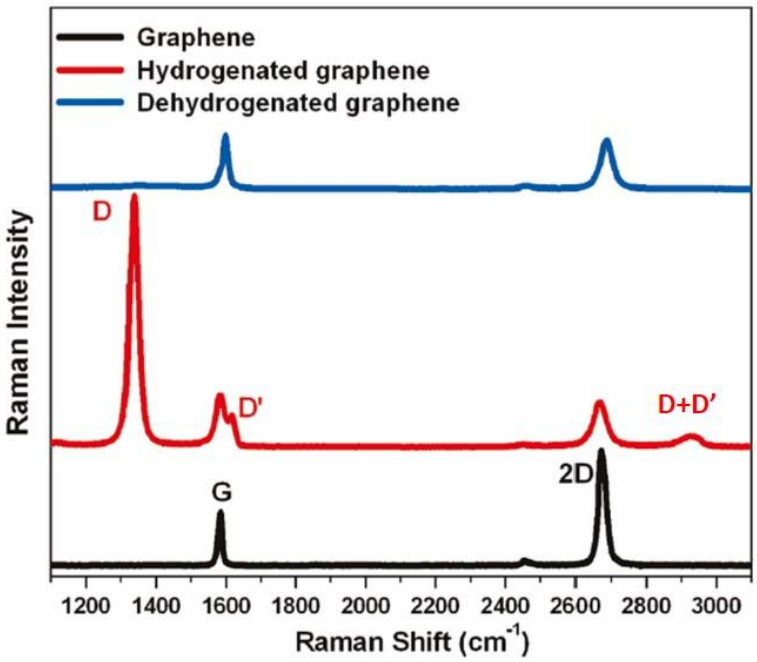


Figure 3.3: Raman spectra of pristine (black), hydrogenated (red), and dehydrogenated (blue) graphene; adapted from [24].

More recently, Wojtaszek *et al* [46] reported graphene hydrogenation enabled by RF plasma (13.56 MHz) using a RIE system (**Figure 3.1**). A plasma power of 3W was used to ionize a gas mixture composed of 15% H_2 in Ar, maintained at a constant pressure of 0.05 mbar by an input flow of 200 sccm.

3.1.2 Hot Filament Chemical Vapor Deposition (HFCVD)

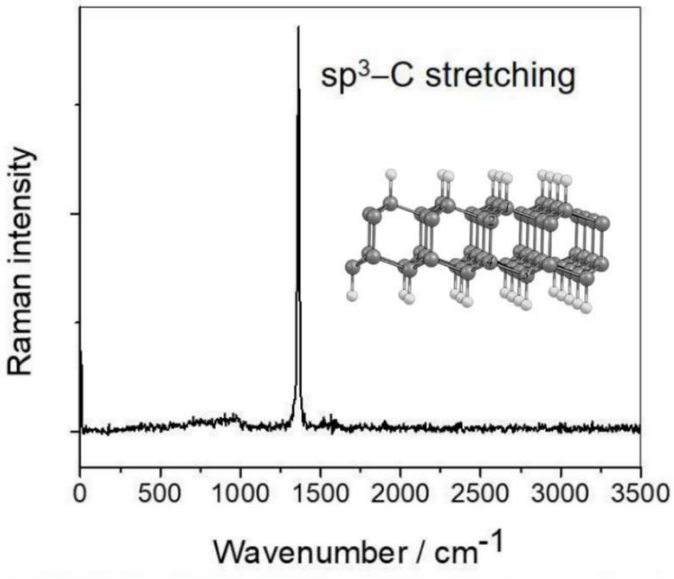


Fig 3.4: UV Raman spectrum of diamane; adapted from [10] with the DFT-optimized diamane's structure from [18]

HFCVD was the primary experimental method employed in this PhD to hydrogenate graphene. It is a CVD process commonly used for the synthesis of 2D diamond materials [10,48-50], where the gas phase is heated by hot filaments. Piazza *et al* [10] successfully performed the transformation of a graphene bilayer into a diamane single-layer (diamond-like C_2H) (**Figure 3.4**) using a commercial hot filament reactor (BWI 1000 from Blue Wave Semiconductors), and the same reactor was used here to hydrogenate graphene.

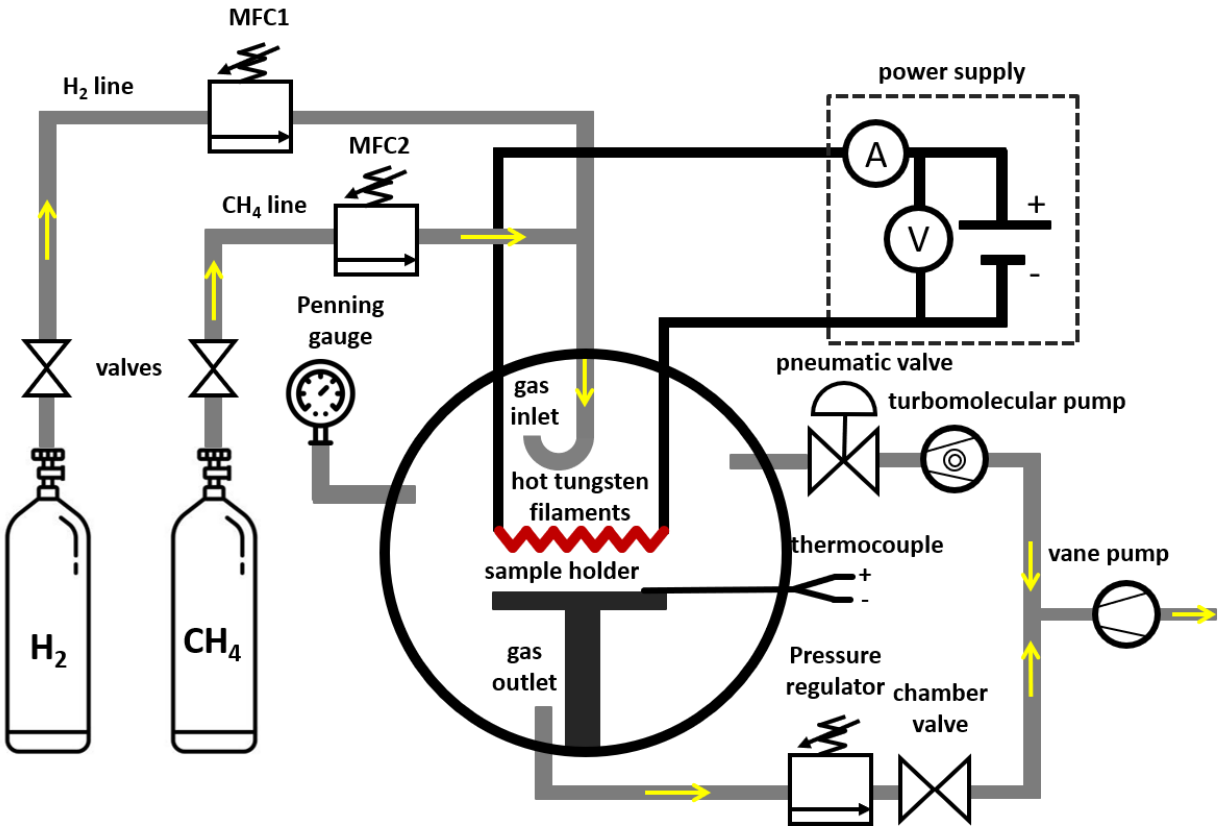


Figure 3.5: Schematic drawing of the HFCVD reactor.

The reactor is a six-way cross stainless-steel vacuum chamber permanently cooled by a liquid (15% water, 85% glycol at 18°C) flow in a closed-loop cooling circuit made of copper pipes covered with aluminium foils. The sample holder is a stainless-steel circular plate positioned horizontally, and its z-position is manually adjustable to set the distance between the sample and the filaments. The temperature of the sample is roughly estimated by a thermocouple (K-type; sheathed wires) positioned at the edge of the sample holder. The bottom part of the reactor contains the gas outlet linked to the primary pump. An automatic valve controlled by a pressure controller (MKS Instruments 640) placed between the outlet and the primary pump allows to keep a constant pressure inside the reactor during the process. The top part of the reactor contains the gas inlet connected to different gas lines (H_2 and CH_4) through MKS mass flow controllers (MFCs). A turbomolecular pump (secondary pump) from Pfeiffer connected to the reactor through a pneumatic gate valve allows evacuation of the chamber down to secondary vacuum values. An N_2 gas line is used for both gate valve opening/closing and chamber venting. The pressure inside the reactor is measured by a Penning gauge from Pfeiffer. Before each process, a pair of parallel tungsten (W) filaments

is attached horizontally between the gas inlet and the sample holder and electrically connected to a power supply (Sorensen DCS-E 3kW series DC). The light intensity of radiations emitted by the hot filaments is measured by a two-colour pyrometer (M90R2 model from Mikron Infrared, Inc.) placed out of the chamber on the other side of a glass window.

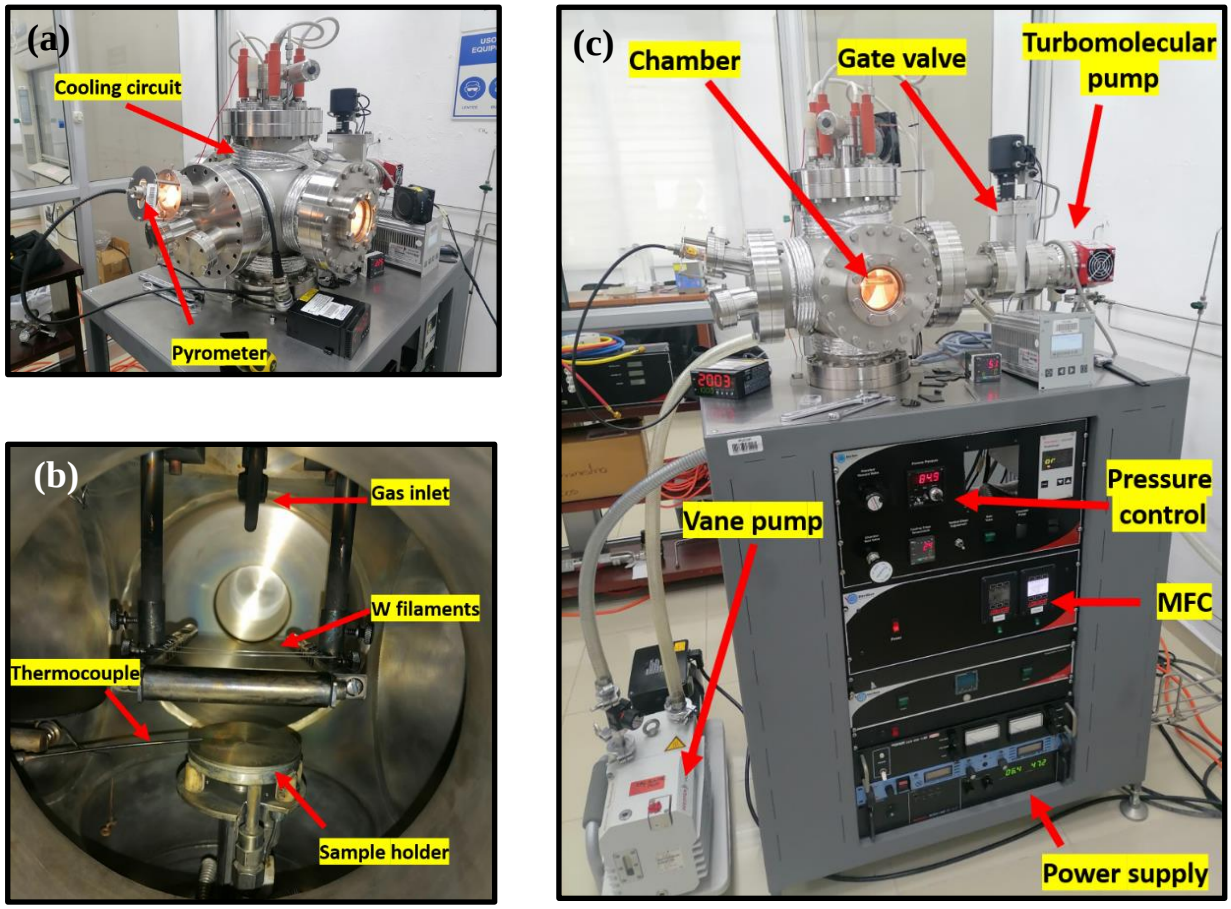


Figure 3.6: Pictures of the experimental setup from different views.

Similar to plasma hydrogenation, where molecular hydrogen is converted into ionic hydrogen to favour the chemical reaction with graphene, HFCVD aims to dissociate H_2 molecules into hydrogen radicals ($H_2 \rightarrow 2H\cdot$) that are more reactive due to their unpaired electron. The dissociation of H_2 molecules is thermally activated at high temperature. In hot filament processes, the thermal energy is provided by filaments heated by the Joule effect. Here, the two parallel W filaments are heated between 1800°C and 2300°C, corresponding to an electrical current between 40 A and 60 A, approximately. In order to enhance the thermal stability of the filaments and avoid W sublimation during the process, a carburization step is required before each hydrogenation process. Carburization consists of enabling carbon diffusion inside the filament, leading to a phase-change from W to W_2C or WC [51,52]. Carbon is provided by methyl radicals arising from the activation of a CH_4 gas phase at 1800°C [51]. To avoid any carbon contamination on the sample, the carburization of the filaments needs to be achieved before introducing the samples inside the chamber. Considering this requirement, the whole process follows this sequence:

(1) Introduction of two W filaments inside the chamber.
(2) Chamber closing and evacuation down to 6.4×10^{-4} torr.
(3) Carburization of the W filaments.
(4) Chamber venting and opening.
(5) Introduction of the sample(s) inside the chamber.
(6) Chamber closing and evacuation down to 6.4×10^{-4} torr.
(7) Hydrogenation of the sample(s).
(8) Chamber venting and opening.

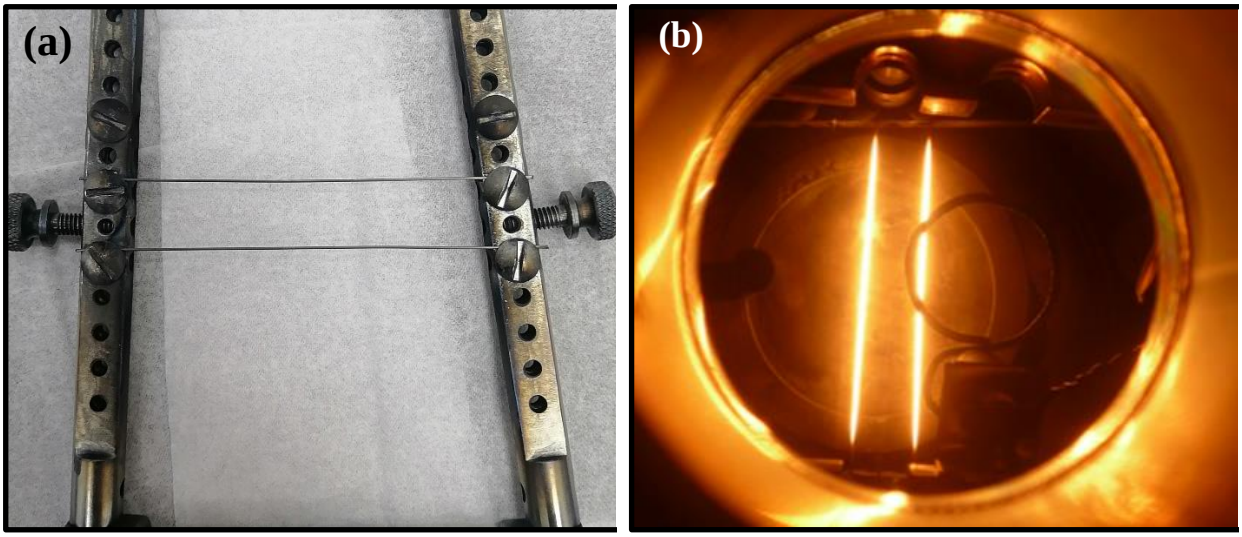


Figure 3.7: Pictures of the tungsten filaments (a) at ambient temperature and (b) at high temperature.

Carburization (step 3) and hydrogenation (step 7) consist of the following procedures:

(3) **Carburization:** Once the pressure inside the chamber is below 6.4×10^{-4} torr (chamber sealing does not allow it to go below), CH_4 is introduced and steady-state conditions (flow: 50 sccm; pressure: 10 torr) are stabilized. Then, an electrical current is injected into the filaments and slowly increases until the filaments' temperature reaches 1800°C (carburization temperature). In the framework of this PhD, W filaments were not completely carburized to avoid filaments breaking caused by thermal strain. Only partial carburization was performed, resulting in a pure tungsten filament carburized at the surface. This compromise allows for preventing surface tungsten atoms from sublimation during hydrogenation without excessively affecting the mechanical properties of the filaments. Thus, carburization was constantly performed for 5 minutes only.

(7) **Hydrogenation:** Once the pressure inside the chamber is below 6.4×10^{-4} torr, H_2 is introduced and steady-state conditions (flow: 1-100 sccm; pressure: 4-85 torr) are stabilized. Then, an electrical current is injected into the filaments and slowly increases until the filaments' temperature reaches the target temperature (between 1800°C and 2300°C). Samples are located 44 mm below the filaments, and their temperature (roughly estimated by a thermocouple) rarely exceeded 200°C. However, since light radiation

emitted by the hot filaments is likely to damage the graphene, it is required to place a shutter between the sample and the filaments. In this work, a Molybdenum disk positioned at either 3 cm or 1 cm above the samples was occasionally used as a shutter. Different process durations ranging from 10 minutes to 6 hours were explored.

3.1.3 Hydrogen beam under ultra-high vacuum

Hydrogen adsorption on graphite is of great interest in the area of interstellar chemistry, leading Liv Hornekaer *et al* [23] in 2006 to use an innovative technique for hydrogenation. The principle is similar to HFCVD (see **3.1.2**): H_2 molecules in the gas phase are dissociated into hydrogen radicals through thermal activation. However, some important differences are to be noted:

(i) The reactor is a scanning tunnelling microscope (STM) chamber evacuated down to ultra-high vacuum (UHV) to eliminate any risk of residual species that could react with the sample or with hydrogen radicals.

(ii) The hydrogen source is a commercial hydrogen atom beam source (HABS 40 from MBE Komponenten) directed toward the sample surface. The gas cracker is a tungsten capillary heated by hot tungsten filaments wrapped around it and heated by the Joule effect. A pure H_2 gas flow injected inside the hot capillary is decomposed at 80 to 99% into a hydrogen radical beam. The advantage of this system is the high directivity of the hydrogen beam that enhances the proportion of hydrogen atoms reaching the sample surface. Moreover, since H_2 cracking is performed out of the chamber, there is no risk for the sample to be exposed to energetic light radiations, and no shutter is required.

The company (HABS) estimates that the hydrogen beam produced is ion-free, and the atomic hydrogen flux density can reach values up to $10^{16} cm^{-2} s^{-1}$. However, since the beam is slightly divergent, the atomic flux density not only depends on the feed pressure and the temperature of the capillary but also on the distance from the source and the angle of emission.

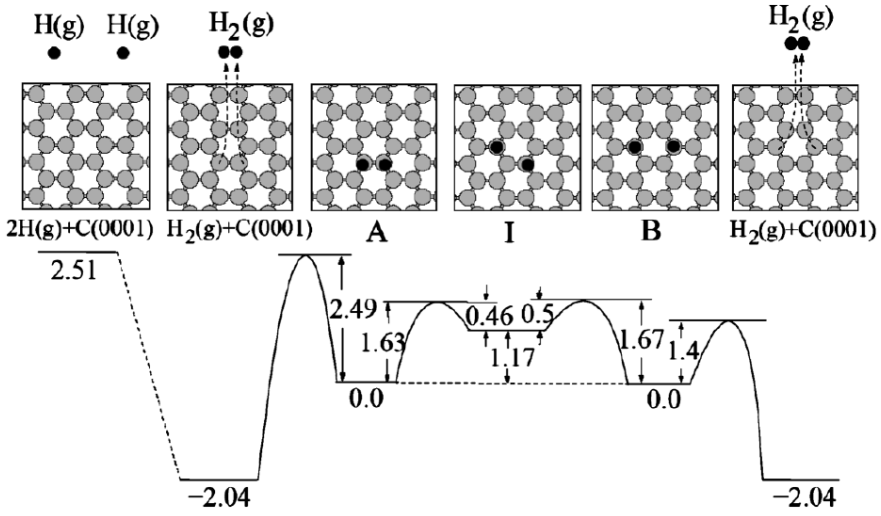


Figure 3.8: Energy barriers for the recombination of different types of hydrogen dimers chemisorbed on a graphite surface; from [23]. States A, I and B are associated with ortho, meta and para dimers, respectively.

With this technique, Hornekaer *et al* [23] published important results of hydrogen adsorbates on graphite imaged by STM. They evidenced that, at low atomic coverage, hydrogen forms dimers rather than monomers (less stable) and that *ortho* or *para* dimers are more energetically favourable than *meta* dimers (**Figure 3.8**).

Similar results were published by Balog *et al* [11] in 2009 on graphene grown on a SiC substrate. The authors provided STM images of different hydrogen coverages, evidencing the same dimer configurations as Hornekaer *et al* for low coverage. The extensively hydrogenated sample was dehydrogenated by annealing at 800°C, and the STM image demonstrates that graphene was completely recovered.

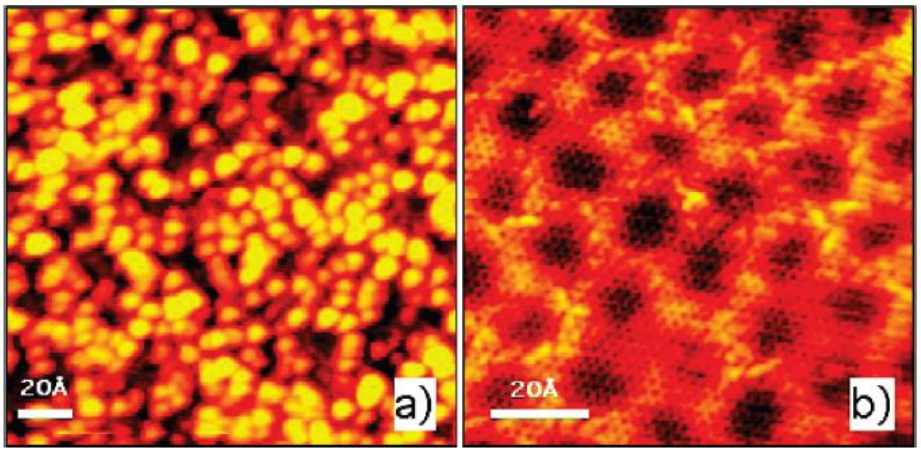


Figure 3.9: STM images of graphene on SiC (a) after hydrogenation and (b) after recovery by thermal annealing at 800°C; from [11]. Bright protrusions on (a) correspond to atomic hydrogen clusters.

In 2010, Balog *et al* [20] performed hydrogen adsorption on graphene grown on Ir (111), and angular-resolved photoemission spectroscopy (ARPES) measurements (**Figure 3.10**) revealed a bandgap opening of more than 450 meV for the highest hydrogen coverage.

This PhD allowed me to have the opportunity to spend a week at Aarhus University (Denmark) in the team directed by Liv Hornekaer. Some samples were brought there and exposed to the hydrogen beam, but, because of technical issues, almost none of them were hydrogenated.

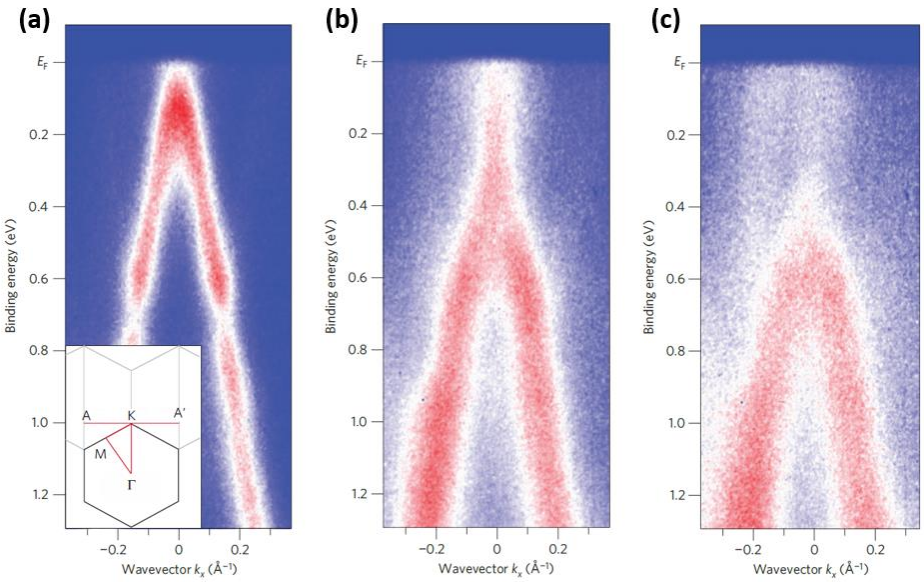


Figure 3.10: ARPES spectra along the AKA' direction of the Brillouin zone for (a) pristine graphene on Ir<111>, and after (b) 30 s and (c) 50 of atomic hydrogen beam exposure, showing a bandgap opening; from [20].

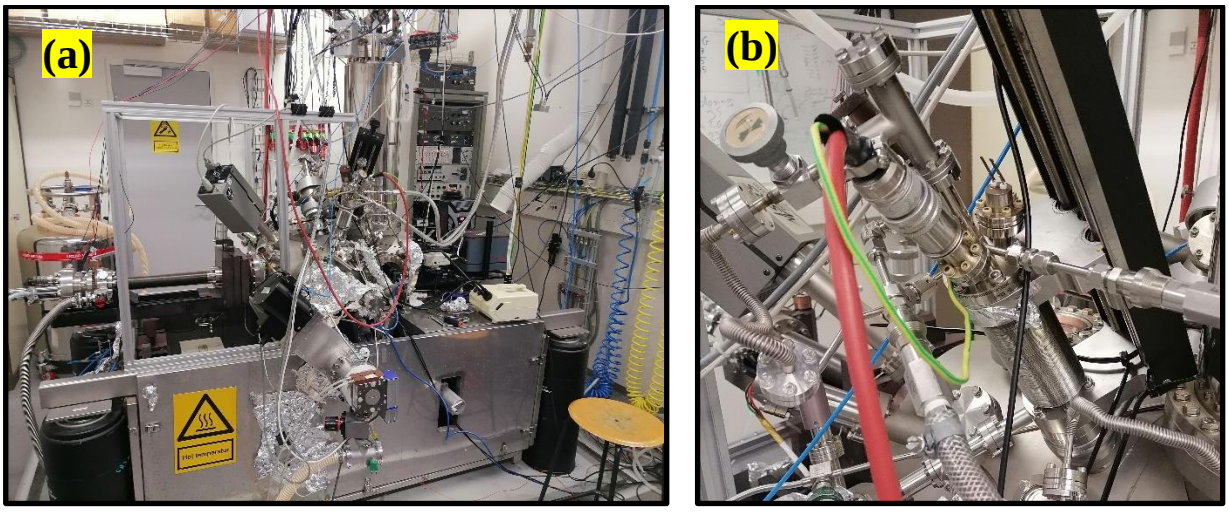


Figure 3.11: Photographs taken at Aarhus University of (a) the entire STM chamber and (b) the hydrogen beam source.

First, we tried with the commercial hydrogen beam source from HABS that was integrated on an STM chamber (**Figure 3.11**), but post-process Raman spectroscopy revealed no changes in graphene samples, even after extended exposure times. Then, we switched to another reactor that uses a UHV chamber coupled with another beam source (**Figure 3.12**). A Temperature Programmable Desorption (TPD) spectrometer was also integrated on this equipment, which allowed us to try detecting low hydrogen coverages. Many experiments were done with this source, even with deuterium instead of hydrogen, but still nothing was detected in Raman spectroscopy, except few samples that exhibited a small D band after exposure to a deuterium beam for 30 minutes using a feed pressure of 2×10^{-2} mbar. Those samples were also preliminarily

annealed at 800 K for 1 hour to remove any potential residue or water.

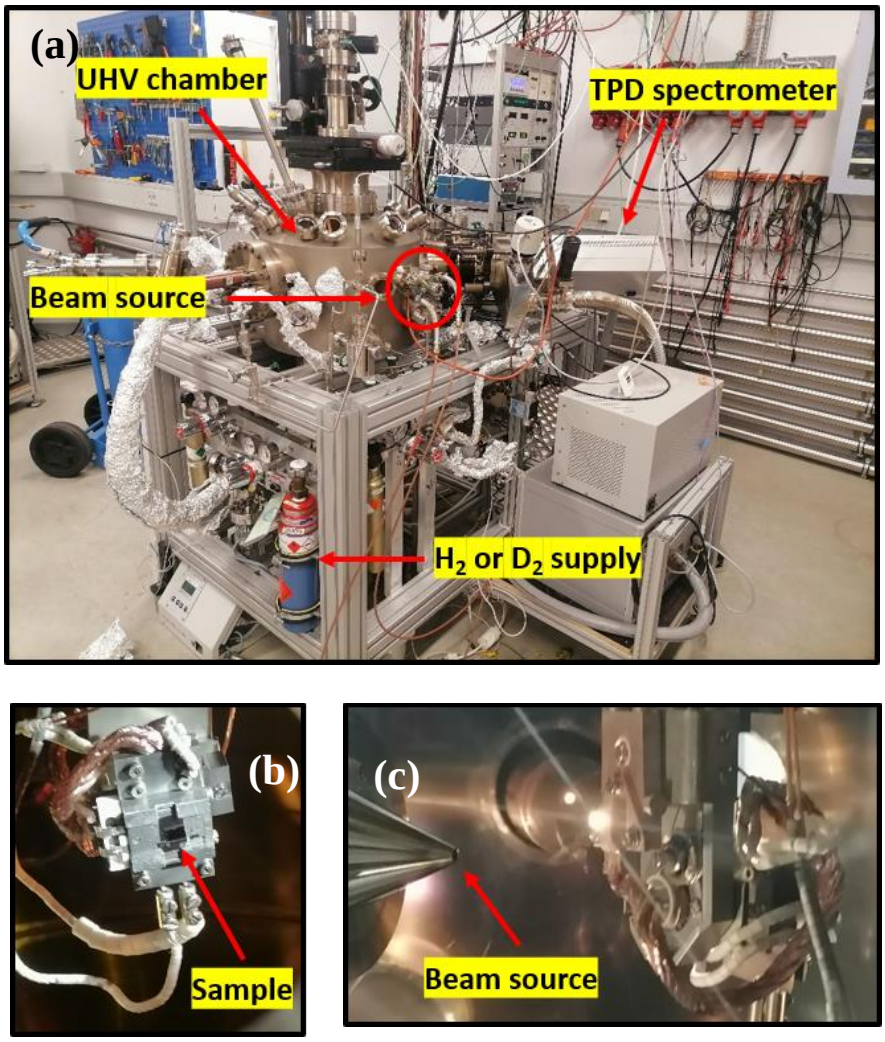


Figure 3.12: Photographs taken at Aarhus University of (a) another UHV chamber coupled with a hydrogen/deuterium beam source and a TPD spectrometer, (b) a sample attached vertically on the sample holder, and (c) the end of the beam source directed toward the sample.

3.1.4 Patterned hydrogenation

The fabrication of sp^2/sp^3 planar heterostructures is of great interest as it is a key issue to fabricate graphene-based 2D electronic devices, such as field effect transistors (FETs) (see **Chapter 1**). This kind of heterostructure requires a mask on top of the graphene layer, or patterned hydrogenation techniques such as hydrogenation enabled by e-beam. In these techniques, the hydrogen source is an electrosensitive resist, and the energy supply is an electron beam. The principle consists of releasing hydrogen from a resist layer covering the sample. Ryu *et al* [14] could hydrogenate graphene using silsesquioxane (HSQ). The Raman spectra of both HSQ and graphene for different electron concentrations (**Figure 3.13**) indicate that Si-H bond cleavage is enabled by e-beam, releasing hydrogen which covalently bonds to the graphene layer

beneath.

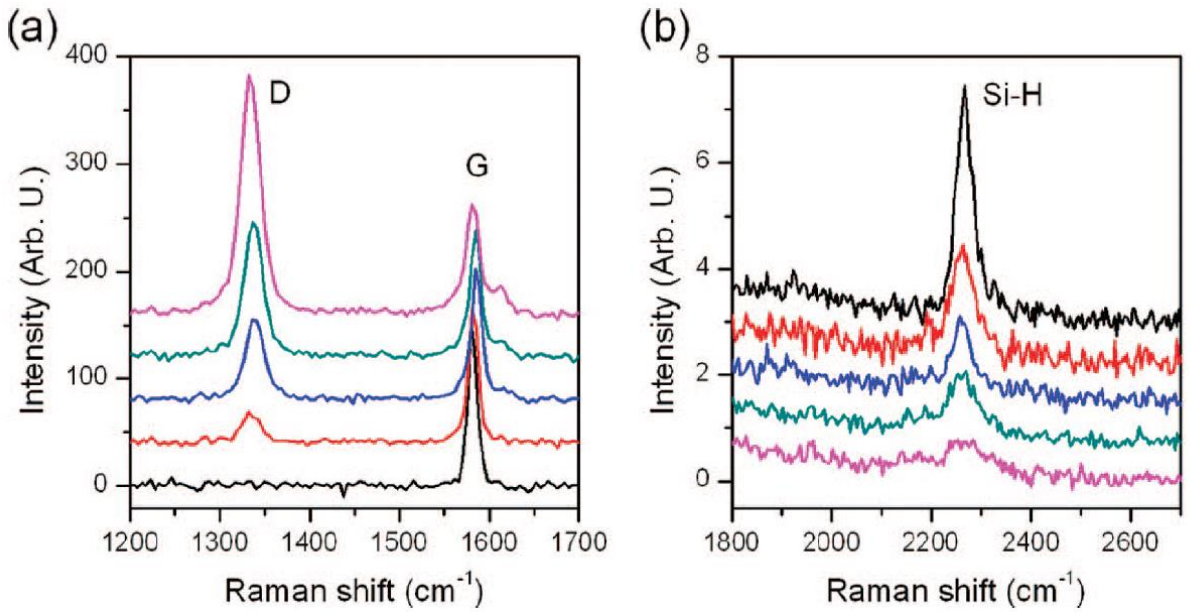


Figure 3.13: Raman spectra of (a) graphene and (b) HSQ after exposure to an electron dose of 0, 1, 2, 4, and 8 mC/cm^2 corresponding to black, red, blue, green and pink lines respectively. From [14].

Emelin *et al* [53] demonstrated similar results on bilayer graphene by releasing hydrogen from PMMA. The authors even claimed to have synthesized diamane nanostructures, but in my opinion, the publication lacks convincing characterization.

In the framework of this PhD, some tests were realized with PMMA and showed some interesting results in Raman spectroscopy. A series of six graphene flakes on a Si/SiO_2 substrate was prepared with the exfoliation technique described in **Chapter 2**. The monolayer nature of the flakes was confirmed by optical observation (see **Chapter 2**) and Raman spectroscopy. Then, approximately 75 nm of PMMA 950 A2 were spin-coated on top using the protocol described in **Chapter 2**, and, above each selected flake, a square area was scanned by an electron beam controlled by a scanning electron microscope (SEM) from JEOL. Every area was scanned by a 99.6 pA electron beam with 4 nm steps. The only varying parameters were the acceleration voltage (V_{AC}) and the electron dose (n). PMMA was then removed in acetone for 10 minutes, except in some scanned areas where the resist was cross-linked and became insoluble in acetone.

Figure 3.14 plots the Raman spectra of the six graphene flakes hydrogenated with different n and V_{AC} values. It shows that the D over G bands intensity ratio tends to increase with increasing n and decreasing V_{AC}. It means that hydrogen release is optimal when PMMA is exposed to a high electron density with low energy. Since C-H bond cleavage is activated by electron bombardment, it seems acceptable that the hydrogenation rate is related to n. The effect of V_{AC} can be tentatively explained by the fact that electrons with lower energies interact with atoms close to the surface (i.e., PMMA), whereas electrons with higher energies will be diffused deeper (i.e., SiO_2) and will have lower interactions with PMMA.

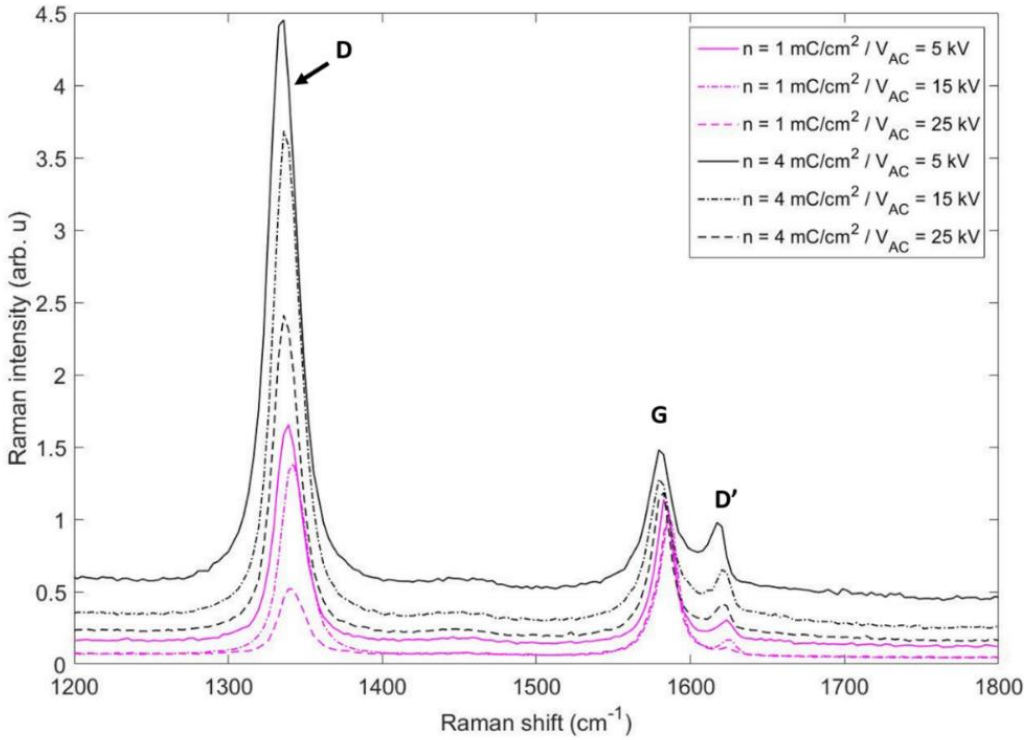


Figure 3.14: Raman spectra of the six graphene flakes hydrogenated with different *n* and V_{AC} values. For comparison purpose, all spectra are normalized with respect to the G band intensity.

3.2 Graphene fluorination

3.2.1 Gas phase fluorination

The most common technique used for fluorination consists of a gas phase process where fluorine chemisorption is thermally activated. Contrary to hydrogenation, which requires either ionic or atomic hydrogen, fluorination is enabled by a chemical reaction between graphene and molecular fluorine. The high reactivity of F_2 molecules constitutes a real challenge to obtaining fluorinated graphene. F_2 generally reacts strongly with graphene, forming volatile fluorocarbons such as CF_4 or C_2F_6 [17]. As an alternative, different approaches are suggested:

(1) <u>Exfoliation of fluorinated graphite</u>

This approach stands in two steps: (i) Fluorination of a graphite bulk crystal and (ii) mechanical exfoliation using the "scotch tape" technique (see **Chapter 2**) to obtain a single layer of fluorinated graphite. Withers *et al* [54] fluorinated HOPG by annealing at 530°C and 600°C in the presence of pure F_2, leading to fluorine concentrations of 28% and 100% respectively, as determined by nuclear magnetic resonance (NMR) spectroscopy. Fluorinated graphene monolayers could be isolated by mechanical exfoliation but, due to structural damages caused by the harsh fluorination conditions, the size of those flakes was found to be too small for device fabrication.

Marc Dubois from the University of Clermont-Ferrand (France) provided us with fluorinated graphite to test mechanical exfoliation on Si/SiO_2. The transferred flakes were found to be quite thick and much smaller than pristine HOPG flakes (**Figure 3.15**).

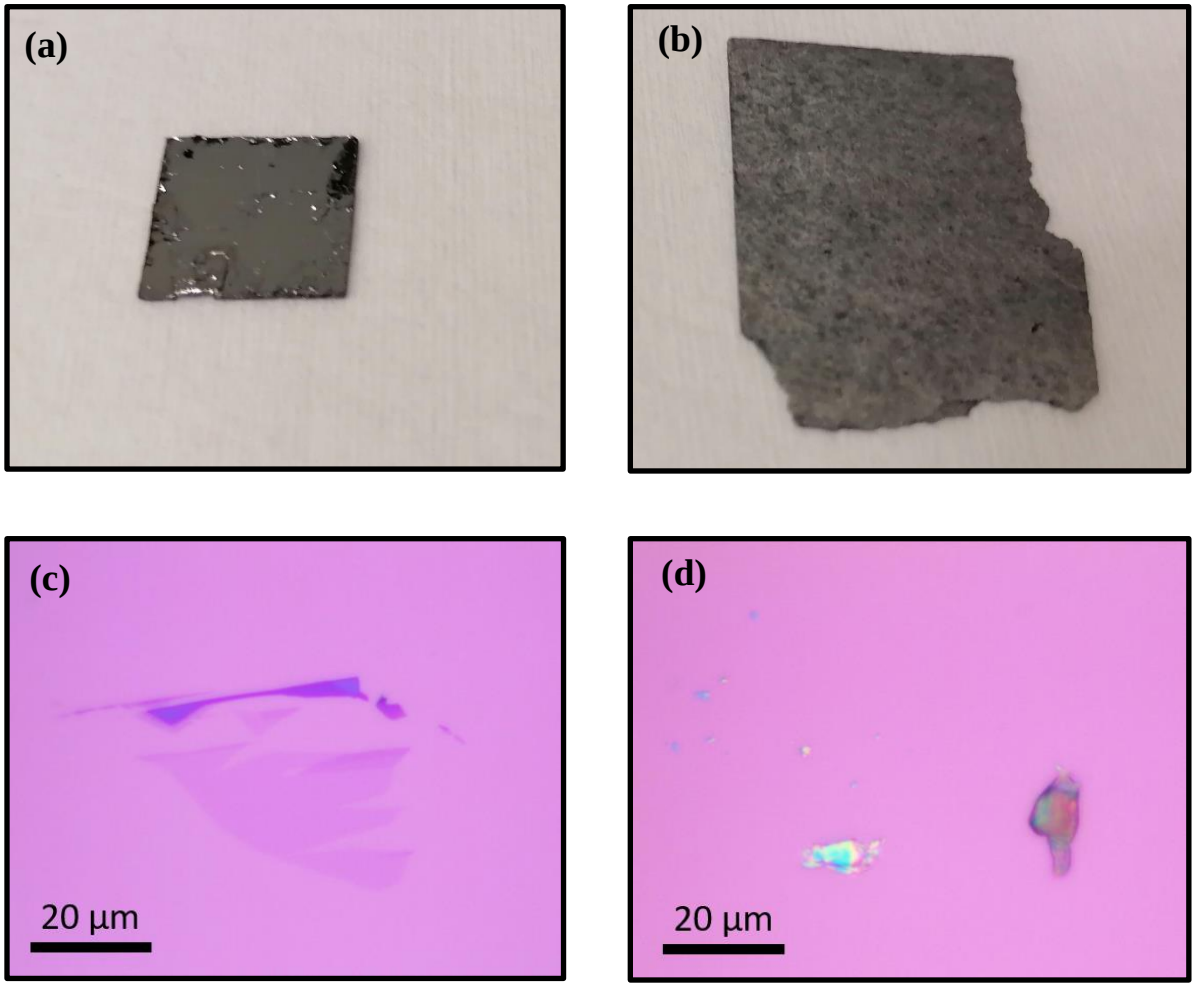


Figure 3.15: Pictures of (a,c) pristine and (b,d) fluorinated HOPG as (a,b) bulk crystals and (c,d) thin flakes deposited on Si/SiO_2 by mechanical exfoliation. The area with the lower optical contrast in (c) was identified as a monolayer.

In order to have large monolayer flakes, Withers *et al* [54] used Xenon difluoride (XeF_2) heated below 120°C to fluorinate HOPG, leading to fluorine concentration between 7% and 28%. XeF_2 is a widely used fluorination agent that allows better control of the reaction and avoids damaging the crystalline structure.

(2) Fluorination with XeF_2

Graphene fluorination can be controllably enabled by exposure to a XeF_2 vapor, a strong but etching-free fluorinating agent. Robinson *et al* [21] reported the formation of a C_4F phase (25% of fluorine) by one-sided exposure of graphene on Si/SiO_2 and a CF phase (50% of fluorine) by double-sided exposure of graphene on silicon on insulator (SOI) (**Figure 3.16**). The temperature of the XeF_2 vapor phase was about

30°C, and exposure times ranged from 30 to 1200 s. The authors also reported results of graphene recovery by reaction with hydrazine (N_2H_4) vapor.

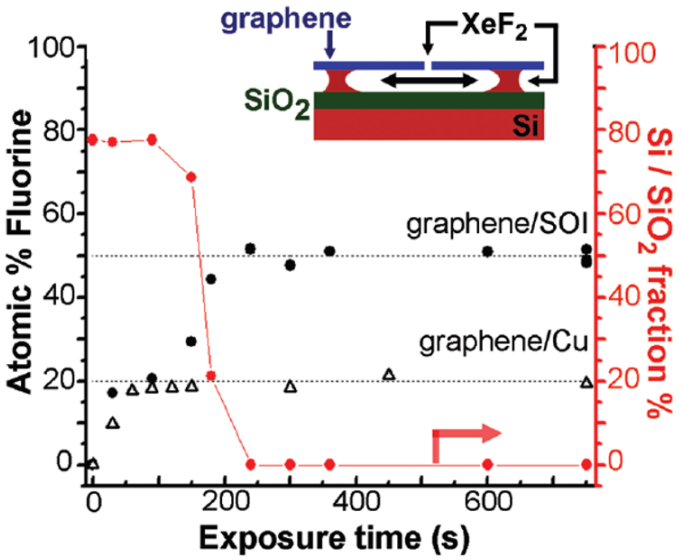
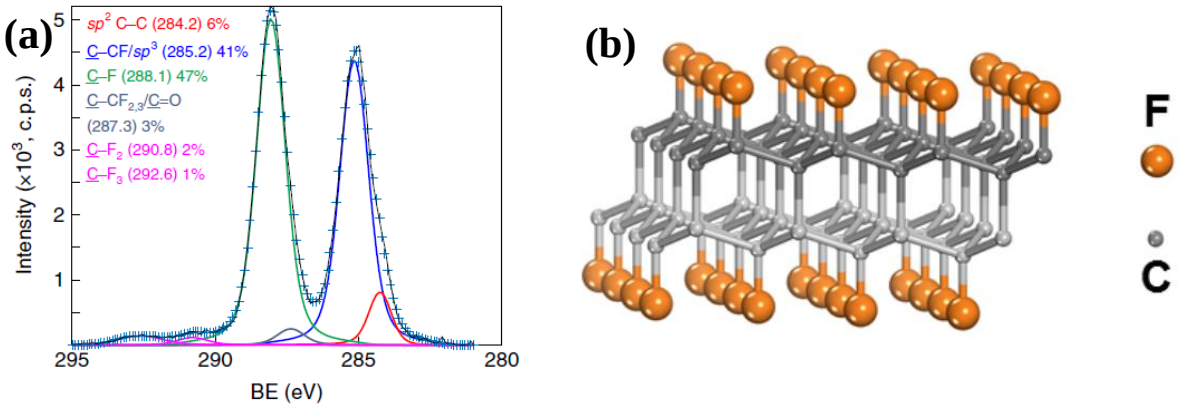


Figure 3.16: Fluorine (black) and silicon (red) fractions measured by XPS for several exposure times to XeF_2, with comparison between one-sided (graphene/Cu) and double-sided (graphene/SOI) fluorination. The inset illustrates the double-sided fluorination of graphene on SOI. From [21].

Interesting results were also reported by Bakharev *et al* [15] with bilayer graphene grown on CuNi(111). The sample was fluorinated at 65°C under approximately 50 torr of XeF_2. Authors were able to form a C_2F phase with interlayer C-C covalent bonding called "F-diamane". Half of the carbon atoms are covalently bonded to a fluorine, and the others are covalently bonded to a carbon atom from the opposite graphene layer (**Figure 3.17b**). In other words, each carbon atom becomes sp^3-hybridized, resulting in a single layer of diamond-like fluorocarbon. The C_2F stoichiometry was confirmed by X-ray photoemission spectroscopy (XPS) (**Figure 3.17a**), and the diamond-like structure was observed in high-resolution transmission electron microscopy (HR-TEM) (**Figure 3.17d**).



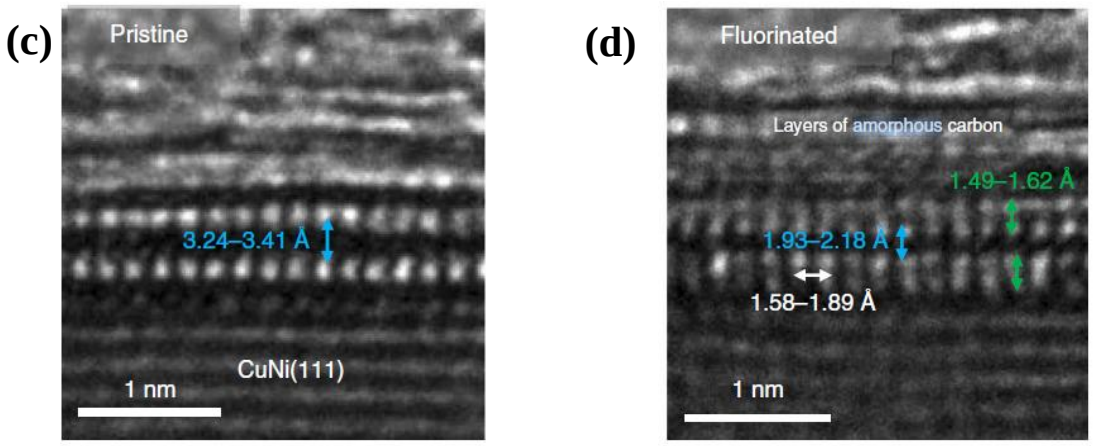


Figure 3.17: (a) C1s spectrum of a bilayer graphene exposed for more than 12 hours to a XeF_2 vapor pressure. (b) DFT-optimized structure of F-diamane. (c,d) HR-TEM images of (c) pristine and (d) fluorinated (> 12 hours) bilayer graphene on Cu/Ni(111). From [15].

(3) <u>This work: soft fluorination conditions by diluting F_2 on N_2.</u>

Our approach was to use a cold vapor phase (15°C to 30°C) composed of F_2 molecules diluted in N_2 (1% to 10%) to limit damage to the graphene lattice. Graphene samples were placed in a commercial flow reactor (**Figure 3.18)** evacuated with a primary pump (10^{-3} mbar). Then, the reactor was heated, and the sample was exposed to a gas flow of 300 mL/min. When the pressure reached 1 atm, the reactor was opened towards a soda lime trap to avoid overpressure in the reactor. At the end of the process, the F_2 gas flux was stopped, and the reactor was flushed with 300 mL/min of N_2 to remove all traces of F_2 molecules in the reactor to recover the sample safely.

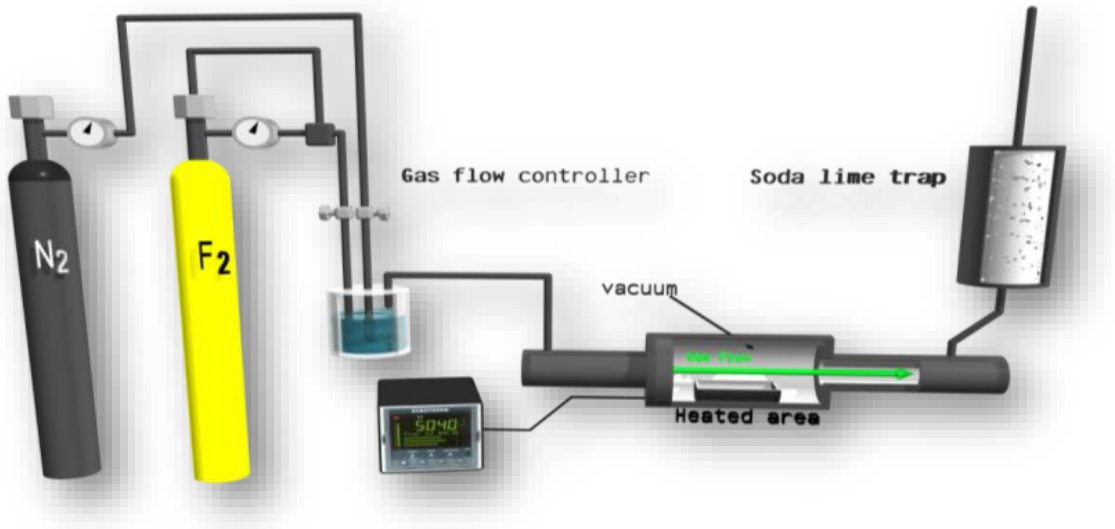


Figure 3.18: schematic representation of the flow reactor used for graphene fluorination.

3.2.2 Patterned fluorination

Similar to patterned hydrogenation with e-beam, spatially selected fluorination can be achieved by laser irradiation of a graphene layer covered by a fluoropolymer, as demonstrated by Lee *et al* [16] in 2012. The principle is the same: A supported graphene layer is covered by a polymer, and radial species are released in selectively irradiated areas where they react with the graphene layer beneath. This technique only differs from patterned hydrogenation in the polymer content and the energy supply, as summarized by **Table 3.1**.

	Hydrogenation	Fluorination
Polymer	PMMA / HSQ	CYTOP (fluoropolymer)
Energy supply	Electron beam	Laser

Table 3.1: Polymer and energy sources used for patterned hydrogenation and fluorination.

Lee *et al* achieved patterned fluorination with a laser wavelength of 488 nm and a laser power up to 3 mW for exposure times between 10 seconds and 5 minutes. The Raman maps demonstrate a non-ambiguous effect of laser irradiation (**Figure 3.19**): the region illuminated by the laser is characterized by a large D band intensity and almost no 2D band, which are expected characteristics of fluorinated graphene (see **Chapter 7**).

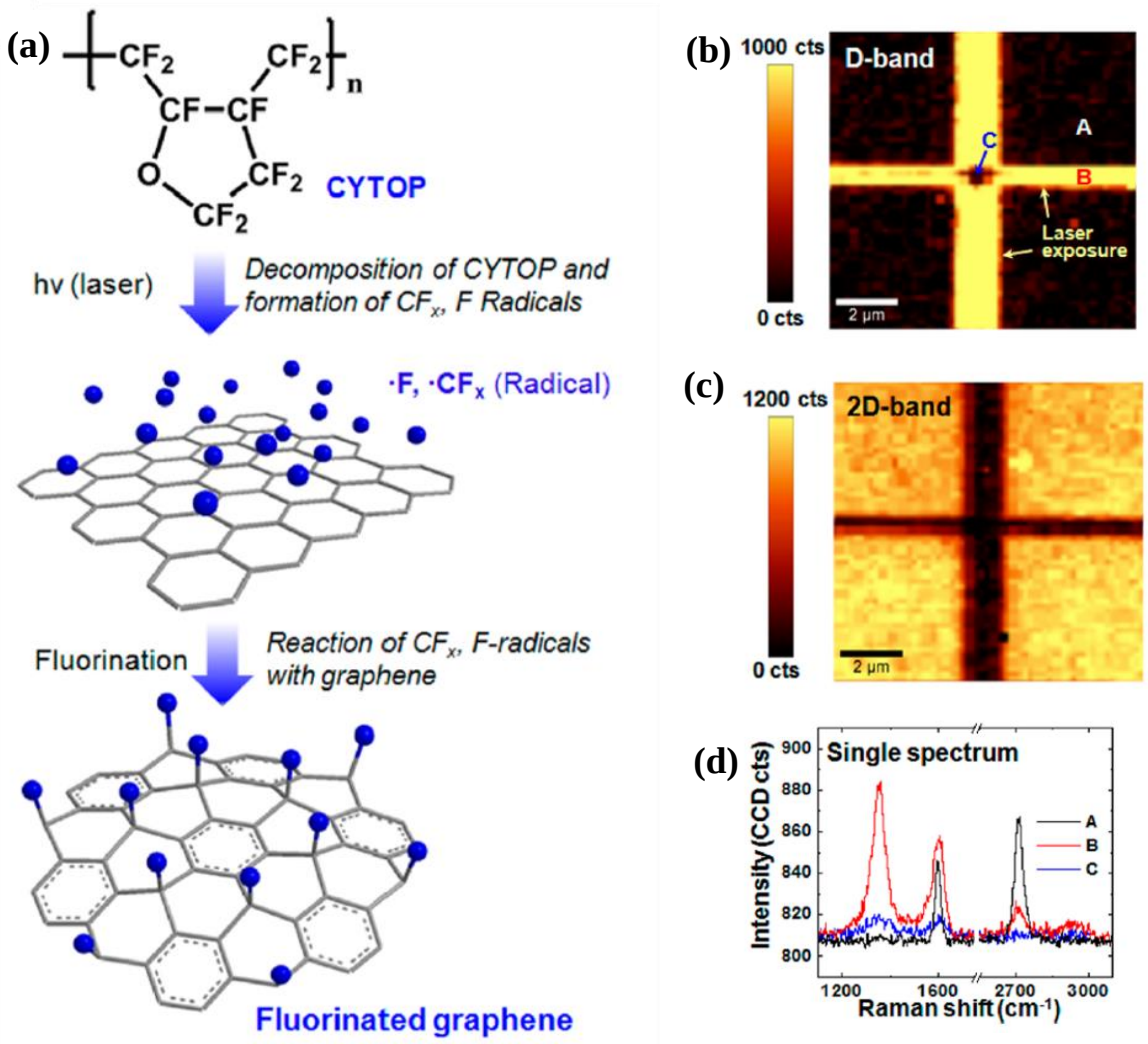


Figure 3.19: (a) Illustration of graphene fluorination enabled by laser illumination of a CYTOP layer covering the graphene. (b,c) Raman maps of (b) the D band and (c) the 2D band intensities after patterned fluorination of a graphene layer. (d) Raman spectra at three different points. From [16].

Chapter 4 Characterization techniques

4.1 Raman spectroscopy in graphene

4.1.1 Raman scattering

Discovered in 1928 by Sir Chandrasekhara Venkata Raman [55], who received the Nobel prize in 1930, Raman scattering is an inelastic light scattering process induced by light interaction with molecular or lattice vibrations.

4.1.1.1 Classical description

An incident electromagnetic field $E(\vec{r},t) = E_0 \cos(\overrightarrow{k_l} \cdot \vec{r} - \omega_i t)$ interacts with a crystal by inducing a polarisation $P(\vec{r},t) = \chi(\omega_i) E_0 \cos(\overrightarrow{k_l} \cdot \vec{r} - \omega_i t)$ oscillating at the same frequency, with $\chi(\omega_i)$ the total material susceptibility. In addition, thermally induced crystal vibrations called *phonons* related to a wavelike atomic displacement $Q(\vec{r},t) = Q(\omega_q)\cos(\vec{q} \cdot \vec{r} - \omega_q t)$ induce a change in χ. Considering $Q(r,t)$ as a small perturbation of the crystal lattice, χ can be expressed as follow:

$$\chi(\omega_i, Q) = \chi_0(\omega_i) + \left(\frac{\partial \chi}{\partial Q}\right)_0 Q(\vec{r},t) + \dots \qquad \text{(eq. 4.1)}$$

The first term in **eq. 4.1** corresponds to the susceptibility of the medium without phonons (i.e. at T = 0 K) and the second term describes its fluctuation with respect to the atomic displacement [56]. Then, the polarisation of the crystal in the presence of phonons is written as:

$$\begin{aligned} P(\vec{r},t,Q) = {} & \chi_0(\omega_i) E_0 \cos(\overrightarrow{k_l} \cdot \vec{r} - \omega_i t) \\ & + \left(\frac{\partial \chi}{\partial Q}\right)_0 Q(\omega_q)\cos(\vec{q} \cdot \vec{r} - \omega_q t) E_0 \cos(\overrightarrow{k_l} \cdot \vec{r} - \omega_i t) \end{aligned} \qquad \text{(eq. 4.2)}$$

The first component in **eq. 4.2** is the *Rayleigh scattering* term, and the second component is attributed to *Raman scattering*. Rayleigh scattering corresponds to the elastic scattering of light, which means that the scattered field oscillates at the same frequency as the incident field. Raman scattering is related to inelastic scattering, which means that the scattered frequency is shifted in comparison to the incident light. The frequency shift, also called *Raman shift*, is equal to the phonon frequency ω_q. **Eq. 4.2** can also be written:

$$P(\vec{r},t,Q) = \chi_0(\omega_i)E_0\cos(\overrightarrow{k_\iota}\cdot\vec{r}-\omega_i t) + \frac{1}{2}\left(\frac{\partial\chi}{\partial Q}\right)_0 Q(\omega_q)E_0 \times\left\{cos\left[(\overrightarrow{k_\iota}+\vec{q})\cdot\vec{r}-(\omega_i+\omega_q)t\right]+cos\left[(\overrightarrow{k_\iota}-\vec{q})\cdot\vec{r}-(\omega_i-\omega_q)t\right]\right\} \quad \text{(eq. 4.3)}$$

The term $cos\left[(\overrightarrow{k_\iota}-\vec{q})\cdot\vec{r}-(\omega_i-\omega_q)t\right]$ represents the **Stokes** scattering and the term $cos\left[(\overrightarrow{k_\iota}+\vec{q})\cdot\vec{r}-(\omega_i+\omega_q)t\right]$ refers to the **anti-Stokes**. These scattering processes induce a redshift (Stokes) or a blueshift (anti-Stokes) of light. Due to energy and momentum conservation, the scattered field oscillates at a frequency $\omega_S = \omega_i \pm \omega_q$ and propagates in space with a wave vector $k_S = k_i \pm q$. Since visible light momentum is very small compared to the size of the Brillouin's zone ($k_i \approx k_S \ll \pi/a$), only zone-centre phonons ($q \approx 0$) are observed in one-phonon Raman scattering. Phonons with $q \neq 0$ can be observed only in scattering processes involving two phonons with opposite momentum.

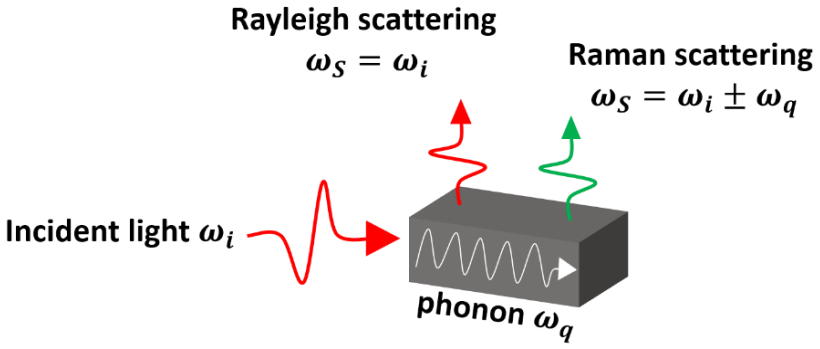


Figure 4.1: Scheme of the basic principle of Raman scattering.

Eq. 4.2 indicates that a phonon mode is Raman-active only if the atomic displacement induces a change in the electronic susceptibility. This is driven by selection rules that consider both the symmetry of the crystal and the light polarization. The intensity of the scattered radiation is proportional to:

$$I_s \propto \left|\overrightarrow{e_\iota}\cdot\left(\frac{\partial\chi}{\partial Q}\right)_0 Q(\omega_q)\cdot\overrightarrow{e_s}\right|^2 \quad \text{(eq. 4.4)}$$

where $\overrightarrow{e_\iota}$ and $\overrightarrow{e_s}$ refer to the polarization vectors of the incident and scattered radiations [56]. As a consequence, the symmetry of a crystal can be studied by analysing the scattered intensity dependence on the incident and scattered polarization.

4.1.1.2 Quantum description

Raman scattering can be described in the framework of the perturbation theory by the intermediate of Feynman's diagrams. A Raman process can be described in three steps:

(1) An incident photon of frequency ω_i creates an electron-hole pair, exciting the material from its initial state $|i\rangle$ of energy E_i to a virtual intermediate state $|n\rangle$ of energy E_n (vertex 1 in **Figure 4.2**). Resonant Raman scattering happens when $E_n - E_i$ is an electronic transition.
(2) The electron or the hole scatters to another intermediate state $|n'\rangle$ of energy $E_{n'} = E_n \pm \hbar\omega_q$ by either emitting (Stokes) or absorbing (anti-Stokes) a phonon of frequency ω_q. (see vertex 2 in **Figure 4.2**).
(3) The electron-hole pair recombines radiatively by emitting a photon at a frequency $\omega_s = \omega_i \pm \omega_q$ (see vertex 2 in **Figure 4.2**). The material comes back in its initial state $|i\rangle$. Resonant Raman scattering happens when $E_n{}' - E_i$ is an electronic transition.

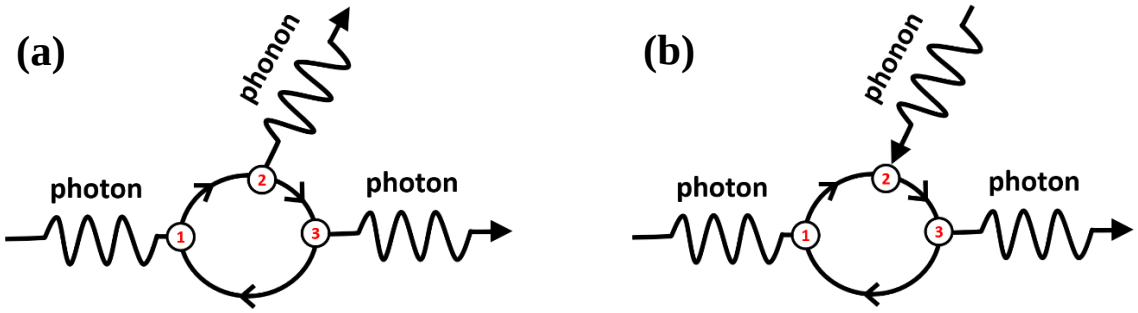


Figure 4.2: Feynman's diagram for (a) Stokes and (b) anti-Stokes scattering.

In this quantum description, phonons are treated as bosons being emitted (Stokes) or absorbed (anti-Stokes), analogously to photons. By consequence, the phonon occupancy N_q at the energy state $\hbar\omega_q$ can be described by the Bose-Einstein statistic:

$$N_q = \frac{1}{e^{\frac{\hbar\omega_q}{k_B T}} - 1} \qquad \text{(eq. 4.5)}$$

And the scattering intensity of the Stokes and anti-Stokes processes is respectively proportional to $N_q + 1$ (creation) and N_q (annihilation) [56]. This result is the consequence of the quantification of the lattice vibration modes into phonons. In a classical approach (**4.1.1.1**), the scattering intensity vanishes in the absence of lattice vibration (**eq. 4.4**), but the quantum description allows a non-zero probability of Stokes scattering at T = 0 K. In this case, the phonon emission is induced by a zero-point motion [56]. On the contrary, the anti-Stokes scattering probability vanishes at low temperature [56].

Thus, the ratio between Stokes and anti-Stokes scattering intensities is temperature-dependent, as given by:

$$\frac{I_{Stokes}}{I_{anti-Stokes}} = \frac{N_q + 1}{N_q} = e^{\frac{\hbar\omega_q}{k_B T}} \qquad \text{(eq. 4.6)}$$

Let us focus on Stokes scattering, through the process described by the Feynman diagram in **Figure 4.2a**. Other Stokes processes are possible, but will not be considered here for the sake of simplicity. The transition rate $\Gamma_{i\to f}$ (in s^{-1}) from an initial state $|i\rangle$ to a final state $|f\rangle$ is given by the Fermi Golden Rule generalized at the third order [56]:

$$\Gamma_{i\to f} = \left(\frac{2\pi}{\hbar}\right)\left|\sum_{n,n'} \frac{\langle f|H_{eR}(\omega_s)|n'\rangle\langle n'|H_{e-ion}(\omega_q)|n\rangle\langle n|H_{eR}(\omega_i)|i\rangle}{[\hbar\omega_i - (E_n - E_i)][\hbar\omega_i - \hbar\omega_q - (E_{n'} - E_f)][\hbar\omega_i - \hbar\omega_q - \hbar\omega_s - (E_i - E_f)]}\right|^2 \qquad \text{(eq. 4.7)}$$

Where H_{eR} and H_{e-ion} correspond respectively to the electron-radiation and electron-phonon interaction Hamiltonians and $|n\rangle$ and $|n'\rangle$ represent the two intermediate states. $\hbar\omega_i$, $\hbar\omega_q$ and $\hbar\omega_s$ are the energies of the incident photon, absorbed phonon and scattered photon and E_n and $E_{n'}$ represent the energies associated with each intermediate state. In Raman scattering, the initial and final electron states are the same, so the third energy term at the denominator in **eq. 4.7** can be simplified by $\hbar\omega_i - \hbar\omega_q - \hbar\omega_s$, and vanishes due to energy conservation. As a consequence, this term must be replaced by a delta function $\delta(\hbar\omega_i - \hbar\omega_q - \hbar\omega_s)$ [56]:

$$\Gamma_{i\to f} = \left(\frac{2\pi}{\hbar}\right)\left|\sum_{n,n'} \frac{\langle f|H_{eR}(\omega_s)|n'\rangle\langle n'|H_{e-ion}(\omega_q)|n\rangle\langle n|H_{eR}(\omega_i)|i\rangle}{[\hbar\omega_i - (E_n - E_i)][\hbar\omega_i - \hbar\omega_q - (E_{n'} - E_f)]}\right|^2 \delta(\hbar\omega_i - \hbar\omega_q - \hbar\omega_s) \qquad \text{(eq. 4.8)}$$

The total transition rate, considering all the possible scattering processes, is derived by summing the transition rates attributed to each process [56].

4.1.1.3 Resonant Raman scattering

Resonant Raman scattering occurs when either the incident or the scattered radiation resonates with an electronic transition (**Figure 4.3b and 4.3c**). There are two types of resonant processes, referred to as *incoming* (**Figure 4.3b**) and *outgoing* (**Figure 4.3c**) resonance. In these cases, the scattering efficiency is strongly enhanced compared to non-resonant processes.

In the case of graphene, since it is a zero-gap semiconductor (i.e., a semi-metal), Raman scattering is resonant, which is convenient for Raman signal detection. Typical laser power and exposure time required to record a graphene Raman spectrum with an acceptable signal-to-noise ratio are of the order of ~1 mW and a few tens of seconds.

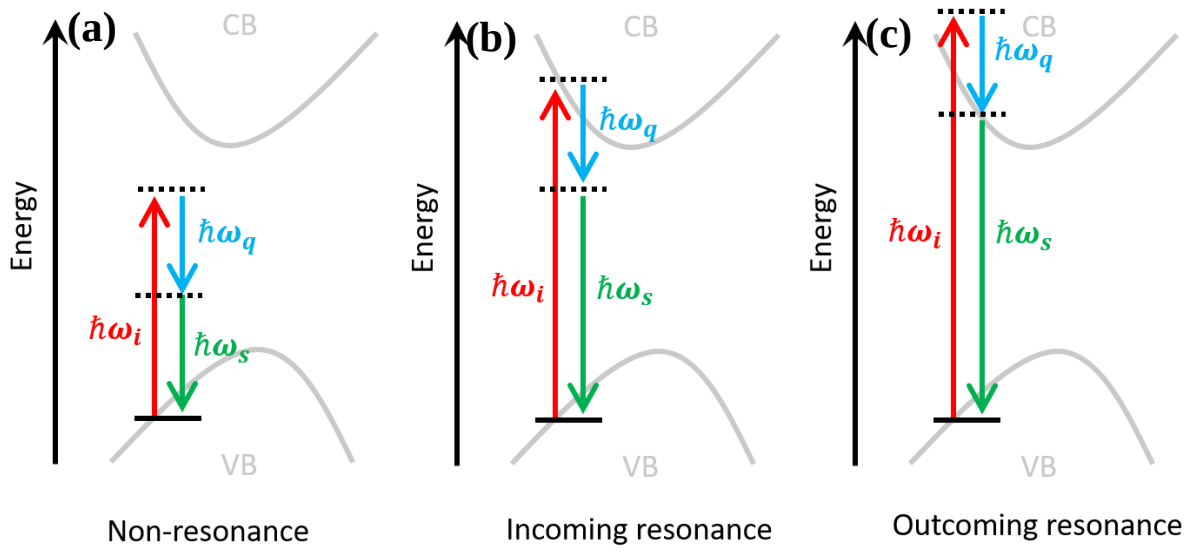


Figure 4.3: Schematic illustration of (a) non-resonant and (b,c) resonant Raman scattering in a semiconductor.

4.1.1.4 Raman spectrum

In a Raman spectrum, the intensity is plotted as a function of the frequency shift between the incident and scattered radiation, commonly referred to as the *Raman shift*. By convention, the Raman shift $\Delta\tilde{\nu}$ is expressed in terms of wavenumber ($\tilde{\nu} = 1/\lambda$) difference in cm^{-1} (1 eV = 8065.7 cm^{-1}). Since Raman scattering is very weak ($\sim 10^{-5}$ of the incident beam) compared to Rayleigh scattering [57], it is necessary to cut the Rayleigh signal with a filter to avoid saturating the detector. In general, a Raman spectrum displays only the Stokes part, which is more intense than the anti-Stokes (see **eq. 4.6**). The spectral lines positions of Stokes and anti-Stokes are symmetric about the Rayleigh spectral line, as they only differ by their intensity and the sign of the Raman shift (negative for Stokes and positive for anti-Stokes). By convention, even if Stokes scattering is in the negative part of the spectrum, Raman shifts are always indicated as positive values.

4.1.2 Raman scattering in graphene

4.1.2.1 Phonon dispersion

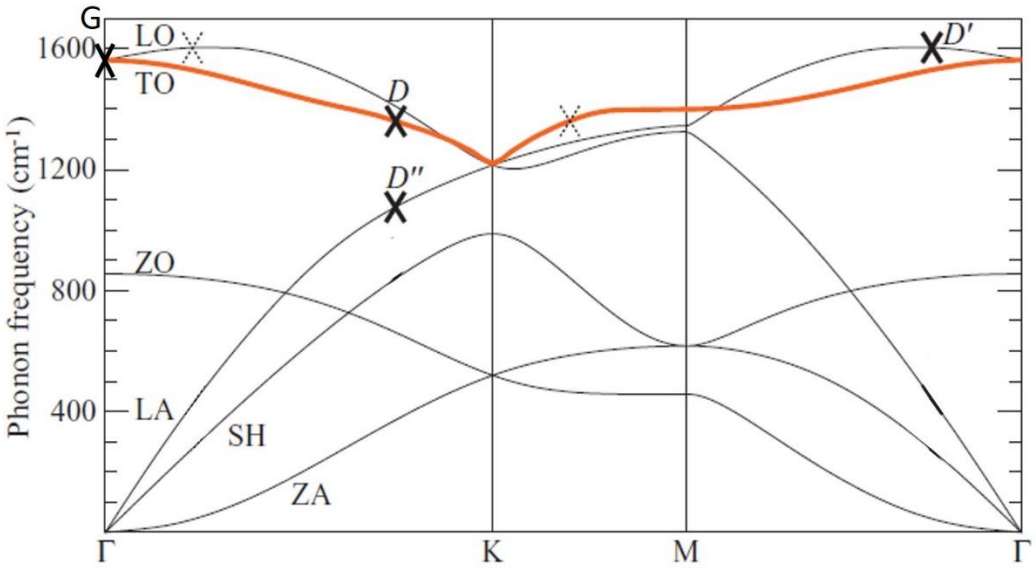


Figure 4.4: Phonon band structure of graphene, adapted from [58]. Crosses indicate the approximate positions of Raman bands. For the D ad D' bands, the dotted crosses indicate the non-dominant (see 4.1.2.3).

Graphene has two carbon atoms per unit cell, which gives six phonon modes divided into three acoustic modes (ZA, SH and LA) and three optical modes (ZO, TO and LO). The acoustic modes are recognizable by their zero-energy at Γ-point (**Figure 4.4**), which makes them non-observable in Raman spectroscopy. Among the three optical phonons, at Γ-point, there is one out-of-plane B_{2g} phonon (ZO in **Figure 4.4**) which is not Raman-active [59] and one doubly degenerated in-plane E_{2g} phonon (LO and TO in **Figure 4.4**) which is Raman-active [59] and gives a spectral line at approximately 1580 cm^{-1} referenced as G band. This Raman band is also observed in graphite and carbon nanotubes since it arises from the sp^2 character of carbon atoms and can be described as the C-C bonds stretching, as illustrated in **Figure 4.5**.

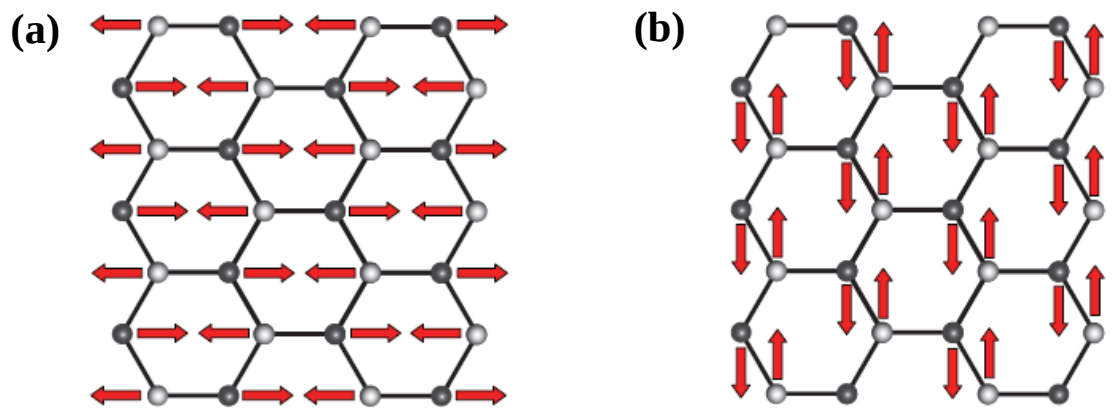


Figure 4.5: (a) Transverse and (b) longitudinal lattice vibrations associated with the doubly degenerated E_{2g} phonon, from [60].

4.1.2.2 Properties of the E_{2g} phonon mode

Experimentally, an upshift of the G band frequency is observed when electrical charges (positive or negative) are injected into the layer (**Figure 4.6**) [61,62], which indicates a strong electron-phonon coupling in graphene.

Let us consider the case of a negatively doped graphene layer (calculations are similar for p-doping). In the vicinity of the K point, the density of states as a function of the energy of the electrons is given by:

$$g(E) = \frac{dN(E)}{dE} = \frac{dk}{dE}\frac{dN(k)}{dk} \qquad \text{(eq. 4.9)}$$

with N the total number of states. Due to the conical dispersion of the electronic band structure near K point, we have $N(k) = \frac{\pi k^2}{4\pi^2}$. In addition, the group velocity of the electrons is $v_g = \frac{1}{\hbar}\frac{dE}{dk} = v_F$. Considering the spin and band degeneracies, **eq. 4.9** can be written as:

$$g(E) = \frac{4}{\hbar v_F}\frac{d}{dk}\left(\frac{\pi k^2}{4\pi^2}\right) = \frac{2k}{\pi\hbar v_F} = \frac{2E}{\pi(\hbar v_F)^2} \qquad \text{(eq. 4.10)}$$

The electron density is given by as:

$$n = \int_{E_{CNP}}^{E_f} f(E - E_f)g(E)dE \qquad \text{(eq. 4.11)}$$

with $f(E-E_f) = \frac{1}{1+exp\left(\frac{E-E_f}{k_BT}\right)}$ is the Fermi-Dirac distribution, E_f is the Fermi level and E_{CNP} the charge neutrality point. At T = 0 K, $f(E-E_f) = 1$ and, by injecting **eq. 4.10** into **eq. 4.11** we obtain:

$$n = \frac{E_f^2}{\pi(\hbar v_F)^2} = \frac{k_f^2}{\pi} \qquad \text{(eq. 4.12)}$$

It results from **eq. 4.12** that doping is directly related to the shift of the Fermi level and, by consequence, an increase of the Fermi surface.

In graphene, the in-plane longitudinal (iLO) phonon dispersion is softened near the Γ-point due to a Kohn anomaly [63]. Briefly, Kohn anomalies are present in every metal and consist of a softening of the phonon dispersion at some points of the reciprocal lattice, induced by a screening of the lattice motion by electrons close to the Fermi surface [64]. By consequence, Kohn anomalies concern phonons of wavevector $q \sim 2k_f$. For undoped graphene ($k_f \approx 0$), the longitudinal E_{2g} phonon, which is associated with a zero-wavevector, is softened (as well as the iLO/iTO phonons at the K-point). However, in the case of doping ($k_f \neq 0$), the increase of the Fermi surface moves the Kohn anomaly away from q = 0, resulting in a stiffening of the E_{2g} phonon [62].

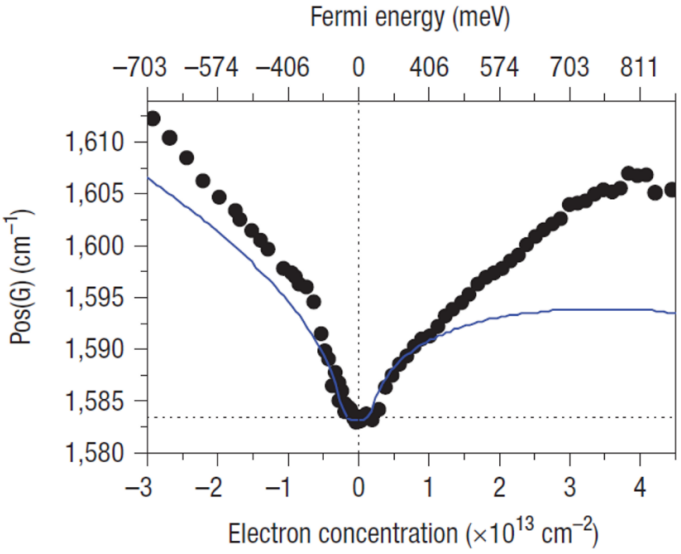


Figure 4.6: Measured position of the G band as a function of the Fermi energy and the electron concentration, from [61]. The blue line represents the non-adiabatic trend from [62].

The G band shift can also be influenced by mechanical strain [65], making the estimation of the charge carrier density a bit more complex. Contrary to doping, which induces an up-shift of the G band frequency independently of the nature of the charge carriers (see **Figure 4.6**), strain can have two opposite effects on the G band frequency. While a compressive strain upshifts the G band position, a tensile strain causes a downshift [65].

4.1.2.3 Double Resonance scattering processes

(a) Two-phonon scattering

As mentioned in **4.1.1.1,** phonons with $q \neq 0$ can be observed in Raman if the scattering process involves two phonons with opposite momentum. This is the case of the 2D and 2D' bands, resulting from processes involving zone-corner and zone-centre phonons, respectively. The 2D band originates from charge carriers' interactions with in-plane transverse optical (iTO) phonons near the K-point, whereas the 2D' band involves in-plane longitudinal optical (iLO) phonons near the Γ-point [66, 67]. By consequence of their phonon wave vectors, the 2D and 2D' bands are related to intervalley and intravalley scattering processes, respectively (**Figure 4.7b** and **4.7c**). This part focuses on intervalley scattering (2D), which can be separated into three categories [58]:

(i) electron-electron processes where momentum is conserved by scattering two electrons.
(ii) hole-hole processes where momentum is conserved by scattering two holes.
(iii) electron-hole processes where momentum is conserved by scattering one electron and one hole.

Previous results from the literature have demonstrated that, due to non-trivial interference effects in the summation of the matrix elements, electron-hole processes are by far dominant [58]. This is more easily understood by describing the scattering process in real space (**Figure 4.7a**). A radiative recombination creating a scattered photon is only possible if the electron and the hole have opposite momentum and meet at the same point in real space after having travelled for the same amount of time, which is possible in electron-hole processes but not in processes involving two electrons or two holes [66]. As a consequence, processes involving only one type of charge carrier can be neglected.

To explain what an electron-hole intervalley scattering consists of, let us consider the case of Stokes scattering. In resonant conditions, a photon of energy $\hbar\omega_L$ promotes an electron from the valence band to the conduction band, thereby creating an electron-hole pair composed of an electron with energy $\hbar\omega_L/2$ and momentum $\hbar$K and a hole with energy $-\hbar\omega_L/2$ and momentum $-\hbar$K. At some point, the electron and the hole are backscattered inelastically by the emission of iTO phonons near K-point with energies $\hbar\omega_{iTO}$ and opposite momenta. Then, the electron and the hole meet at the same point in space with opposite momenta $\hbar$K' and $-\hbar$K' and recombine radiatively by emitting a photon of energy $\hbar\omega_s = (\hbar\omega_L/2 - \hbar\omega_{iTO}) - (\hbar\omega_{iTO} - \hbar\omega_L/2) = \hbar\omega_L - 2\hbar\omega_{iTO}$.

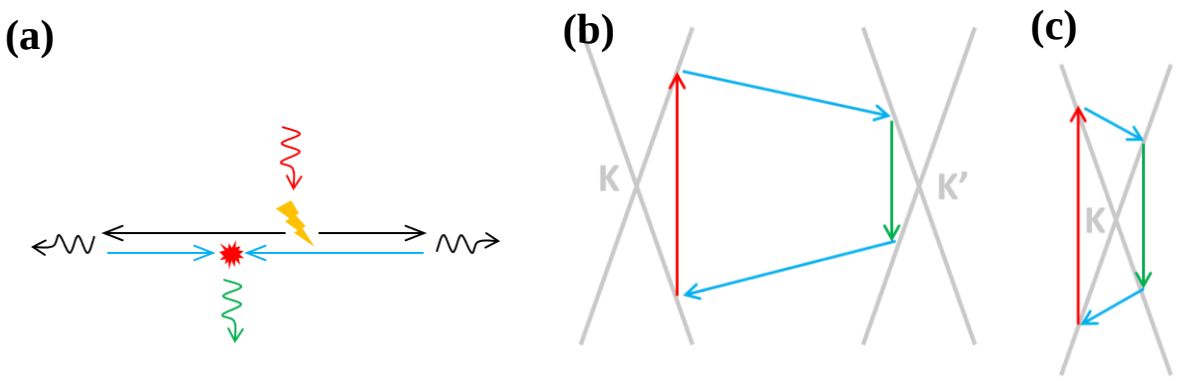


Figure 4.7: Dominant processes for two-phonon Stokes scattering. (a) Description is real space: The incident photon (red wave) creates an electron hole pair (lightning). The electron and the hole travel toward opposite directions in space (black arrows) due to their opposite momentum. At some point, they emit phonons (black waves) and are backscattered inelastically (blue arrows) until they recombine (flash) to emit a photon (green wave). (b) Description in k-space of the intervalley scattering at the origin of the 2D band and (c) the intravalley scattering relative to the 2D' band. The photon absorption and emission are represented by red and green arrows whereas charge carriers scattering is embodied by blue arrows.

To summarise, the 2D band originates from a double resonant process where momentum is conserved by two zone-corner phonons, scattering inelastically an electron and a hole from the K-valley to the K'-valley. As a result, the 2D band is sensitive to the electronic band structure. In particular, its position is strongly dispersive with laser energy (~ 100 cm^{-1}/eV) [66]. For a green laser excitation of (2.33 eV), it corresponds to a Raman shift of approximately 2680 cm^{-1} (see **Figures 4.10** and **4.12**).

The 2D band position can also be influenced by doping [68] and mechanical strain [65], as for the G band. Work from Lee *et al* [69] has demonstrated that the contributions of strain and doping can be separated regarding the 2D over G band frequency shifts $\Delta\omega_{2D}/\Delta\omega_G$. This study found out that $\Delta\omega_{2D}$ is related to $\Delta\omega_G$ by:

$$\Delta\omega_{2D} = \Delta\omega_{2D-strain} + \Delta\omega_{2D-doping} = 2.2 \times \Delta\omega_{G-strain} + 0.7 \times \Delta\omega_{G-doping} \qquad \text{(eq. 4.13)}$$

The description in k-space (**Figure 4.7b**) considers a phonon with a wave vector in the Γ-K direction, but the iTO phonon can also have a wave vector in the K-M direction. These two contributions are commonly referred to as *inner* (i.e., phonon in Γ-K) and *outer* (i.e., phonon in K-M) processes. However, calculations in the literature [58] demonstrated that inner processes are the dominant contributions (**Figure 4.8**). As a result, two-phonon intervalley scattering processes in graphene give birth to a sharp spectral line fitted by one Lorentzian with a full-width at half maximum of approximately 24 cm^{-1} (**Figure 4.10**).

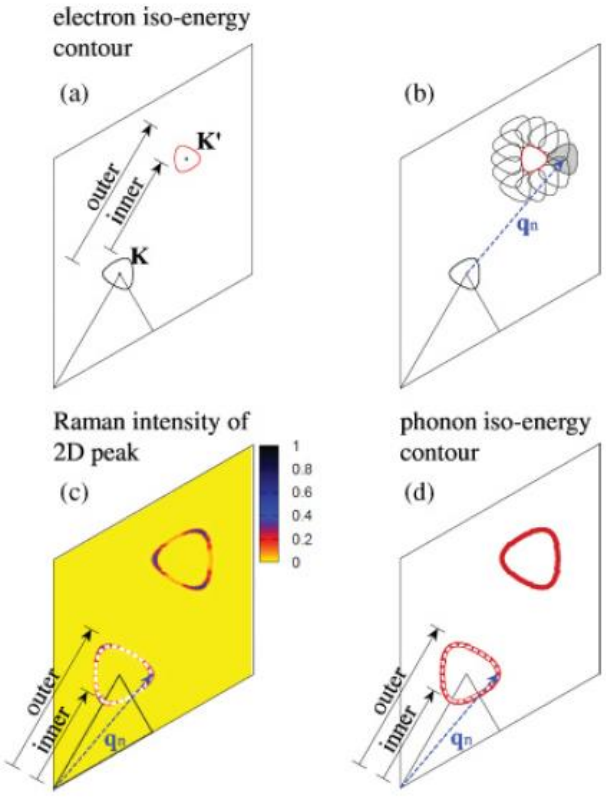


Figure 4.8: Calculations from [58] of the (a,b) electron and (c,d) phonon states inside the Brillouin's zone contributing to the 2D band for an excitation of 2.4 eV. The triangular contours in (a,b) are the electron iso-energy states around the K and K' points. (b) draws all the possible q-vectors for intervalley scattering from K to K' and (a) indicates the vectors attributed to inner and outer processes. The triangle contours in (d) are the phonon iso-energy states around K and K' points, characterized by distortions opposite to the electron iso-energy contours. (c) shows the 2D band intensity along these contours. In (c,d), the phonon wave vectors involved in inner and outer scattering are represented by the black arrows.

The 2D band sensitivity to the electronic band structure is particularly useful to discriminate monolayer from bilayer graphene. The interlayer interactions in bilayer graphene split the electronic bands into two valence bands (π_1 and π_2) and two conduction bands (π_1^* and π_2^*) (**Figure 4.9**) [66,70]. As a consequence, each double resonance process can be either symmetric (scattering between the same energy bands) or anti-symmetric (scattering between different energy bands) [66,70]. It gives four types of intervalley scattering processes:

(1) Symmetric scattering between $\pi_1^{(*)}$ bands
(2) Symmetric scattering between $\pi_2^{(*)}$ bands
(3) Anti-symmetric scattering from $\pi_1^{(*)}$ to $\pi_2^{(*)}$
(4) Anti-symmetric scattering from $\pi_2^{(*)}$ to $\pi_1^{(*)}$

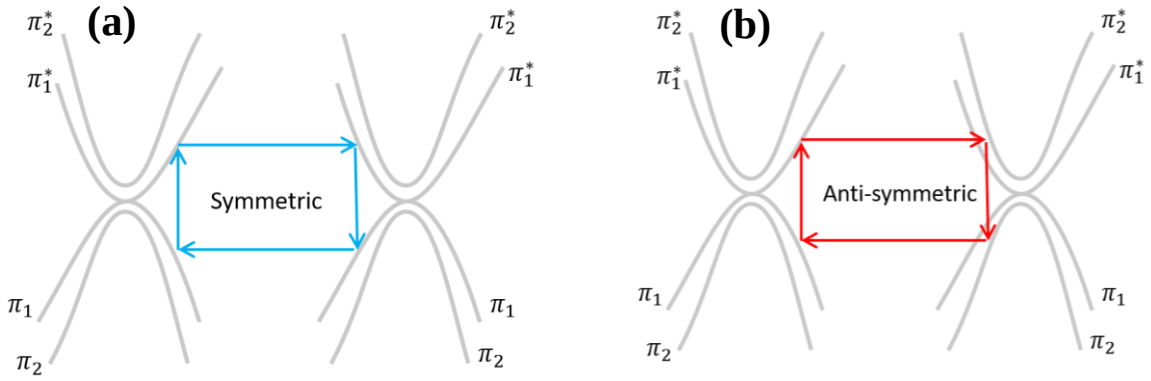


Figure 4.9: Schematic representation of (a) symmetric and (b) antisymmetric intervalley scattering processes in bilayer graphene.

Consequently, in bilayer graphene, the 2D band has four components instead of one, as demonstrated by the fit in **Figure 4.10**. For more than two layers, there are more contributions, but this will not be detailed in this chapter. In the framework of this PhD, the difference between a monolayer and a bilayer was intuited from the optical contrast of graphene on SiO_2, but Raman spectroscopy was constantly carried out for confirmation.

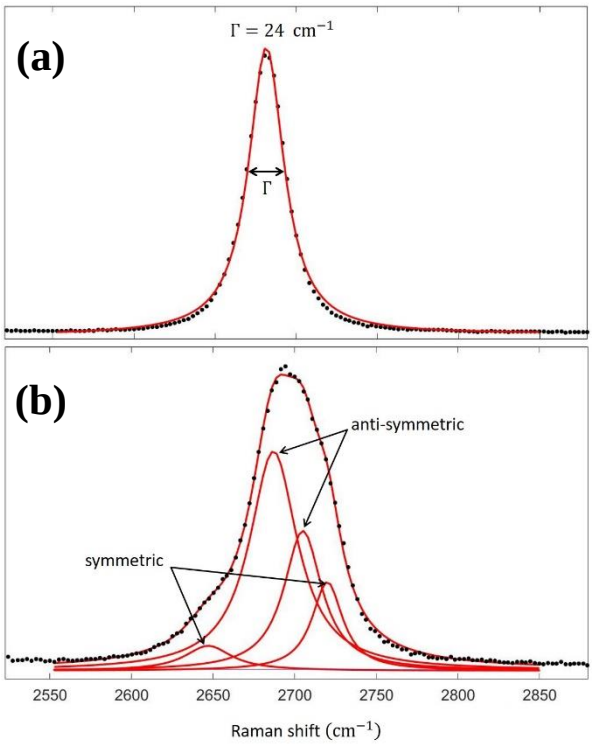


Figure 4.10: 2D band of (a) monolayer and (b) bilayer graphene at an excitation energy of 2.33 eV. (a) The 2D band is fitted by one Lorentzian at 2681 cm^{-1} with a full width at half maximum of about 24 cm^{-1}. (b) Fit by four Lorentzian components decomposed into symmetric scattering at 2647 cm^{-1} and 2720 cm^{-1} and anti-symmetric scattering at 2687 cm^{-1} and 2705 cm^{-1}.

(b) One-phonon scattering

In the presence of defects, the momentum in double-resonance scattering can be conserved by processes enabled by one phonon and one defect. This is the case of the D and D' bands, the undertones of the 2D and 2D' bands.

The D band originates from intervalley scattering enabled by one defect and one iTO phonon near the K-point [66,67]. In resonant conditions, a photon of energy $\hbar\omega_L$ promotes an electron from the valence band to the conduction band, thereby creating an electron-hole pair composed of an electron with energy $\hbar\omega_L/2$ and momentum $\hbar$K and a hole with energy $-\hbar\omega_L/2$ and momentum $-\hbar$K. At some point, the electron (respectively the hole) is inelastically backscattered by the emission of an iTO phonon near K-point with energy $\hbar\omega_{iTO}$ and the hole (respectively the electron) is elastically backscattered by a defect, keeping its energy. They meet at the same point in space with opposite momenta $\hbar$K' and $-\hbar$K' and recombine radiatively by emitting a photon of energy $\hbar\omega_s = (\hbar\omega_L/2 - \hbar\omega_{iTO}) + \hbar\omega_L/2 = \hbar\omega_L - \hbar\omega_{iTO}$. By consequence, the Raman shift corresponds to the half of the 2D band frequency.

To summarise, the D band originates from a double resonant process where momentum is conserved by an inelastic scattering process involving a zone-corner phonon and an elastic scattering process of an electron (hole) induced by a defect. Both inelastic and elastic processes scatter the charge carriers from the K-valley to the K'-valley. Consequently, the D band is sensitive to the electronic band structure. In particular, its position is strongly dispersive with laser energy (~ 50 cm^{-1}/eV) [66]. For a green laser excitation (2.33 eV), it corresponds to a Raman shift of approximately 2680/2 = 1340 cm^{-1} (see **Figures 4.10** and **4.12**).

Lucchese *et al* [47] developed a model that allows for determining the defect density on a graphene layer from the intensity ratio between the D and the G ands $\left(\frac{I_D}{I_G}\right)$. This model will be described in detail in **Chapter 5**.

The D' band consists of a similar process but for intravalley scattering enabled by one defect and one iLO phonon near the Γ-point. It is assigned to a spectral line at approximately 1620 cm^{-1}.

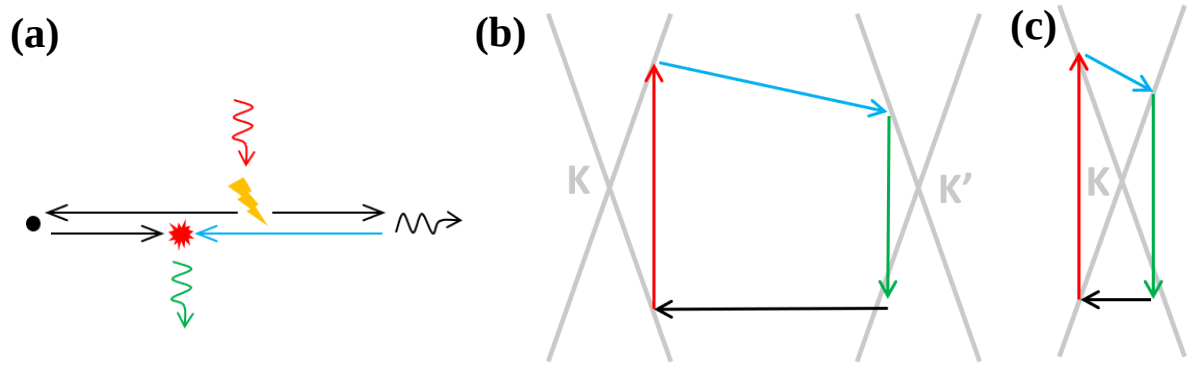


Figure 4.11: Dominant processes for one-phonon Stokes scattering. (a) Description is real space: The incident photon (red wave) creates an electron hole pair (lightning). The electron and the hole travel toward opposite directions in space (black arrows) due to their opposite momentum. At some

point, the electron (respectively the hole) emits a phonon (black wave) and is backscattered elastically (blue arrow) while the hole (respectively the electron) is backscattered elastically (black arrow) by a defect (dot). The electron-hole pair recombines (flash) by emitting a photon (green wave). (b) Description in k-space of the intervalley scattering at the origin of the D band and (c) the intravalley scattering relative to the D' band. The photon absorption and emission are represented by red and green arrows. In this example, the electron is inelastically scattered by a phonon (blue arrow) while the hole is elastically scattered by a defect (black arrow).

4.1.2.4 Graphene Raman spectrum

Figure 4.12 shows a Raman spectrum of a pristine graphene and a defective graphene sample (defects introduced by fluorination), thereby confirming that, contrary to the G and the 2D bands, the D and D' bands are only activated by the presence of defects. The D+D'' band at approximately 2450 cm^{-1} was not mentioned before, but results from a double resonant process that combines an iTO phonon (D) and a longitudinal acoustic (LA) phonon (D''). For defective graphene, a broad band is visible near 2960 cm^{-1}, as it corresponds to the D+D'. This band originates from a triple resonant process activated by defects.

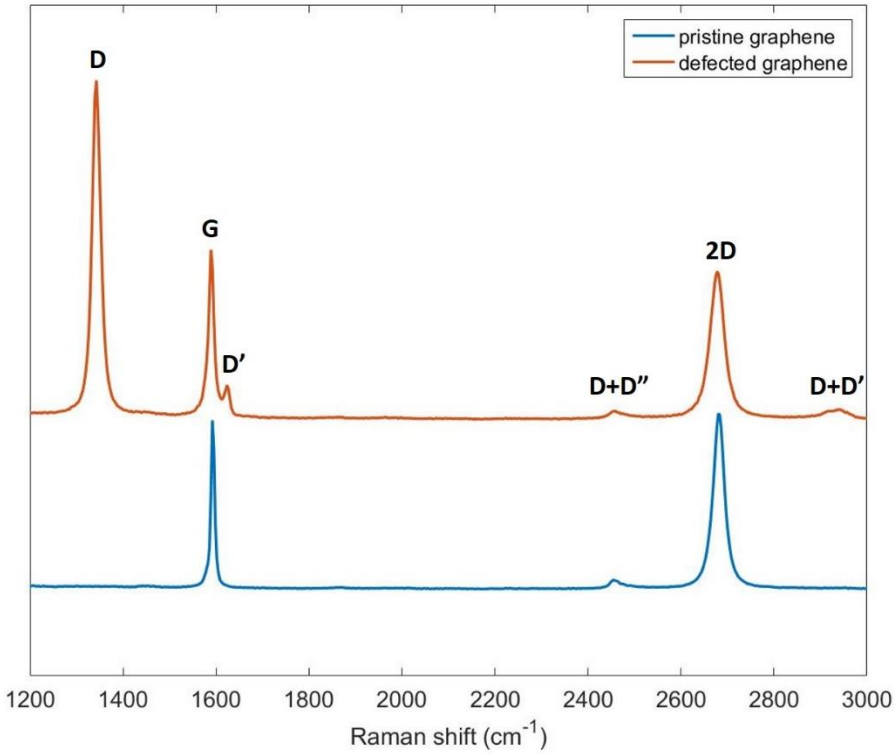


Figure 4.12: Raman spectra of pristine and defected (fluorinated) graphene samples on SiO_2/Si with a laser excitation of 532 nm. The spectra are normalized with respect to the G band intensity.

A previous work from Eckman *et al* [71] reported an empirical model to determine the nature of defects in graphene from the intensity ratio between the D and the D' bands $\left(\frac{I_D}{I_{D'}}\right)$. This model was established from a large statistical study over many graphene samples with different kind of defects induced by

functionalization (sp^3 defects) or ion-bombardment (vacancies). It demonstrates that, at low defect density (stage 1 in **Figure 4.13**), $\frac{I_D}{I_{D'}}$ is correlated to the nature of the defects. sp^3-type defects are characterized by $\frac{I_D}{I_{D'}} \approx 13$, vacancies by $\frac{I_D}{I_{D'}} \approx 7$ and edges by $\frac{I_D}{I_{D'}} \approx 3.5$.

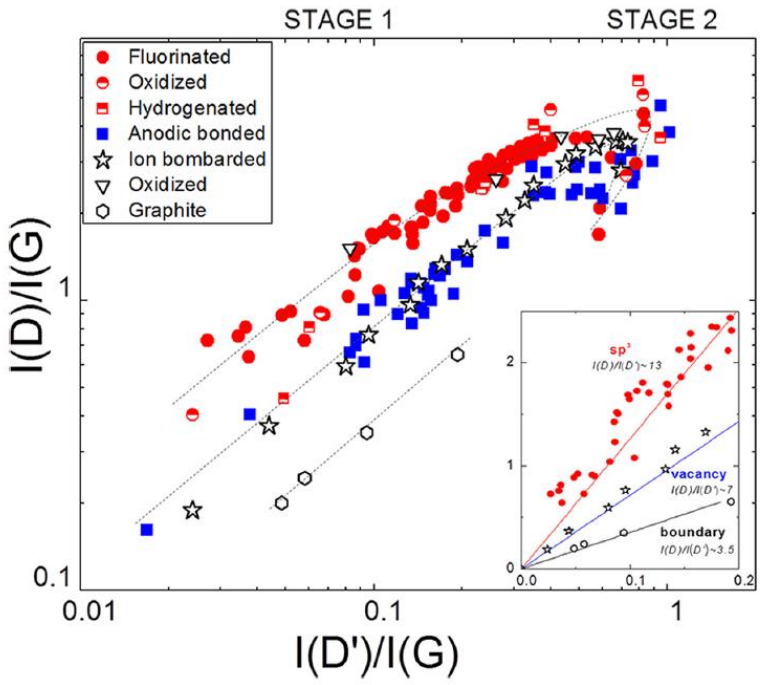


Figure 4.13: $\frac{I_D}{I_G}$ versus $\frac{I_{D'}}{I_G}$ for different graphene samples showing a correlation for stage 1 (low defects density) between $\frac{I_D}{I_{D'}}$ and the nature of defects. The inset shows the linear dependence between the two parameters in stage 1. From [71].

4.1.2.2 Substrate effect on Raman signal intensity

In **Chapter 2** it was demonstrated that the optical contrast of a graphene layer on Si/SiO_2 can be amplified by interference effects. The Raman signal intensity can be enhanced similarly [72,73]. The different Raman bands in graphene originate from a succession of two processes:

(1) Absorption of a photon of energy $E_{photon_ab} = \hbar\omega_{laser}$
(2) Inelastic scattering: emission of a photon of energy $E_{photon_sc} = \hbar(\omega_{laser} \pm \omega_{phonon})$

Thus, the total Raman intensity I_{Raman} integrated over the graphene thickness (d_1) can be expressed by:

$$I_{Raman}(\lambda) = \frac{1}{d_1}\int_0^{d_1} |E_{Raman}(x,\lambda)|^2 dx = \frac{1}{d_1}\int_0^{d_1} |\alpha_{ab}(x,\lambda)\alpha_{sc}(x,\lambda)E_{laser}|^2 dx \qquad \text{(eq. 4.14)}$$

E_{laser} is the incident electric field emitted by the laser and α_{ab} and α_{sc} correspond to absorption and scattering coefficients. In other words, α_{ab} is the proportion of the incident electric field that is absorbed by the graphene and $\alpha_{sc}(x,\lambda) = \eta_{sc}(\lambda)T_{sc}(x,\lambda)$ represents the scattering efficiency (η_{sc}) multiplied by the transmission coefficient (T_{sc}) from graphene to the outside medium. These terms arise from an infinite number of reflections and transmissions at the interfaces (**Figure 4.14**). The different possible paths followed by the light interfere constructively or destructively depending on the laser wavelength and the oxide thickness. In the following, the SiO_2 thickness is treated as a constant equal to 285 nm as it is the case for all the samples prepared within this PhD.

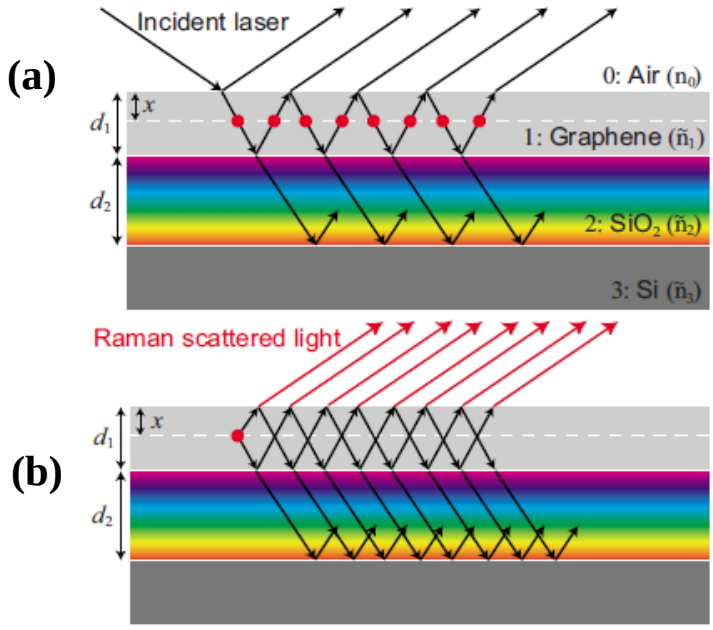


Figure 4.14: Schematic diagrams from [73] of the multiple reflections and transmissions contributing to (a) absorption and (b) scattering processes.

Now, let us determine the intensity of the Raman signal. In this case, the transfer matrix formalism is not adapted to calculate α_{sc} because the light source (Raman scattering) originates from the optical system itself. To overcome this issue, one alternative consists in summing the probability amplitudes associated to each possible path, considering free propagation terms in the different media as well as the Fresnel's coefficients at the interfaces. Those calculations are based on the following rules:

(1) The probability amplitude for a plane wave of wavelength λ to propagate along a distance x in a medium of optical index ñ(λ) = n(λ) + ik(λ) is equal to $exp(-i\frac{2\pi}{\lambda}\tilde{n}(\lambda)x)$.

(2) A plane wave of wavelength λ propagating from a medium of optical index $\tilde{n}_1(\lambda)$ to a medium of optical index $\tilde{n}_2(\lambda)$ can be reflected at the interface with a probability amplitude equal to the reflexion coefficient $r_{12}(\lambda) = -r_{21}(\lambda) = \frac{\tilde{n}_1(\lambda)-\tilde{n}_2(\lambda)}{\tilde{n}_1(\lambda)+\tilde{n}_2(\lambda)}$.

(3) A plane wave of wavelength λ propagating from a medium of optical index $\tilde{n}_1(\lambda)$to a medium of optical index $\tilde{n}_2(\lambda)$ can be transmitted with a probability amplitude equal to the transmission coefficient

$$t_{12}(\lambda) = -t_{21}(\lambda) = \frac{2\tilde{n}_1(\lambda)}{\tilde{n}_1(\lambda)+\tilde{n}_2(\lambda)}.$$

In the following, air, graphene, SiO_2 and Si are described as media of complex refractive indexes $\tilde{n}_0(\lambda)$, $\tilde{n}_1(\lambda)$, $\tilde{n}_2(\lambda)$ and $\tilde{n}_3(\lambda)$, respectively. Then, t_{12} represents the transmission coefficient from graphene to SiO_2, r_{23} the reflexion coefficient from SiO_2 to Si, and so on… For the sake of simplicity, we set $\beta_1 = \frac{2\pi\tilde{n}_1 d_1}{\lambda}, \beta_1 = \frac{2\pi\tilde{n}_2 d_2}{\lambda}$ and $\beta_x = \frac{2\pi\tilde{n}_1 x}{\lambda}$.

(a) Calculation of the absorption coefficient

The total electric field absorbed by graphene at a given depth x can be decomposed into two components:

$$\alpha_{ab} = \alpha_{ab}^{(1)} + \alpha_{ab}^{(2)} \qquad \text{(eq. 4.15)}$$

$\alpha_{ab}^{(1)}$ is associated to the part of the electric field absorbed after propagation in graphene only (**Figure 4.15a**) and $\alpha_{ab}^{(2)}$ to the part of the electric field absorbed after propagation in both graphene and SiO_2 (**Figure 4.15b**).

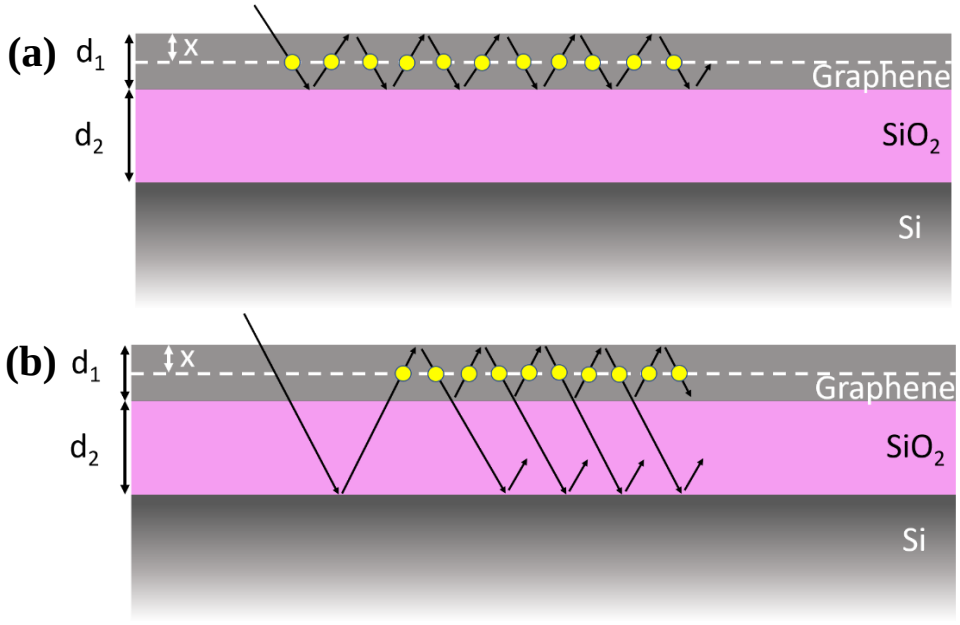


Figure 4.15: Schematic diagrams of the multiple paths contributing to (a) $\alpha_{ab}^{(1)}$ and (b) $\alpha_{ab}^{(2)}$. The total electric filed absorbed at a given depth in graphene is derived by summing the electric filed amplitudes at the points represented by yellow dots.

The first component is derived by summing the probability amplitudes associated to the yellow dots in **Figure 4.15a**:

$$\alpha_{ab}^{(1)} = (t_{01}e^{-i\beta_x} + t_{01}r_{12}e^{-i(2\beta_1-\beta_x)}) \lim_{n\to\infty}\left(\sum_{k=0}^{n}(r_{10}r_{12}e^{-i2\beta_1})^k\right) \quad \text{(eq. 4.16)}$$

$$= \frac{t_{01}e^{-i\beta_x} + t_{01}r_{12}e^{-i(2\beta_1-\beta_x)}}{1 - r_{10}r_{12}e^{-i2\beta_1}}$$

The calculation of the second component requires considering the following possible events:

(a) An incident plane wave has a certain probability amplitude to be transmitted by graphene, which is given by the following coefficient:

$$\alpha_{0\to2} = t_{01}t_{12}e^{-i\beta_1} \lim_{n\to\infty}\left(\sum_{k=0}^{n}(r_{10}r_{12}e^{-i2\beta_1})^k\right) = \frac{t_{01}t_{12}e^{-i\beta_1}}{1 - r_{10}r_{12}e^{-i2\beta_1}} \quad \text{(eq. 4.17a)}$$

(b) The transmitted wave has a probability amplitude to be reflected by Si and transmitted back from SiO_2 to graphene, which corresponds to the following term:

$$\alpha_{2\to1} = r_{23}t_{21}e^{-i2\beta_2} \lim_{n\to\infty}\left(\sum_{k=0}^{n}(r_{23}t_{21}e^{-i2\beta_2})^k\right) = \frac{r_{23}t_{21}e^{-i2\beta_2}}{1 - r_{23}t_{21}e^{-i2\beta_2}} \quad \text{(eq. 4.17b)}$$

(c) The reflected wave has a given probability amplitude to be absorbed by graphene at a depth x, which is written:

$$\alpha_x = \left(e^{-i(\beta_1-\beta_x)} + r_{10}e^{-i(\beta_1+\beta_x)}\right) \lim_{n\to\infty}\left(\sum_{k=0}^{n}(r_{10}r_{12}e^{-i2\beta_1})^k\right) \quad \text{(eq. 4.17c)}$$

$$= \frac{e^{-i(\beta_1-\beta_x)} + r_{10}e^{-i(\beta_1+\beta_x)}}{1 - r_{10}r_{12}e^{-i2\beta_1}}$$

(d) The non-absorbed electric field can be reflected back to the substrate with the following probability amplitude:

$$\alpha_{1\to2} = r_{01}t_{12}e^{-i\beta_1} \lim_{n\to\infty}\left(\sum_{k=0}^{n}(r_{10}r_{12}e^{-i2\beta_1})^k\right) = \frac{r_{01}t_{12}e^{-i\beta_1}}{1 - r_{10}r_{12}e^{-i2\beta_1}} \quad \text{(eq. 4.17d)}$$

Finally, it follows that the second component, which corresponds to the sum of the probability amplitudes associated with the yellow dots in **Figure 4.15b**, is given by:

$$\alpha_{ab}^{(2)} = \alpha_{0\to2}\alpha_{2\to1}\alpha_x \lim_{n\to\infty}\left(\sum_{k=0}^{n}(\alpha_{1\to2}\alpha_{2\to1})^k\right) = \frac{\alpha_{0\to2}\alpha_{2\to1}\alpha_x}{1 - \alpha_{1\to2}\alpha_{2\to1}} \quad \text{(eq. 4.18)}$$

(b) Calculation of the scattering coefficient

The total electric field scattered by graphene from a given depth x and transmitted toward the detector can be decompose in two components:

$$\alpha_{sc} = \alpha_{sc}^{(1)} + \alpha_{sc}^{(2)} \qquad \text{(eq. 4.19)}$$

$\alpha_{sc}^{(1)}$ is associated to a scattered signal sent the detector after propagation in graphene only (**Figure 4.16a**) and $\alpha_{sc}^{(2)}$ to a scattered signal sent the detector after propagation in both graphene and SiO_2 (**Figure 4.16a**).

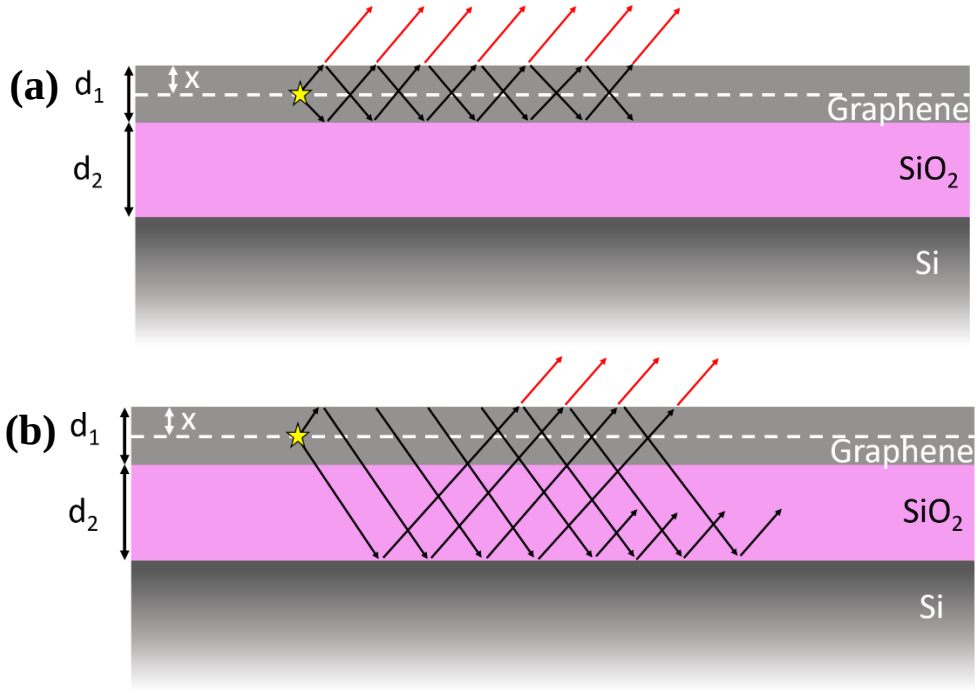


Figure 4.16: Schematic diagrams of the multiple paths contributing to (a) $\alpha_{sc}^{(1)}$ and (b) $\alpha_{sc}^{(2)}$. The total electric filed scattered from a given depth in graphene (yellow star) to the air is derived by summing the electric filed amplitudes associated to the red arrows.

The first component is derived by summing the probability amplitudes associated to the red arrows in **Figure 4.16a**:

$$\alpha_{sc}^{(1)} = (t_{01}e^{-i\beta_x} + t_{10}r_{12}e^{-i(2\beta_1-\beta_x)}) \lim_{n\to\infty}\left(\sum_{k=0}^{n}(r_{10}r_{12}e^{-i2\beta_1})^k\right) \qquad \text{(eq. 4.20)}$$

$$= \frac{t_{01}e^{-i\beta_x} + t_{10}r_{12}e^{-i(2\beta_1-\beta_x)}}{1 - r_{10}r_{12}e^{-i2\beta_1}}$$

The calculation of the second component requires considering the following possible events:

(a) A plane wave which is scattered at a depth x has a certain probability amplitude to be transmitted to the substrate, which given by the following coefficient:

$$\alpha_{x\to 2} = \left(t_{12}e^{-i(\beta_1-\beta_x)} + r_{10}t_{12}e^{-i(\beta_1+\beta_x)}\right)\lim_{n\to\infty}\left(\sum_{k=0}^{n}(r_{10}r_{12}e^{-i2\beta_1})^k\right) \qquad \text{(eq. 4.21a)}$$
$$= \frac{t_{12}e^{-i(\beta_1-\beta_x)} + r_{10}t_{12}e^{-i(\beta_1+\beta_x)}}{1 - r_{10}r_{12}e^{-i2\beta_1}}$$

(b) The transmitted wave has a probability amplitude to be reflected by Si and transmitted back from SiO_2 to graphene, which corresponds to the following term:

$$\alpha_{2\to 1} = r_{23}t_{21}e^{-i2\beta_2}\lim_{n\to\infty}\left(\sum_{k=0}^{n}(r_{23}r_{21}e^{-i2\beta_2})^k\right) = \frac{r_{23}t_{21}e^{-i2\beta_2}}{1 - r_{23}t_{21}e^{-i2\beta_2}} \qquad \text{(eq. 4.21b)}$$

(c) The reflected wave has a given probability amplitude to be transmitted by graphene, which is written:

$$\alpha_{1\to 0} = t_{10}e^{-i\beta_1}\lim_{n\to\infty}\left(\sum_{k=0}^{n}\left(r_{10}r_{12}e^{-i2\beta_1}\right)^k\right) = \frac{t_{10}e^{-i\beta_1}}{1 - r_{10}r_{12}e^{-i2\beta_1}} \qquad \text{(eq. 4.21c)}$$

(d) The non-transmitted electric field can be reflected back to the substrate with the following probability amplitude:

$$\alpha_{1\to 2} = r_{10}t_{12}e^{-i\beta_1}\lim_{n\to\infty}\left(\sum_{k=0}^{n}\left(r_{10}r_{12}e^{-i2\beta_1}\right)^k\right) = \frac{r_{10}t_{12}e^{-i\beta_1}}{1 - r_{10}r_{12}e^{-i2\beta_1}} \qquad \text{(eq. 4.21d)}$$

Finally, it follows that the second component, which corresponds to the sum of the probability amplitudes associated with the red arrows in **Figure 4.16b**, is given by:

$$\alpha_{sc}^{(2)} = \alpha_{x\to 2}\alpha_{2\to 1}\alpha_{1\to 0}\lim_{n\to\infty}\left(\sum_{k=0}^{n}(\alpha_{2\to 1}\alpha_{1\to 0})^k\right) = \frac{\alpha_{x\to 2}\alpha_{2\to 1}\alpha_{1\to 0}}{1 - \alpha_{2\to 1}\alpha_{1\to 0}} \qquad \text{(eq. 4.22)}$$

The case of graphene on gold substrate can also be studied, since this PhD involves graphene transfer on ultra-flat gold (see **Chapter 2**). It corresponds to the exact same calculations but without SiO_2 and with gold instead of Si. In other words, $d_2 = 0\ nm$, $\tilde{n}_2 = 1$ and $\tilde{n}_3(\lambda) = \tilde{n}_{Au}(\lambda)$.

The Raman enhancement factor (F) is defined as the Raman intensity for supported graphene normalized to the intensity for free-standing graphene:

$$F = \frac{I_{supported}}{I_{free-standing}} \qquad \text{(eq. 4.23)}$$

The enhancement factor of the G, D and 2D bands Raman signal is plotted in **Figure 4.17** as function of

the laser wavelength for both graphene on Si/SiO_2 and graphene on gold. Concerning the D' band, its frequency is close enough to the G band to consider that the enhancement of the G band makes a good estimation of the one of the D' band.

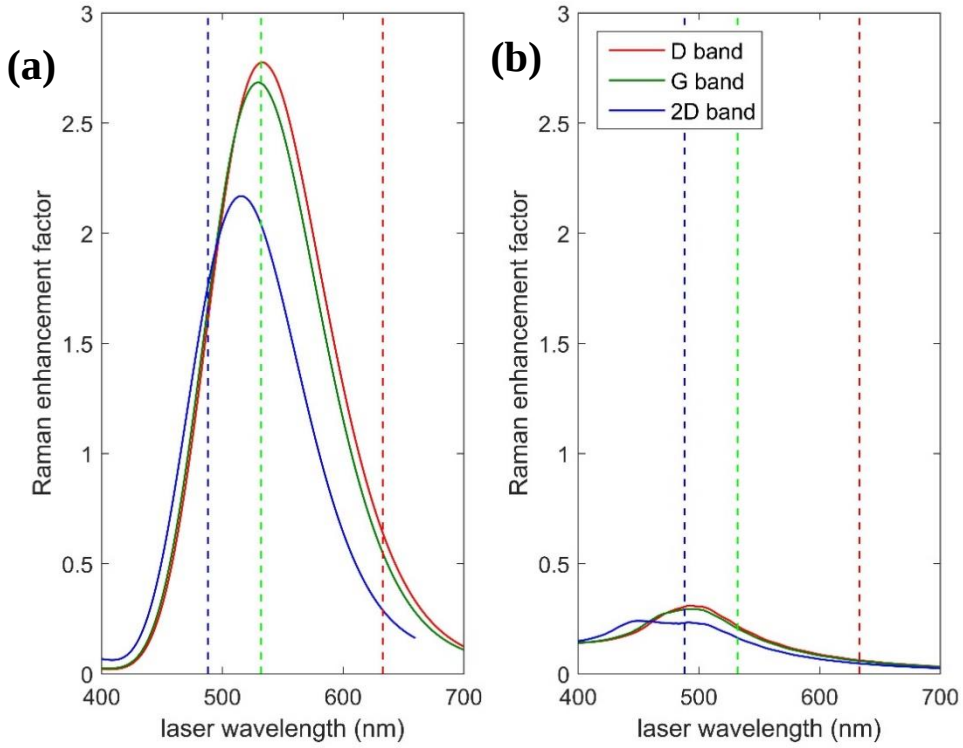


Figure 4.17: Raman enhancement factor associated to the D, G and 2D bands as function of the excitation wavelength for (a) Si/SiO_2 (285 nm) and gold substrates. The vertical dashed lines indicate the excitations wavelength used during this PhD: 488 nm (blue), 532 nm (green) and 633 nm (red).

Three different laser sources were frequently used for Raman spectroscopy during this PhD: 488 nm, 633 nm (He-Ne) and 532 nm (ND-YAG). These three laser excitations are indicated in **Figure 4.17**, which demonstrates that, for graphene on Si/SiO_2, the Raman signal is attenuated (in comparison to free-standing graphene) with a 633 nm laser excitation but significantly enhanced with a 488 nm or a 532 nm laser excitation. The strong wavelength dependency witnesses strong interference effects caused by the substrate. It must be reminded that the present calculations only consider a SiO_2 thickness of 285 nm, and that different results are expected for other thickness values. Since gold is a metal, the wavelength dependency is significantly smaller. In addition, the graphene Raman signal on gold is attenuated for all the wavelengths. One way to enhance the Raman signal on gold consists of strengthening the excitation field at the nanoscale using a gold-coated AFM tip, which is achieved in tip-enhanced Raman spectroscopy (TERS) (see **4.3**).

4.1.3 Experimental set-up

In this PhD, three different commercial Raman spectrometers were used: two were manufactured by Horiba, and the third was manufactured by Renishaw. To describe briefly what a Raman set-up consists of, it can be decomposed into different elements: a laser, a confocal microscope, a filter, a diffraction grating and a CCD detector. Let us detail these elements briefly:

The Laser: Since Raman spectroscopy is a measurement of light inelastic scattering, it requires a monochromatic excitation, which means a laser. Among the different Raman set-up used during this PhD, different laser emitters were used: one He-Ne laser with an emission at 1.96 eV (633 nm); one ND-YAG with an emission at 2.33 eV (532 nm), one laser with emission at 2.54 eV (488 nm); and three laser diodes with emissions at 1.56 eV (785 nm), 1.94 eV (638 nm) and 2.33 eV (532 nm). Different filters placed on the path of the laser beam allow the control of the laser power.

The microscope objective: The microscope objective allows for focalization of the laser on the sample's surface to have a good spatial resolution and a large photon density at the focal point. Most of the Raman spectra in this PhD were recorded using a ×100 magnification objective with a large numerical aperture (usually 0.9) to optimize the spatial resolution and the photon density. In general, the laser spot size on the sample's surface is about approximatively 1 μm^2. The area of the graphene flakes was usually in the range of 100 to 300 μm^2, which means that it was generally not difficult to illuminate a graphene surface fraction without getting contributions from the edges. The scattered light is collected by the objective and sent to the filter.

The filter: The role of the filter is to block the Rayleigh component of the scattered light and transmit the Raman component. This can be done with a notch filter that allows for blocking a narrow band around the laser frequency and transmitting other frequencies. Sometimes, Raman spectrometers use an edge filter, which can be either a low-pass or high-pass filter depending on whether the Stokes or anti-Stokes signal is to be analyzed.

The confocal pinhole: The filtered signal is sent through a confocal pinhole to block the light that is not coming from the focal plane. It is used to remove the background signal emitted, for instance, by the substrate, optimizing by this method the signal-noise ratio. It must be specified that, in the case of graphene, the signal coming from the substrate is always detected because the depth of focus is always larger than the graphene thickness.

Diffraction grating: The diffraction grating allows for the decomposition of light at different angles depending on the wavelength. Different gratings are integrated in commercial spectrometers, allowing for playing with the spectral resolution and the spectral bandwidth. A grating with a higher groove density ensures higher spectral resolution but lower spectral bandwidth. Since the graphene Raman spectrum covers a large frequency range, gratings with low groove density (generally 300 grooves/mm) were mostly used in order to record the entire spectrum in one acquisition.

The CCD detector: The CCD detector, placed after the diffraction grating, is a matrix of photosensitive elements based on charge transfer. Each photoelectron is associated with one pixel, which means one optical frequency.

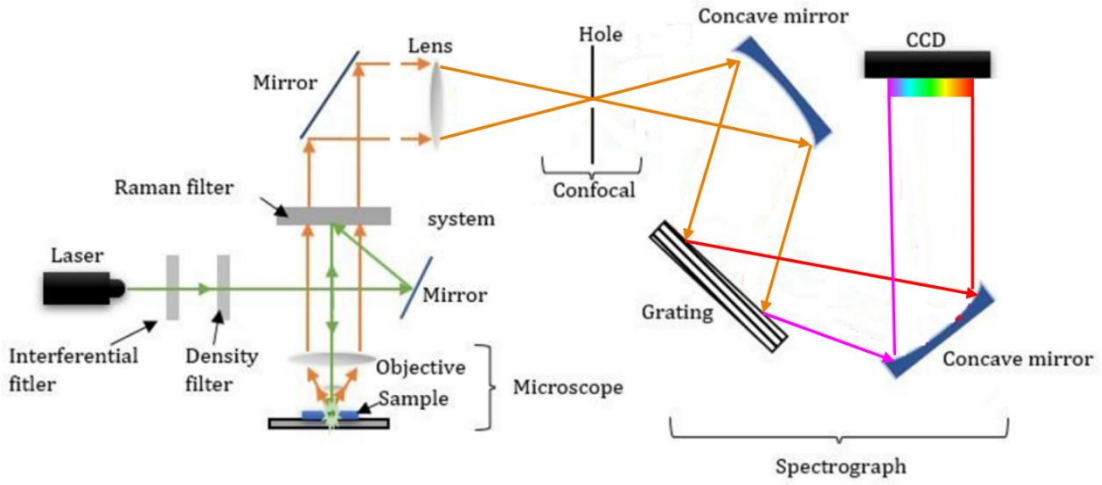


Figure 4.18: Schematic representation of a Raman spectrometer.

4.2 Atomic Force Microscopy (AFM)

4.2.1 Basic Principle (Contact mode)

AFM is a powerful microscopy technique that is sensitive to the electrostatic near-field at the surface of a sample. The principle consists in approaching a nanoprobe at a very small distance from the surface (~few nm) and thereby measuring the force between the surface and the probe, which is related to the gradient of the interaction energy potential ($\vec{F} = -\overrightarrow{grad}U$). At a distance where there is no overlap between the electronic clouds, the force exerted between the probe and the surface is attractive (i.e. $\vec{F} = -\|F\|\overrightarrow{e_z}$) and increases with decreasing distance. This force can have several possible origins such as van der Waals interactions, capillarity or adhesion forces. When the electronic clouds start overlapping, the force becomes repulsive (i.e. $\vec{F} = \|F\|\overrightarrow{e_z}$) due to the Pauli exclusion principle.

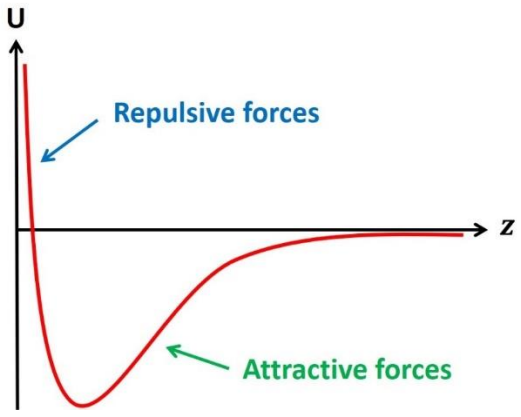


Figure 4.19: Interaction potential as function of the distance between the tip and the surface.

The probe is constituted of a cantilever with a tip at the end so that any vertical force applied on the tip induces a deflection of the cantilever. This deflection can be measured by different methods, but for the AFM used within this PhD (NanoObserver from CSI), it is done with a laser beam that illuminates the end of the cantilever and is reflected to a 4-quadrant photodiode. The vertical deflection of the cantilever leads to a deviation of the reflected beam, thereby inducing a variation of the signal detected by the photodiode. The modulus of the force between the probe is given by Hooke's law:

$$F = k\delta z \qquad \text{(eq. 4.24)}$$

where k is the effective spring constant of the cantilever, which depends on the cantilever geometry and the Young's modulus, and δz is the vertical deflection measured at the end of the cantilever by the 4-quadrant photodiode. In general, the effective spring constant of the cantilevers is in the range 0.01-10 N/m. For k = 0.01 N/m, the sensitivity is about 1 pN/Å.

The AFM image of a given surface is obtained by horizontally translating the sample with respect to the probe. The sample is usually placed on a piezoelectric stage to allow a minimal step size. The resolution of an AFM image depends rather on the tip sharpness. There are two possible imaging modes:

- Feedback OFF: The z-coordinate of the sample is kept constant during the scan. Changes in the topography of the surface (steps, holes, …) conduct to fluctuations of the distance between the tip and the nearest surface atoms, inducing flections and deflections of the cantilever.
- Feedback ON: The force between the tip and the surface is kept constant during the scan by continuously adjusting the z-coordinate of the sample. At each point of the surface, the measured force F_{mes} is compared with the locker value F_{set} and a voltage V_z is applied to the piezoelectric stage via a feedback loop to adjust the z-coordinate of the sample. The topography of the surface is determined from the variation of V_z.

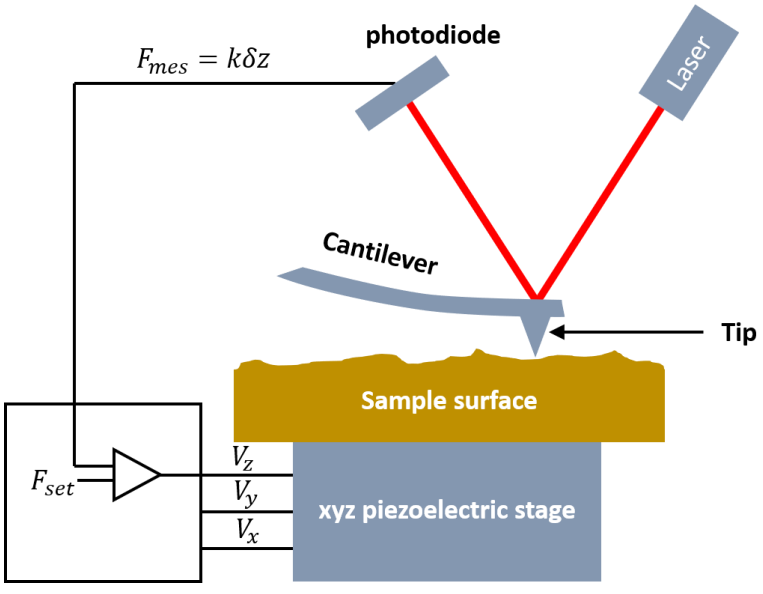


Figure 4.20: Schematic representation of an AFM used in contact mode.

In general, AFM images are done with “feedback ON” to avoid damaging the tip. This scanning mode is referred to as *contact mode* and, since the tip is always in interaction with the surface, it can be destructive for fragile samples.

4.2.2 Tapping mode

Another scanning mode commonly used to minimize the interactions is the *tapping mod*e, where the cantilever is not continuously in contact with the surface. In this mode, the probe is placed further away from the surface (in the attractive region) and oscillates at a given frequency and amplitude imposed by a sinusoidal excitation $A_0 \cos(\omega t)$. One can treat the vertical motion of the cantilever as a harmonic oscillator:

$$m_e \ddot{z} + c\dot{z} + kz = A_0 \cos(\omega t) \qquad \text{(eq. 4.25)}$$

where m_e is the effective mass of the cantilever, c is the friction coefficient, and k is the spring constant. Since the spring constant is related to the resonance pulsation ω_0 of the cantilever by $\omega_0 = \sqrt{\frac{k}{m_e}}$, **eq. 4.25** can be written as:

$$\ddot{z} + \gamma\dot{z} + \omega_0^2 z = \frac{A_0}{m_e}\cos(\omega t) \qquad \text{(eq. 4.26)}$$

where $\gamma = \frac{c}{m_e}$. The harmonic solution of **eq. 4.26** is:

$$z(t) = A(\omega)\cos(\omega t - \varphi(\omega)) \qquad \text{(eq. 4.27)}$$

were $A(\omega) = \frac{A_0}{m_e}\frac{1}{\sqrt{(\omega_0^2-\omega^2)^2+\gamma^2\omega^2}}$ is the amplitude and $\varphi(\omega) = arctan\left(\frac{\gamma\omega}{\omega_0^2-\omega^2}\right)$ is the phase. The vertical amplitude of the cantilever is maximized when the excitation frequency is close to the resonance frequency of the tip. Thus, it is required to primarily record the frequency response of the cantilever to find its resonance frequency.

When the tip gets close to the surface, its amplitude of vibration is impacted by its interaction with the sample. As a consequence, **eq. 4.26** becomes:

$$\ddot{z} + \gamma\dot{z} + \omega_0^2 z = \frac{A_0}{m_e}\cos(\omega t) + \frac{F(z)}{m_e} \qquad \text{(eq. 4.28)}$$

were F(z) corresponds to the resulting force between the tip and the surface. In general, F(z) is non-linear, which means that **eq. 4.27** cannot be a solution of **eq. 4.28**. Considering low amplitude oscillations, the force can be approximated by the limited development at the average position z_0:

$$F(z) \approx F(z_0) + z\frac{\partial F}{\partial z}(z_0) \qquad \text{(eq. 4.29)}$$

and **eq. 4.28** becomes:

$$\ddot{z} + \gamma\dot{z} + \left(\omega_0^2 - \frac{1}{m_e}\frac{\partial F}{\partial z}(z_0)\right)z = \frac{A_0}{m_e}\cos(\omega t) + \frac{F(z_0)}{m_e} \qquad \text{(eq. 4.30)}$$

In other words, the resonance frequency of the cantilever is renormalized due to the interactions with the surface of the sample. The effective frequency of the cantilever becomes $k_e = k - \frac{\partial F}{\partial z}(z_0)$. It gives a resonance pulsation $\omega_1 \approx \sqrt{\omega_0^2 - \frac{1}{m_e}\frac{\partial F}{\partial z}(z_0)} \approx \omega_0\left(1 - \frac{1}{2k}\frac{\partial F}{\partial z}(z_0)\right)$. The tapping mode works at constant amplitude, which means that $\Delta\omega = |\omega_1 - \omega_0| = \omega_0\frac{1}{2k}\frac{\partial F}{\partial z}(z_0)$ is maintained constant. In other words, the tapping mode regulates the force gradient between the tip and the surface.

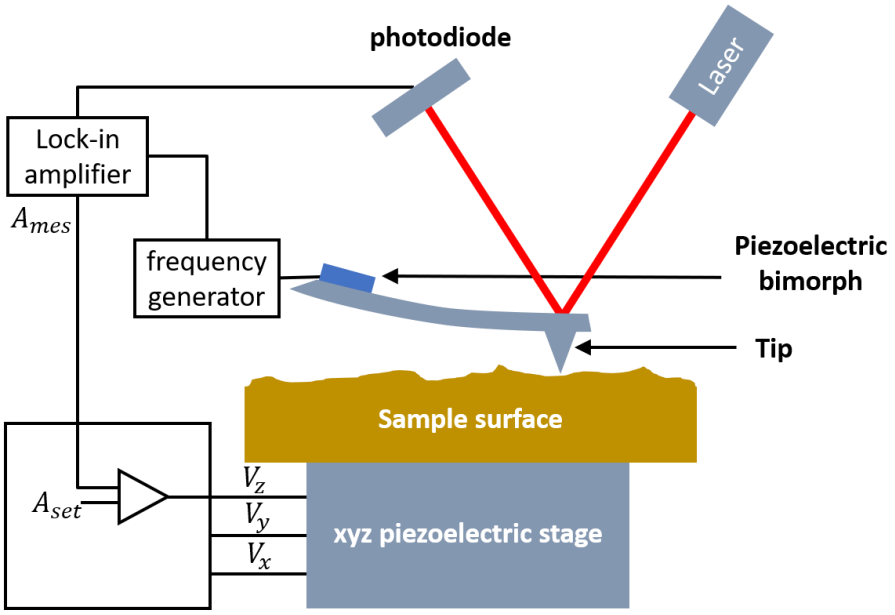


Figure 4.21: Schematic representation of an AFM used in tapping mode.

4.2.3 Experimental details

In the framework of the PhD, AFM was used to investigate the topography of graphene's surface after hydrogenation and fluorination. For hydrogenation, the calculations of the structure relaxation with hydrogen covalently bonded to graphene [74] estimate an out-of-plane displacement of the sp^3-hybridized carbon atom of about 0.58 Å and the C-H bond length given by previous theoretical work from the literature is about 1.11 Å [18]. Considering these values, one can expect a step of ~ 1.7 Å at the border between a pristine region and a hydrogenated region. Such a small step is undetectable experimentally if the graphene is not perfectly flat and clean. At the laboratory, there are two AFM (NanoObserver from CSI), including one in a glove box purged with nitrogen. To minimize the presence of residues on the surface, all the samples were imaged using the AFM in glove box, which means under an N_2 atmosphere of high purity ($O_2 < 0.1\ ppm$ *and* $H_2O < 0.1\ ppm$). However, even under UHV, it would be difficult to detect a step of

1.7 Å because of the SiO_2 roughness which is about 2.2 Å (root mean squared value) and even 2.6 Å after 300s of O_2 plasma treatment [75]. In addition, there might be some water or residues trapped at the interface between graphene and SiO_2 during exfoliation, and that would modify the height of the step.

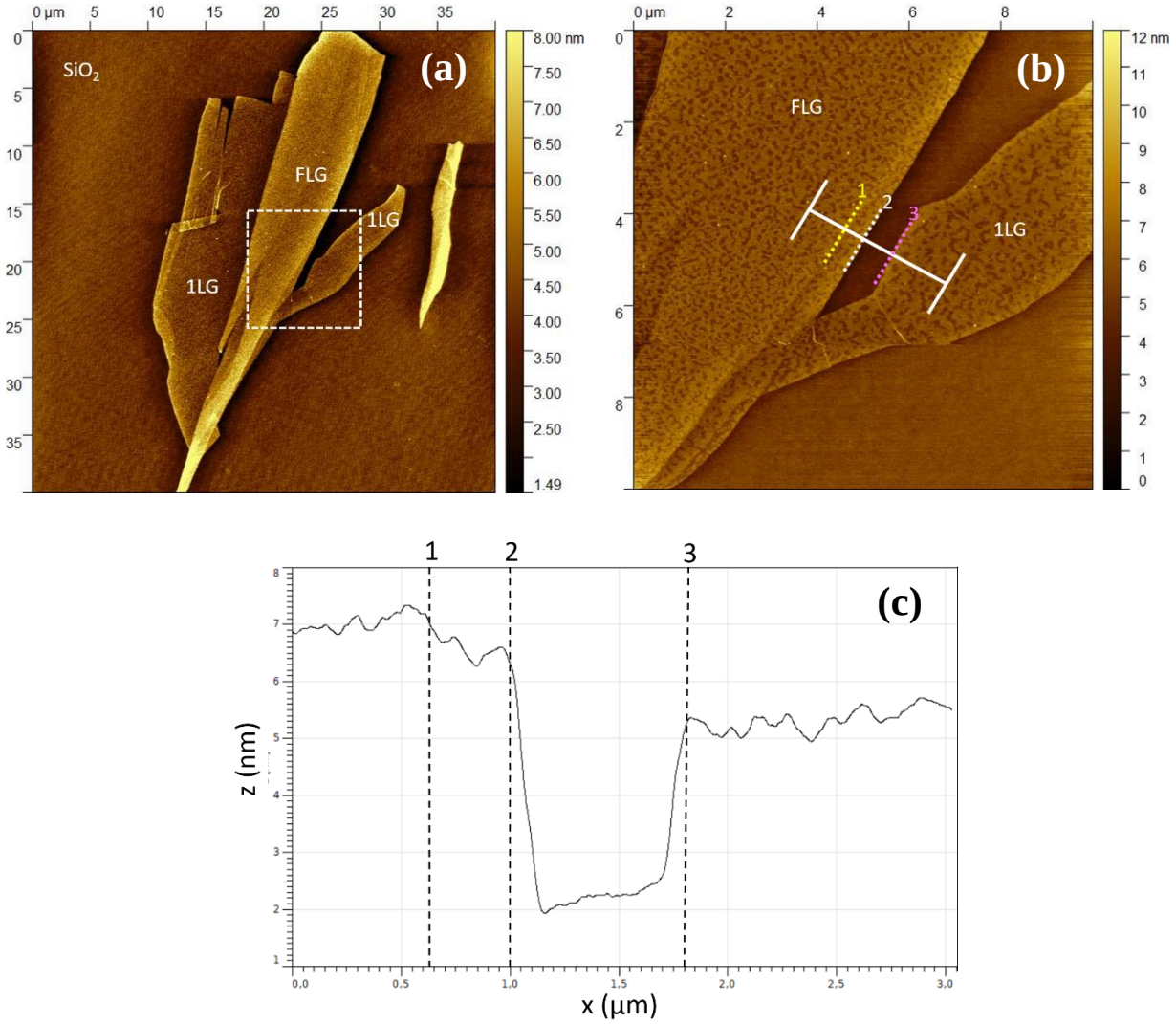


Figure 4.22: (a) topography of a graphene flake composed of FLG and 1LG on SiO_2. The image was done in tapping mode and treated with the software Gwyddion. (b) 10×10 µm scan of the region designed by the dashed square in (a). (c) Average 1D profile along the segment drawn in (b). Three borders are identified by numbers and assigned to the three corresponding borders visible in (b).

Figure 4.22a shows a pristine graphene flakes on Si/SiO_2 imaged with AFM tapping mode. The steps between regions of different number of layers are clearly visible in this image and two monolayer regions (1LG) are distinguishable from the few-layer region (FLG). In the 10×10 µm scan presented in **Figure 4.22b**, some local fluctuations of the graphene's surface topography are visible and do not originate from the substrate roughness since they are not visible on SiO_2 and similar fluctuations can be observed for

graphene on hexagonal boron nitride (h-BN). The origin of these fluctuations was not investigated in this work. In **Figure 4.22c**, which shows the average profile along the segment drawn in **Figure 4.22b**, the three borders are distinguishable, but the step at the border between 1LG and SiO_2 is much larger than the 1LG thickness (3.34 Å). Indeed, the vertical resolution if often affected by interactions between the tip and the surface (contamination, vdW forces, …). It is likely that, despite being in glove box, a thin layer of water could remain on the surface.

In this work, AFM was mainly used as a complementary technique to confirm the origin of the defects probed in Raman spectroscopy. Although it is not possible to detect sp^3-type defects with AFM, other types of structural deformations (holes, cracks, wrinkles, …) contributing to the D band can be resolved with AFM.

The spatial resolution depends on different parameters such as the radius of curvature of the tip and the scanning parameters (velocity and step size). The laboratory purchases AFM probes from the company App Nano, and the ones used in this work were SPM-probe model cantilevers with a Silicon tip characterized by a radius of curvature of 6 nm. All the AFM images in this work were obtained using the tapping mode. The spring constants of the cantilevers for these models are in the range of 0.6-3.5 N/m, and their resonant frequencies were in the range of 43-81 kHz.

4.3 Tip Enhanced Raman spectroscopy (TERS)

4.3.1 Basic concept

4.3.1.1 Raman signal enhancement and nanoscale resolution

In Raman spectroscopy, as in any conventional optical characterization technique, the spatial resolution is limited by diffraction. The Raman scattered signal is collected by a microscope objective of numerical aperture $NA = n \times \sin\theta$ (n being the optical index and θ the half-angle of the objective) and the spatial resolution Δx corresponding to the full width at half maximum of the focus for a wavelength λ is given by:

$$\Delta x = \frac{0.61\lambda}{NA} \qquad \text{(eq. 4.31)}$$

For visible laser excitation, Δx corresponds to a few hundred nm. The maximum resolution is achieved for $\theta = \pi/2$ (which is not realized in practice) but even this case remains insufficient for nanoscale resolution. This can be understood by considering a plane wave $E(x, y, z = 0)$ on the sample's surface. The electric field on a given image plane at a distance $z \neq 0$ from the surface is obtained by multiplying the 2D Fourier transform by the propagation term $e^{ik_z z}$ such as:

$$E(x, y, z) = \iint_{-\infty}^{+\infty} \hat{E}(k_x, k_y)\, e^{i(k_x x + k_y y)} e^{\pm i k_z z}\, dk_x dk_y \qquad \text{(eq. 4.32)}$$

Since the total wave vector of the propagating wave is given by $k = \frac{2\pi n}{\lambda} = \sqrt{k_x^2 + k_y^2 + k_z^2}$, the k_z component is real for $\frac{2\pi n}{\lambda} \geq \sqrt{k_x^2 + k_y^2}$ and imaginary for $\frac{2\pi n}{\lambda} < \sqrt{k_x^2 + k_y^2}$. From **eq. 4.32** it can be concluded that only low spatial frequencies can propagate away from the surface, whereas the amplitude of the electric field associated with high frequencies decays exponentially with distance. Thus, the scattered electric field is decomposed into an evanescent and a propagating part, also referred to as the *near-field* and the *far-field*. Since conventional Raman spectroscopy can only detect the far-field, the spatial resolution is limited. However, in tip-enhanced Raman spectroscopy (TERS), a metallic AFM tip is approached in contact with the sample's surface, in the near-field region. By illuminating the tip with the laser, the strength of the excitation field is localized in the vicinity of the tip, leading to an enhancement of the Raman signal at the nanoscale. Moreover, the interaction between the tip and the sample allows the near field to propagate into the far field. In other words, TERS allows both Raman signal enhancement and nanoscale spatial resolution. Contrary to conventional Raman spectroscopy, where the spatial resolution is limited by diffraction, the TERS resolution is only limited by the sharpness of the tip. In addition, since TERS is a coupling between AFM and Raman spectroscopy, it allows for correlating both the surface topography and the spatially resolved Raman response, which is very powerful in the case of samples presenting inhomogeneities at the nanoscale [76].

4.3.1.2 Tip-sample interactions

The strengthening of the excitation field is induced by the excitation of surface plasmons at the tip apex. A plasmon is a quasiparticle described by a collective oscillation of an electron gas at a given frequency (called *plasmon frequency*) in response to an electromagnetic excitation. Close to the resonance, the excitation field induces a coherent oscillation of the free electrons at the surface of the metallic tip, i.e., excites surface plasmons. The induced electric dipole contributes to locally enhancing the excitation field. Then, the Raman signal scattered by the sample can either propagate directly to the far-field or interact with the tip to excite surface plasmons that reradiate into the far-field.

In this work, TERS was performed on graphene deposited on gold substrates, and the AFM tips were either Au-coated or Ag-coated, giving them a strong plasmonic response in the visible range with a resonance at 1.9 eV for Au-coated tips and 2.4 eV for Ag-coated tips [77]. In addition, the gold substrate allowed for increasing the enhancement factor via both plasmonic resonance and cavity effect. It must be specified that, with the TERS set-up used in this work, the tip-surface distance is extremely small (a few Angstroms) compared to conventional TERS systems. The size of the cavity is below the nanometer, which means that the electric field confined in the cavity has a quantum nature.

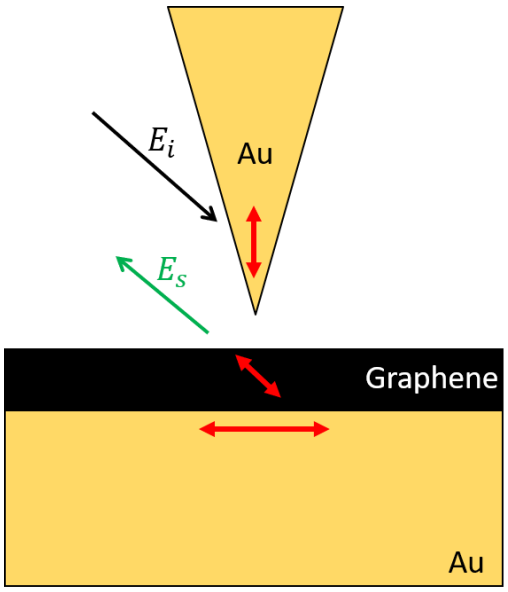


Figure 4.23: Simplified representation of the tip-sample interactions. Black and green arrows represent respectively the incident and the scattered field. Red arrows in the tip and in the substrate correspond to the induced polarization near gold plasmonic resonance and the red arrow in graphene represents the polarization induced by the electric field in the cavity.

4.3.2 C-H and C-F vibrational modes

In the framework of this PhD, TERS was used with the objective of detecting Raman signal from the C-H and C-F bonds in hydrogenated and fluorinated graphene, respectively. The associated vibrational modes were calculated by Ibrahim Arshad during his internship at CEMES, using a DFT-based code from the software ORCA. All ORCA calculations used the BP functional (Becke–Perdew GGA) and the def2-TZVP basis set, with RI-J approximation (def2/J) for efficient Coulomb integral evaluation. Geometry optimization was followed by numerical frequency analysis (Opt NumFreq) to extract vibrational modes and confirm the optimized structure as a true energy minimum. Results are summarized in **Table 4.1**.

Functional group	Wagging mode (cm^{-1})	Bending mode (cm^{-1})	Stretching mode (cm^{-1})
Hydrogen (H)	317	542	2740
Fluorine (F)	146	233	518

Table 4.1: Raman shifts associated to different modes calculated for two different functional groups.

Figure 4.24 plots the theoretical Raman activity calculated by ORCA for each vibrational mode mentioned in **Table 4.1**. According to these theoretical results, the stretching modes are the dominant contributions.

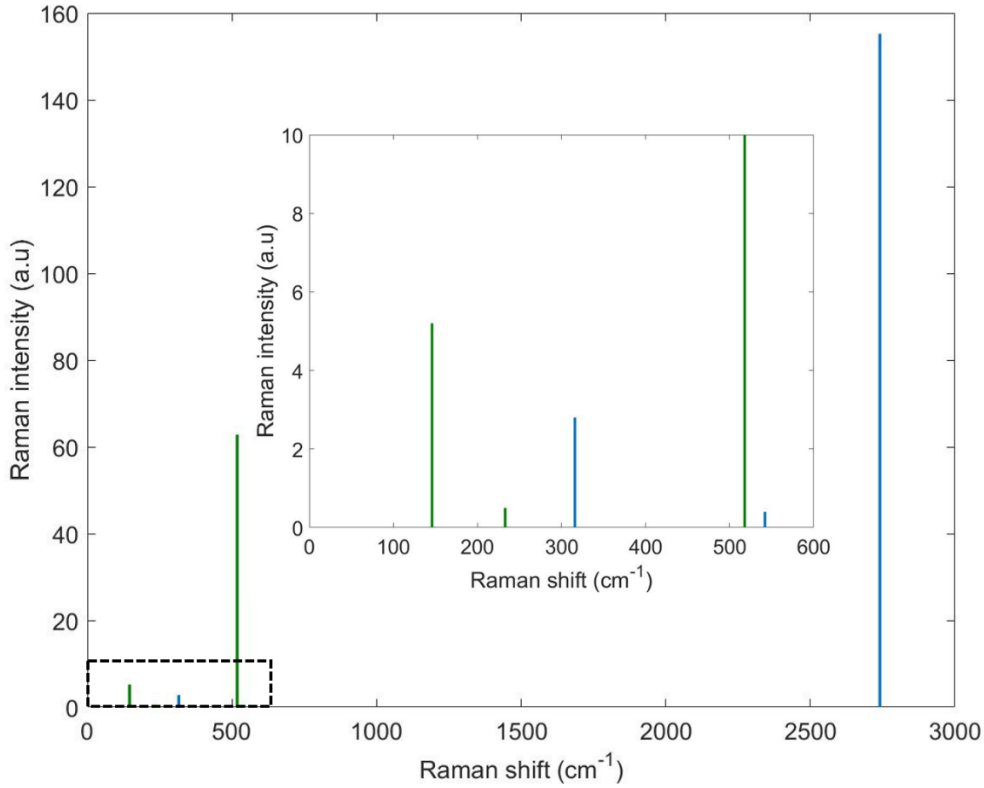


Figure 4.24: Plot of the different theoretical Raman lines for hydrogenated (blue) and fluorinated graphene (green). The inset provides a close-up of the framed region.

4.4 Electrical transport measurement

4.4.1 Electronic properties of pristine graphene

4.4.1.1 Electric field effect

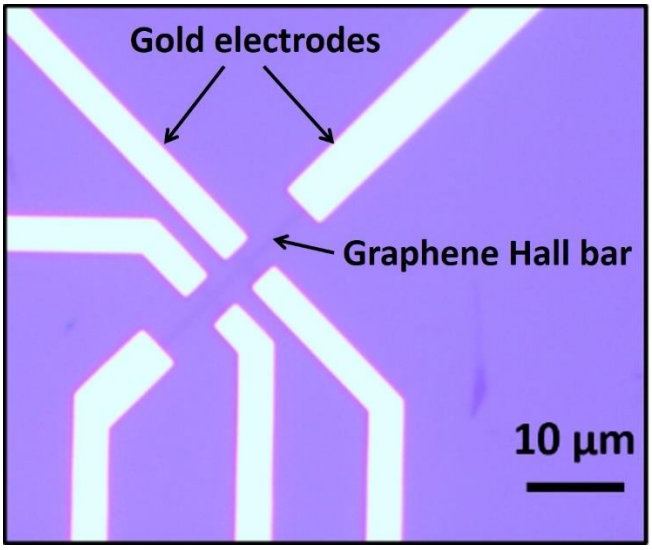


Figure 4.25: Photography of a graphene Hall bar on Si/SiO2 contacted by gold electrodes.

Let us consider a graphene Hall bar with finite dimensions connected by microelectrodes (**Figure 4.25**). Since graphene is fundamentally ambipolar, the electrical current is carried by both holes and electrons and the total current density must be described using the two-channel model:

$$\vec{J} = \overrightarrow{J_n} + \overrightarrow{J_p} \qquad \text{(eq. 4.33)}$$

Where $\overrightarrow{J_n}\ and\ \overrightarrow{J_p}$ are respectively the current density for electrons and holes. Since the current density is driven by the charge carrier density and the average velocity, **eq. 4.33** can be written:

$$\vec{J} = en\langle\overrightarrow{v_e}\rangle + ep\langle\overrightarrow{v_h}\rangle \qquad \text{(eq. 4.34)}$$

With n and p corresponding respectively to electrons and holes density and $\langle\overrightarrow{v_e}\rangle$ and $\langle\overrightarrow{v_h}\rangle$ their average velocity vectors. Then, the Ohm's low can be written:

$$\vec{J} = (en\mu_e + ep\mu_h)\vec{E} \qquad \text{(eq. 4.35)}$$

With μ_e and μ_h corresponding respectively to electrons and holes mobility. For the sake of simplicity, the mobility of holes and electrons can be considered equals such as $\mu_e = \mu_h = \mu$. As a result, the conductivity is given by:

$$\sigma = e(n + p)\mu \qquad \text{(eq. 4.36)}$$

As mentioned before in section **4.1.1.2**, the charge carrier density is temperature-dependent and the electrons and holes density at finite temperature can be given by:

$$n = \int_{E_{CNP}}^{E_f} f(E - E_f) g(E) dE \qquad \text{(eq. 4.37a)}$$

$$p = \int_{E_f}^{E_{CNP}} \left(1 - f(E - E_f)\right) g(E) dE \qquad \text{(eq. 4.37b)}$$

With the Fermi-Dirac distribution $f(E - E_f) = \frac{1}{1+exp\left(\frac{E-E_f}{k_B T}\right)}$.

n and p, as well as n+p, which corresponds to the total charge carrier's density, are plotted as function of the Fermi level for T=300 K in **Figure 4.26a**. It must be noticed that, due to thermal activation, n+p never falls to zero. Its minimum value $n_0 + p_0$ corresponding to $n(E_f = 0) + p(E_f = 0)$ is equal to $1.6 \times 10^{15}\ m^{-2}$ for $v_f = 10^6\ m/s$. **Figure 4.26b** shows that this value decreases at low temperature. Using the Sommerfeld development, it can be demonstrated that the value of $n_0 + p_0$ in pristine graphene follows a quadratic dispersion given by [78]:

$$n_0(T) + p_0(T) = \frac{\pi}{3}\left(\frac{k_B T}{\hbar v_F}\right)^2 \qquad \text{(eq. 4.38)}$$

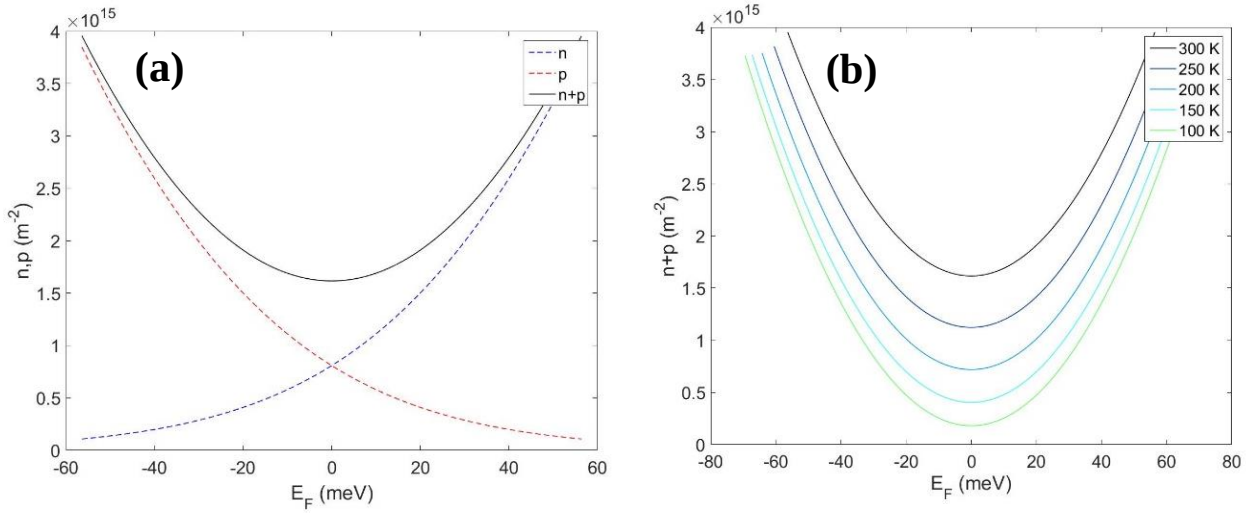


Figure 4.26: Plot of the charge carrier's density in graphene as a function of the Fermi level (a) for T = 300 K and (b) for T = 300, 250, 200, 150 and 100 K.

For graphene on Si/SiO_2, the Fermi level can be tuned with capacitive effect. Since the graphene/SiO_2/Si heterostructure forms a capacitor **(Figure 4.27)**, the total electrical charge Q_g injected in graphene relates to the electrical potential difference between graphene and silicon which is called the gate voltage (V_g).Thus

we have $Q_g = C_g V_g$, with $C_g = \frac{\varepsilon_0 \varepsilon_{Sio2}}{t_{Sio2}}$ corresponding to the capacitance that depends on the SiO_2 thickness t_{Sio2} and the relative dielectric permittivity ε_{Sio2}. Then, by considering a residual charge Q_0 which can come from contamination, the total electrical charge in graphene can be approximated by:

$$Q_t \approx Q_g + Q_0 \qquad \text{(eq. 4.39)}$$

Then, the charge neutrality point corresponds to a non-zero gate voltage $V_g = V_{CNP}$ so we have $Q_g \approx C_g(V_g - V_{CNP})$ and the relation between the gate voltage and the charge carrier density is given by:

$$C_g(V_g - V_{CNP}) \approx e(n - p) \qquad \text{(eq. 4.40)}$$

The nature of the charge carriers depends on the sign of $V_g - V_{CNP}$: when $V_g > V_{CNT}$ electrons are dominants which means that graphene is n-doped and the Fermi level is in the conduction band whereas for $V_g < V_{CNP}$ graphene is p-doped and the Fermi level is in the valence band.

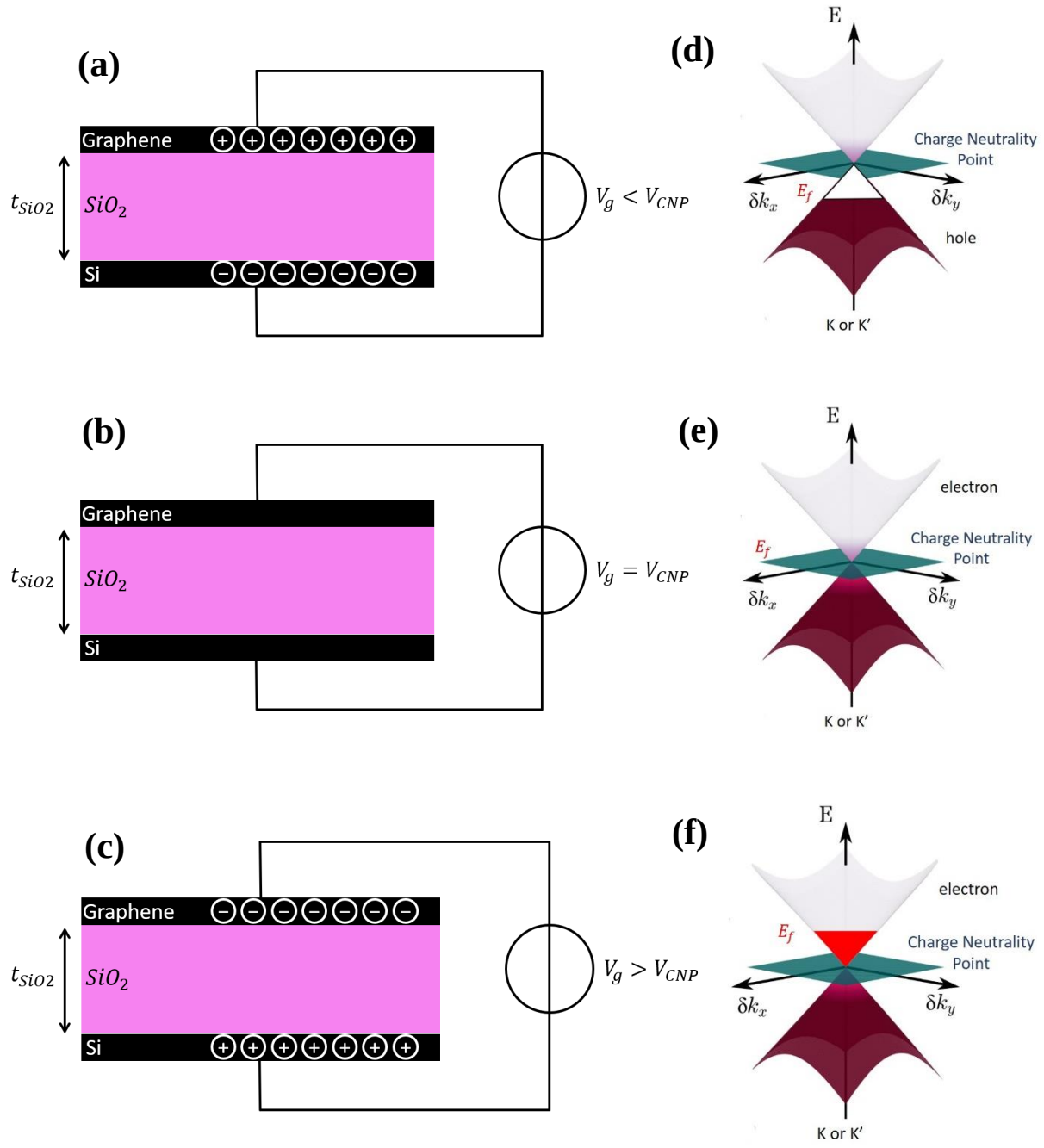


Figure 4.27: Gate control of the charge carrier density by capacitive effect. (a,b,c) Capacitor representation of graphene on SiO_2/Si. (d,e,f) Fermi level position in the Dirac Cone relatively to the CNP. (a,d) illustrate the case $V_g < V_{CNT}$, (b,e) $V_g = V_{CNT}$ and (c,f) $V_g > V_{CNT}$.

An empirical model proposed by Meric *et al* [79] allows to describe the total charge carrier density in graphene by:

$$n + p = \sqrt{(n - p)^2 + (n_0 + p_0)^2} \qquad \text{(eq. 4.41)}$$

Combining **eq. 4.40** and **eq. 4.41**, the charge carrier density expressed as function of the gate voltage is written:

$$n + p = \sqrt{\left[\frac{C_g}{e}(V_g - V_{CNP})\right]^2 + (n_0 + p_0)^2} \qquad \text{(eq. 4.42)}$$

The gate voltage dependence of the conductivity is given by combining **eq. 4.36** and **eq. 4.42**, which gives:

$$\sigma = e\mu\sqrt{\left[\frac{C_g}{e}(V_g - V_{CNP})\right]^2 + (n_0 + p_0)^2} \qquad \text{(eq. 4.43)}$$

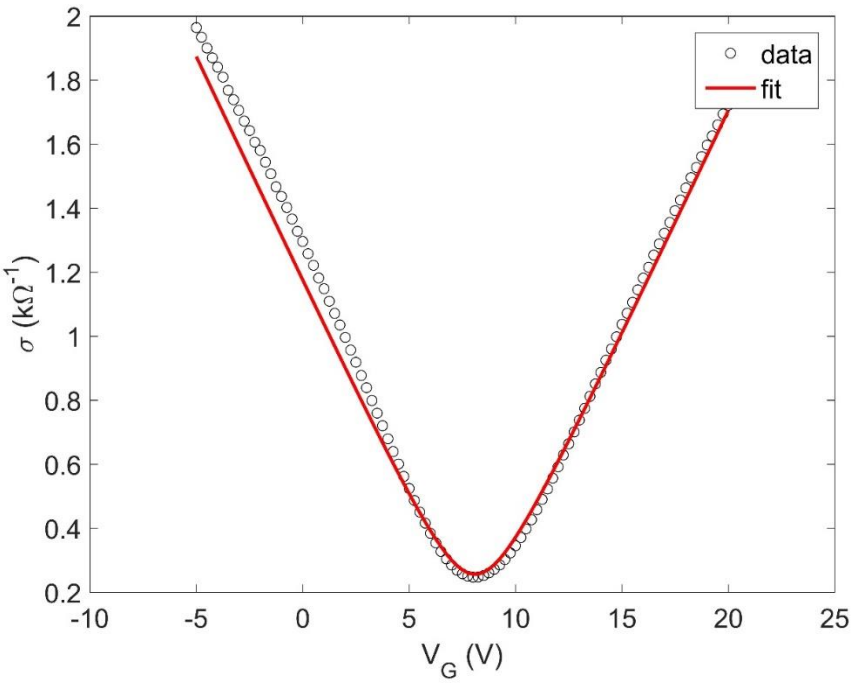


Figure 4.28: Measurement of the conductivity of a graphene sample on Si/SiO₂ as function of the gate voltage. Data are fitted by eq. 4.43 with $\mu = 1.6\ m^2 \cdot V^{-1}.s^{-1}$, $n_0 + p_0 = 1.2 \times 10^{15} m^{-2}$ and $V_{CNP} = 8.1\ V$. Here, the residual doping is lower than $1.6 \times 10^{15}\ m^{-2}$, but for this sample, v_f is renormalized to 1.2×10^6 m/s.

The charge carrier mobility in graphene is driven by two types of defects [80]:

(1) short-range defects: neutral defects, vacancies, etc…
(2) The long-range defects: charged defects present in the substrate, graphene corrugation, etc…

As a consequence, the mobility depends on these two contributions such as:

$$\mu = \left(\frac{1}{\mu_{sr}} + \frac{1}{\mu_{lr}}\right)^{-1} = \frac{\mu_{sr}\mu_{lr}}{\mu_{sr}+\mu_{lr}} \qquad \text{(eq. 4.44)}$$

With μ_{sr} the mobility induced by short-range defects, which is inversely proportional to doping [81] and μ_{lr} the mobility induced by long-range defects, which is constant. It follows from **eq. 4.44** that at low doping the mobility is mainly driven by long-range defects, which means that the conductivity is linearly dependent on doping, whereas at high doping the mobility is mostly driven by the short-range defects and the conductivity adopts a sublinear behaviour. In general, the transition from linear to sublinear dispersion depends on the quality of the graphene sample. In the case of encapsulated graphene, for instance, the long-range contribution is very low compared to the short range, which gives to conductivity a sublinear dispersion even at low doping. However, for graphene on SiO_2, since there is a large amount of trapped charges in the substrate, the mobility is mostly driven by the long-range, which gives a linear behaviour even at high doping. In this work, the mobility can be taken as a constant since graphene is on SiO_2. This is confirmed by the linear dispersion observed in **Figure 4.28** where the conductivity of a graphene Hall bar is plotted as a function of the gate voltage. Concerning the resistivity, it is given by:

$$\rho = \frac{1}{e\mu\sqrt{\left[\frac{C_g}{e}(V_g - V_{CNP})\right]^2 + (n_0 + p_0)^2}} \qquad \text{(eq. 4.45)}$$

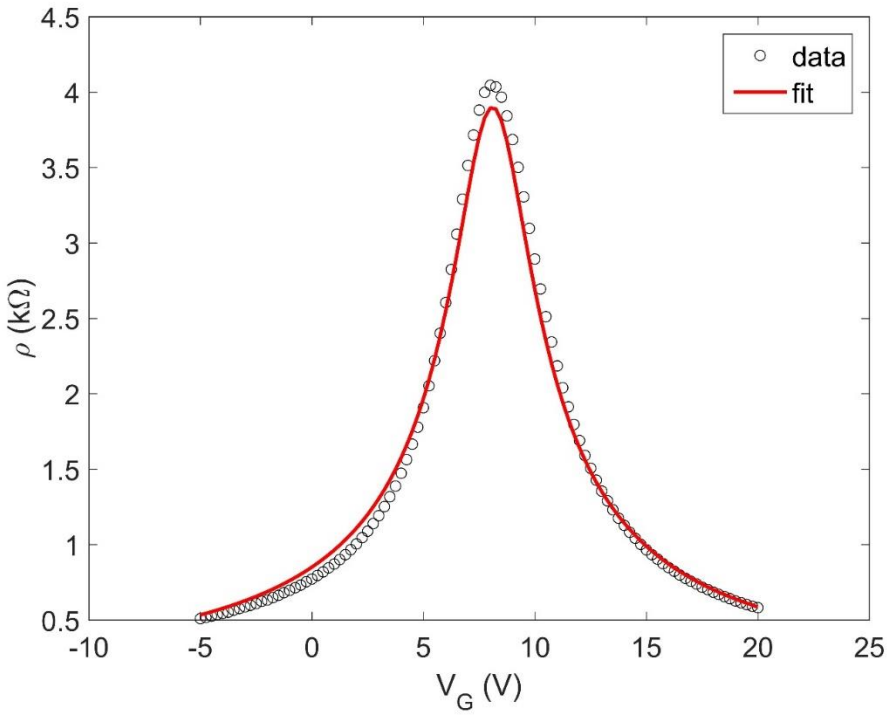


Figure 4.29: Measurement of the conductivity of a graphene sample on Si/SiO_2 as function of the gate voltage. Data are fitted by eq. 4.45 with $\boldsymbol{\mu = 1.6\ m^2 \cdot V^{-1}.s^{-1}, n_0 + p_0 = 1.2 \times 10^{15} m^{-2}}$ and $\boldsymbol{V_{CNP} = 8.1\ V}$.

Comparing the gate-voltage dependence of both the resistivity and the charge carrier density allows to distinguish three regions, as illustrated in **Figure 4.30**:

(1) The ambipolar region corresponding to $V_g \approx V_{CNT}$ where two types of carriers co-exist so we have $n + p \approx n_0$ and $\rho \approx \rho_{max} = \frac{1}{e\mu(n_0+p_0)}$

(2) The p-doped region corresponding to $V_g \ll V_{CNP}$ where we have $n + p \approx p \approx \sqrt{p^2 + (n_0 + p_0)^2}$ and $\rho \approx \rho_{min}$

(3) The n-doped region corresponding to $V_g \gg V_{CNP}$ where we have $n + p \approx n \approx \sqrt{n^2 + (n_0 + p_0)^2}$ and $\rho \approx \rho_{min}$

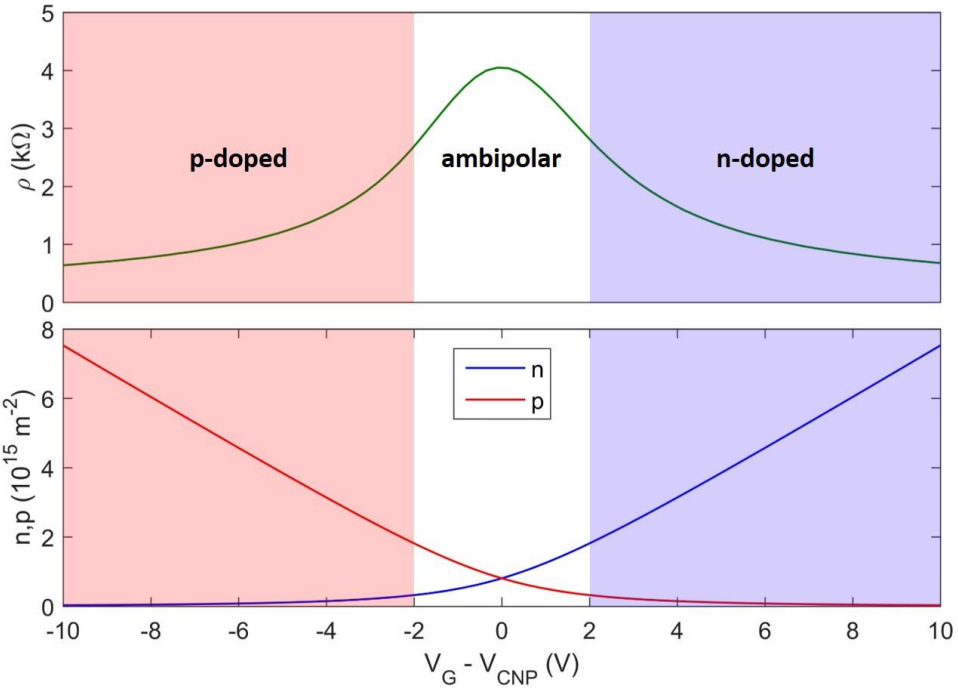


Figure 4.30: Evolution of ρ (experimental data from Figure 4.29), n and p (theorical values at 300K) as function of $V_g - V_{CNP}$.

4.4.1.2 Magnetic field effect

Now, in the presence of an out-of-plane magnetic field $\vec{B} = B_z\vec{e_z}$, one needs to consider the Hall effect that induces a transverse electric field [82]. As a consequence, the conductivity becomes a tensor and the Ohm's law is given by:

$$\begin{pmatrix} J_x \\ J_y \end{pmatrix} = \begin{pmatrix} \sigma_{xx} & \sigma_{xy} \\ -\sigma_{xy} & \sigma_{xx} \end{pmatrix} \begin{pmatrix} E_x \\ E_y \end{pmatrix} \quad \text{(eq. 4.46)}$$

The total current density is no longer colinear to the electric field because of the Lorentz's Force. It can be written as:

$$\vec{J} = \sigma_{xx}\vec{E} + \sigma_{xy}\vec{E} \wedge \vec{B} \qquad \text{(eq. 4.47)}$$

In the framework of the two-channel model, **eq. 4.47** can be decomposed for holes and electrons such as:

$$\vec{J} = \overrightarrow{J_n} + \overrightarrow{J_p} = (\sigma_{xx,n} + \sigma_{xx,p})\vec{E} + (\sigma_{xy,n} + \sigma_{xy,p})\vec{E} \wedge \vec{B} \qquad \text{(eq. 4.48)}$$

Using the Boltzmann formalism to derive the longitudinal and transverse components [5,83] **eq. 4.48** can be written:

$$\vec{J} = \frac{e(n+p)\mu}{1+(\mu B)^2}\vec{E} + \frac{e(p-n)\mu^2 B}{1+(\mu B)^2}\vec{E} \wedge \vec{B} \qquad \text{(eq. 4.49)}$$

The resistivity tensor is given by:

$$\bar{\bar{\rho}} = \begin{pmatrix} \rho_{xx} & \rho_{xy} \\ -\rho_{xy} & \rho_{xx} \end{pmatrix} = \begin{pmatrix} \frac{e(n+p)\mu}{1+(\mu B)^2} & \frac{e(p-n)\mu^2 B}{1+(\mu B)^2} \\ -\frac{e(p-n)\mu^2 B}{1+(\mu B)^2} & \frac{e(n+p)\mu}{1+(\mu B)^2} \end{pmatrix}^{-1}$$
$$= \begin{pmatrix} \frac{(n+p)(1+(\mu B)^2)}{e\mu\left((n+p)^2+\left((n-p)\mu B\right)^2\right)} & \frac{(p-n)(1+(\mu B)^2)B}{e\left((n+p)^2+\left((n-p)\mu B\right)^2\right)} \\ -\frac{(p-n)(1+(\mu B)^2)B}{e\left((n+p)^2+\left((n-p)\mu B\right)^2\right)} & \frac{(n+p)(1+(\mu B)^2)}{e\mu\left((n+p)^2+\left((n-p)\mu B\right)^2\right)} \end{pmatrix} \qquad \text{(eq. 4.50)}$$

At low magnetic field, (μB << 1), **eq. 4.50** can be approximated to:

$$\bar{\bar{\rho}} \approx \begin{pmatrix} \frac{1}{e(n+p)\mu} & \frac{(p-n)B}{e(n+p)^2} \\ -\frac{(p-n)B}{e(n+p)^2} & \frac{1}{e(n+p)\mu} \end{pmatrix} \qquad \text{(eq. 4.51)}$$

We find that the transverse component is linearly dependent on the magnetic field, whereas the longitudinal component is not magnetic field-dependent and is still expressed by **eq. 4.45**. Using **eq. 4.40** and **4.42**, the transverse components of the resistivity at low magnetic field can be expressed as a function of the gate voltage by:

$$\rho_{xy} \approx -\frac{C_g(V_g - V_{CNT})B}{e^2\left(\left[C_g(V_g - V_{CNP})\right]^2 + (n_0 + p_0)^2\right)} \qquad \text{(eq. 4.52)}$$

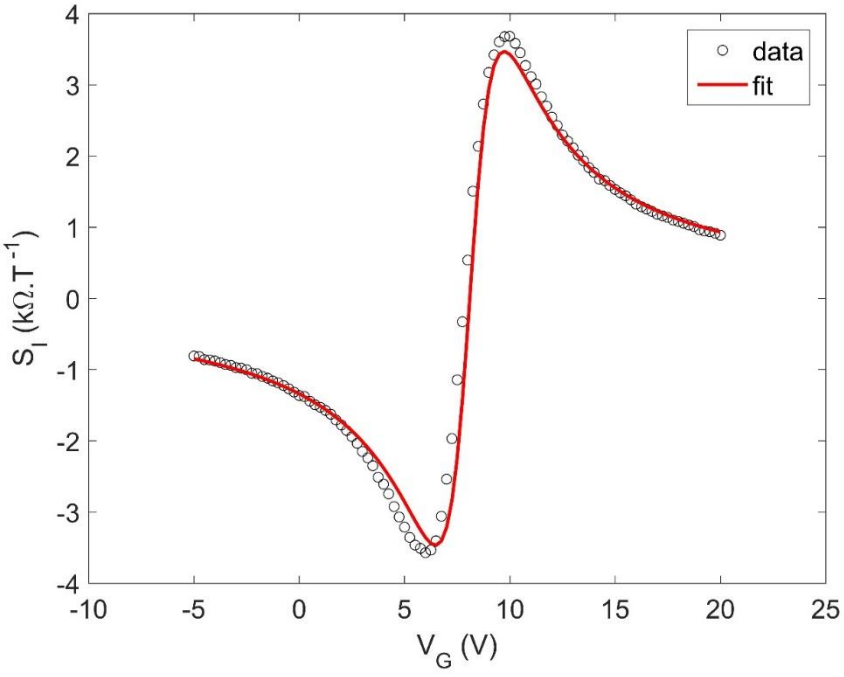


Figure 4.31: Measurement of the Hall sensitivity of a graphene sample on Si/SiO₂ as a function of the gate voltage. Data are fitted by eq. 4.52 with $n_0 + p_0 = 1.2 \times 10^{15} m^{-2}$ and $V_{CNP} = 8.1\ V$.

It must be mentioned that, contrary to the longitudinal component, the transverse component is not dependent on the mobility. The derivative of the expression in **eq. 4.52** as a function of the electrical charge $C_g(V_g - V_{CNP})$ is equal to zero for $C_g(V_g - V_{CNP}) = \pm e n_0$, which means the maximum of the transverse resistivity is written:

$$\rho_{xy,max} \approx \left| \frac{B}{2e(n_0 + p_0)} \right| \qquad \text{(eq. 4.53)}$$

It arises from **eq. 4.53** that the residual charge carrier concentration at CNP can be determined from the maximum value of the transverse resistivity.

4.4.2 Electronic properties of functionalized graphene

Although graphene's electronic properties have been widely studied since graphene was evidenced for the first time by A. K. Geim and K. S. Novoselov, the properties induced by chemisorption of adatoms are quite complex to study experimentally. Some reports claim the evidence of a bandgap and a metal-insulator transition, but the characterization is not always convincing and often wrongly interpreted. According to me, it is important to distinct two different cases:

(1) The proportion of sp^3-hybridized carbon atoms is large enough to have opened a bandgap in graphene electronic band structure.

(2) The proportion of sp^3-hybridized carbon atoms is relatively low or not homogenously distributed (sp^3 domains among large sp^2 regions), inducing disorder and doping fluctuations.

In (1), due to the thermal activation of charge carriers across the bandgap E_g, the resistivity at charge neutrality point (ρ_{max}) follows the well-known temperature behaviour for intrinsic semiconductors:

$$\frac{\rho_{max}(T)}{\rho_{max}(0)} = exp\left(\frac{E_g(T)}{2k_BT}\right) \quad \text{(eq. 4.54)}$$

The bandgap is temperature-dependent and can be approached by the Varshni equation [84]:

$$E_g(T) = E_g(0) + \frac{\alpha T^2}{T+\beta} \quad \text{(eq. 4.55)}$$

where α and β are constant coefficients.

In (2), the charge carriers' density is not described by a thermal activation law. The disorder in metals can lead to a "pseudogap" where conduction occurs by hopping [85]. In the literature, the Mott's law is commonly used to describe the behaviour of the resistivity at the charge neutrality point in a disordered graphene [12,54]. The Mott's law depends on the dimensionality of the material, and for 2D materials it is written [86]:

$$\frac{\rho_{max}(T)}{\rho_{max}(0)} = exp\left[\left(\frac{T_0}{T}\right)^{1/3}\right] \quad \text{(eq. 4.56)}$$

with T_0 a fitting parameter.

Another model from Li *et al* [78] considers that disordered graphene conductivity is driven by electron-hole puddles that correspond to spatial fluctuations of the charge carrier density. Those puddles were observed by STM by Matin *et al* [87] (**Figure 4.32**) and provide a good estimation of the disorder degree in graphene. Using this model, a key parameter to estimate the disorder degree is the standard deviation of the potential fluctuations responsible for the electron-hole puddles' appearance, which is embodied by a parameter *s*. In the framework of this model, the temperature-dependence of charge carriers' density at CNP is given by:

$$\frac{n_0(T)+p_0(T)}{n_0(0)+p_0(0)} = 1 + \frac{\pi^2}{3}\left(\frac{k_BT}{s}\right)^2 \quad \text{(eq. 4.57)}$$

With $n_0(0)+p_0(0) = \frac{s^2}{\pi(\hbar v_F)^2}$, represents the residual charge carrier's density at T = 0 K. Then, by performing Hall effect measurement at different temperatures, one can plot, using **eq. 4.53**, the evolution of the charge carrier concentration at CNP with the temperature, and extract the temperature dependence of the charge carrier density to determine if a bandgap is open or disorder dominates the graphene conductivity.

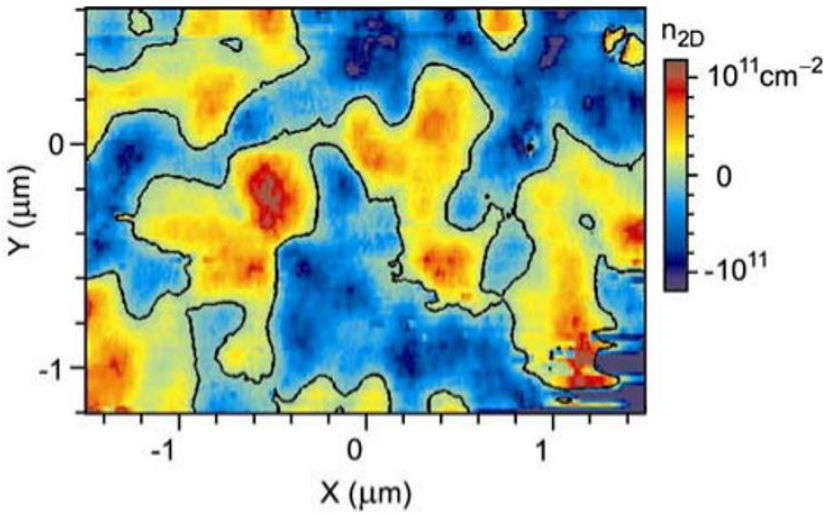


Figure 4.32: STM image from [87] showing electron-hole puddles on graphene.

4.4.3 Measurement set-up

4.4.3.1 Ambient conditions measurement with probe station

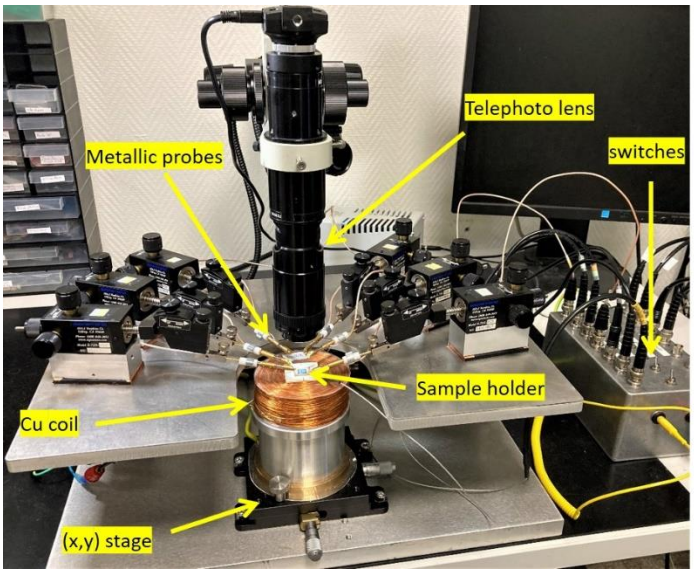


Figure 4.33: Photography of the probe station.

Measurements were always performed using a probe station (**Figure 4.33**) to gain an initial insight into graphene's electronic properties without bonding, which can be time-consuming and potentially damage the sample. The bonding is only necessary for measurements in a physical properties measurement system (PPMS) that allows measurements to be taken within stable and controlled conditions in terms of pressure and temperature. In general, measurements at the probe station are not suitable for advanced measurements because important shifts of the Dirac point are usually observed due to doping induced by charged species

in the environment. Therefore, samples are primarily measured at the probe station to control graphene properties at ambient conditions before going to more controlled conditions with the PPMS.

The probe station is composed of the following elements:

- Stage with (x,y)-micromanipulators for an accurate control of the sample position.
- Copper coil of 80 mT/A placed on the stage connected to a power supply.
- Sample holder placed on top of the copper coil.
- Telephoto lens, camera and white light lamp for sample observation.
- Set of metallic (Cu-Be alloy) probes attached to (x,y,z)-micromanipulators for an accurate control of the probes' position.
- Set of Keithley measurement devices connected to the metallic probes through a set of switches.

A measurement starts by putting each metallic probe in contact with its respective electrode using the micromanipulators and the telephoto lens. During this process, the samples and the probes are connected to the ground via a resistance of 10 MΩ to avoid any electrical discharge that could damage the sample. The user is also connected to the ground with an electrostatic strap. A complete measurement is performed with six probes: two probes for current injection, two probes for longitudinal voltage measurement and two probes for transverse voltage measurement. In this configuration, the contact resistance vanishes and the graphene resistivity can directly be extracted from the resistance measurement. The gate voltage is applied directly at the back of the substrate by electrical contact with the substrate holder made of copper.

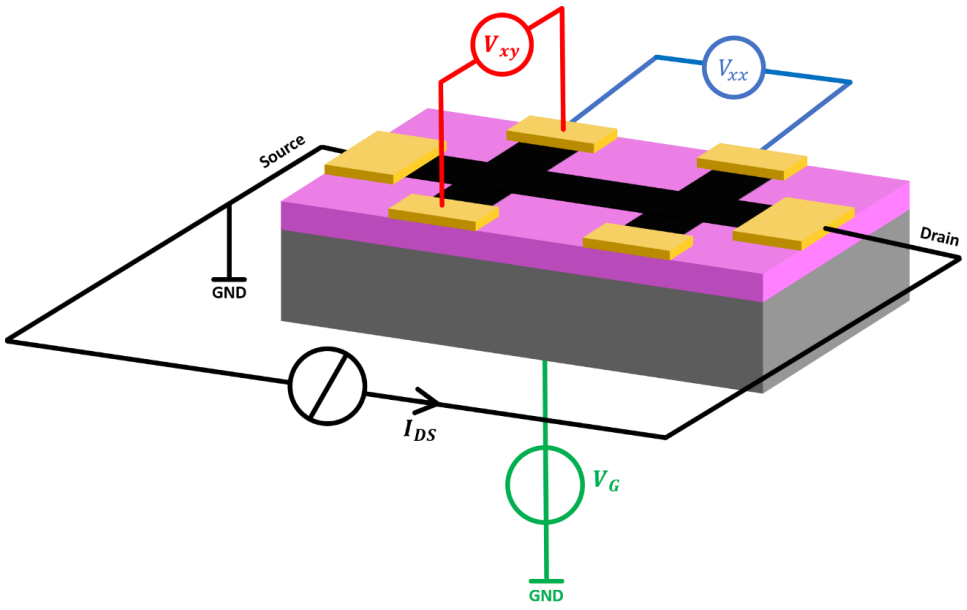


Figure 4.34: Measurement configuration for the four-probes longitudinal resistivity and the transverse (Hall) resistivity of a graphene Hall bar on Si/SiO_2 with a current polarization and a gate voltage.

Once the probes are in contact, they are connected to the devices using the switches and the user executes a measurement program from a computer. In general, the drain source current is maintained at about 10 µA and, in the case of Hall effect measurement, the magnitude of the out-of-plane magnetic field is about 100 mT.

4.4.3.2 Low-pressure and low temperature measurements with a physical properties measurement system (PPMS)

As mentioned in the previous section, measurements under controlled atmosphere and at low temperature are performed in a PPMS from Quantum Design **(Figure 4.36)**. Although this system was designed to perform measurements, we prefer using our own measurement setup similar to the one described before. In this work, the PPMS was only used to perform electrical transport measurements at low temperatures and high magnetic fields. The temperature is controlled by a cryostat cooled by liquid Helium flowing in a closed loop circuit by a compressor. The atmosphere where the sample is located is composed of a residual Helium pressure of about 15 mbar after three cycles. The accessible temperature range offered by the cryostat goes from 1.9 K to 400 K. The magnetic field is enabled by a superconducting coil inside the cryostat and can reach a magnitude of 9 T.

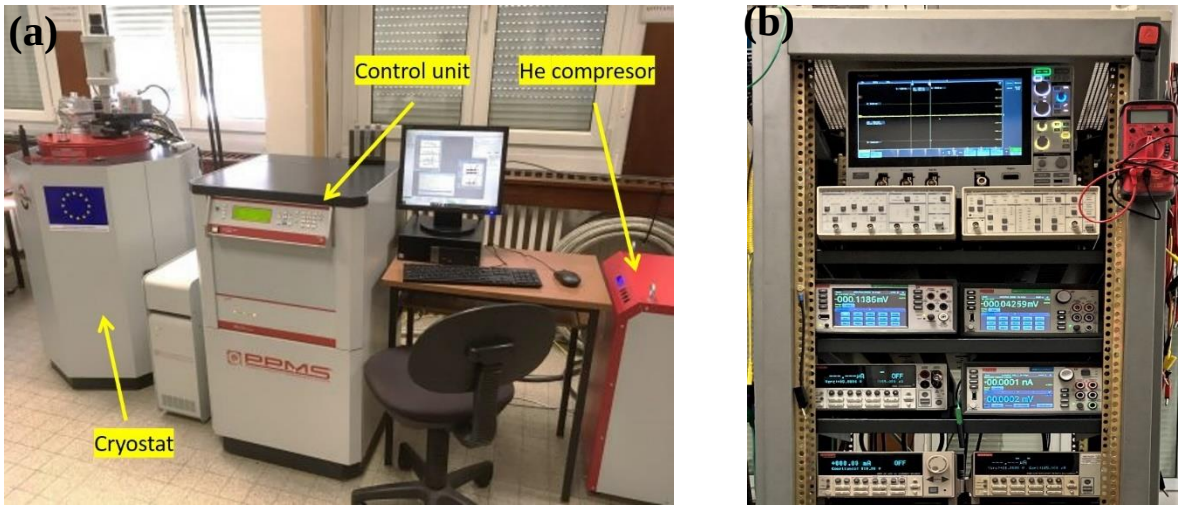


Figure 4.35: Photography of (a) the PPMS and (b) the associated set of electrical measurement devices.

Chapter 5 Raman model to quantify the sp^3/sp^2 ratio in functionalized graphene

5.1 Empirical point-defects model based on ion-bombardment

5.1.1 Description and limits of the model

In **Chapter 4**, the Raman responses of pristine and defective graphene were compared, showing that the double resonance D and D' bands are activated by defects. In those processes, an electron (respectively a hole) is elastically backscattered by a defect and recombines radiatively with a hole (respectively an electron) inelastically backscattered after interaction with a phonon. The D band involves zone-corner phonons whereas the D' band originates from zone-centre phonons. As a consequence, these two bands can provide fruitful information concerning disorder in graphene. It was mentioned in **Chapter 4** that the intensity ratio $I_D/I_{D'}$ between D and D' bands is representative of the nature of the defects [71] whereas the intensity ratio I_D/I_G between D and G bands can be used to quantify the defects density [47,88]. Lucchese *et al* [47] developed an empirical model to describe the relationship between I_D/I_G and the defect density in the case of point-defects introduced by ion-bombardment. Their model is widely used by the scientific community, even for other types of point-defects such as sp^3-type defects. In their model, the authors define an ion impact in graphene by a point-defect around which the D-band signal originates from two distinct regions (**Figure 5.1a**):

(i) The S-region corresponding to the structurally damaged graphene area. This region is defined by a circular area of radius r_S.
(ii) The *A*-region that likely consists of the pristine hexagonal lattice, where strain relaxation is suppressed due to interactions between the graphene layer and the substrate. This region surrounding the S-region is defined by an internal radius r_S and an external radius r_A.

In [47], the evolution of the total surfaces S_S and S_A associated with these two regions is described by the following rate equations:

$$\frac{dS_S}{dN} = \pi r_S^2 \left(\frac{S_T - S_S}{S_T}\right) \quad \text{(eq. 5.1a)}$$

$$\frac{dS_A}{dN} = \pi (r_A^2 - r_S^2) \left(\frac{S_T - S_S - S_A}{S_T}\right) \quad \text{(eq. 5.1b)}$$

where N is the number of impacts and S_T the total graphene surface. Defining the defect density by $\sigma = N/S_T$ and the normalized surface fractions by $f_S = S_S/S_T$ and $f_A = S_A/S_T$, the above rate equations can be written:

$$\frac{df_S}{d\sigma} = \pi r_S^2 (1 - f_S) \quad \text{(eq. 5.2a)}$$

$$\frac{df_A}{d\sigma} = \pi (r_A^2 - r_S^2)(1 - f_S - f_A) \quad \text{(eq. 5.2b)}$$

The resolution of these two rate equations gives:

$$f_S(\sigma) = 1 - e^{-\pi r_S^2 \sigma} \quad \text{(eq. 5.3a)}$$

$$f_A(\sigma) = \frac{r_A^2 - r_S^2}{r_A^2 - 2r_S^2}\left(e^{-\pi r_S^2 \sigma} - e^{-\pi (r_A^2 - r_S^2)\sigma}\right) \quad \text{(eq. 5.3b)}$$

In their model, Luchese *et al* suggest that I_D/I_G must be a linear combination of f_S and f_A, as given by the following law:

$$\frac{I_D}{I_G}(\sigma) = C_S f_S(\sigma) + C_A f_A(\sigma) \quad \text{(eq. 5.4)}$$

where C_S are C_A are coefficients related to the ratio between D and G bands cross sections in each region. In the literature, **eq. 5.4** is generally given as a function of the average distance $L_D = 1/\sqrt{\sigma}$ between the point-defects, leading to the following expression:

$$\frac{I_D}{I_G}(L_D) = C_S(1 - e^{-\pi r_S^2/L_D^2}) + C_A \frac{r_A^2 - r_S^2}{r_A^2 - 2r_S^2}(e^{-\pi r_S^2/L_D^2} - e^{-\pi (r_A^2 - r_S^2)/L_D^2}) \quad \text{(eq. 5.5)}$$

The model parameters (C_S, r_S, C_A and r_A) were determined to fit **eq. 5.5** with experimental points (**Figure 5.1b**). Different defect concentrations were induced in graphene samples on Si/SiO_2 using a 90 eV Ar^+ ion beam at different doses between 10^{11} and 10^{14} Ar^+/cm^2. The L_D value for each ion dose was calibrated with STM on bombarded bulk HOPG. Authors demonstrate that experimental data can be well fitted with **eq. 5.5** using $C_S = 0.86$, $r_S = 1\,nm$, $C_A = 4.56$ and $r_A = 3\,nm$. However, these parameters are not universal since C_A is dependent on the laser energy [89,90] and the radii must be dependent on the type of point-defects. Some adaptations were proposed in the literature, such as the work from Wang *et al* that suggests using $r_S = 0.07\,nm$ and $r_A = 1\,nm$ for sp^3-type defects induced by chemical functionalization with organic diazonium salts [91]. In the framework of this PhD, several points concerning the truthfulness and the versatility of this phenomenological model were raised:

(1) The second term in **eq. 5.5** is erroneous and leads to a non-normalized total surface fraction (*i.e.*, $f_S + f_A > 1$), making the model lack physical meaning (see **5.1.2**).
(2) Functionalized graphene is generally inhomogeneous, making calibration of the model's parameters with experimental data much more challenging than for bombarded graphene and would require a large statistical study (see **5.1.3**).
(3) The model describes a point-defect with two regions contributing to the D band, but such a description does not work for sp^3-type defects since the sp^3-hybridized region does not contribute to resonant Raman processes in the visible range (see **5.1.4**).

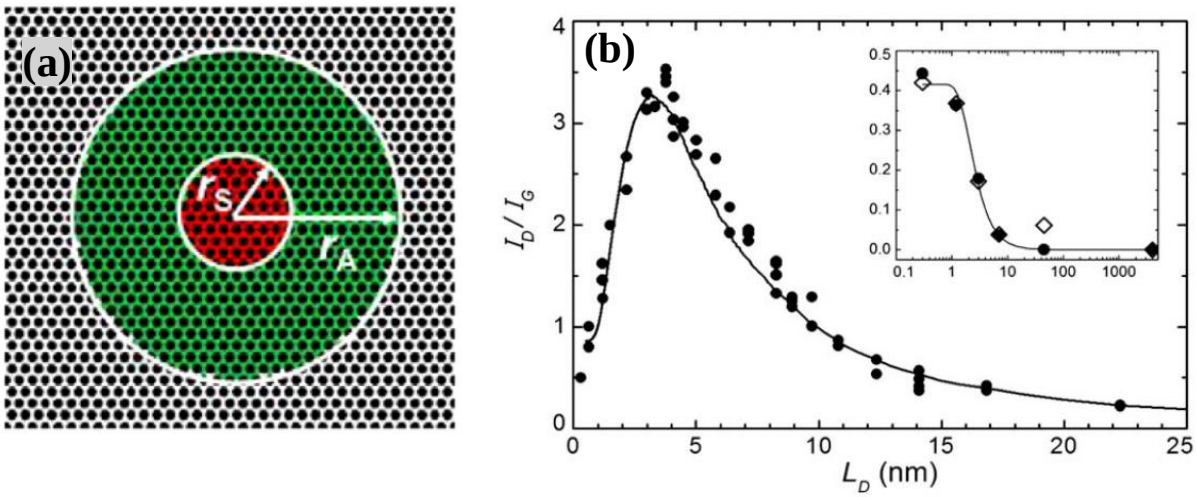


Figure 5.1: (a) Definition of the ion-induced point defect with the S (red) and A (green) regions from [47]. (b) I_D/I_G $vs.$ L_D dependence given by experimental data (dots) fitted by eq. 5.8 (line) using $C_S = 0.86$, $r_S = 1\ nm$, $C_A = 4.56$ and $r_A = 3\ nm$. The inset represents reference values on bulk HOPG.

5.1.2 Correction of the model's equation

Figure 5.2 plots the total surface fraction $f_S + f_A$ given in [47] as a function of L_D with $r_S = 1\ nm$ and $r_A = 3\ nm$, revealing a normalization issue. The error originates from the rate equation for f_A (**eq. 5.2b**). Let us consider two disks of radius r_S and r_A. The rate equations for the evolution of the surface fractions $f_{disk,S}$ and $f_{disk,A}$ are given by:

$$\frac{df_{disk,S}}{d\sigma} = \pi r_S^2\left(1 - f_{disk,S}\right) \quad \text{(eq. 5.6a)}$$

$$\frac{df_{disk,A}}{d\sigma} = \pi r_A^2\left(1 - f_{disk,A}\right) \quad \text{(eq. 5.6b)}$$

The solutions of these equations are:

$$f_{disk,S} = 1 - exp(-\pi r_S^2\sigma) \quad \text{(eq. 5.7a)}$$

$$f_{disk,A} = 1 - exp(-\pi r_A^2\sigma) \quad \text{(eq. 5.7b)}$$

$f_{disk,S}$ corresponds directly to f_S (**eq. 5.3a**) and f_A is given by:

$$f_A(\sigma) = f_{disk,A}(\sigma) - f_{disk,S}(\sigma) = exp(-\pi r_S^2\sigma) - exp(-\pi r_A^2\sigma) \quad \text{(eq. 5.8)}$$

This relation is obviously different from **eq. 5.3b**, notably by the lack of the term $({r_A}^2 - {r_S}^2)/({r_A}^2 - 2{r_S}^2)$, explaining the origin of the normalization issue. This can be understood from the rate equation for $f_A(\sigma)$. Since $f_A(\sigma) = f_{disk,A}(\sigma) - f_S(\sigma)$, we have:

$$\frac{df_A(\sigma)}{d\sigma} = \frac{d(f_{disk,A}(\sigma) - f_S(\sigma))}{d\sigma} = \pi {r_A}^2 \left(1 - f_{disk,A}(\sigma)\right) - \pi {r_S}^2 \left(1 - f_S(\sigma)\right) \quad \text{(eq. 5.9)}$$

Which can be rewritten as follows:

$$\frac{df_A(\sigma)}{d\sigma} = \pi({r_A}^2 - {r_S}^2)\left(1 - f_A(\sigma) - f_S(\sigma)\right) - \pi {r_S}^2 f_A(\sigma) \quad \text{(eq. 5.10)}$$

The first term, $\pi({r_A}^2 - {r_S}^2)\left(1 - f_A(\sigma) - f_S(\sigma)\right)$, similar to **eq. 5.2b**, corresponds to the creation of the activated surface f_A. The second term, $-\pi {r_S}^2 f_A(\sigma)$, absent in **eq. 5.2b**, corresponds to the destruction of the activated surface by the creation of a defect in this area. The omission of this term is responsible for the inconsistency in the model. The correct equation is plotted in **Figure 5.2** and compared with the erroneous equation, showing that the difference is significant for L_D between approximately 0.8 and 8 nm.

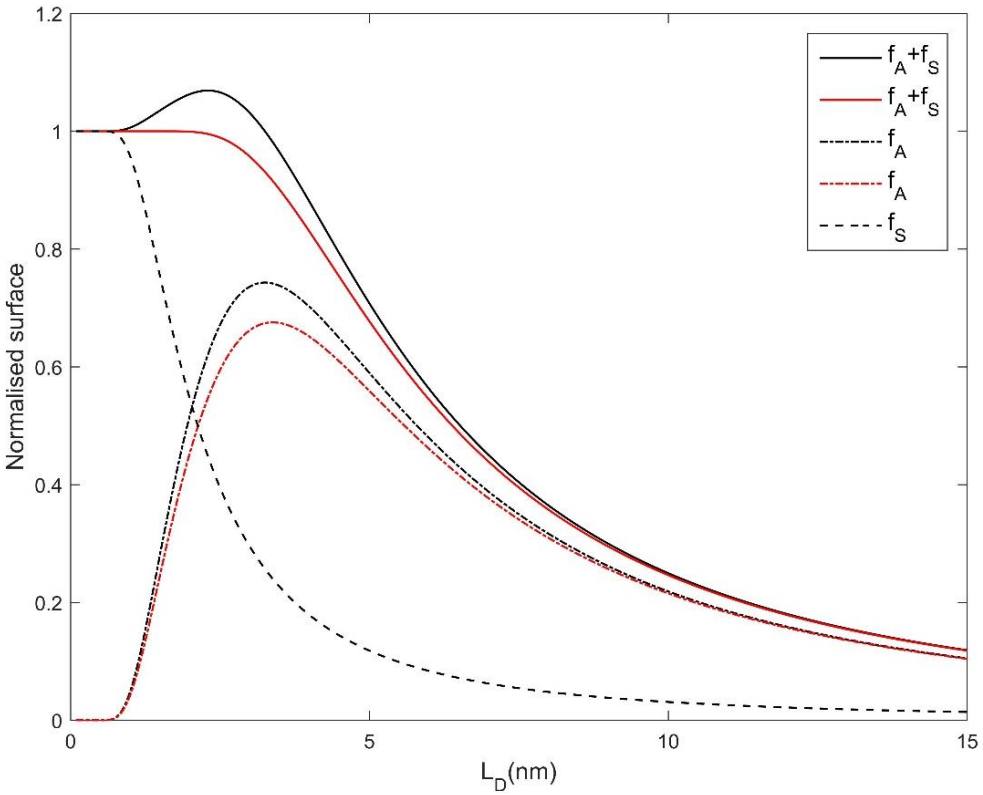


Figure 5.2: Plot of the total surface fraction decomposed into the elementary surface fractions f_A and f_S. The original curves from [47] (in black) are compared with the corrected curves (in red).

5.1.3 Challenges related to model calibration

To apply this model to functionalization, the size of the two regions must be adapted accordingly. Combining Raman spectroscopy with complementary characterization techniques on graphene samples exposed to various degrees of functionalization could facilitate the model calibration. However, this approach remains challenging at low coverage rates, and strong spatial inhomogeneities are observed at high coverage rates. **Figure 5.3** shows Raman spectra of fluorinated (*samples 1* and *2*) and hydrogenated (*samples 3* and *4*) graphene on Si/SiO_2 substrates. Samples were all prepared by mechanical exfoliation of HOPG, as described in **Chapter 2**. Several monolayer graphene flakes were identified by optical contrast (see **Chapter 2**) and analyzed in Raman spectroscopy for confirmation (see **Chapter 4**). Fluorination was performed in gas phase using the flow reactor described in **Chapter 3**. Samples were heated at 30°C while exposed to a gas flow of 300 mL/min for 10 min. The gas phase was composed of 3 % of F_2 and 97 % of N_2 for *sample 1* and 5 % of F_2 and 95 % of N_2 for *sample 2*. Hydrogenation was performed with the HFCVD reactor described in **Chapter 3**. For *sample 3*, the process was carried out for 10 minutes under a pressure of 4 Torr and a flow rate of 10 sccm, with the filament temperature maintained at approximately 2100°C. For *sample 4*, the exposure time was extended to 1 hour, with a hydrogen pressure of 50 Torr, a flow rate of 50 sccm, and a filament temperature of approximately 1900 °C. For each sample, Raman spectra were recorded at the same excitation energy for each flake. Inhomogeneities are evident across most samples, except for *sample 3*, which corresponds to mild hydrogenation conditions. In *sample 2*, both the I_D/I_G ratio and the full width at half maximum (*FWHM*) of the D band exhibit significant variations, indicating that the reactivity of the graphene layer varies substantially from one flake to another.

Such inhomogeneities have previously been reported for fluorinated graphene [15] and could possibly originate from inhomogeneous reactivity among graphene regions. Two main factors may contribute to this variability:

(1) Charge-carriers inhomogeneities induced by trapped charges in the substrate.
(2) Pre-existing chemisorbed species or added during functionalization. According to calculations from the literature [92] and from our own consortium (see **5.2**), an atom grafted on graphene's surface induces local fluctuations of the absorption energy around the sp^3-site. In addition, since these fluctuations are related to localized electronic states, they might contribute to charge-carrier inhomogeneities.

It is well known that graphene on Si/SiO_2 exhibits charge-carrier inhomogeneities, manifested as electron-hole puddles [87], which significantly impact graphene chemical reactivity [91]. In the case of diazonium functionalization, for example, a significant dispersion in the I_D/I_G values has been observed across different regions of the same sample [91]. This variability is substrate-dependent; for plasma-cleaned Si/SiO_2 substrates, I_D/I_G can range from 0.8 to 1.3 under identical conditions. Considering these inhomogeneity issues, calibrating the model parameters becomes highly complex.

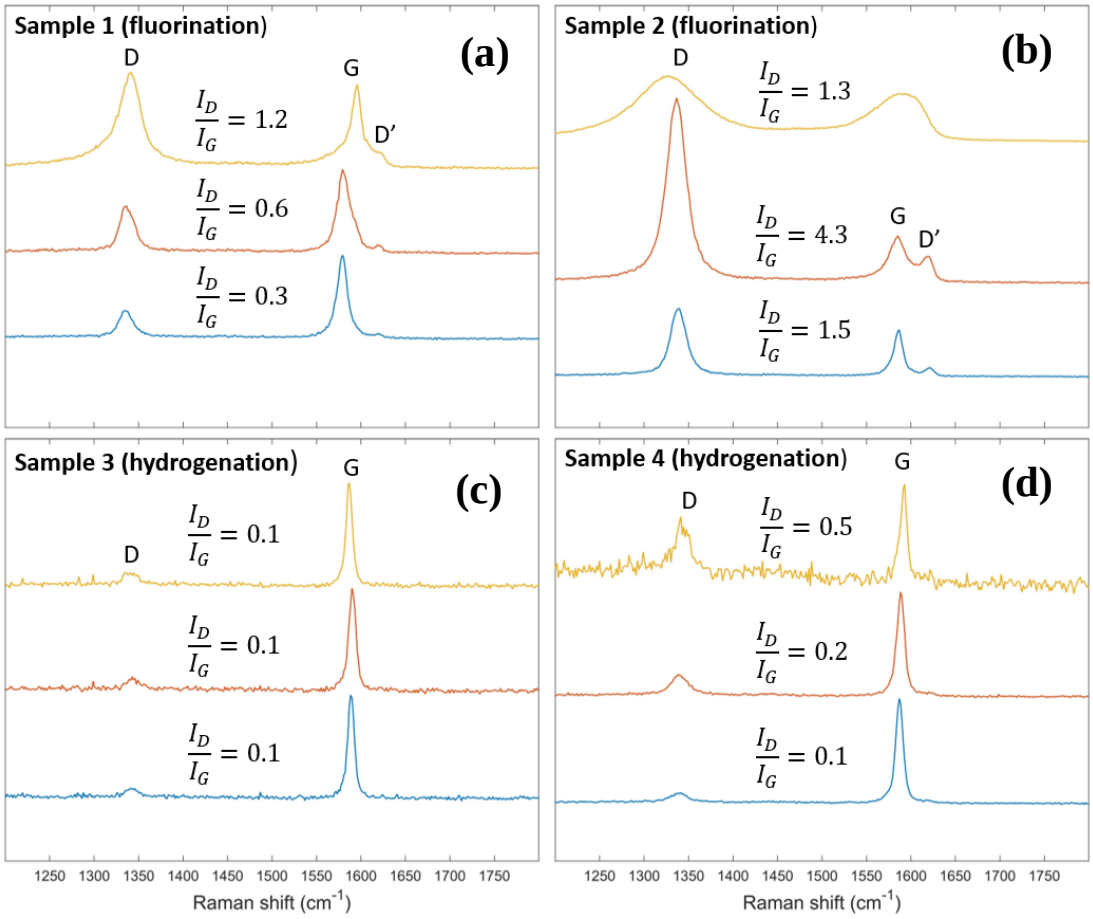


Figure 5.3: Raman spectra of (a,b) fluorinated and (c,d) hydrogenated samples recorded with a 532 nm laser. In each figure, three spectra are gathered from different flakes and normalized to the G band intensity.

5.1.4 Failure in model adaptation to functionalized graphene

Wang *et al* [91] proposed an adaptation of the input parameters of the model to make it more adapted to functionalization, choosing radii $r_S = 0.07\,nm$ and $r_A = 1\,nm$ and keeping the same coefficients $C_S = 0.86$ and $C_A = 4.56$. **Figure 5.4** plots $I_D/I_G\ vs.\ L_D$ using the erroneous Lucchese's model and our corrected model with parameters from [47] and [91] for both models. Although it shows a significant difference between the curves obtained with parameters given in [47] the error almost completely vanishes for parameters given in [91]. This comes from low r_S value used in [91] that makes the factor $\frac{r_A^2 - r_S^2}{r_A^2 - 2r_S^2}$ very close to 1 and the term $r_A^2 - r_S^2$ in the exponential approximated by r_A^2. Thus, with $r_S = 0.07\,nm$, the erroneous expression for f_A can be approximated by the correct form given by **eq. 5.8**.

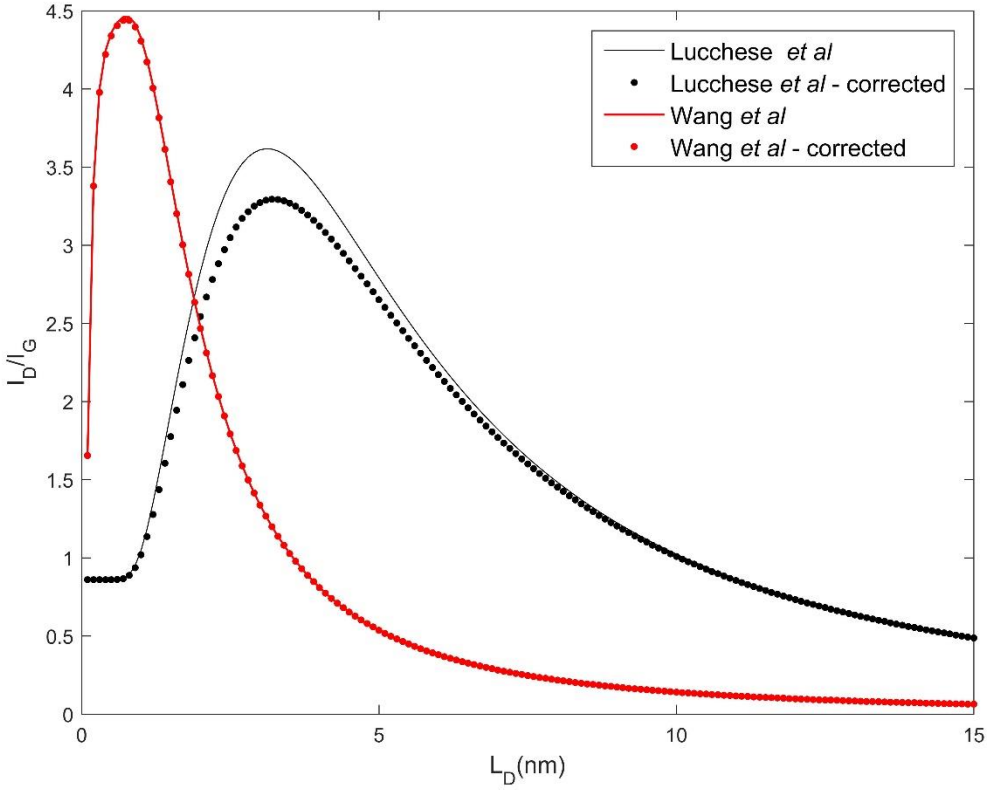


Figure 5.4: Comparison between $I_D/I_G\ vs.\ L_D$ dependence laws given by two models from the literature. The curves of same colors differ from the term f_A, which is unchanged (continuous line) or corrected by eq. 5.13 (dots).

However, even using a correct equation and adapted parameters, the model remains not adapted for properly describing the $I_D/I_G\ vs.\ L_D$ dependence in the case of functionalization. Lucchese's model considers only regions contributing to the D band, i.e., where the Dirac cone is mostly conserved, whereas covalent functionalization induces sp^3 domains at high coverage rates with a vanishing of the Dirac cones [20]. Thus, the sp^3 regions must be considered as deactivated areas where Raman processes are non-resonant. As it was previously demonstrated for highly fluorinated graphene [15], the Raman response from sp^3 areas is not detectable with visible light excitation. As a consequence, a third region must be considered in the definition of the sp^3-type point-defect, corresponding to the deactivated sp^3 region.

5.2 Non-empirical model based on quantum chemistry calculations

5.2.1 Description of the sp^3-type point-defect

To address the previously mentioned limitations, this work proposes a non-empirical model adapted to covalent functionalization in graphene (including hydrogenation and fluorination) with input parameters derived from quantum chemistry calculations. Atomic or molecular adsorption on a graphene layer can be modelled as point defects that perturb the electron-phonon coupling within the surrounding sp^2-carbon network. In the framework of the present model, three concentric regions are defined around each

chemisorbed site, characterized by the radii r_{sp3}, r_S and r_A (**Figure 5.5**):

(1) A deactivated region (brown disk) corresponding to a central disk of radius r_{sp^3} around the sp^3-hybridized carbon atom. This region does not contribute to the resonant Raman scattering in the visible range.
(2) A structurally distorted region (orange ring) as a ring extending from r_{sp^3} to r_S where structural distortions in the sp^2-C lattice activate the D band through double-resonance Raman processes.
(3) An activated region (yellow ring): An outer ring between r_S and r_A, where the hexagonal structure is preserved, but where the D mode is activated via local modulation of the electronic density of states, enabling double-resonant scattering.

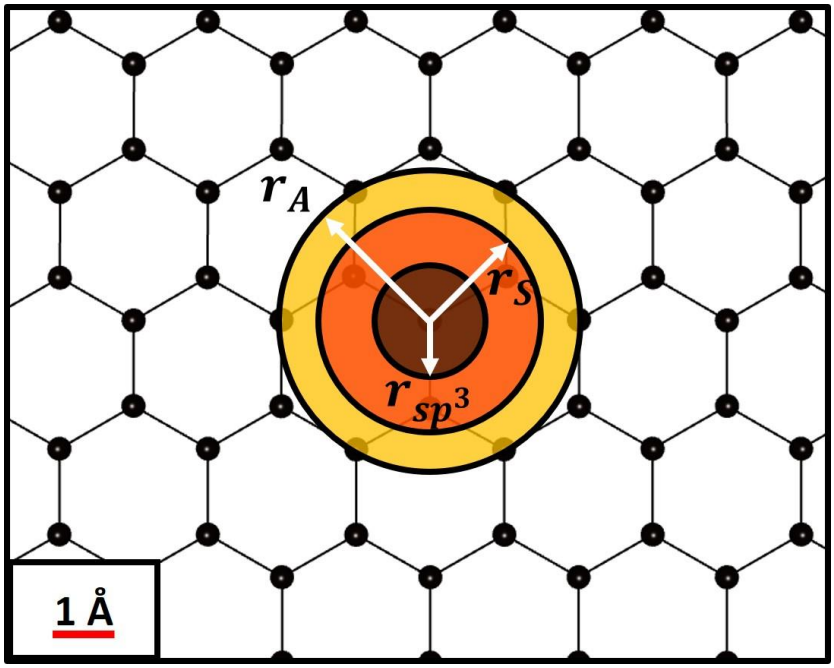


Figure 5.5: Definition of the sp^3-type point defect representing the deactivated (brown disk), structurally distorted (orange ring) and activated (yellow ring) regions.

5.2.2 Equations of the model

The evolution of the total surfaces S_{sp^3}, S_S and S_A associated to these three regions are described by the following rate equations:

$$\frac{dS_{sp^3}}{dN} = \pi r_{sp^3}^2 \left(\frac{S_T - S_{sp^3}}{S_T}\right) \quad \text{(eq. 5.11a)}$$

$$\frac{dS_S}{dN} = \pi(r_S^2 - r_{sp^3}^2)\left(\frac{S_T - S_{sp^3} - S_S}{S_T}\right) - \pi r_{sp^3}^2 \left(\frac{S_S}{S_T}\right) \quad \text{(eq. 5.11b)}$$

$$\frac{dS_A}{dN} = \pi(r_A^2 - r_S^2)\left(\frac{S_T - S_{sp^3} - S_S - S_A}{S_T}\right) - \pi r_S^2 \left(\frac{S_A}{S_T}\right) \quad \text{(eq. 5.11c)}$$

where N is the number of atoms or molecules covalently bonded to graphene and S_T the total graphene surface. Defining the defect density by $\sigma = N/S_T$ and the normalized surface fractions $f_{sp^3} = S_{sp^3}/S_T$ by $f_S = S_S/S_T$ and $f_A = S_A/S_T$, the above rate equations can be written:

$$\frac{df_{sp^3}}{d\sigma} = \pi r_{sp^3}^2 \left(1 - f_{sp^3}\right) \quad \text{(eq. 5.12a)}$$

$$\frac{df_S}{d\sigma} = \left(\pi r_S^2 - \pi r_{sp^3}^2\right)\left(1 - f_{sp^3} - f_S\right) - \pi r_{sp^3}^2 f_S \quad \text{(eq. 5.12b)}$$

$$\frac{df_A}{d\sigma} = \left(\pi r_A^2 - \pi r_S^2\right)\left(1 - f_{sp^3} - f_S - f_A\right) - f_A \pi r_S^2 \quad \text{(eq. 5.12c)}$$

The resolution of those rate equations gives:

$$f_{sp^3}(\sigma) = 1 - e^{-\pi r_{sp^3}^2 \sigma} \quad \text{(eq. 5.13a)}$$

$$f_S(\sigma) = e^{-\pi r_{sp^3}^2 \sigma} - e^{-\pi r_S^2 \sigma} \quad \text{(eq. 5.13b)}$$

$$f_A(\sigma) = e^{-\pi r_S^2 \sigma} - e^{-\pi r_A^2 \sigma} \quad \text{(eq. 5.13c)}$$

f_{sp^3} physically corresponds to the sp^3-converted surface fraction, where both the crystalline and electronic-band structures of graphene are significantly altered. As a result, the G band, associated with the C=C stretching mode, is suppressed. Additionally, the D band, which arises from resonant intervalley scattering, is also deactivated due to the loss of the Dirac cone in the electronic structure. For these reasons, the area defined by f_{sp^3} is referred to as the "deactivated region".

f_S physically corresponds to a region where the crystalline structure is locally distorted. This structural distortion activates the D band due to modulations of the electronic bands, enabling charge carrier backscattering.

f_A corresponds to a surface where the D band is activated without the presence of topological defects. Instead, the activation arises from modulations in the DOS, which enables charge-carrier backscattering. Actually, from an electronic perspective, a "defect" does not necessarily imply a topological singularity but can also be described as any form of translational symmetry breaking in the π electronic band structure, including those with topological origins. Structurally disorder-free D band activation, resulting from such symmetry breaking, has been observed in flattened carbon nanotubes, also known as "dogbone" nanotubes [93]. Similarly, the adsorption of chemical species on the graphene surface modulates the DOS within the region defined by f_A, leading to symmetry breaking in the electronic potential.

As a result, the D band intensity has two distinct contributions, arising from the structurally distorted (f_S) and activated (f_A) regions, while the G band intensity is proportional to the remaining sp^2-C surface, i.e., $1 - f_{sp^3}$. The intensity ratio I_D/I_G can, therefore, be expressed as a linear combination of $f_S/(1 - f_{sp^3})$ and $f_A/(1 - f_{sp^3})$ and as a function of L_D as following:

$$\frac{I_D}{I_G}(L_D) = \frac{C_S f_S(L_D) + C_A f_A(L_D)}{1 - f_{sp^3}(L_D)} \quad \text{(eq. 5.14)}$$

Where C_S and C_A are fitting coefficients. It must be specified that L_D cannot be lower than the minimal distance between two defects which is given by r_{sp^3}. As a consequence, the atomic coverage rate, which is the number of chemisorbed species per carbon atom, can be defined by:

$$F_{sp3} = \left(\frac{r_{sp^3}}{L_D}\right)^2 \qquad \text{(eq. 5.15)}$$

With this definition, an atomic coverage rate F_{sp3} = 100% corresponds to one chemisorbed species per carbon atom.

5.2.3 Input parameters

5.2.3.1 The radii

The characteristic radii used in the model were based on calculations for the case of one atomic hydrogen adsorbed on a 12×12 graphene supercell. These calculations were done by our collaborator Cedric Crespos from the Molecular Science Institute in Bordeaux. The relaxed structure reveals significant out-of-plane displacement of 0.58 Å for the sp^3-hybridized carbon atom and a distortion of its three neighbouring sp^3-hybridized C–C bonds accompanied by a slight out-of-plane displacement of 0.22 Å for the three first neighbours. The second-nearest neighbours retain their sp^2 character though with a tiny out-of-plane displacement of 0.13 Å.

As a consequence, it seems physically reasonable to define the sp^3 region by the area occupied by one carbon atom. Since graphene has two atoms per primitive cell and the size of one primitive cell is equal $3a_{CC}^2 \cos\left(\frac{\pi}{6}\right)$, $a_{cc} = 0.142\ nm$ being the C-C bond length, the radius r_{sp^3} of the circular region occupied by the sp^3-hybrisized carbon atom is equal to:

$$r_{sp^3} = \sqrt{\frac{3}{2\pi} a_{CC}^2 \cos\left(\frac{\pi}{6}\right)} \approx 0.09 \text{ nm} \qquad \text{(eq. 5.16)}$$

The radius of the structurally distorted region is therefore associated with the sp^2-hybridized atoms immediately beyond the C(sp^3) core. Specifically, the immediate neighbours of the hydrogenated carbon lack sufficient p_z-orbital overlap to sustain a π bond, whereas the subsequent ring of atoms keeps this orbital interaction. Then, the sum of the sp^3 and distorted regions can be defined by the area covered by four carbon atoms (the sp^3-hybridized carbon and its three first neighbours), which means that we have:

$$r_S = 2 \times r_{sp^3} \approx 0.18 \text{ nm} \qquad \text{(eq. 5.17)}$$

To estimate the spatial extent of the activated region, the influence of a chemisorbed hydrogen atom on the surrounding electronic structure (**Figure 5.6**) was investigated by means of spin-polarized first-principles calculations performed by Professor Cedric Crespos. The results (**Figure 5.6a**) demonstrate that the adsorption of a single hydrogen atom induces a spin density localization on the atoms belonging to the opposite sublattice. In particular, the ortho-sites and para-sites become strongly spin-polarized. Adsorption

energies of a second hydrogen atom positioned at various distances from the sp^3-defect have also been calculated with the same method (**Figure 5.6b**) and compared with the adsorption energy on a pristine graphene layer, which is equal to -0.85 eV according to the calculations. These calculations were conducted for both A-type sites (same sublattice) and B-type sites (opposite sublattice). The results show that B-type sites are energetically more favorable for second adsorption because of spin density delocalization, while A-type sites are slightly unfavorable. The adsorption energy decreases with increasing distance and stabilizes beyond approximately 1.36 nm, indicating the decay length of the spin and electronic perturbation induced by the first hydrogen atom. This distance defines the spatial limit of electronic influence relevant to Raman double-resonance processes, particularly the elastic backscattering of charge carriers. No residual spin polarization is observed at 1.36 nm, suggesting that this distance marks the maximum extent of the activated region.

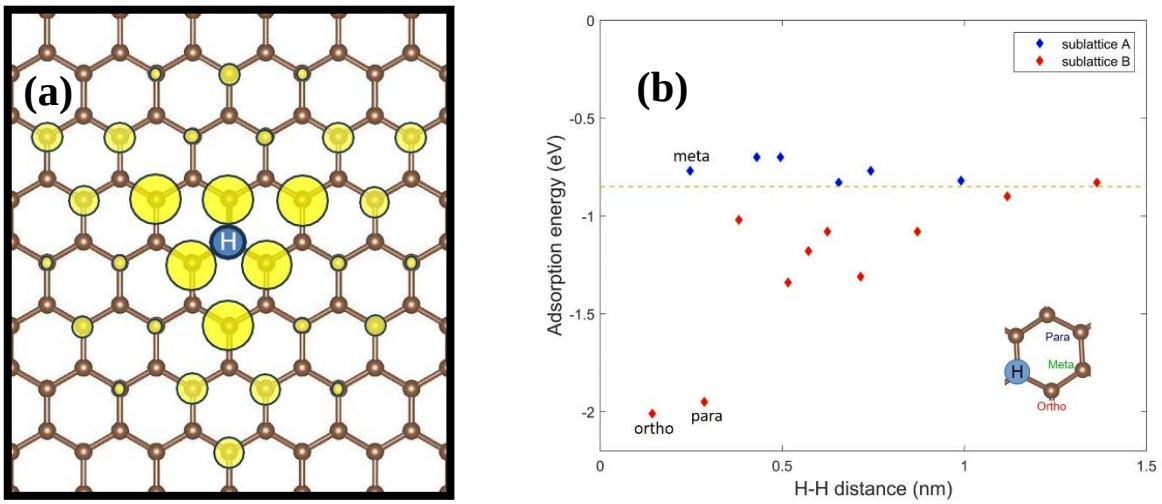


Figure 5.5: (a) Electronic spin density around a *sp*^{3}-C–H point defect. Disks (yellow) with radii proportional to the adsorption energy of a second hydrogen atom are shown for sublattice B. (b) Adsorption energy as a function of the distance from the *sp*^{3}-C–H point defect for selected sites on sublattices A and B reported around a first chemisorbed hydrogen on sublattice A. The adsorption energy of the first hydrogen (-0.85 eV) is represented by the dashed line.

It is interesting to note that we can relate the r_A radius to the electronic modification around the chemisorbed species. The question is whether it is the same for fluorine or other species. Theoretical calculations have already been carried out for fluorination, and the energies and spin effects are identical [92].

5.2.3.2 C_S and C_A coefficients

The parameters C_S and C_A, attributed respectively to the activated and structurally disturbed area, require reconsideration. Experimental data from this work reveal that I_D/I_G can reach values as high as 5.5 (**Figure 5.10**), which significantly exceeds the maximum value predicted using the C_A parameter reported in the literature [47]. This discrepancy suggests that the conventional value of C_A may not be universally applicable and should be treated with caution. For highly hydrogenated or fluorinated samples, the value C_S= 0.86 remains consistent and physically meaningful. This parameter represents the asymptotic limit of

I_D/I_G at full functionalization and is expected to be largely independent of experimental conditions. The C_A value determined in previous work [47] is closely linked to the radii r_A and r_S. Since r_{sp^3}, r_S, and r_A are fixed based on theoretical considerations, the C_A parameter must be treated as an adjustable quantity to reproduce the maximum experimental I_D/I_G values. It is important to note that the ratio I_D/I_G is dependent on the fourth power of the excitation wavelength [89] and this dependence is only driven by C_A [89,90]. The wavelength dependence of the C_A parameter will be treated in **5.2.4.3**. For now, let us determine C_A for an excitation energy of 2.33 eV (532 nm), corresponding to the laser energy used to carry out this study. The reader must keep in mind that the C_A values suggested below stand for this wavelength and should be adapted in case of Raman spectra recorded at other excitation energies. Regarding the radii values determined previously, C_A = 5.89 appears to be a good approximation to reproduce the maximum experimental I_D/I_G values (see **Figure 5.10**).

5.2.3.3 Refinement of r_A and C_A based on experimental data from the literature

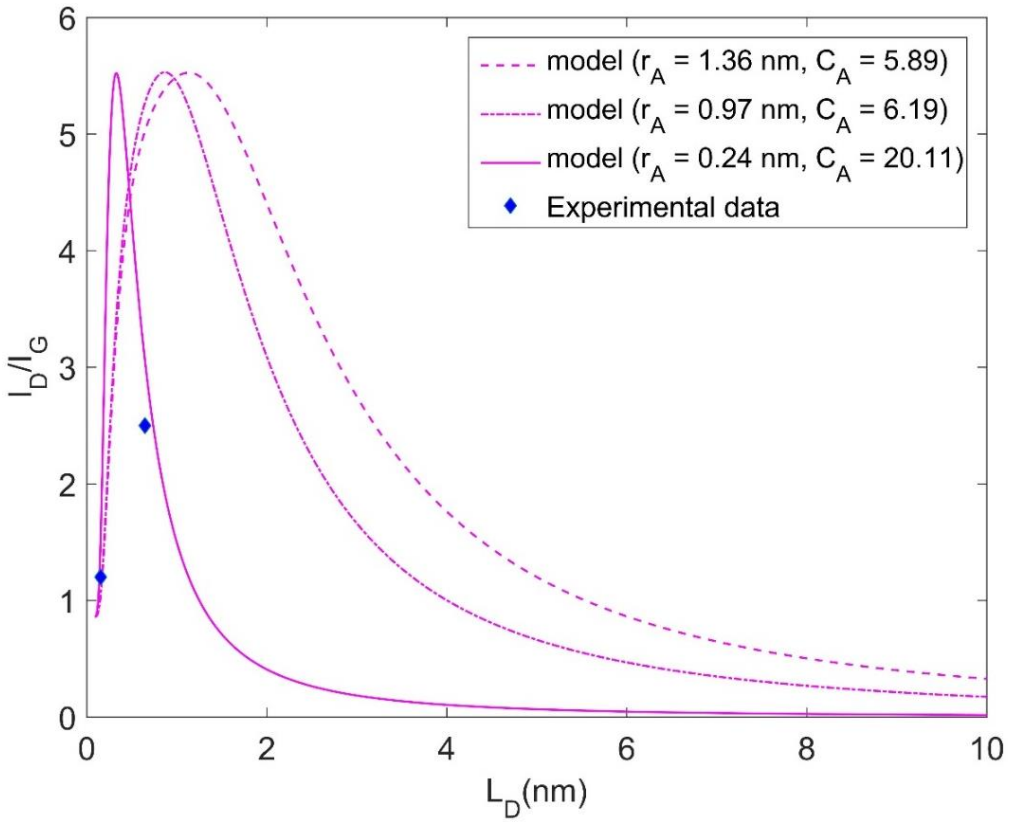
The $I_D/I_G\ vs.\ L_D$ dependence is plotted in **Figure 5.7** using **eq. 5.14** with the parameters determined above and compared with the experimental data from Cheng *et al* [94] corresponding to fluorinated graphene. The article reports a fluorine coverage rate of 35 % determined by XPS which is assigned to a ratio I_D/I_G= 1.2. According to **eq. 5.15**, such an atomic coverage corresponds to L_D = 0.15 nm and the model is in good agreement with this value. However, Cheng *et al* also report a sample with a low fluorine coverage rate estimated at 2 % by XPS (which means L_D = 0.65 nm) and assigned to I_D/I_G= 2.5. Regarding the linewidth of the D band (see **Figure 5.10**), this point should be placed in the decreasing part of the curve, which is not the case. Consequently, the parameter values determined previously fail to describe the experimental results from the literature. By analyzing the influence of each parameter on the final curve, decreasing r_A is a good solution to address this inconsistency. A reasonable approach would be to determine r_A similarly to the other radii by considering the surface influenced by the spin density delocalization. Regarding **Figure 5.6b**, A-type sites exhibit negligible influence, which means that r_A can be reasonably defined by the extent of the circular area occupied by only the sp^3-defect and the B-type sites, which is given by:

$$r_A = \sqrt{\frac{1.36^2}{2} + {r_{sp3}}^2} \approx 0.97 \text{ nm} \qquad \text{(eq. 5.18)}$$

As a consequence, C_A must be renormalized to 6.19 to reproduce the maximum experimental I_D/I_G value. Unfortunately, although this r_A value slightly improves the model, the above refinement is insufficient to explain the experiments (see **Figure 5.7**). The extent of the activated region must be much lower to fit the experimental data. This issue can be addressed making the hypothesis that only the B-sites with a relatively large spin density contribute significantly to charge carriers back-scattering. Regarding the ttheoretical data from **Figure 5.6**, it would be reasonable to consider that the dominant contributors are the ortho and para sites. To be more specific, since the activated region is composed of *sp*^{2}-hybrisized carbon atoms, only para sites are involved (ortho sites belong to the distorted region). Consequently, the area of the external disk corresponding to the sum of the three regions can be defined by the surface occupied by seven atoms (1 *sp*^{3} site + 3 ortho sites + 3 para sites), which means that r_A is given by:

$$r_A = \sqrt{7} \times r_{sp3} \approx 0.24 \text{ nm} \qquad \text{(eq. 5.18)}$$

As a consequence of this small value for r_A, C_A must be significantly increased to reproduce the maximum experimental I_D/I_G value. With C_A = 20.11, the model is found to be in reasonably good agreement with the experiments. In any case, since r_A is a discrete parameter by its definition, it makes no sense using smaller values. The renormalized C_A value is found to be much larger than the initial one suggested in [47], but such a difference is understandable in this case due to the very small r_A value compared to the one from [47]. Since high I_D/I_G values are obtained experimentally, it means that the small spatial extent of the activated region is compensated by a large Raman cross section.



Figures 5.7: I_D/I_G *vs.* L_D curves plotted with different couples C_A, r_A and compared with two experimental data points from [94].

5.2.4 Results and discussion

5.2.4.1 I_D/I_G vs. L_D dependence

Figure 5.8 plots I_D/I_G ratio as a function of L_D, calculated using the input parameters determined previously. The results are compared with experimental data from the literature and with the two empirical laws previously mentioned, thereby demonstrating that the model largely outperforms its predecessors, at least concerning sp^3-type point-defects. The improvement is due to three key-points:

(i) Normalization of the term f_A, which was erroneously non-normalized in the model developed by Lucchese *et al*.

(ii) Introduction of an additional term f_{sp^3}, not present in the equation from Lucchese *et al*, making the model applicable for sp^3-type point-defects.

(iii) Different input parameters determined by calculation and adjustments based on experimental data.

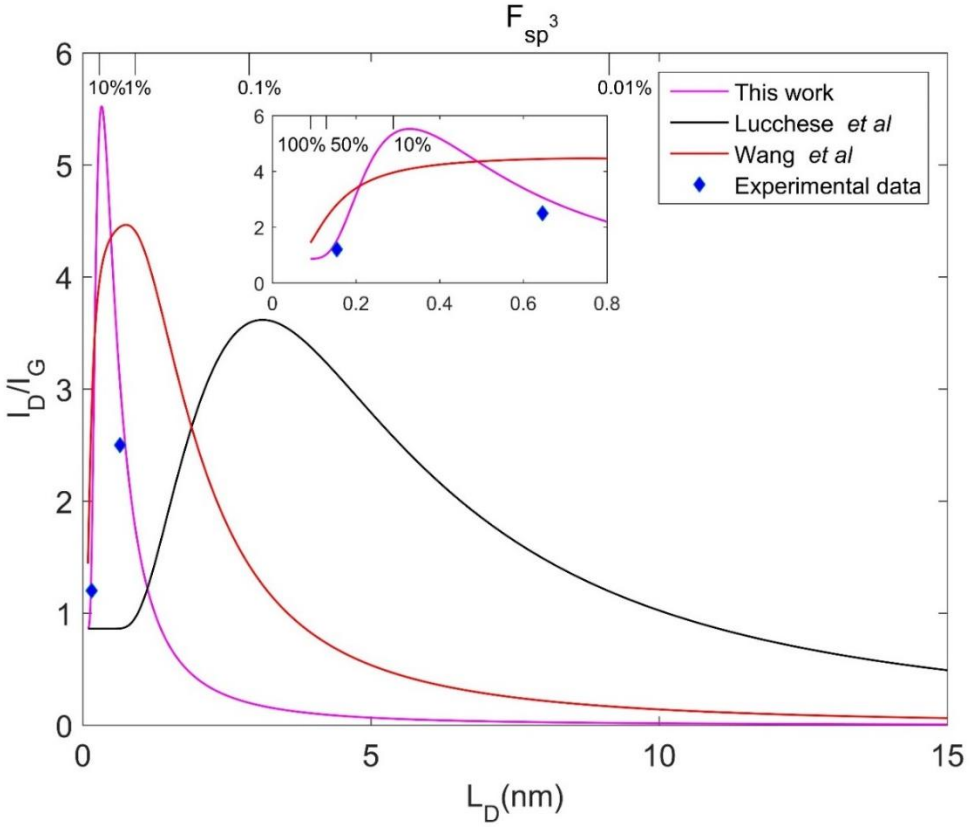


Figure 5.8: I_D/I_G plotted as a function of both the distance L_D and the coverage rate F_{sp^3} and compared with experimental data points from Cheng *et al* [94]. The magenta curve to the present model, the black curve corresponds to the model by Lucchese *et al* [47], the red curve to Wang *et al* [91]. The inset provides a close-up view for L_D < 0.8 nm.

5.2.4.2 Stages of disorder

The common point between the three models is the presence of two distinct regimes: (i) a hyperbolic behavior at low defect concentration and (ii) a parabolic regime at high defect concentration. Increasing the defects density induces an increase in the I_D/I_G ratio until a certain L_D value from which I_D/I_G drops down and stabilizes to an asymptotic value equal to C_S. This is explained by overlaps between the different regions enabled at high defect concentration, transforming highly active regions into less active ones. In the literature [71, 88], these two regimes are commonly referred as *stage 1* and *stage 2* of disorder. **Figure 5.9** presents the model decomposed in two components $\frac{C_S f_S}{1-f_{sp^3}}$ and $\frac{C_A f_A}{1-f_{sp^3}}$ to evidence the contribution of

the structurally distorted and activated areas. In stage 1, due to the large C_A value compared to C_S, I_D/I_G is mostly governed by the activated area. Stage 2 starts at $L_D = r_A + r_{sp^3}$, corresponding to the point where the activated regions start being converted into distorted and sp^3 regions. Since the D band scattering efficiency is drastically reduced in distorted regions and completely vanishes in sp^3 regions, the global D band signal decreases significantly. At some point, the activated area disappears, leaving a surface entirely composed of sp^3 regions separated by tiny distorted regions. This corresponds to the *stage 3* of disorder which is characterized by the absence of remaining pristine sp^2 regions. It is interesting to notice that, even at a coverage rate of 100 %, I_D/I_G is not equal to zero. This is due to the limit of using a continuous model. The objective was to propose a simple model based on continuous equations, but a discrete model would be more accurate to describe high coverage regimes where L_D is of the order of magnitude of the carbon-carbon bond length. In the proposed continuous model, a coverage rate of 100 % corresponds to $L_D = r_{sp^3}$ = 0.09 nm, which is smaller than the carbon-carbon distance in graphene. Additionally, regarding **Figure 5.9**, the sp^3 surface does not cover 100 % of the total surface, and a tiny distorted area remains. By consequence, a continuous description lacks physical meaning at high coverage. The development of a discrete model that considers the lattice structure requires further investigations but would help improve the present model.

To summarize, the transition from the fully sp^2-hybridized phase to the fully sp^3-hybridized phase can be decomposed into three distinct stages:

(1) Stage 1 characterized by low sp^3-C-concentration and a quasi-random distribution of grafted species across the surface. The Raman signal is dominated by the contribution of f_A (due to the large value of C_A).

(2) Stage 2 characterized by higher sp^3-C-concentration, leading to the formation of sp^3-C "clusters", i.e., areas in the graphene layer where sp^3-C atoms concentrate. This induces significant overlaps between affected regions, which reduces the total structurally affected area f_S and the activated area f_A relatively to the number of defects, thereby causing a decrease in the I_D/I_G ratio for high coverage rates.

(3) Stage 3 corresponds to a fully sp^3-hybridized C-layer, in which I_D/I_G tends to C_S.

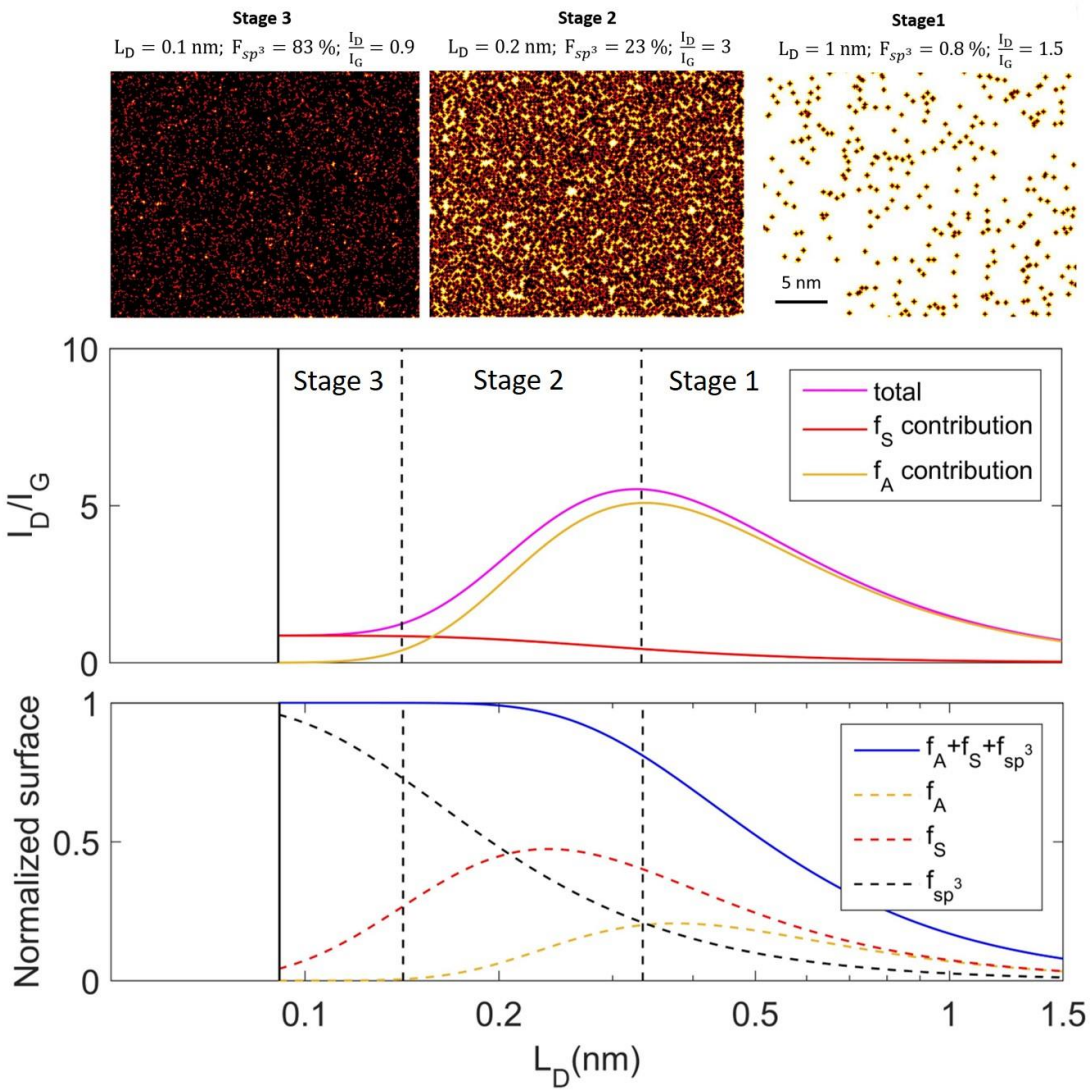


Figure 5.9: (a) Simulated images of the areas covered by sp^3 (black), structurally distorted (red) and activated (yellow) regions for three different L_D values (one in each stage). (b) I_D/I_G vs. $L_D$curve decomposed into its f_S and f_A components to evidence the three stages. (c) Evolution of the three elementary normalized surface fractions across the three stages.

As a consequence, the I_D/I_G ratio alone is insufficient to determine the sp^3-content, as it may correspond to two distinct values of L_D. However, stages 1 and 2 can be reliably distinguished by analyzing the FWHM of the D band (Γ_D). According to the confinement model, localization in real space leads to delocalization in k-space, resulting in the activation of additional vibrational modes and a broadening of the Raman peaks. This model has been successfully applied to graphene with finite-size domains [95]. In the case of isolated point-defects, Γ_D is expected to remain constant. This is because the Fourier transform of the distribution of non-overlapping disks yields a diffraction pattern equivalent to that of a single disk [96], differing only in the Raman background due to the activation of all k-vectors in the Brillouin zone. As shown in **Figure 5.10**, two distinct behaviors are observed. At low coverage rates, where disk-overlapping is minimal, Γ_D remains nearly constant. Few sp^3 defects dispersed on the graphene sheet give the same D band linewidth; only the I_D/I_G ratio reflects the number of defects. At large coverage rates, where significant overlapping

occurs, the confinement model holds due to the creation of small domains: Γ_D increases as I_D/I_G decreases.

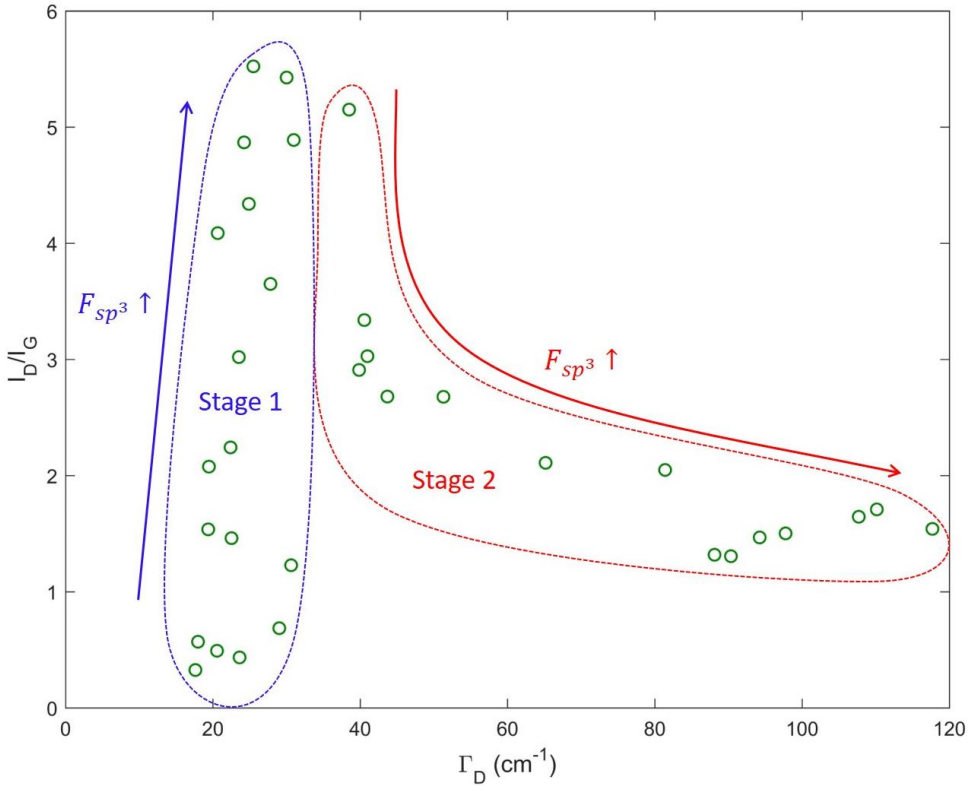


Figure 5.10: Plot of the I_D/I_G ratio as a function of the full width at half maximum of the D band ($FWHM_D$) for fluorinated graphene. Every point corresponds to a 532 nm laser excitation. The data points are separated un two distinct groups corresponding to stage 1 and 2 of disorder. The arrows indicate the sense of increasing coverage rate.

5.2.4.3 Excitation energy dependence of I_D/I_G

As mentioned in **5.2.3.2**, the laser energy dependence of the I_D/I_G ratio is driven by C_A. In case the laser energy is different from 2.33 eV, the C_A is no longer equal to 20.11, and must be adjusted to conserve the accuracy of the model. Data obtained from ion bombarded graphene follow a dispersion $C_A = 160 \times E_L^{-4}$ [89], giving $C_A = 5.43$ for $E_L = 2.33\ eV$. At this laser energy, data from functionalized graphene are well reproduced with $C_A = 20.11$ (see **5.2.3.3**), which indicates that the excitation energy dependence is different. Considering that C_A remains inversely proportional to the fourth power of the laser energy, functionalized graphene must have $C_A = (20.11/5.43) \times 160 \times E_L^{-4}$ =592.6× E_L^{-4} (**Figure 5.11a**), which gives $C_A = 40.15$ for $E_L = 1.96\ eV$ (633 nm) and $C_A = 14.24$ for $E_L = 2.54\ eV$ (488 nm) (**Figure 5.11b**).

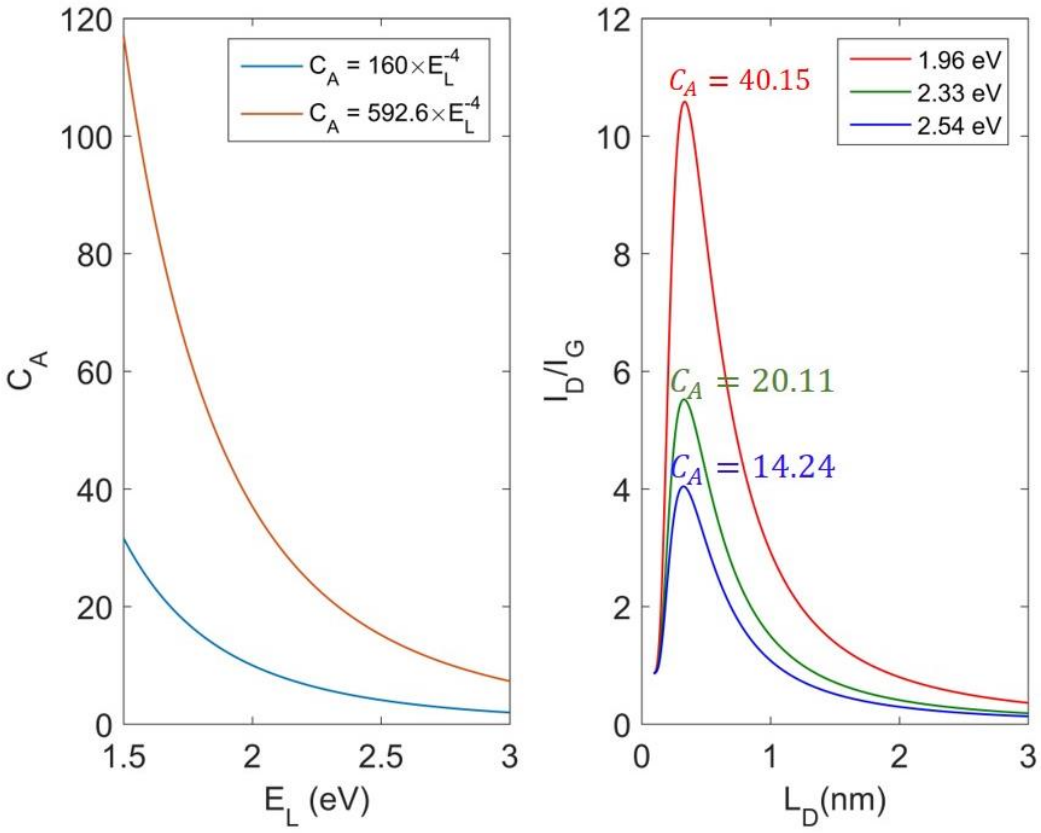


Figure 5.11: (a) C_A $vs.$ E_L estimated for ion-bombarded [89] and functionalized graphene (this work). (b) I_D/I_G $vs.$ L_D for functionalized graphene (our model) and for three distinct laser energies used during this PhD.

Chapter 6 Results and analysis of hydrogenated graphene

6.1 Experimental parameters

Graphene samples were prepared at LPCNO in Toulouse with the protocols detailed in **Chapter 2** and hydrogenated at the Pontificia Universidad Católica Madre y Maestra (PUCMM) in Santiago de los Caballeros (Dominican Republic), where I had the opportunity to work for a few months during this PhD. Our contact is Professor Fabrice Piazza, an expert in the synthesis and characterization of carbon materials (amorphous carbon, diamond, diamane, graphene, …). The experimental method used to hydrogenate was the HFCVD described in **Chapter 3**. Different sets of experimental conditions were tested to obtain different hydrogen coverage rates. In this synthesis technique, there are five main parameters susceptible to impact hydrogenation:

(1) The H_2 residual pressure inside the chamber
(2) The H_2 gas flow
(3) The temperature of the filaments
(4) The distance between the sample and the filaments
(5) The exposure time

In this PhD, all the hydrogenation processes were performed using the same sample-filament distance of about 4.4 cm, and most of them lasted 1 hour. The other parameters were frequently modified from one process to another. Tens of samples were hydrogenated under many different conditions, exploring a large range of parameters. The temperature of the filaments ranged between 1800°C and 2300°C, the H_2 flow between 1 and 50 sccm, and the H_2 residual pressure between 4 and 85 torr. However, among these tens of experimental conditions, only a few provided exploitable results (**Table 6.1**).

Process number	H_2 pressure (torr)	H_2 flow (sccm)	Filament temperature (°C)
1	50	1	1900
2	50	10	1900
3	50	50	1900
4	85	10	2000
5	85	50	1900
6	85	50	2000

Table 6.1: Main experimental conditions that provided exploitable results.

A few experiments were performed at different exposure times, ranging from 10 minutes to 6 hours, and some of them also provided interesting results.

6.2 Raman spectroscopy

6.2.1 Raman features of hydrogenated graphene

Raman spectroscopy was performed on each sample before and after hydrogenation using different laser sources, including 488 nm, 532 nm and 633 nm wavelengths. A typical Raman spectrum of a pristine monolayer graphene flake on Si/SiO_2 is shown in **Chapter 4**. The 2D band is fitted by one Lorentzian with a FWHM around 24 cm^{-1}, which is representative of a monolayer. In addition, the absence of D and D' bands indicates the high quality of the exfoliated graphene.

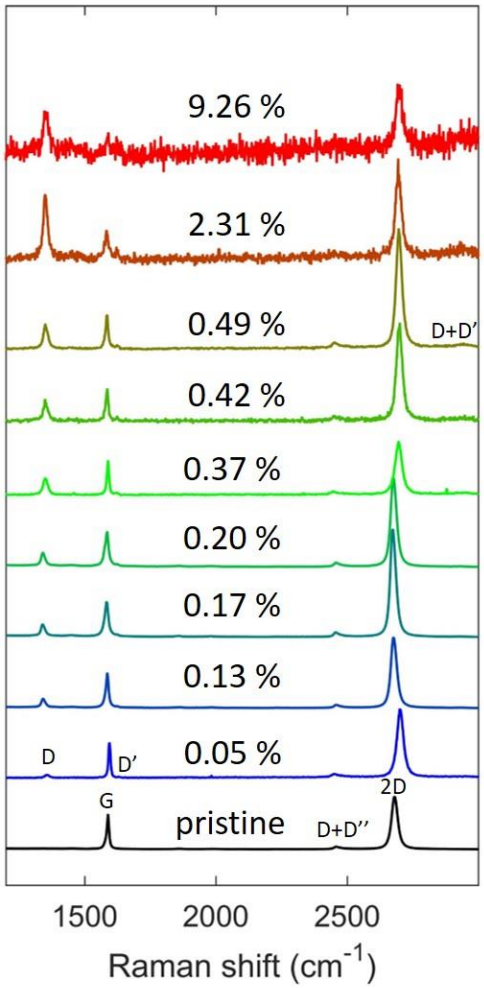


Figure 6.1: Raman spectra of graphene samples with different hydrogen contents ranged from 0% (pristine) to 9.26%. Each spectrum is the response to an excitation of either 532 nm or 488 nm and is normalized to the G band intensity for comparison.

Figure 6.1 displays a set of Raman spectra corresponding to different hydrogen coverage rates, calculated using the model presented in **Chapter 5**, with C_A = 20.11 for the spectra at 532 nm and C_A = 14.24 for those at 488 nm (see **Chapter 5**). Both the D and D' bands appear at the lowest coverage rate of 0.05 %,

though with a very low intensity for the D' band. The maximum I_D/I_G ratio reaches a maximum value of 4 at a coverage rate of 9.26 % corresponding roughly to the border between stage 1 and stage 2 (see **Chapter 5**), whereas the $I_{D'}/I_G$ ratio does not exceed 0.5. Interestingly, the signal-to-noise ratio tends to strongly decrease with increasing coverage rate, which could be interpreted as a decreasing sp^2 surface fraction. By consequence, the fitting of the D' band, which is generally the least intense peak, becomes challenging, making the estimation of its intensity ($I_{D'}$) approximative. Thus, I am concerned about warning the reader that the $I_{D'}/I_G$ ratios given in the following should be treated cautiously, especially for the most hydrogenated samples.

To analyse these Raman spectra and investigate the link with the different experimental conditions, **Figure 6.2** displays the I_D/I_G ratio as function of both the linewidth of the D band and the $I_{D'}/I_G$ ratio for several samples exposed to the hydrogenation conditions given in **Table 6.1**. These data can be interpreted as follows:

(1) The plot of I_D/I_G $vs.$ Γ_D indicates that all the samples are in stage 1 of disorder, characterized by a sharp D band due to the absence of large sp^3 domains (see **Chapter 5**).
(2) The samples hydrogenated with an H_2 residual pressure of 85 torr have the least I_D/I_G ratio and a $I_D/I_{D'}$ ratio above 13, whereas the other samples hydrogenated at a lower pressure (50 torr) are characterized by $7 < I_D/I_{D'} < 13$. According to both our model (see **Chapter 5**) and the empirical model from Eckmann *et al* [71], samples hydrogenated at 85 torr are characterized by a low defect density that corresponds to grafted hydrogen atoms whereas samples hydrogenated at 50 torr have a higher defect density corresponding to either vacancies ($I_D/I_{D'} \approx 7$) or a mixed between both grafted hydrogen and vacancies ($7 < I_D/I_{D'} < 13$). Assuming that the pressure drives the temperature gradient in the gas phase between the sample holder and the filaments, as well as the collision and recombination rate, it is expected that at "high" pressure (i) fewer radicals are reaching the samples and (ii) these radicals have a lower kinetic energy. Consequently, hydrogenation at low pressure (i.e. 50 torr) might increase the hydrogenation rate, but not without damaging the graphene's lattice.
(3) Two samples hydrogenated under similar conditions have different I_D/I_G and $I_D/I_{D'}$ ratios, confirming again that hydrogenation can be inhomogeneous (see **Chapter 5**). Considering this, (2) remains purely hypothetical and requires a large statistical study for confirmation.
(4) Since some samples might present an unknown proportion of vacancies that contribute to the D band, the model described in **Chapter 5,** determining the hydrogen concentration, becomes inaccurate since point defects are not necessarily chemisorbed hydrogen atoms. A solution to overcome this issue would be to remove the hydrogen from the graphene and measure the change in the D band intensity to determine the proportion of the D band signal that originates from hydrogenation.

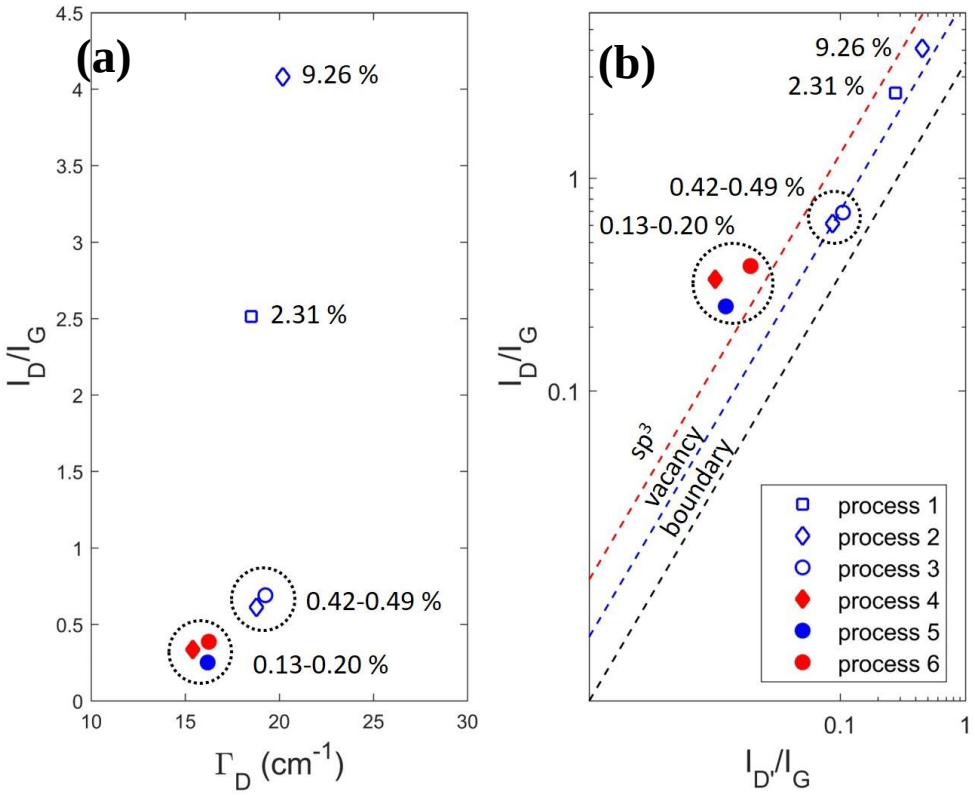


Figure 6.2: (a) I_D/I_G *vs.* Γ_D in linear scale and (b) I_D/I_G *vs.* $I_D/I_{D'}$ in logarithmic scale for several samples hydrogenated with hot filament processes given in Table 6.1. The corresponding hydrogen coverage rates are indicated. In (b) the dotted lines represent $I_D/I_{D'} = 3.5$ (black), $I_D/I_{D'} = 7$ (blue) and $I_D/I_{D'} = 13$ (red).

6.2.2 Raman analysis of hydrogen thermal stability

6.2.2.1 Dehydrogenation enabled by thermal annealing

Determining precisely the hydrogen desorption temperature for hydrogenated graphene is quite important, in particular for device fabrication, as well as layer transfer and stacking. As mentioned in **Chapter 2**, the fabrication process of a graphene device involves several annealing steps at 170°C, and the hot pick-up technique [41] used to transfer graphene layers requires different annealing steps ranging between 80°C and 180°C. Several studies of hydrogen thermal stabilities on graphite are reported in the literature [23, 97], but the annealing temperature at which chemisorbed hydrogen is removed from a graphene layer remains unclear. Values range from 150°C [14] to 500°C [24], although conditions were not exactly the same. Based on the evolution of the I_D/I_G ratio, Luo *et al* [98] suggested a mechanism involving two desorption thresholds, one at 100-150°C and another at 260-300°C. It is interesting to mention that these thresholds are strongly dependent on the number of graphene layers. For hydrogen chemisorbed on graphite, temperature programmed desorption (TPD) spectra also reveal two desorption thresholds attributed by Hornekaer *et al* [23] to energy barriers for desorbing hydrogen dimers respectively chemisorbed in para and ortho positions.

The large heterogeneity of data reported in the literature does not solve the problem of hydrogen thermal stability on graphene. By consequence, thermally activated dehydrogenation of monolayer graphene was investigated in Raman spectroscopy. To anneal the samples and investigate the subsequent dehydrogenation process, a Linkam cryostat/heater (-195 to 600°C) in ultra-high purity N_2 at atmospheric pressure with water cooling was used. A graphene flake hydrogenated with process 6 (see **Table 6.1)** and characterized by a ratio I_D/I_D, above 13 (see **Figure 6.2**) was heated incrementally from 20 to 350°C as follows: once the cryostat was closed, the specimen was heated up to the first set temperature (i.e., 40°C) with a 5 min dwell, then cooled down to 20°C, and characterized by Raman spectroscopy with the cryostat opened. Then the cryostat was closed again, and the sample was heated up to the second set temperature (i.e., 60°C) with a 5 min dwell, and so on. Both heating and cooling rates were 50°C/min. This specific heat-treatment procedure was used instead of carrying out the Raman while the specimens were heated up because it was observed that cumulating the laser energy with the thermal energy from the annealing procedure resulted in the material modification and variation of the relative intensity of the D band. Raman spectra were acquired using a green excitation (532 nm) with a laser power of 1 mW (obtained with a 1 % filter applied to the full laser power of 100 mW) for 100 s. The laser power value was measured after the objective lens; hence, it corresponds to the power actually received by the sample.

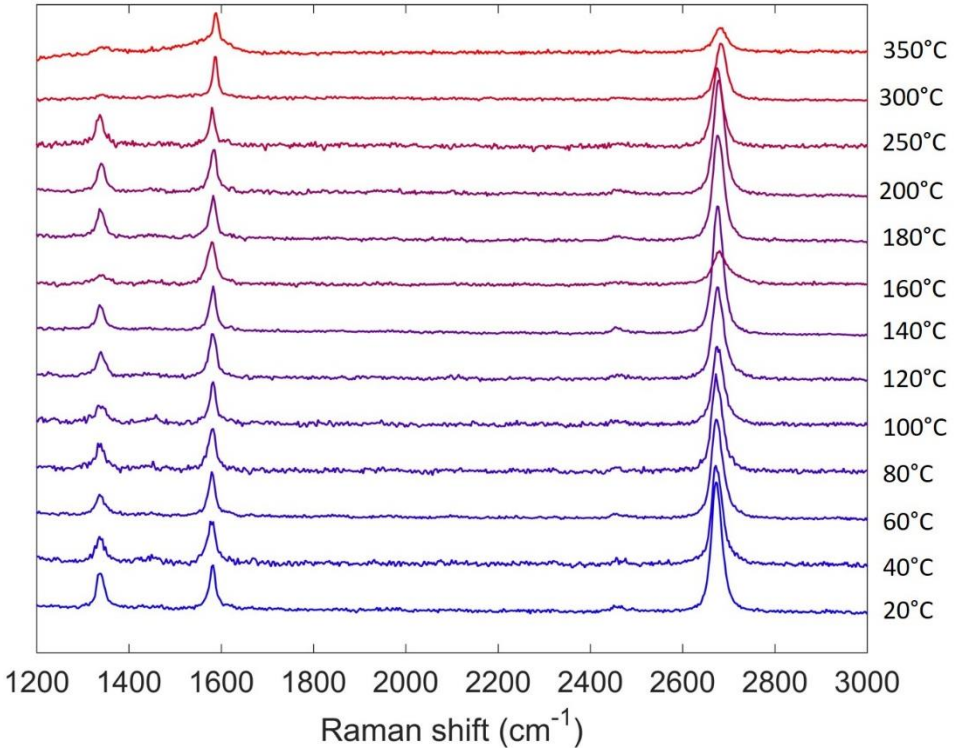


Figure 6.3: Raman spectra obtained on hydrogenated graphene after annealing at temperatures incrementally increased from 20 to 350°C.

Figure 6.3 shows the Raman spectra obtained on the hydrogenated area after annealing. Spectra appear to be quite inhomogeneous, but the relative intensity of the D band remains quite significant up to an annealing temperature of 250°C**.** From 300°C, the relative intensity of the D band becomes very low or vanishes. Using a 350°C annealing temperature allowed obtaining spectra similar to those obtained by Elias *et al*

[12]. From these observations, it seems that hydrogen remains bonded to graphene up to 250°C. Annealing the sample above this temperature is likely to enable hydrogen desorption, thereby recovering the graphene layer. However, due to spatial inhomogeneities observed in the hydrogen coverage rate, a large statistical study would be required to confirm these observations. From one spectrum to another, the relative position between the sample and the laser spot might be slightly shifted, thereby explaining the observed inhomogeneities among Raman spectra.

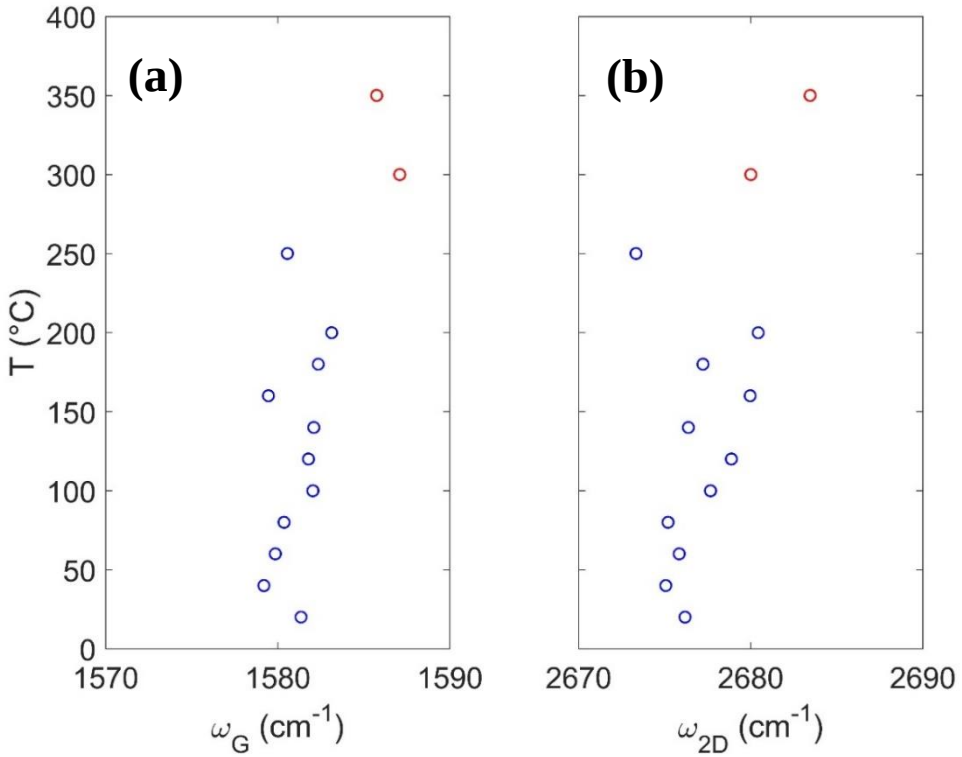


Figure 6.4: Temperature dependence of (a) the G band and (b) the 2D band wavenumbers determined by fitting the spectra in Figure 6.3.

The decrease of the D band signal is not the only effect induced by dehydrogenation. By looking closely at the spectra in **Figure 6.3**, an upshift of both the G band and the 2D band frequencies is observed above 250°C. In **Chapter 4**, it was mentioned that the frequency shift of the G band can be induced by both doping and mechanical strain, with contributions being separated by the shift of the 2D band relatively to the shift of the G band. According to Lee's model [69], $\Delta\omega_{2D}/\Delta\omega_G = 0.7$ is characteristic of doping whereas $\Delta\omega_{2D}/\Delta\omega_G = 2.2$ is related to mechanical strain. The average frequencies of the G and 2D bands are respectively equal to 1581 cm^{-1} and 2677 cm^{-1} before dehydrogenation (T ≤ 250°C), whereas they are shifted to respectively 1586 cm^{-1} and 2682 cm^{-1} after dehydrogenation (T > 250°C) (**Figure 6.4**). It gives $\Delta\omega_{2D}/\Delta\omega_G = 1.0$, meaning that the major contribution is doping. This could be interpreted as a recovery of the Dirac cone at the K-point, previously deteriorated by hydrogenation. Charged impurities from the environment can dope the sample if the Fermi level fluctuations are larger than the bandgap induced by hydrogenation. After dehydrogenation, the bandgap falls to zero as the Dirac cone is recovered, thereby restoring the doping. However, the initial hydrogen coverage rate was determined to be around 0.2 % (see

Figure 6.2), which is quite moderate. In my consortium, DFT calculations of the electronic band structure corresponding to a hydrogen coverage rate of 2 % revealed the opening of a small bandgap in the K-valley, but it is not evident that this induced bandgap remains large enough at 0.2 % to preserve graphene from doping.

For some samples, graphene was not completely recovered by thermal annealing above 300°C. It is the case, for instance, of a sample hydrogenated for 10 minutes with an operating pressure and gas flow of 4 Torr and 10 sccm, respectively, and a filament temperature of 2100°C. A molybdenum shutter, positioned 3 cm above the sample, shielded the graphene sample from direct exposure to the filament's thermal radiation, ensuring the substrate remained at low temperatures (typically < 100°C, as measured by a K-type thermocouple with sheathed wires, placed on the substrate holder's surface). The dehydrogenation process was performed by annealing at 400°C under an Ar/H_2 atmosphere (95/5 vol.%) for 1 hour. The Ar/H_2 flow was maintained at 500 sccm until the temperature dropped to 100°C. The Raman spectra acquired before and after annealing, using a red excitation (633 nm) laser with a power of 0.5 mW, are plotted on **Figure 6.5**.

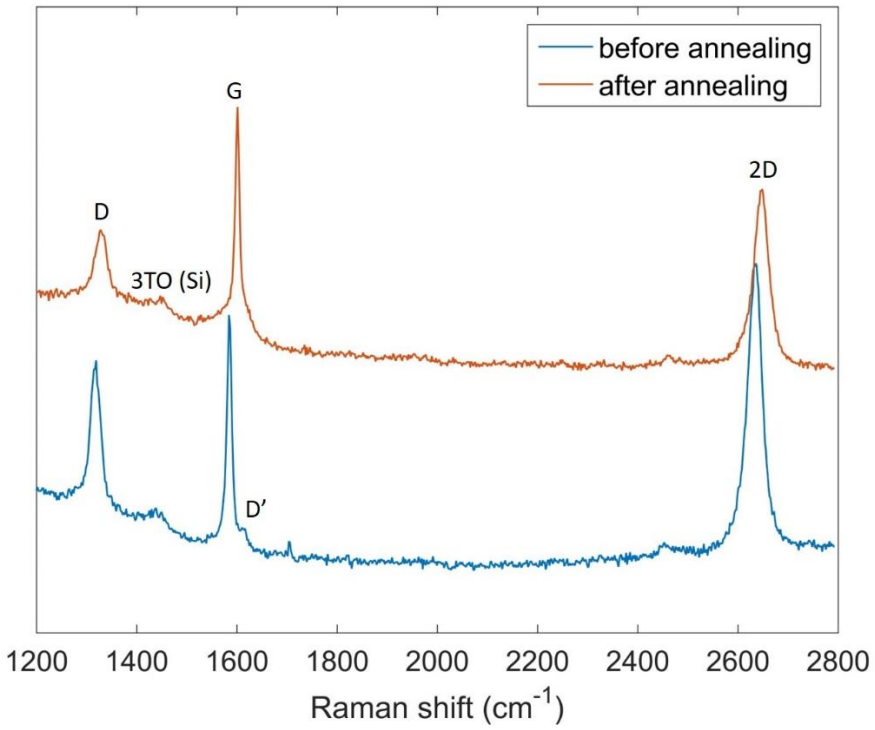


Figure 6.5: Raman spectra acquired with a 633 nm laser excitation before and after annealing the sample at 400°C for 1h under an inert atmosphere.

After hydrogenation, the I_D/I_G ratio was about 0.6 and the linewidth of the D band was about 22 cm^{-1}, which is characteristic of stage 1 of disorder (see **Chapter 5**). The $I_D/I_{D'}$ ratio is about 10.6, suggesting that defects induced by hydrogenation might be composed of sp^3-C atoms and vacancies. After annealing, the I_D/I_G and $I_D/I_{D'}$ ratios drop down to 0.3 and 7 respectively, indicating that the hydrogen was completely removed and the remaining defects are vacancies. Simultaneously, both the G and 2D bands are upshifted, with $\Delta\omega_G$ = +12 cm^{-1} and $\Delta\omega_{2D}$ = +9 cm^{-1}, respectively. This results in a $\Delta\omega_{2D}/\Delta\omega_G$ ratio of

0.75, characteristic of doping. Again, this doping effect could be interpreted by the recovery of the Dirac cone after hydrogen removal, but that remains hypothetical and requires further investigation. Regarding the change in the I_D/I_G ratio, it can be concluded that sp^3–C covalent bonds contribute to half of the D band intensity, i.e. $I_D/I_G = 0.3$. Considering the fourth power dependence on the laser energy of the I_D/I_G ratio [89, 90], the model described in **Chapter 5** to determine the hydrogen coverage rate must be used with a coefficient $C_A = 40.15$ corresponding to an excitation at 633 nm (see **Chapter 5).** The model gives a hydrogen coverage rate of 0.8 % for this sample, which is still low compared to the coverage rate value considered in DFT calculations.

6.2.2.2 Dehydrogenation enabled by laser irradiation

Another important question concerns the stability under photoirradiation by a laser. Theoretical results from the literature [99] demonstrated that with increasing hydrogen coverage rate up to 30% the thermal conductivity of hydrogenated graphene decreases continuously down to 27% of that of pristine graphene. For a hydrogen coverage rate of 5%, which is closer to the values obtained in this work, this study reports a thermal conductivity value equal to 65% of that of pristine graphene. Thus, illuminating the sample with a laser might probably induce a local elevation of the temperature in the area exposed to the laser spot, thereby inducing hydrogen desorption. To study this effect, the dependence of the Raman spectrum features on the laser power was investigated. A series of Raman spectra was acquired on the same area every minute up to 60 minutes for a 633 nm wavelength on a graphene flake hydrogenated with process 2 (see **Table 6.1**). This sample presents a D band linewidth of about 19 cm^{-1} and an I_D/I_G ratio of 0.6 with a 488 nm laser excitation, which is attributed to a hydrogen coverage rate of 0.42 %. The power was started at 0.15 mW to acquire Raman spectra for the first time series, and then the power was successively increased to 0.5, 2, 4, and 8 mW to acquire the spectra for the other time series, respectively. Again, the laser power values were measured after the objective lens; hence, they correspond to the power actually received by the sample.

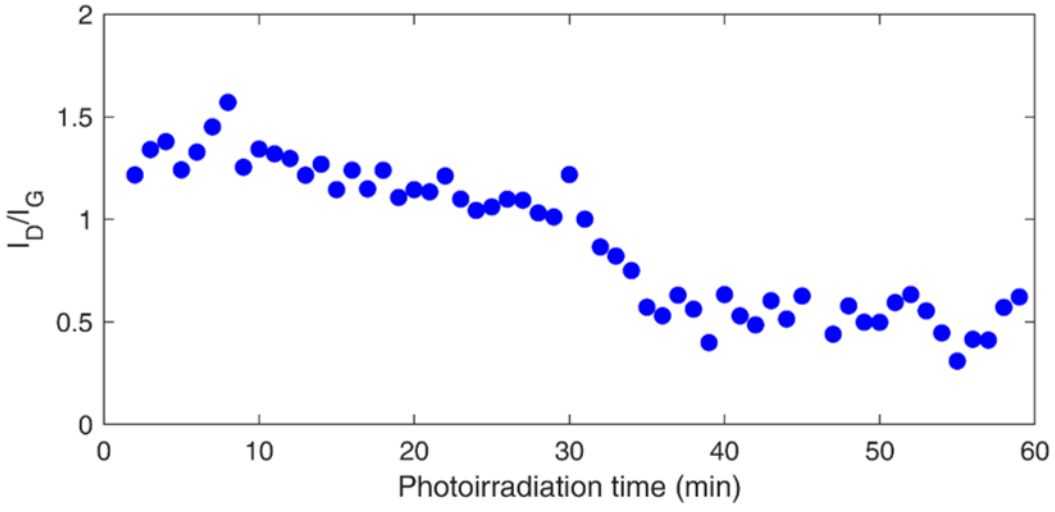


Figure 6.6: Variation of the I_D/I_G ratio as a function of the photoirradiation time for a hydrogenated graphene sample subjected to photoirradiation with a 4 mW 633 nm laser.

At a laser power lower than 4 mW, no significant effect was observed. In **Figure 6.6** is reported the variation of the I_D/I_G ratio as a function of the photoirradiation time at 4 mW. The I_D/I_G intensity decreases with increasing photoirradiation time, which can be interpreted by hydrogen desorption caused by overheating. After the irradiation series at 4 mW, the I_D/I_G ratio remained constant when using a higher power (8 mW), meaning that the graphene could not be modified further. The explanation can be that the defects corresponding to hydrogenation were removed, and the remaining defects correspond to vacancies and edges. However, it is not certain that only dehydrogenation is induced by the laser. For instance, the release of hydrogen atoms from the surface is likely to result in reactive carbon atoms able to subsequently oxidize, due to air (oxygen) interaction. As a consequence, oxygenated functions (e.i., hydroxyl, epoxy) can be grafted while the carbon atoms involved remain sp^3.

This dehydrogenation method was employed on a graphene hydrogenated for 20 minutes with an operating pressure and gas flow were 4 Torr and 10 sccm, respectively, and a filament temperature of 2100°C. For this sample, both optical contrast (**Figure 6.7b**) and the Raman signal vanished after hydrogenation, making it impossible to estimate the coverage rate. There are two possible interpretations:

(1) Graphene was (almost) fully hydrogenated: its electronic band structure is strongly modified, changing the optical properties.
(2) Graphene was destroyed.

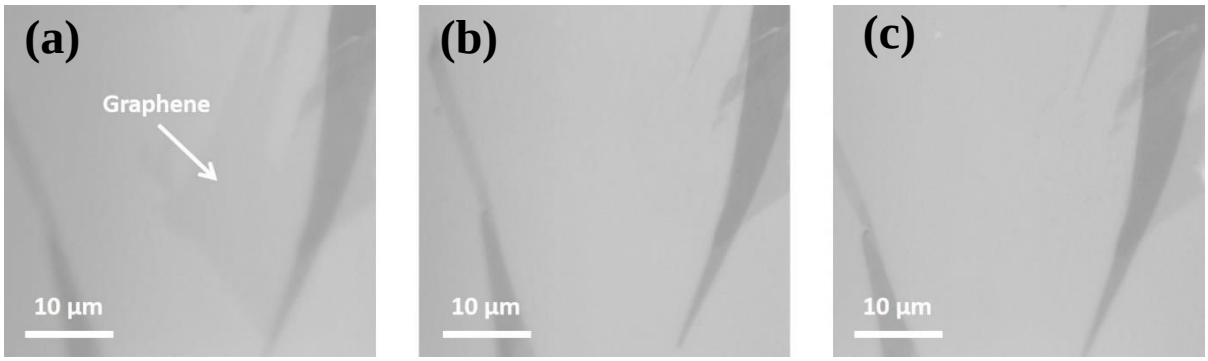


Figure 6.7: Optical microscope images of a graphene flake on Si/SiO_2 hydrogenated for 20 minutes with an operating pressure and gas flow of 4 Torr and 10 sccm, respectively, and a filament temperature of 2100°C. Images are presented in black and white for a better comparison. (a) Image before hydrogenation. The monolayer is visible by optical contrast (see Chapter 2), appearing slightly darker than the substrate. (b) Image after hydrogenation. The monolayer is no longer visible. (c) Image after annealing at 400°C under an Ar/H_2 atmosphere for 1 hour, showing no change in the optical contrast.

Figure 6.8 displays the spectra obtained by exposing the sample to increasing power during Raman measurements. The spectra are normalized per laser power for direct intensity comparison. The data show that some graphene Raman signal is gradually recovered starting at a 1.2 mW laser power, although the relative intensity of the 2D band remains low. This recovery is not due to a lack of material or detector

nonlinearity, as evidenced by the minimal increase in the Si support signal (3TO peak) with increasing laser power, while the D band intensity increases significantly. This suggests that increasing the laser power during Raman measurements has recovered the graphene Raman signal and promotes dehydrogenation. However, even after annealing at 400°C under an Ar/H_2 atmosphere for 1 hour, the optical contrast is not recovered (**Figure 6.7c**) and the Raman signal-to-noise ratio remains very low. This indicates that the absence of optical contrast and Raman signal after hydrogenation does not only originate from the modification of the electronic band structure but also from a lack of graphene surface. Similar hydrogenation conditions were used for 10 minutes on another sample, and the dehydrogenation process revealed a significant concentration of vacancies induced by hydrogenation. It seems very probable that exposing graphene to a flow of hydrogen radicals in these experimental conditions results in two simultaneous effects: (i) hydrogen chemisorption and (ii) etching. That was investigated in AFM.

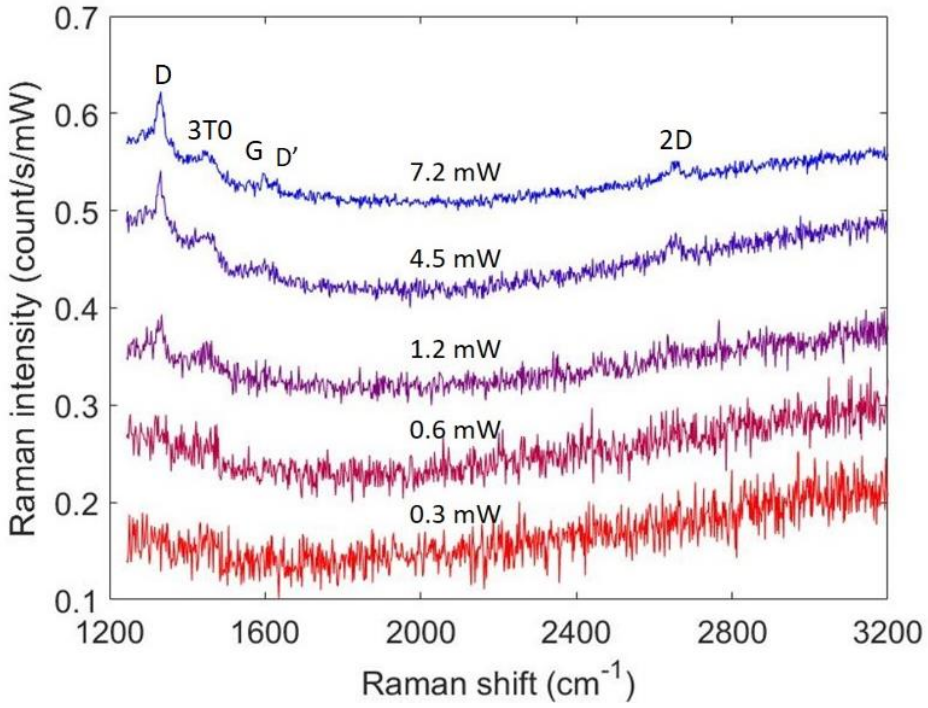


Figure 6.8: Raman spectra of a graphene sample after over-exposure to hydrogen radicals, followed by exposure to increasing laser power during Raman measurements. The spectra are normalized by laser power for direct intensity comparison.

6.3 Atomic Force Microscopy

Topographic AFM was carried out on two samples hydrogenated in similar conditions (H_2 pressure: 4 torr; H_2 flow: 10 sccm; filaments temperature: 2100°C) but with different exposure times (10 and 20 minutes). It must be remembered that a molybdenum shutter, positioned 3 cm above the samples, shielded the graphene sample from direct exposure to the filament's thermal radiation. In the following, these samples are referred to as *sample 1* (10 minutes) and *sample 2* (20 minutes) for simplicity. The AFM images (**Figure 6.8**) realized in tapping mode under N_2 atmosphere (see **Chapter 4**) reveal significant changes in the topography of the graphene flakes exposed to these hydrogenation conditions.

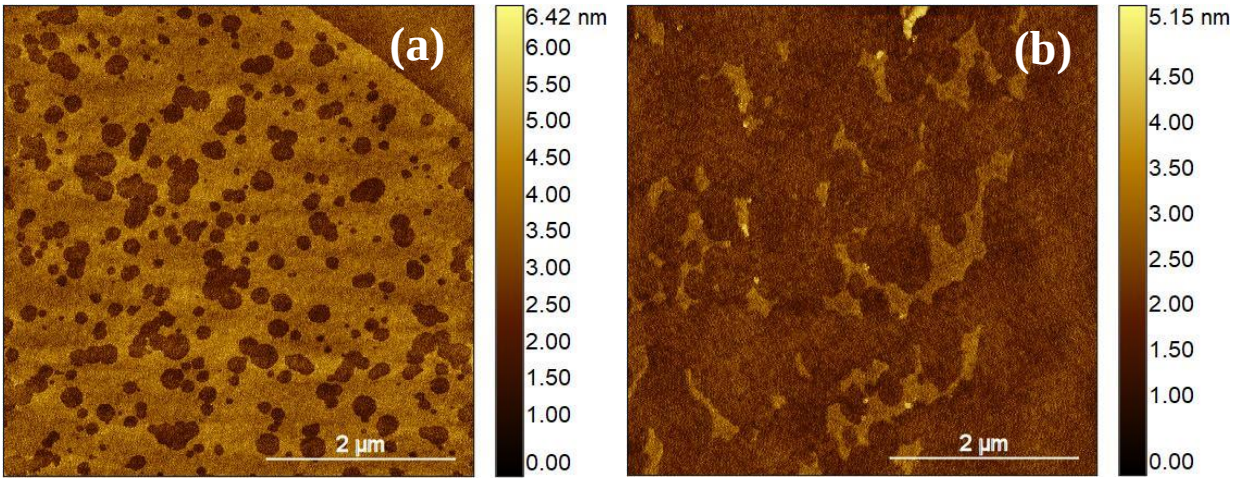


Figure 6.9: Topographic AFM images of (a) sample 1 and (b) sample 2 after exposure to hydrogen radicals for respectively (a) 10 minutes and (b) 20 minutes.

For sample 1, the AFM image (**Figure 6.8a**) reveals a high density of sub-micrometer-sized holes on the surface, which appear as circular dark contrasts. The hole size distribution, shown in **Figure 6.10**, provides insight into the dynamics of hole formation. The polymodal distribution suggests the involvement of various formation mechanisms, consistent with the observation of varying hole shapes (roughly round or roughly hexagonal) and/or different stages of hole formation. The broad nature of the distribution indicates considerable variation in the formation process, suggesting that some local configurations are more conducive to hole formation than others. The longer tail of the distribution, extending toward larger sizes, indicates the "coalescence" of holes.

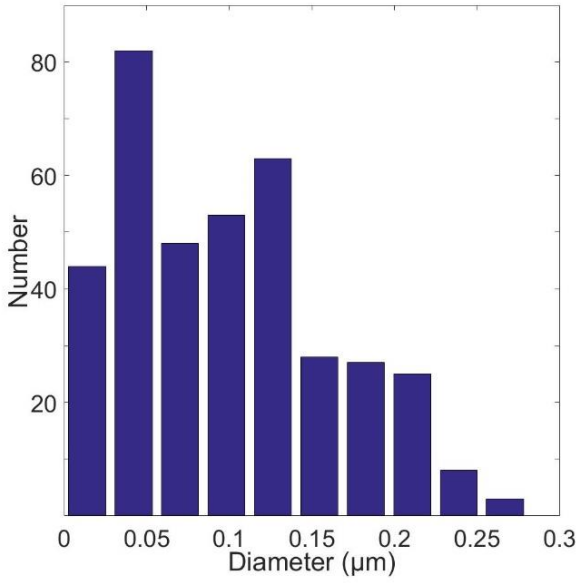


Figure 6.10: Hole size distribution in Figure 6.9a.

For sample 2, the topographic AFM image (**Figure 6.9b**) reveals that a large fraction of the layer has been etched, leaving only some areas intact. Since the hydrogenation of this sample differs from that of sample 1 only by a larger exposure time, it suggests that these large etched domains result from a continuous growth of holes with exposure time. From the size of the largest circular holes observed in **Figure 6.9a** (0.27 µm), which are presumably the first to have been created at t = 0 min and subsequently expanded without merging with others, it can be estimated that the hole radius increased at an average rate of 13 nm/min during the first 10 minutes. The linearity of hole expansion—and hence the etching process—was maintained over the following 10 minutes, as shown in **Figure 6.9b**. This is supported by the results of a linear model (**Figure 6.11**), which assumes random pit creation at a rate of 40 pits/min over a 5 µm × 5 µm surface (as deduced from **Figure 6.10**), and a linear etching speed of 13 nm/min. The etching rate observed here at a substrate temperature below 100°C can be compared to the extrapolated rate of 10 nm/min at 100°C for monolayer graphene, as reported in [100], confirming previous observations.

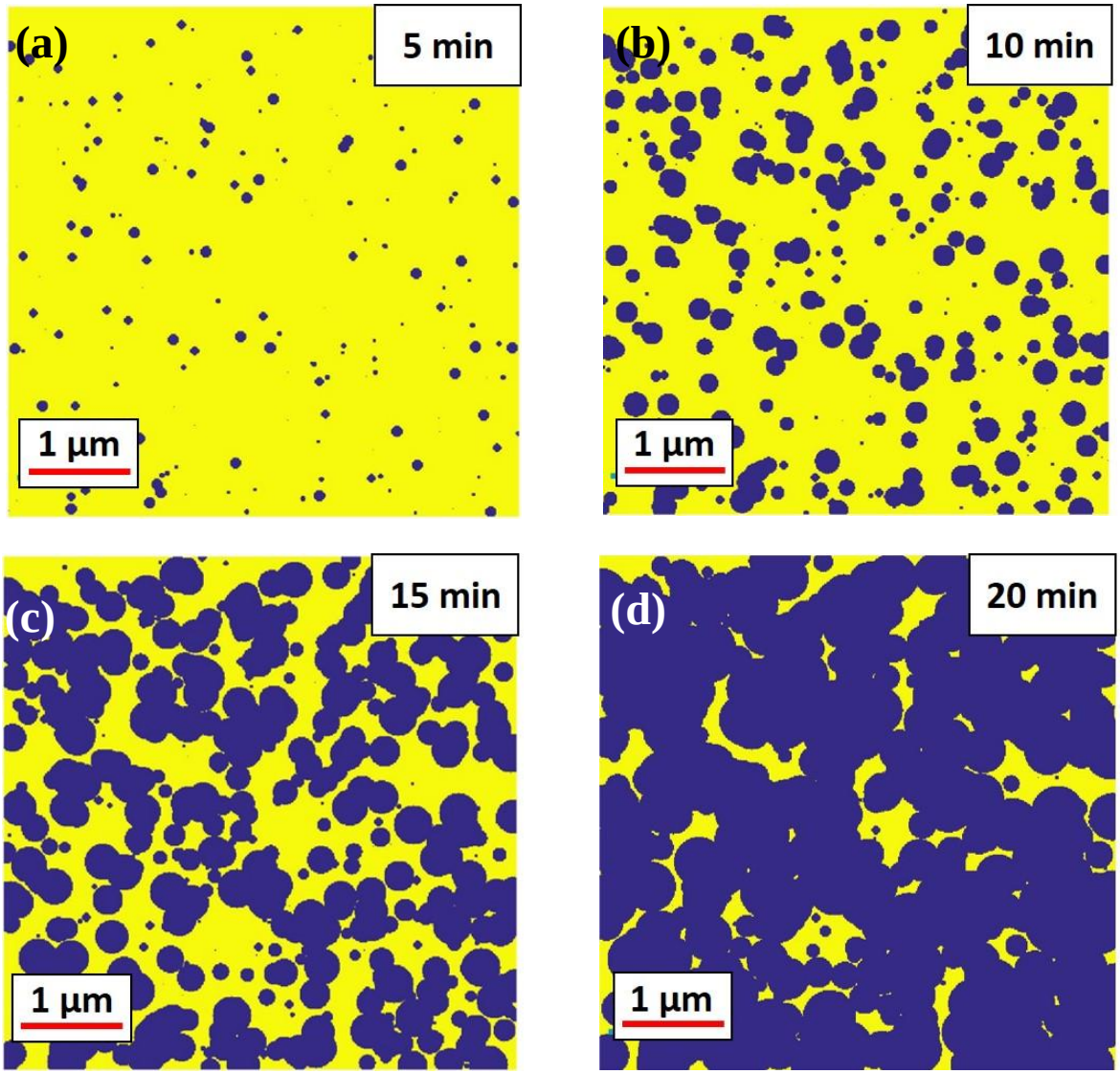


Figure 6.11: Simulated evolution of the graphene surface (yellow) during etching at different time intervals: (a) 5 minutes, (b) 10 minutes, (c) 15 minutes, and (d) 20 minutes.

These results confirm that exposing graphene to a flow of hydrogen radicals can have two effects: (i) hydrogen chemisorption and (ii) etching. The etching mechanism was studied by DFT and molecule dynamics simulations realized in our consortium, focusing on the first C-C bond breakage [101]. The calculations considered the case of a graphene sheet hydrogenated on one side to reproduce experiments. The results demonstrated that, in the presence of hydrogen clusters, the lattice relaxation induced by mechanical strain forms dome-like structures [101] (**Figure 6.12**). Although C-C bond cleavage was found to be more energetically favourable in these over-hydrogenated regions, the corresponding energy barriers determined from molecular dynamics calculations remain too large to be considered accessible at the experimentally measured temperatures. At 2100°C, the kinetic energy $E_c = \frac{3}{2} k_B T$ of a hydrogen radical is about 0.3 eV, which is far below the calculated energy barrier for C-C bond cleavage of about 2 eV [101].

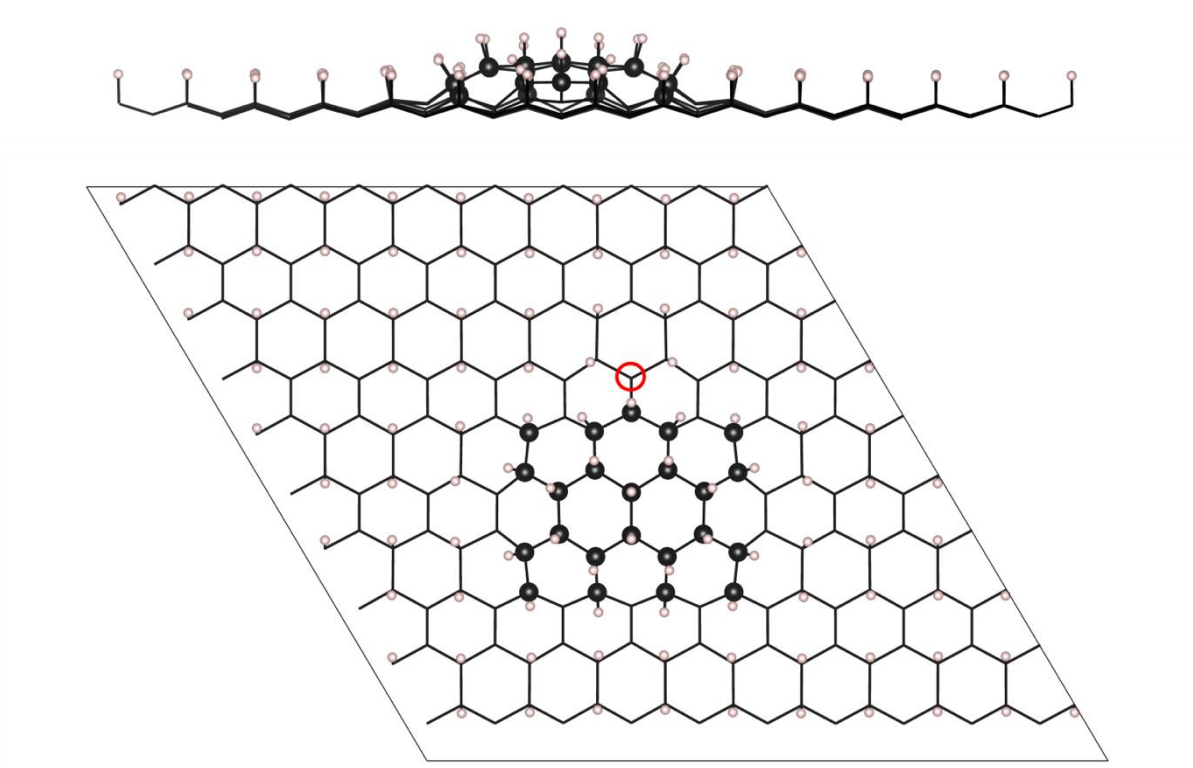


Figure 6.12: Side and top views of a largely hydrogenated *sp*^{3}-C layer with 7 additional chemisorbed hydrogens (high-coverage model). The red circle highlights one carbon atom free of hydrogen, where C-C band cleavage is more energetically favourable. This work was carried out by Iann Gerber from LPCNO.

Thus, a hydrogen radical alone cannot be solely responsible for the creation of holes. An additional agent or process is required to lower the activation energy. It has been suggested that the substrate polarity or the presence of charged impurities within the substrate could be responsible for the observed phenomena [102]. However, we also observed the formation of holes in graphene deposited on BN flakes (**Figure 6.13a**), where the charged impurity density is extremely low. This suggests that the etching process is not driven by charged impurities. The process could involve residual water or other molecules trapped between the graphene flake and SiO_2 during the transfer. However, the formation of holes was also observed in graphene

membranes (**Figure 6.13b**), ruling out this interpretation as well. Additionally, the effect of H_2O molecules on the sample surface is unlikely, as holes were still observed even after applying a thermal pre-treatment. A hypothetical hydrocarbon contamination effect (from the backing pump) is also ruled out, as etching was not consistently observed [22]. These observations suggest the likely involvement of energetic hydrogen species, such as ions or atomic hydrogen, with energies around 2 eV [103]. The hot-filament process is not expected to generate hydrogen ions [104]. Even if some hydrogen ions were produced, they could not be accelerated toward the substrate, as ions cannot be accelerated in the absence of a plasma sheath or external bias. Therefore, the potential effects of hydrogen ions on the sample can be ruled out. However, these ions may be involved in plasma hydrogenation processes [100,105,106]. In the hot-filament process, most hydrogen radicals reaching the sample will have thermalized to the local gas temperature, meaning their energy is well below 0.5 eV [107]. This energy is insufficient for thermal atomic hydrogen to bind with the basal plane (0.85 eV), as supported by molecular dynamics calculations [103]. Upon dissociation of H_2 molecules, some atomic hydrogen may leave the filament with kinetic energy approximately half of the bond dissociation energy (4.52 eV). If these atoms reach the graphene surface without collisions, their kinetic energy would be around 2.25 eV. Molecular dynamics simulations have shown that nanopores in the graphene basal plane can be formed when the ion energy is approximately 2 eV for circular holes [103].

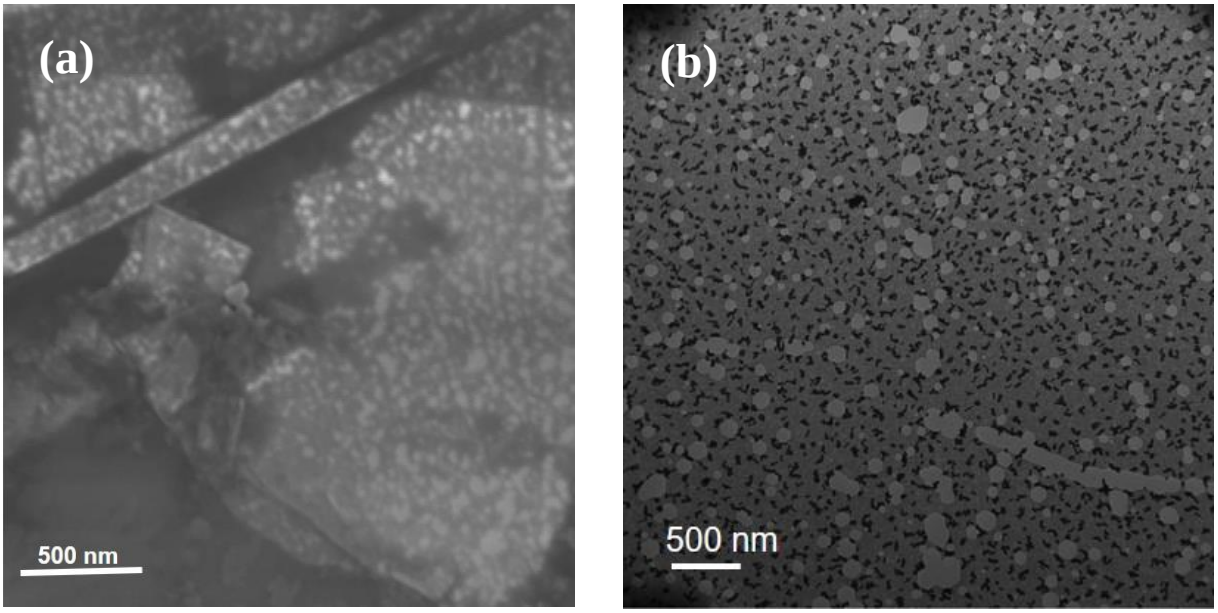


Figure 6.13: (a) Scanning electron microscopy image taken at 3 keV of graphene deposited on a BN flake and subsequently exposed to atomic hydrogen. Light areas are holes in the graphene layer (dark areas). (b) Transmission electron microscopy (TEM) image at 5 keV with a LVEM5 microscope from Delong Instruments, showing graphene transferred onto a TEM grid and subsequently exposed to atomic hydrogen. Light areas represent holes in the graphene layer (dark areas).

Once a hole is formed and remains exposed to hydrogen radicals, hydrogen chemisorption can

occur at the edges. Subsequently, when an additional hydrogen radical interacts with the chemisorbed hydrogen, etching can occur, as observed in long-term experiments. This is because, as mentioned above, the release of CH_4 (or more complex species) from hydrogenated polyaromatic molecules interacting with hydrogen species has a quasi-zero energy barrier [108-110].

6.4 Tip-enhanced Raman spectroscopy

TERS measurements were carried out with a red (633 nm) laser excitation on CVD graphene deposited on ultra-flat gold substrate and hydrogenated using process 6 (see **Table 6.1**) with a molybdenum shutter positioned 3 cm above the samples. The main interest was to detect the C-H stretching mode at 2740 cm^{-1} (see **Chapter 4**). The CVD graphene was transferred from copper foil to a gold substrate with the wet transfer technique described in **Chapter 2**. Unfortunately, the C-H mode could not be detected, suggesting that (i) either hydrogen could not bind to graphene (ii) or the spectra were acquired in regions with poor hydrogen content. The case (i) could be explained by different interactions between graphene and gold compared to SiO_2, thereby changing the absorption energy. However, this remains purely hypothetical. Another plausible explanation is the presence of PMMA residues remaining on graphene after the transfer process. These residues were observed several times in AFM and Raman spectroscopy, and could be problematic for interactions between hydrogen and graphene. The case (ii) is possible if the hydrogen coverage is low and not evenly distributed over the surface.

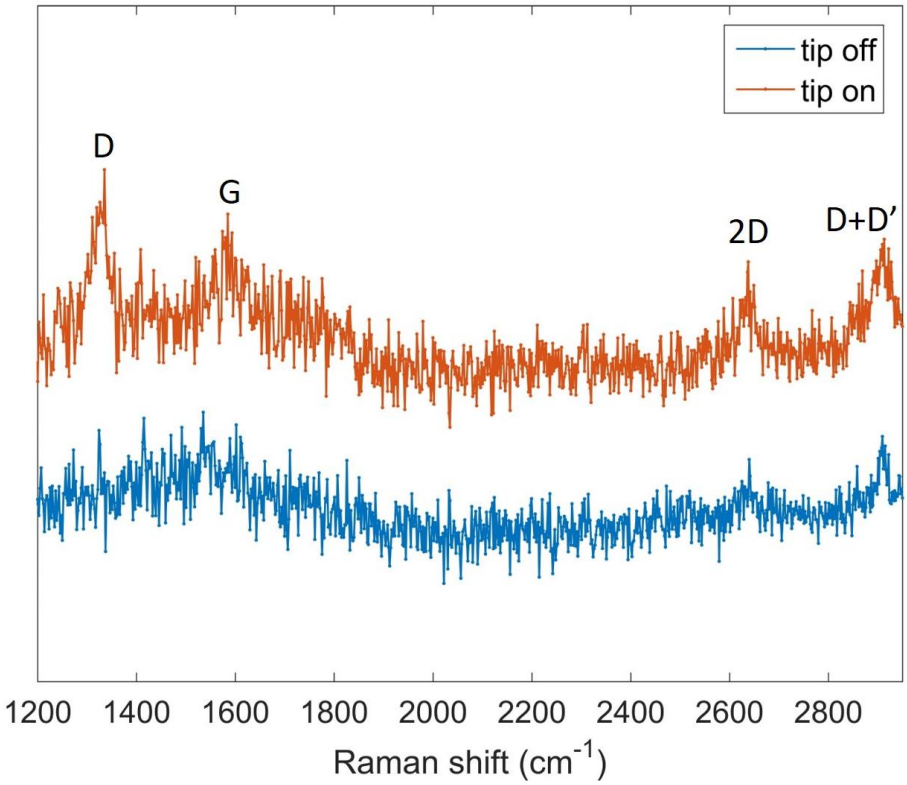


Figure 6.14: Raman (tip off) and TERS (tip on) spectra of CVD graphene transfer on gold substrate and exposed to hydrogen radicals, acquired using a 633 nm laser excitation.

Despite the lack of a C-H stretching mode in the acquired spectra, the scattering enhancement was evidenced for other phonon modes. **Figure 6.14** compares Raman spectra acquired with the tip off and onto the surface. As a reminder from **Chapter 4**, the *tip-off* configuration consists of conventional far-field Raman spectroscopy, whereas the *tip-on* configuration measures both the far-field and the near-field and locally enhances the excitation field. The background signal emitted by the substrate was removed numerically to keep only the signal from graphene. In **Figure 6.14**, the far-field spectrum (tip off) presents no peak in the measured spectral range except for one at ~2900 cm^{-1}, which could correspond to D+D', whereas the TERS spectrum (tip on) reveals the D, G and 2D bands at frequencies around 1320 cm^{-1}, 1595 $cm^{-1,}$ and 1640 $cm^{-1,}$ respectively. That clearly illustrates the enhancement induced by the gold tip. As mentioned in the literature [40], the TERS enhancement factor is much larger for the D band. By the way, the origin of the D band remains unclear in this case because the D' band is not detected. It could originate from sp^3-C atoms covalently bound to hydrogen atoms, but that would be opposed to the absence of the C-H mode. It most likely arises from structural damage in graphene induced during the transfer process, such as cracks, riddles, or wrinkles, for instance.

6.5 Perspectives: Patterned hydrogenation enabled by electron beam irradiation

As mentioned in **Chapter 3**, graphene hydrogenation can be achieved using e-beam to release hydrogen from a PMMA layer spin-coated on the sample. This technique was reported in the literature [53] and reproduced at LPCNO on graphene flakes exfoliated on a Si/SiO_2 substrate during this PhD (see **Chapter 3**) to compare with the hot filament process. All the details related to the sample's preparation and the e-beam parameters used for hydrogenation are given in **Chapter 2** and **Chapter 3**. The graphene flakes were characterized in Raman spectroscopy with a green laser excitation (532 nm) before and after hydrogenation. Raman spectra after hydrogenation are plotted in **Figure 3.14** (**Chapter 3**), showing the I_D/I_G ratio increases with decreasing acceleration voltage and increasing electron density, which is understandable from a physical point of view.

Figure 6.15 plots the I_D/I_G ratio as function of both the $I_{D'}/I_G$ ratio and the linewidth of the D band (Γ_D). It shows that both Γ_D and $I_D/I_{D'}$ values are roughly constant. The D band linewidth remains close to 20 cm^{-1}, whereas the ratio stays around 13 for every sample, indicating that sp^3-type point defects were induced in the graphene flakes, outperforming the majority of the results obtained with HFCVD. Additionally, no kind of holes were observed in AFM. The I_D/I_G ratio evolves from 0.5 ($V_{AC} = 25\ kV;\ n = 1\ mC/cm^2$) to 4.3 ($V_{AC} = 5\ kV;\ n = 4\ mC/cm^2$), corresponding to hydrogen coverage rates of 0.25% and 3.3% respectively.

Investigation was not pushed further, but as a first insight, this technique looks very promising, especially for the fabrication of sp^2/sp^3 planar heterostructures, as it represents a very convenient method to create sp^3 patterns in a sp^2 graphene layer. The only inconvenience is the presence of remaining PMMA residues at the end of the process, as well as the PMMA cross-linking observed in some experimental conditions (see **Chapter 3**).

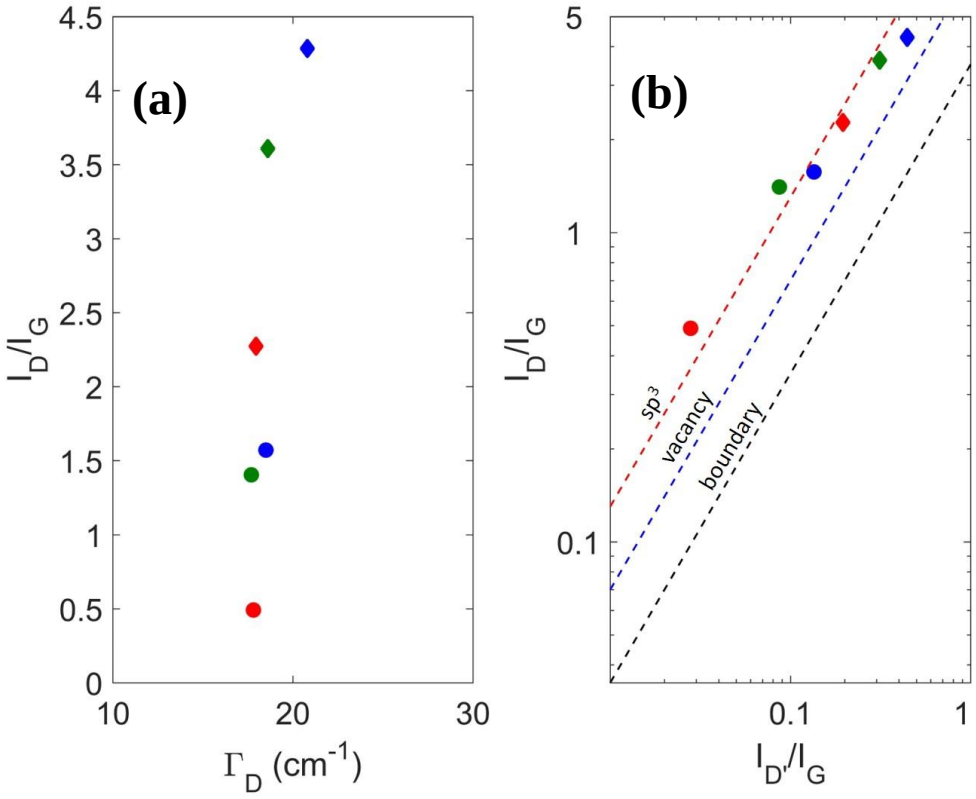


Figure 6.15: (a) I_D/I_G $vs.\Gamma_D$ in linear scale and (b) I_D/I_G $vs.I_D/I_{D'}$ in logarithmic scale for several graphene flakes on Si/SiO$_2$ after being coated by a PMMA layer from which hydrogen was released by electron concentrations of 1 mC/cm^2 (circle) and 4 mC/cm^2 (diamonds) injected by an electron beam accelerated at 5 kV (blue), 15 kV (green) and 25 kV (red). In (b) the dotted lines represent $I_D/I_{D'} = 3.5$ (black), $I_D/I_{D'} = 7$ (blue) and $I_D/I_{D'} = 13$ (red).

Chapter 7 Results and analysis of fluorinated graphene

7.1 Experimental parameters

Graphene samples were prepared at LPCNO in Toulouse with the protocols detailed in **Chapter 2** and fluorinated by our collaborator, Professor Marc Dubois, at the University of Clermont-Ferrand, with the experimental technique described in **Chapter 3**. Different sets of experimental conditions were tested to obtain different fluorine coverage rates. Different key parameters can impact the fluorination, such as the exposure time, the pressure, the temperature, the gas flow, the fluorine concentration, etc… For the sake of simplicity, this work focused on two parameters: (i) the temperature and (ii) the fluorine concentration. The other experimental parameters were not modified from one experiment to another. The flow reactor was evacuated down to approximately 10^{-3} mbar and a constant gas flow of 300 mL/min was maintained for 10 minutes. The fluorination rate was only controlled by the temperature and the fluorine concentration composing the gas mixture. The high fluorine reactivity with graphene enables fluorination at relatively low temperatures compared to hydrogenation. Thus, two temperature values were used in this work, 15°C and 30°C, and the concentrations in the F_2/N_2 gas mixture ranged from 1% to 10%. Intuitively, the fluorination rate should increase with both the temperature and the fluorine concentration.

7.2 Raman spectroscopy

Raman spectroscopy was performed before and after every experiment with a green laser (532 nm) excitation to investigate the changes induced by fluorination. A typical Raman spectrum of a pristine monolayer graphene flake on Si/SiO_2 is shown in **Chapter 4**. The 2D band is fitted by one Lorentzian with a FWHM around 24 cm^{-1}, which is representative of a monolayer. In addition, the absence of D and D' bands witnesses to the good quality of exfoliated graphene. In contrast, these two bands become activated after fluorination due to the creation of defects (see **Figure 7.4**). The nature of these defects can be discussed at low defect density (stage 1 of disorder) from the empirical model established by Eckmann *et al* [71], which is based on the intensity ratio between D and D' bands $I_D/I_{D'}$ (see **Chapter 4**). **Figure 7.1** plots $I_D/I_G \ vs. I_{D'}/I_G$ for several samples in stage 1 after exposure to three different fluorination conditions. Most of the points are located between the line $I_D/I_{D'} = 7$ assigned to vacancies and the line $I_D/I_{D'} = 13$ assigned to sp^3-type defects, meaning that, as for hydrogenation, fluorine chemical reaction with graphene can have two effects: (i) fluorine chemisorption and (ii) C-C bond breaking. Consequently, the model described in **Chapter 5** to determine the fluorine concentration becomes inaccurate since point defects are not necessarily chemisorbed fluorine atoms. One method to solve this issue would be to desorb the fluorine under thermal annealing, as performed on hydrogenated graphene (see **Chapter 6**), to determine its contribution to the D band. However, fluorine thermal stability was not studied in the framework of this PhD due to a lack of time and a small number of fluorinated samples. Instead, AFM imaging (see **7.3**) was performed on some fluorinated graphene flakes, and the results suggest that fluorination induces mostly sp^3 covalent bonding. Based on that, the model described in **Chapter 5** remains a reasonable approximation.

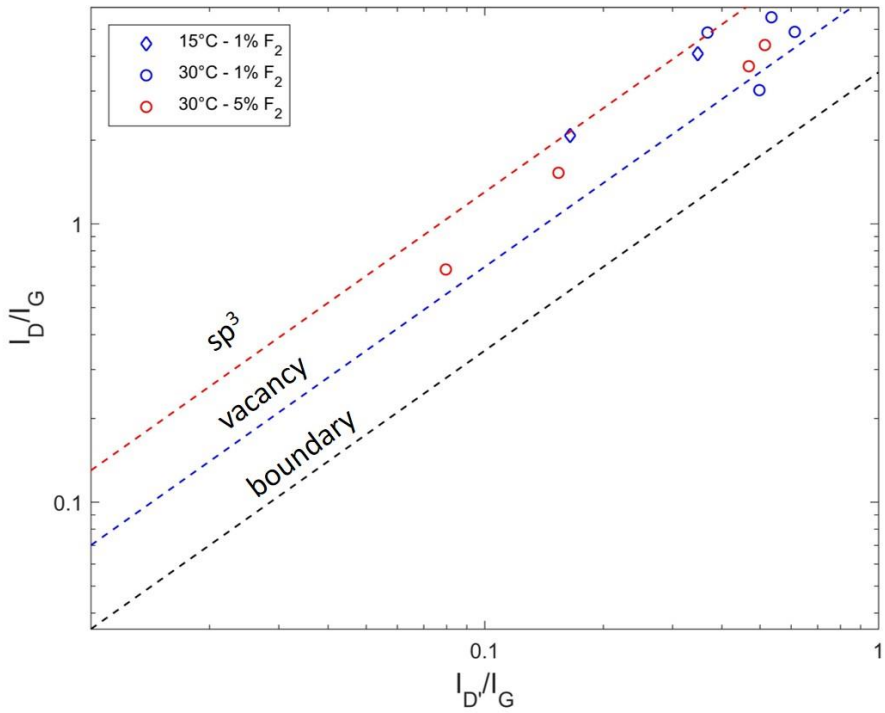


Figure 7.1: Logarithmic plot of I_D/I_G $vs.$ $I_{D'}/I_G$ for several samples in stage 1 after exposure to three different fluorination conditions. The dotted lines represent $I_D/I_{D'} = 3.5$ (black), $I_D/I_{D'} = 7$ (blue) and $I_D/I_{D'} = 13$ (red).

Figure 7.2a plots I_D/I_G vs. Γ_D for various samples and indicates the fluorination conditions they were exposed to, showing that similar conditions can lead to strongly inhomogeneous fluorine coverage rates, as demonstrated in **Chapter 5**. Fluorination is so inhomogeneous that both stage 1 and 2 are observed under similar conditions. Using the model described in **Chapter 5**, the fluorine coverage rate (F_{sp^3}) was determined for each sample, and both I_D/I_G and Γ_D are plotted as function of F_{sp^3} in **Figure 7.2b**. The coverage values are strongly dispersed over a large range and seem to be completely independent of the temperature and the fluorine content in the gas phase. The most extreme example is the case of fluorination at 30°C with a gas flow composed of 5% of F_2. These experimental conditions were applied to a few samples, including some graphene flakes on the same substrate, and the fluorine coverage rates predicted by the model ranged between 0.4% to 42%.

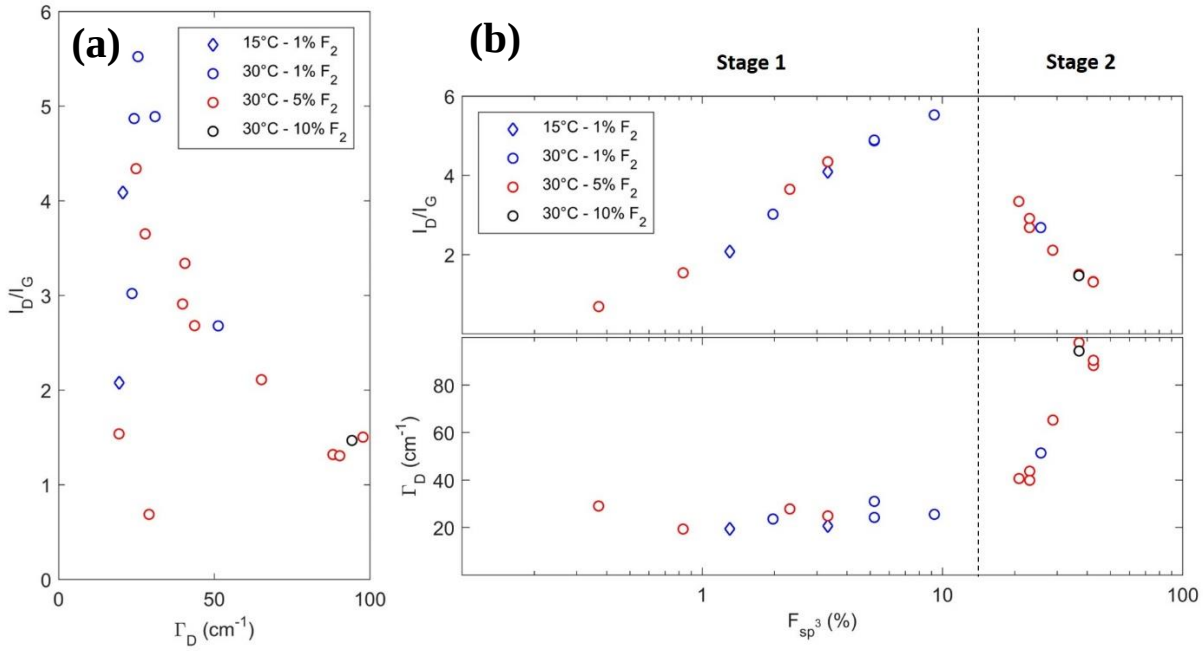


Figure 7.2: (a) I_D/I_G vs. Γ_D for several samples exposed to different fluorination conditions and (b) Fluorine coverage (F_{sp^3}) dependence of I_D/I_G and Γ_D for these samples.

Although it is impossible to assign a typical Raman signature for each fluorination condition, **Figure 7.3a** shows that the Raman spectrum appears to be quite well representative of the fluorine coverage rate. Then, samples with different fluorine contents are plotted together in **Figure 7.3b** to show the evolution of the Raman response from 0% (pristine) to 42.5%. According to **Figure 7.3b**, the transition from stage 1 to stage 2 occurs between approximately 10% and 20%. The spectra assigned to stage 1 exhibit a sharp D band with an increasing relative intensity (I_D/I_G) with the fluorine concentration, and a well-defined D' band detached from the G band. In stage 2, the increasing fluorination rate not only contributes to decreasing the D band relative intensity and increasing its linewidth, but also makes the G and D' bands coalesce to form a single broad band. The 2D band finds its relative intensity decreasing continuously with increasing fluorine content (i.e., increasing disorder) until it almost completely vanishes. A frequency shift of the D band can also be observed, especially in stage 2, due to the modification of the electronic band structure that induces a change in the resonance condition.

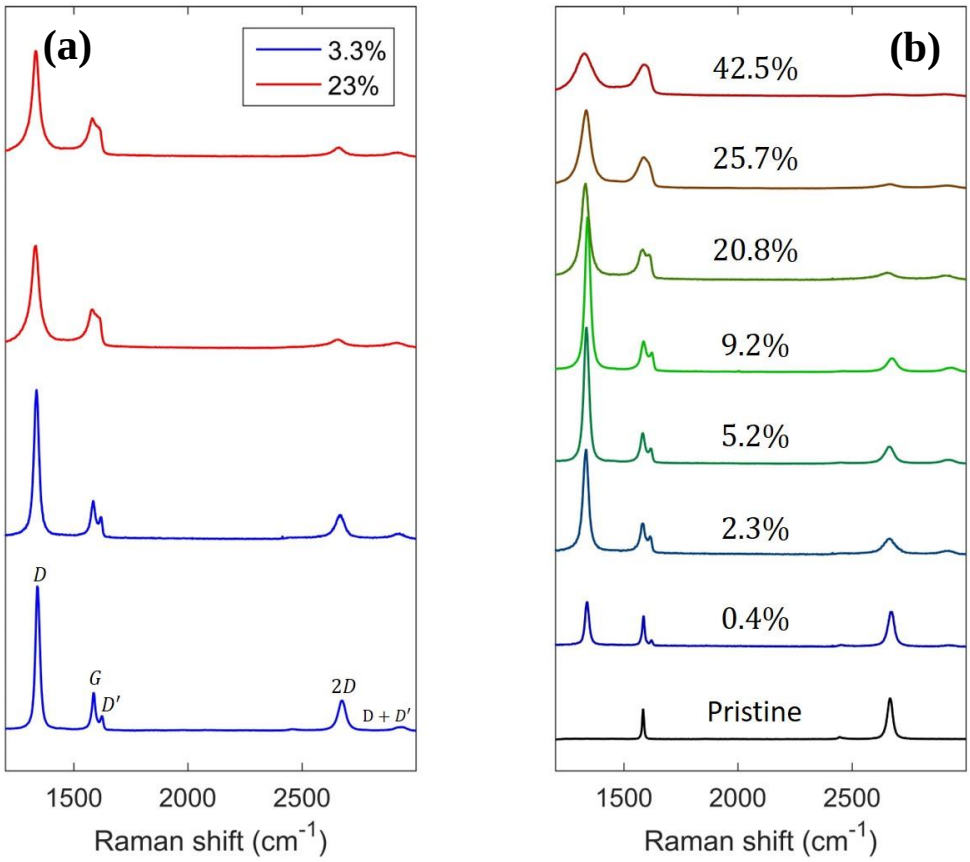


Figure 7.3: (a) Raman spectra corresponding to four graphene samples with fluorine coverage rates of 3.3% (blue) and 23% (red). (b) Raman spectra of eight graphene samples with distinct fluorine coverage rates ranged from 0% to 42.5%. Each spectrum in (a) and (b) is the response to a laser excitation at 532 nm and is normalized to the G band intensity for comparison.

7.3 Atomic Force Microscopy

AFM imaging was performed on a sample (**Figure 7.4**) with a fluorine coverage rate of 3.3% to investigate the surface topography of graphene samples after fluorination. The main concern was to validate the presence of holes in the structure, as for hydrogenated graphene (see **Chapter 6**), that could explain the $I_D/I_{D'} = 8.6$ for this sample. If the etching mechanism is similar to hydrogenation, it is expected that such a significant coverage would lead to the formation of holes (i.e., vacancy clusters) sufficiently large to be resolved by AFM. The horizontal resolution obtained with AFM is hard to define since it depends on both the tip geometry and the scanning parameters. For a 5×5 µm scan with 512×512 points, the image resolution given by the size of one pixel is equal to approximately 9.8 nm. However, this value lacks physical meaning if the tip diameter is larger than the pixel size. As mentioned in **Chapter 4**, the AFM tips used in this work have a radius of curvature of 6 nm (according to the manufacturer App Nano). Thus, since the tip diameter is larger than the pixel size, the horizontal resolution is rather driven by the tip geometry. However, the real

resolution might also be dependent on the scanning velocity and would require some calibration study.

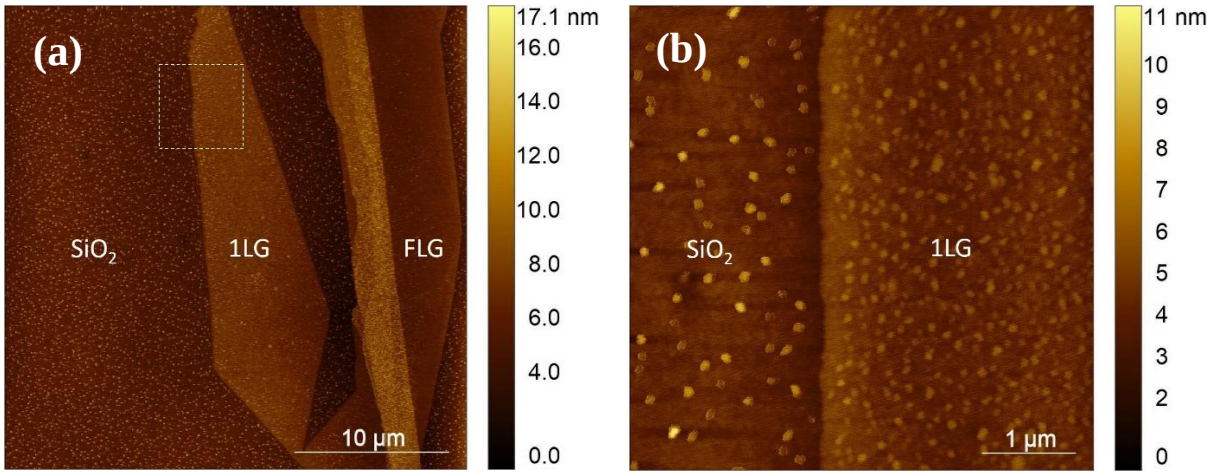


Figure 7.4: (a) 30 × 30 µm AFM image of a fluorinated graphene flake on a Si/SiO_2 substrate with a fluorine content of 3.3%. (b) 5 × 5 µm AFM image corresponding to the framed area in (a).

The two different scans realized on the sample (**Figure 7.4**) do not reveal any hole or other structural damages (cracks, wrinkles, etc…). This observation can lead to different interpretations:

(i) Fluorine reaction induces either spatially isolated vacancies or tiny holes that are not resolved by the AFM.

(ii) Fluorine reaction mostly induces sp^3-type defects, contrary to what is predicted by the empirical model from Eckmann *et al* [71].

Instead of structural damage, the AFM images reveal the presence of residues. Their origin was not investigated, but their size and spatial distribution seem quite inhomogeneous. These residues are also present on SiO_2, though in a reduced concentration, and their presence was also observed in other samples like the one presented in **Figure 7.5**. This sample has an unknown fluorine content because it was selected to make a device for electrical transport measurements, and, consequently, the Raman spectrum was not acquired to avoid the risk of removing fluorine with the laser. At this time, we did not have knowledge of the strong spatial inhomogeneities of fluorination, and we used to consider erroneously that graphene samples exposed to similar conditions would have similar fluorine coverage.

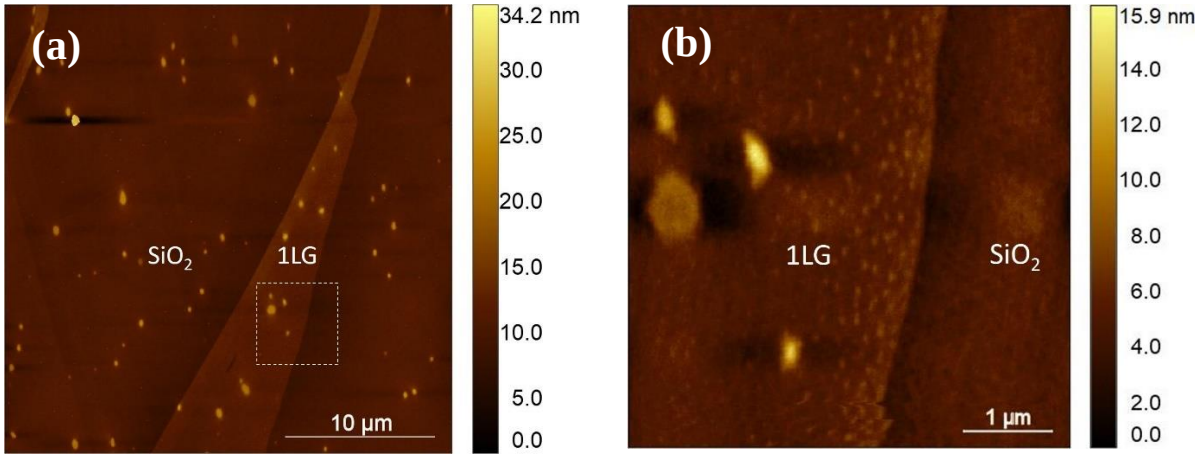


Figure 7.5: (a) 30 × 30 µm AFM image of a fluorinated graphene flake on a Si/SiO_2 substrate with an unknown fluorine content. (b) 5 × 5 µm AFM image corresponding to the framed area in (a).

The differences observed between fluorinated and hydrogenated graphene could be related to the processes since fluorination occurs at relatively low temperature (15-30°C), whereas hydrogenation enabled by HFCVD involves hydrogen radicals created at high temperature (1800-2300°C).

7.4 Tip-enhanced Raman spectroscopy

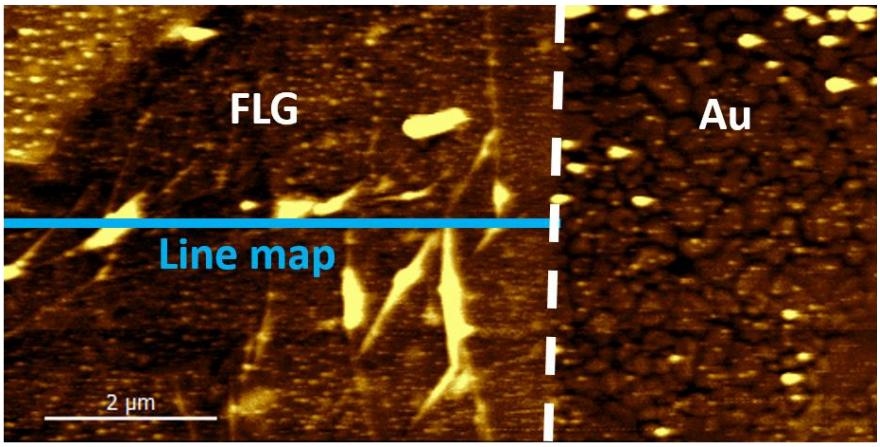


Figure 7.6: AFM image of a few-layer graphene (FLG) flake on a gold substrate. The white dashed line indicates the border between the FLG region and the gold substrate region. A line map was realized in the FLG region, along the blue line.

TERS measurements were performed by Ibrahim Arshad during his internship at CEMES. Samples were prepared by mechanical exfoliation of HOPG on a gold substrate, as described in **Chapter 2**, and measurements were done using a Raman spectrometer coupled with a 532 nm laser and an AFM with Au-coated tips. Unfortunately, for some unexplainable reason, the fluorine appeared to have chemically reacted with the gold substrate, leaving an unexploitable sample. The AFM image in **Figure 7.6** reveals a few-layer graphene flake on a gold substrate after fluorination, showing a wrinkled area corresponding to graphene

and a granular region corresponding to the uncovered gold area.

A line map was realized with both configurations: (i) tip on the surface and (ii) tip off the surface, showing a strong exaltation of the Raman signal in the near-field region. However, the near-field spectra are inhomogeneous and present many unidentified peaks. Two examples are given in **Figure 7.7**. The sharp peak at 868 cm^{-1} in **Figure 7.7a** is not a cosmic ray since it is observed in both near-field and far-field spectra. The molecular signatures in this range correspond only to ozone, to be confirmed with other samples. On **Figure 7.7b**, the broad band at 1305 cm^{-1} could be attributed to a broad D band or another unidentified peak.

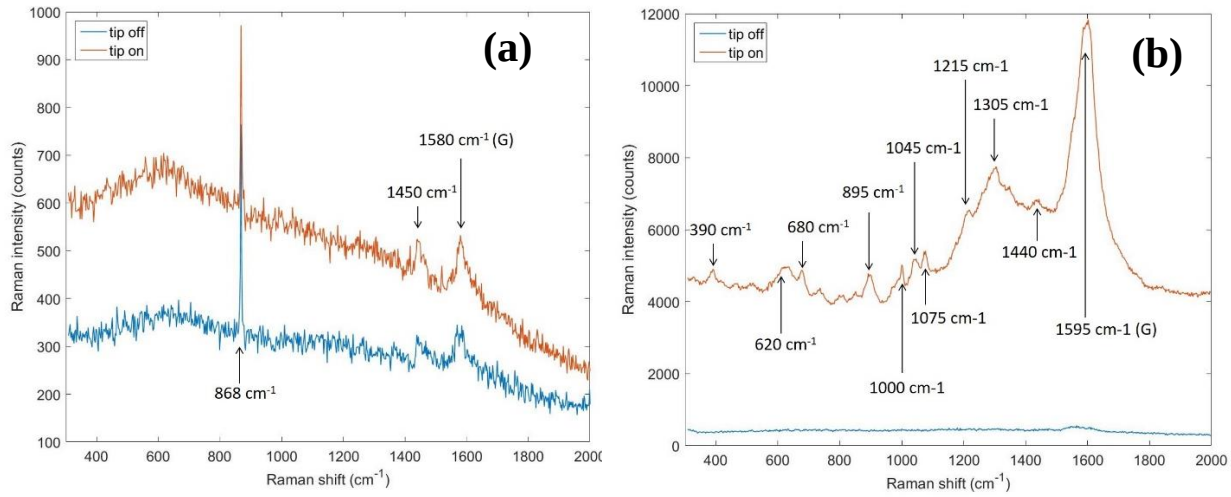


Figure 7.7: Two selected Raman (blue) and TERS (red) spectra from the line map represented in Figure 7.6.

7.5 Electrical transport measurements

7.5.1 Devices

Two fluorinated samples were selected for electrical transport measurements:

(1) Sample 1: A graphene Hall bar (**Figure 7.8a**) fabricated with the protocol described in **Chapter 2** before being exposed for 10 minutes to a gas flow composed of 3% of F_2. The temperature of the gas could not be determined here due to an experimental issue.
(2) Sample 2: A graphene flake exposed for 10 minutes to a gas flow composed of 1% of F_2 at 30°C.

The fluorine content is unknown for these two samples because Raman spectroscopy was not performed for the reason mentioned in paragraph **7.3**. At this time, basing our intuition on the I_D/I_G ratio of other graphene flakes exposed to similar fluorination conditions, we were arbitrarily expecting a "reasonable" fluorine concentration that modifies graphene's electronic properties without inducing a metal-insulator transition.

For sample 2, the graphene flake was first capped with a hexagonal boron nitride (h-BN) flake before being patterned to avoid any risk of defluorination during the device fabrication. The different fabrication steps required to create a graphene device involve different thermal annealing, resist deposition, and chemical cleaning with solvents (see **Chapter 2**). Since fluorine stability was not studied in this work, the safest solution was to passivate the fluorinated graphene flake with an insulator. h-BN was found to be convenient for this purpose since it is a vdW material like graphene that can be easily transferred from one substrate to another and is a good electrical insulator. h-BN from HQ graphene was exfoliated on Si/SiO_2 substrate and transferred on top of the fluorinated graphene flake using the hot pick-up technique [41]. Then, the fluorographene/h-BN heterostructure was patterned and connected to metallic electrodes with the protocol described in **Chapter 2**. The resulting device is presented in **Figure 7.8b**. Due to the presence of h-BN on top of the sample, the profile of the heterostructure was customized to allow one-dimensional electrical contact [111].

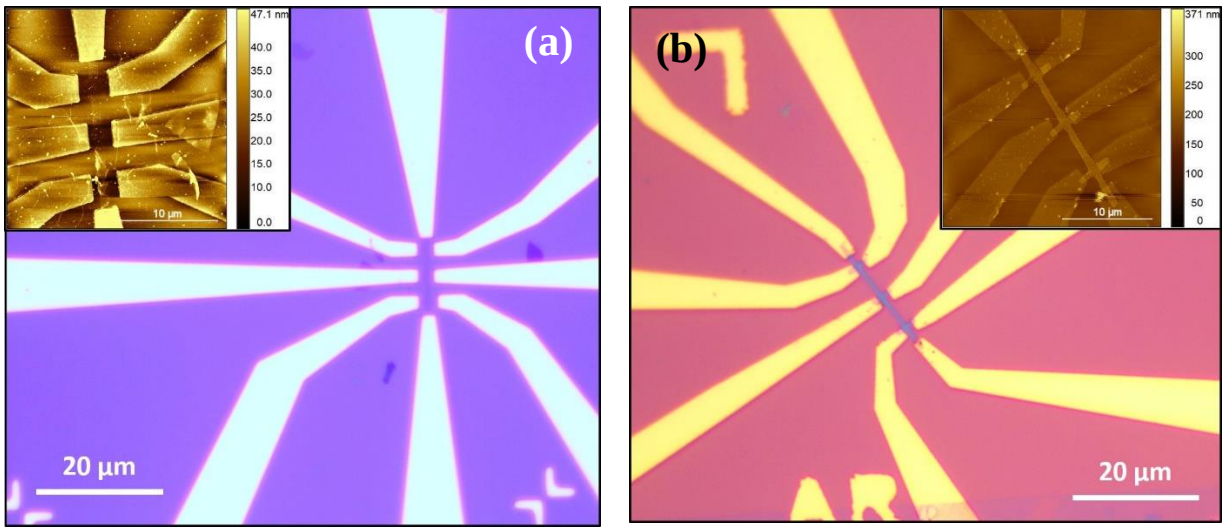


Figure 7.8: Optical and AFM (insets) images of (a) sample 1 and (b) sample 2.

The two devices presented in **Figure 7.8** are triple Hall crosses, which means that they have two longitudinal electrodes used for current polarisation and six transverse electrodes for voltage measurements. This design allows to have access to the longitudinal resistivity *via* four-probe measurement and, in the presence of a perpendicular magnetic field, the Hall voltage.

7.5.2 Measurements

The electronic properties of the two fluorinated graphene devices described in **7.5.1** were investigated via electrical measurements under an out-of-plane magnetic field and at different temperatures ranged from 10 to 300 K using a PPMS (see **Chapter 4**). For each temperature, the longitudinal conductivity σ_{xx} and the Hall sensitivity normalized in current $S_I = \frac{\rho_{xy}}{B}$ were measured for different gate voltages. The Hall effect was measured for sample 1 under 100 mT. Unfortunately, sample 2 appeared to be strongly p-doped, making the Hall voltage measurement ambiguous because only the p-doped regime was completely visible within the range of applied gate voltages. For this reason, the following result analysis does not consider

the Hall sensitivity for this sample. The residual p-doping in this case might be rather caused by fluorination than by trapped charges in SiO_2. This hypothesis seems quite reasonable because fluorine is more electronegative than carbon, meaning that the electron involved in the covalent bond should be localized close to the fluorine, leaving a hole on graphene's π-cloud.

7.5.2.1 Sample 1

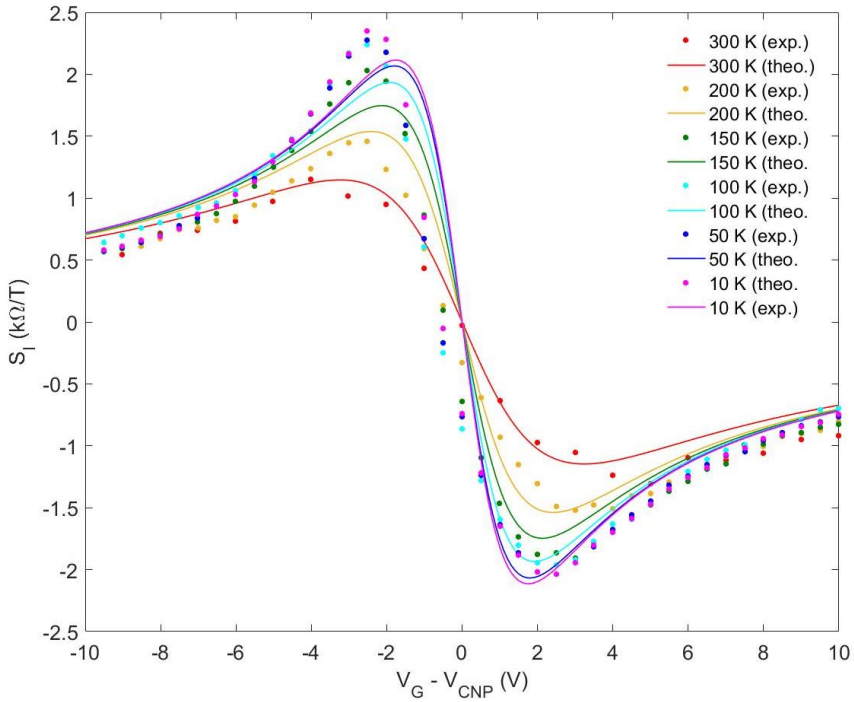


Figure 7.9: Comparison between experimental (dots) and theoretical (lines) curves of the Hall sensitivity normalized in current for different temperatures.

The gate voltage dependence of S_I is plotted in **Figure 7.9** for T = 10, 50, 100, 150, 200 and 300 K. It shows that the absolute values of the S_I maximum and minimum tend to increase when the temperature decreases. As a reminder of **eq. 4.53** (**Chapter 4**), the absolute value of S_I is related to the residual charge carrier density by $S_{I,max} \approx |1/(2e\{n_0 + p_O\})|$. By consequence, the experimental data plotted in **Figure 7.9** reveal that the residual charge carrier density increases with the temperature, due to thermal doping. In pristine graphene, the residual charge carrier density evolves quadratically with the temperature, as described by **eq. 4.38** (**Chapter 4**). According to Li's model [78], when disorder is introduced in graphene, the temperature dependence stays quadratic but is modified by the introduction of a parameter *s* representing the degree of disorder (see **eq. 4.57** in **Chapter 4**). To be more accurate, *s* represents the strength of the electronic potential fluctuation caused by the electron-hole puddles, which is representative of disorder. Thus, the temperature-dependent expression of the Hall sensitivity at low magnetic field (μB << 1) derived from **eq. 4.52** (**Chapter 4**) is written:

$$S_I(T) = -\frac{C_g(V_g - V_{CNT})}{e\left(\left[C_g(V_g - V_{CNP})\right]^2 + (n_0(T) + p_0(T))^2\right)} \qquad \text{(eq. 7.1)}$$

Injecting **eq. 4.57** into **eq. 7.1** gives:

$$S_I(T) = -\frac{C_g(V_g - V_{CNT})}{e\left(\left[C_g(V_g - V_{CNP})\right]^2 + \left[\frac{s^2}{\pi(\hbar v_F)^2} + \frac{\pi}{3}\left(\frac{k_B T}{\hbar v_F}\right)^2\right]^2\right)} \qquad \text{(eq. 7.2)}$$

For graphene on Si/SiO_2, the Fermi velocity needs to be renormalized to $1.2 \times 10^6\ m \cdot s^{-1}$ to consider the electron-electron interactions, as demonstrated in previous works [5]. An oxide thickness of 285 nm corresponds to a gate capacity of 120 µF. Then, the experimental curves in **Figure 7.9** are fitted by **eq. 7.2** with s = 0.051×e. The curves from 10 to 150 K do not perfectly fit the experimental points at the maximum sensitivity. This may be due to the thermal instability of electrical contacts in this temperature range. In contrast, the minimum sensitivity points are quite well reproduced by the model. Then, the residual charge carrier concentration at a given temperature can be approximated by the average absolute value between the maximum and the minimum Hall sensitivity points:

$$n_0(T) + p_O(T) \approx \frac{1}{4e}\left(\frac{1}{S_{I,max}(T)} + \frac{1}{\left|S_{I,min}(T)\right|}\right) \qquad \text{(eq. 7.3)}$$

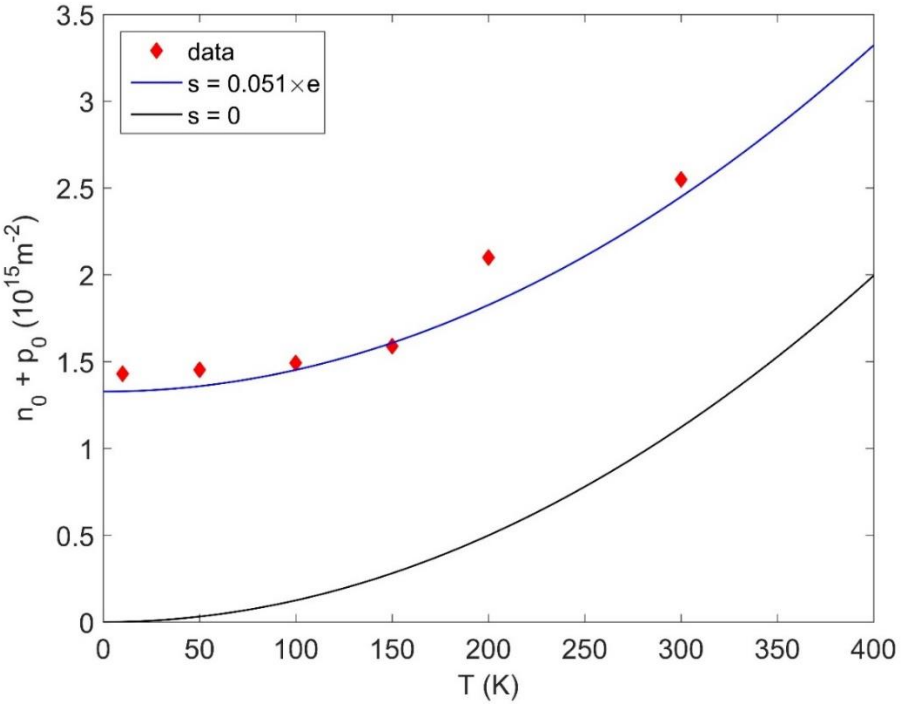


Figure 7.10: Temperature dependence of the residual charge carrier density plotted for experimental data (diamonds) and theorical values (lines) obtained with Li's model using *s* = 0.051×e and s = 0.

Figure 7.10 compares the experimental values with Li's model for *s* = 0.051×e and s = 0 (pristine graphene). The data points fit with a rather good agreement with the theoretical curve. It can be concluded that the temperature dependence on the residual charge carrier's concentration is reasonably well described by Li's

model with a disorder parameter s = 0.051×e, which is quite significant. This disorder is embodied by electron-hole puddles and is expected to have an impact on the charge carrier's mobility, which can be determined by measuring the gate voltage dependence of the longitudinal conductivity σ_{xx} (**Figure 7.11**). These measurements reveal a linear dispersion of the conductivity with the gate voltage below -5 V and above 5 V corresponding to high doping and one type of charge carrier, i.e., hole or electron. This behaviour suggests that the mobility is mostly driven by long-range scattering (i.e. charge impurities). In this case, the line slope is given by $C_g\mu$. The slope (i.e. the mobility) happens to slightly change with the temperature and the type of carriers. Considering the p-doped regime ($V_g < V_{CNP}$) that appears to have the lowest temperature dependence, the average value of the mobility can be approximated to $0.25\ m^2 \cdot V^{-1}s^{-1}$. As a reminder, the mobility of the pristine graphene sample presented in **Chapter 4** was about $1.6\ m^2V^{-1}s^{-1}$, which is around six times larger. It means that, as expected, fluorination induces a global deterioration of the mobility.

However, an inconsistency appears when comparing the experimental data with the theoretical values for $\sigma_{xx}(T)$ derived from combination of **eq. 4.43** and **eq. 4.57** (**Chapter 4**) such as:

$$\sigma_{xx}(T) = e\mu\sqrt{\left[\frac{C_g}{e}(V_g - V_{CNP})\right]^2 + \left[\frac{s^2}{\pi(\hbar v_F)^2} + \frac{\pi}{3}\left(\frac{k_B T}{\hbar v_F}\right)^2\right]^2} \qquad \text{(eq. 7.4)}$$

Figure 7.11a compares the measurements of the longitudinal conductivity σ_{xx} at T = 10, 200 and 300 K with the corresponding theoretical curves obtained with **eq. 7.4** using the parameters defined previously and a mobility of $0.25\ m^2V^{-1}s^{-1}$ determined to fit approximately the linear dispersion observed in the experiment. It demonstrates that **eq. 7.4** fails to reproduce experimental data. The issue does not come from the mobility value because the experimental slope is reasonably well reproduced. Using a higher mobility value to fit the minimal conductivity would fail to reproduce the slope. Another approach could be to consider a larger residual charge carrier density, but this would fail to reproduce the Hall effect measurements. The only reasonable explanation for this inconstancy is the presence of some conductive residues acting as parallel resistances on the device. This hypothesis seems quite acceptable regarding the optical and AFM images of the device (**Figure 7.8a**) that show some remaining graphite flakes as well as some kind of contamination. By consequence, the inconstancy can be raised by introducing an offset value of $9 \times 10^{-5}\ \Omega^{-1}$ in **eq. 7.4** to mimic this parasite conductivity (**Figure 7.11b**).

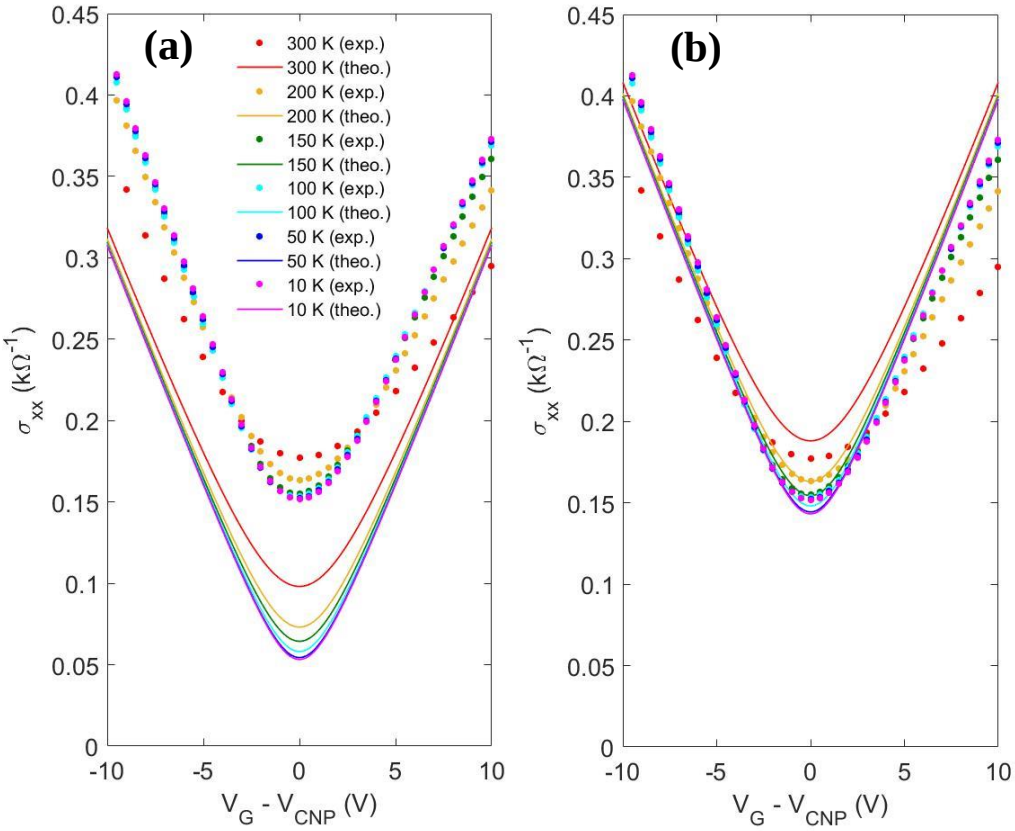


Figure 7.11: Comparison between experimental (dots) and theorical (lines) curves of longitudinal conductivity for different temperatures without (a) and with (b) consideration of the parasite conductivity term.

Experiments are still not perfectly reproduced by the corrected form of **eq. 7.4** because the mobility is considered constant and equal for holes and electrons. In reality, charge carriers' mobility is dependent on the temperature and can be different for holes and electrons. On one hand, the temperature dependence of the mobility is quite difficult to determine because it can be dependent on the charge carriers' interactions with phonons and defects [56]. On the other hand, using different mobility values for holes and electrons has a strong impact on the expression of the conductivity tensor derived from the two-channel model. In particular, the terms $\mu(n+p)$ and $\mu^2(n-p)$ become respectively $n\mu_e + p\mu_h$ and $n\mu_e^2 - p\mu_h^2$, which is quite embarrassing to connect the conductivity tensor components to the gate voltage. In addition, the Hall resistance becomes dependent on the charge carriers' mobilities. For the sake of simplicity, we stay in the approximation $\mu_e = \mu_h = \mu$, thereby ignoring the asymmetry of the conductivity.

7.5.2.2 Sample 2

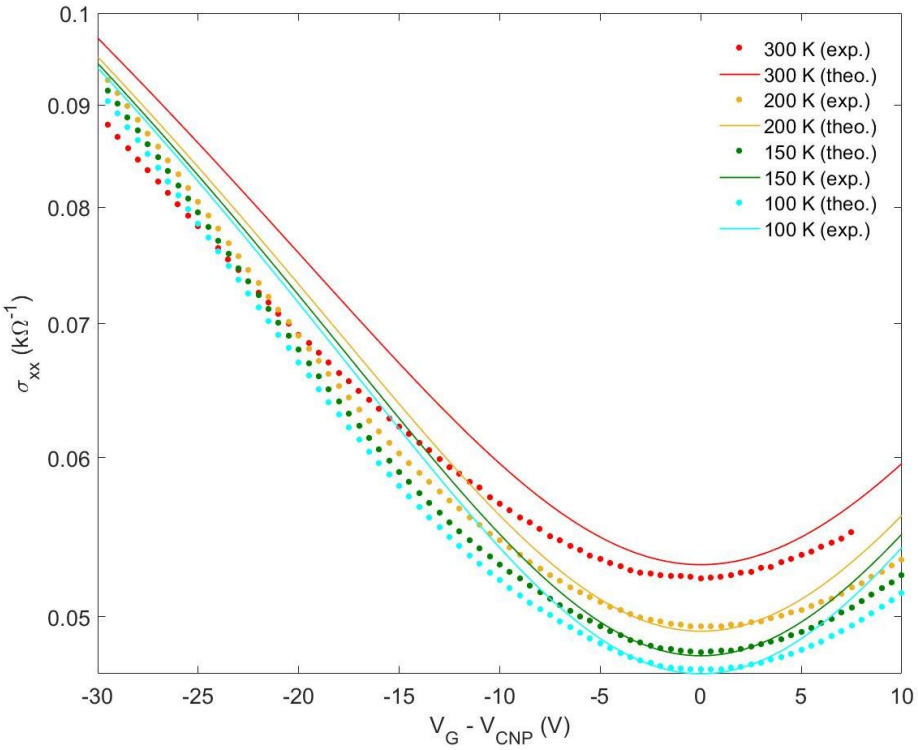


Figure 7.12: Comparison between experimental (dots) and theoretical (lines) curves of longitudinal conductivity for different temperatures.

The gate voltage dependence of the longitudinal conductivity is plotted in **Figure 7.12** for T = 100, 150, 200, and 300 K, showing a linear behaviour over a large gate voltage range, signifying that the mobility is driven by long-range defects. The long-range mobility extracted from the average linear slope in the p-doped region is about $0.022\, m^2 \cdot V^{-1}s^{-1}$, which is approximately ten times lower than sample 1. In addition, the temperature dependence can be reasonably well reproduced by Li's model with a disorder parameter *s* = 0.16×e, which is more than three times larger than the value determined for sample 1. All of this suggests that this sample has a larger disorder degree, i.e. larger fluorination rate, than sample 1.

As mentioned previously, Hall effect measurements were not convincing for this sample, which means that the residual charge carrier density had to be extracted from the minimum conductivity given by the expression of σ_{xx} (**eq. 7.4**) at CNP:

$$\sigma_{xx,min}(T) = e\mu(n_0(T) + p_0(T)) \qquad \text{(eq. 7.5)}$$

Or equivalently:

$$\sigma_{xx,min}(T) = e\mu\left(\frac{s^2}{\pi(\hbar v_F)^2} + \frac{\pi}{3}\left(\frac{k_B T}{\hbar v_F}\right)^2\right) \qquad \text{(eq. 7.6)}$$

Figure 7.13 compares the residual doping values extracted from experimental data with theoretical curves from Li's model for s = 0.16×e (this sample), s = 0.051×e (sample 1) and s = 0 (pristine graphene), showing a reasonably good agreement between measurements and **eq. 7.6** evaluated at s = 0.16×e.

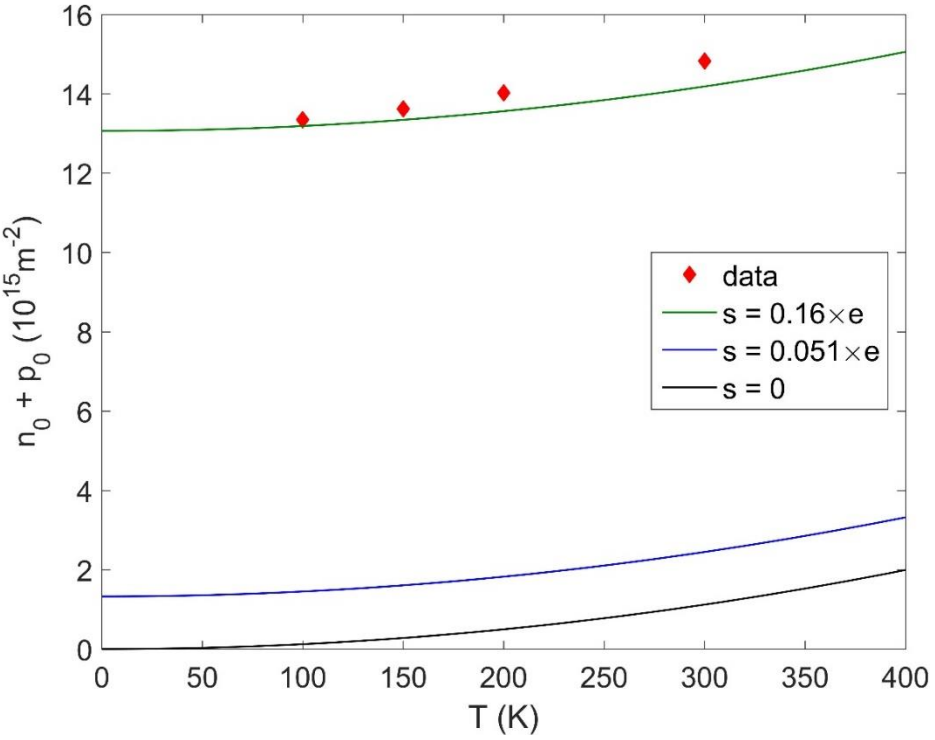


Figure 7.13: Temperature dependence of the residual charge carrier density plotted for experimental data (diamonds) and theoretical values (lines) obtained with Li's model using s = 0.16×e, s = 0.051×e, and s = 0.

Another approach to fit the data is to consider a possible renormalization of the Fermi velocity caused by a modification of the Dirac cone happening for sufficient fluorine content. So far, v_F was considered as a fixed parameter equal to $1.2 \times 10^6\, m \cdot s^{-1}$, but considering different values could improve the data fit. **Figure 7.14** compares the experimental values of the charge carrier's concentration with the Li's equation for two different couples of parameters $\{s\,; v_F\}$, showing that using $v_F = 0.9 \times 10^6\, m \cdot s^{-1}$ and $s = 0.12 \times e$ gives a better approximation of the experiments.

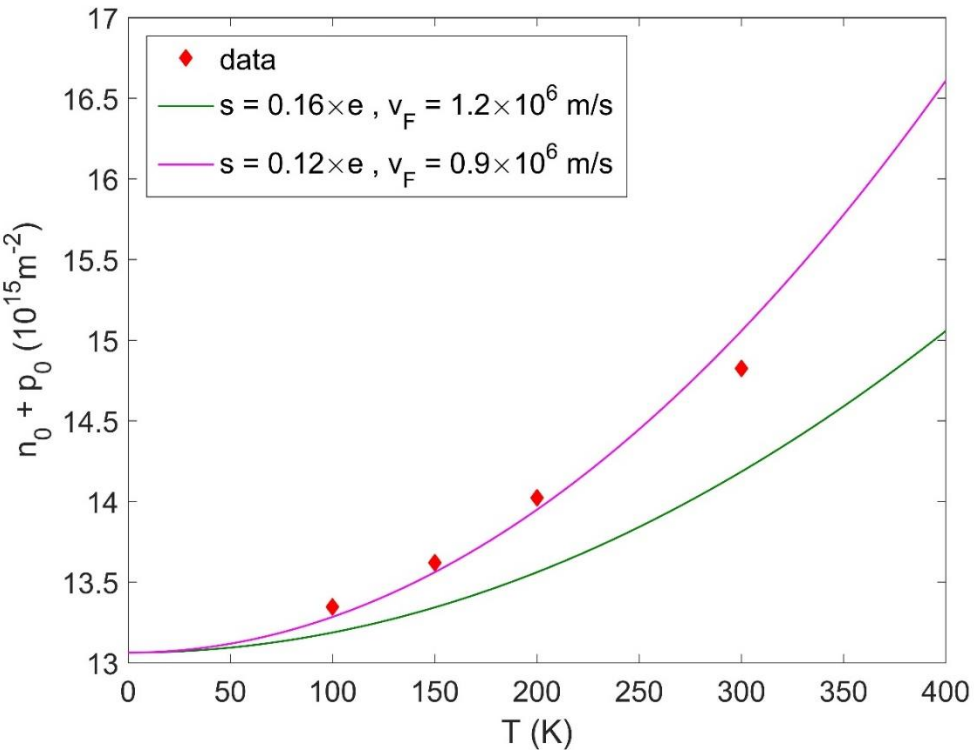


Figure 7.14: Temperature dependence of the residual charge carrier density plotted for experimental data (diamonds) and theoretical values (lines) obtained with Li's model using two distinct couples of parameters $\{\mathbf{s}\,;\mathbf{v_F}\}$.

Since this deterioration of the Fermi velocity could be explained by a modification of the electronic band structure, the possibility of having induced either a bandgap or a pseudo-bandgap could be considered. However, as demonstrated by **Figure 7.15**, the experimental values of the maximum resistivity $\rho_{max} = 1/\sigma_{min}$ do not follow T^{-1} nor $T^{-1/3}$ exponential laws, meaning they are not described by thermal activation (**eq. 4.54** from **Chapter 4**) nor by Mott's law (**eq. 4.56** from **Chapter 4**). In other words, this fluorinated graphene device keeps a semi-metallic nature (absence of energy gap) and does not present the signature of hopping conduction via localised states. Another possible explanation could be that this sample presents a small bandgap hidden by the strong electronic potential fluctuations given by the disorder parameter *s*.

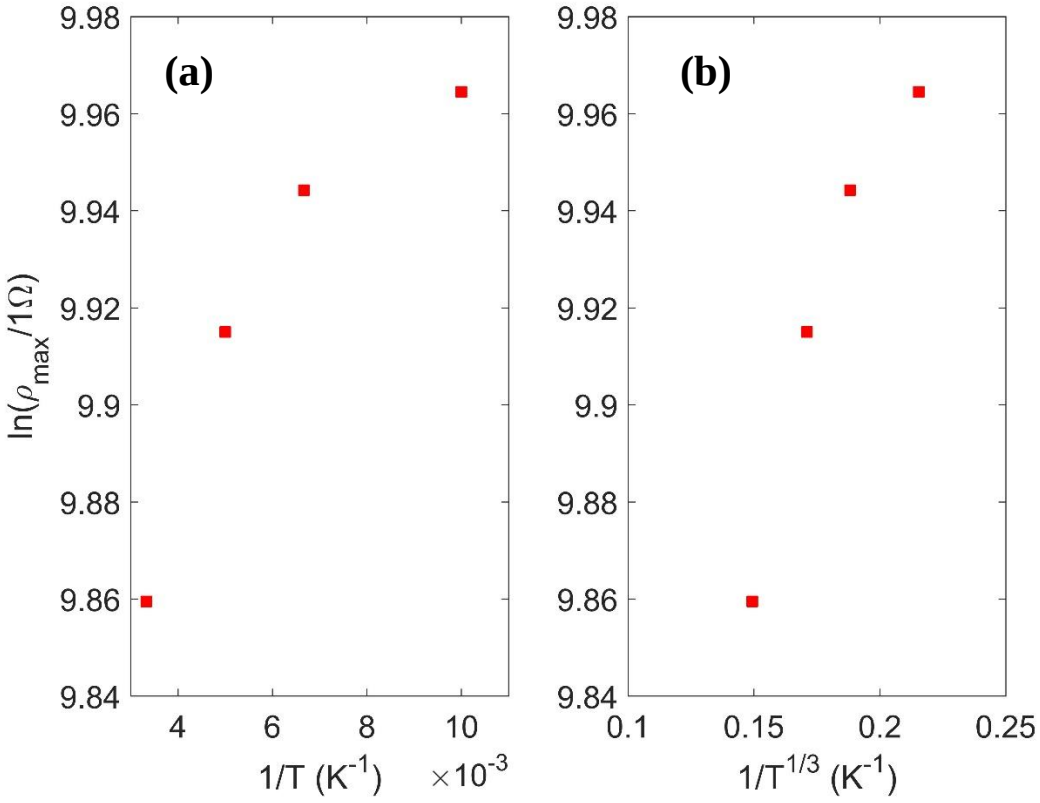


Figure 7.15: Evidence of the non-exponential behaviours of the maximum experimental resistivity values in contrast to (a) thermal activation law and (b) Mott's law. If one of these laws were able to reproduce the data, the red points would be aligned on a straight line, which is obviously not the case here.

These Fermi level fluctuations likely originate from an inhomogeneous fluorination. Some fluorine clusters might form highly p-doped regions, whereas some other areas characterized by a low fluorine content should be more electrically neutral.

Additionally, DFT calculations of the electronic band structure of fluorinated graphene were realized in our consortium and compared with similar calculations for hydrogenated graphene. The results show that, contrary to hydrogenation, fluorination induces a particular band structure where the Fermi level is in the conduction band. Nonetheless, in the case of a large and homogeneous fluorine coverage rate, an activation barrier should be visible via electronic transport measurements at different gate voltages, as performed in this study. However, since the experimental data are interpreted by a strong disorder induced by inhomogeneous fluorination, the absence of an activation barrier might be explained by some alignments of Fermi levels from different doped regions when performing gate voltage scans.

7.5.3 Perspectives

These two fluorinated graphene devices were fabricated and characterized at the end of this PhD, leaving not enough time to go further in the characterization and analysis. Additional measurements and more advanced numerical simulations based on the Boltzmann formalism and finite element method, as performed in [5] by L. Petit, a former PhD student at the LPCNO, would be required for a complete analysis and a better understanding of the electronic properties induced by fluorination. This work is still in progress, and additional samples are being prepared to provide more experimental data.

Conclusion & Perspectives

The chemisorption of hydrogen and fluorine atoms on one side of a supported graphene monolayer was investigated experimentally during this PhD with the main objective to open a band gap in the graphene electronic structure. The preparation of the graphene samples, as well as their characterization, was entirely carried out at CEMES and LPCNO. The samples were mostly characterized in Raman spectroscopy, but some were also analyzed with atomic force microscopy (AFM), tip-enhanced Raman spectroscopy (TERS), and electrical transport measurements. Two kinds of substrates were used depending on the characterization:

(1) Si substrates with 285 nm of SiO_2 to perform electrical transport measurements, as well as to enhance the optical contrast and the Raman signal by interferential effects.
(2) Ultra-flat gold substrates to enhance the TERS signal.

Graphene was transferred to these substrates by mechanical exfoliation of highly oriented pyrolytic graphite (HOPG), using the "scotch tape" technique. For ultra-flat gold substrates, some samples were also prepared by polymer-assisted wet transfer techniques of large-area graphene grown by chemical vapor deposition (CVD). To carry out the electrical transport measurements, devices were fabricated from graphene flakes on Si/SiO_2, using conventional microfabrication techniques.

Hydrogenation and fluorination processes were carried out in collaboration with two specialists: Prof. Fabrice Piazza from the PUCMM at Santiago de los Caballeros (Dominican Republic) and Prof. Marc Dubois from the University of Clermont-Ferrand (France). I had the opportunity to spend a few months at the PUCMM and a few days at the University of Clermont-Ferrand. The hydrogenation process consists of a hot filament CVD (HFCVD) process, where H_2 molecules are dissociated by thermal activation at very high temperature (>1800°C) inside a vacuum chamber. The fluorination process occurs at much lower temperatures (15-30°C) due to the high reactivity of fluorine. It is carried out inside a gas flow reactor and uses a gas mixture composed of 1 to 10 % of F_2 diluted in N_2.

In parallel, two other hydrogenation processes were tested for comparison:

(1) The hydrogen beam process under ultra-high vacuum (UHV), which was developed at Aarhus University (Denmark) by the team of Prof. Liv Hornekaer. Unfortunately, due to experimental issues during my visit to their laboratory, only a few samples could be hydrogenated, and with a very low coverage rate.
(2) The patterned hydrogenation enabled by e-beam, which consists of releasing hydrogen locally from specific areas of a PMMA film on top of a graphene layer using an e-beam. This was tested at LPCNO, and the first results seem very promising.

Raman spectroscopy was used to investigate the modifications in graphene's properties induced by hydrogenation and fluorination. Since graphene is a semi-metal and has a strong electron-phonon coupling, Raman scattering is resonant and sensitive to the electronic band structure, as well as to Fermi level fluctuations. By consequence, the analysis of the Raman spectrum allows us to determine many properties such as doping, strain, or the number of layers. In particular, Raman spectroscopy was constantly used to confirm the monolayer nature of graphene flakes, even those selected by optical contrast on Si/SiO_2

substrates. In addition, the frequency shift ratio between the 2D and the G bands $\frac{\Delta\omega_{2D}}{\Delta\omega_G}$ allows us to evaluate doping and mechanical strain in graphene. In the presence of defects (i.e., any translational symmetry breaking in the electronic potential), the charge carriers can be scattered elastically, leading to defect-activated modes: D and D' bands. According to a phenomenological model developed by Casiraghi *et al* [71], their intensity ratio $\frac{I_D}{I_{D'}}$ is representative of the nature of the defects at low defect density (stage 1). This model was frequently used for the analysis of the Raman spectra of hydrogenated and fluorinated graphene samples, since sp^3-type defects are attributed to a specific $\frac{I_D}{I_{D'}}$ ratio. For the determination of the defect density, an empirical model developed by Lucchese *el al* [47], based on point defects induced by ion bombardment, considers the intensity ratio between the D and the G bands $\frac{I_D}{I_G}$. However, this PhD allowed for the identification of three issues in this widely used model:

(1) One of the model's equations presents an erroneous term, making the model lack physical meaning.
(2) The calibration of the model's parameters is very challenging in the case of graphene functionalization, as it was discovered during this PhD that both hydrogenation and fluorination can be inhomogeneous.
(3) Since the model was developed for point defects created by ion bombardment, it is not directly applicable to functionalization, which creates a different kind of point defects.

By consequence, this PhD includes the development of a new point-defect, adapted to sp^3-type defects, where the parameters are determined theoretically. In this model, the sp^3-type point defect is represented by three concentric regions around the sp^3 carbon atom: (i) deactivated (sp^3), (ii) structurally distorted, and (iii) activated regions. The D band signal originates from both the distorted and the activated region. Thus, the $\frac{I_D}{I_G}$ ratio increases with increasing sp^3 coverage rate up to approximately 10 % due to the increase of the surface fraction contributing to the D band and the decrease of the sp^2 surface fraction at the origin of the G band. At some point, when the sp^3 coverage exceeds 10 %, significant overlaps between regions cause the $\frac{I_D}{I_G}$ ratio to drop until it stabilizes to an asymptotic value at a coverage of 100 %. In addition, due to the formation of large sp^3 domains responsible for the spatial confinement of phonons within small sp^2 domains, the linewidth of the D band increases. This effect allows us to discriminate similar $\frac{I_D}{I_G}$ values attributed to different coverage rates, thereby identifying three stages of disorder. Our model was found to be in good agreement with experimental data reported in the literature.

Raman spectroscopy was also used to study the stability of hydrogen atoms grafted to graphene (i) undergoing thermal annealing under an inert atmosphere or (ii) exposed to laser illumination. Under thermal annealing, the hydrogen remains grafted to graphene up to approximately 250°C. Above this temperature, the hydrogen is released, and the graphene partially recovers. This result indicates that a hydrogenated graphene device could be fabricated without decreasing the hydrogen concentration. However, the experiments were performed under an inert atmosphere, which is generally not the case in standard microfabrication protocols. Two solutions were found to overcome this issue:

(1) Device fabrication before hydrogenation. However, some resist residues might remain after the fabrication process, which is not ideal for hydrogenation.
(2) Capping the hydrogenated graphene layer before starting the device fabrication. This can be done, for

instance, by transferring a flake of hexagonal boron nitride (h-BN) on top of the hydrogenated graphene flake. However, if the stacking process is performed with the hot pick-up technique, which involves heating the sample to 180°C, it is highly recommended to proceed with heating only once the h-BN is stacked on top of the graphene. Otherwise, hydrogen might be desorbed before capping the graphene.

Concerning laser illumination, it was found that hydrogen remains stable up to a laser power of approximately 2 mW. Above this value, extended laser exposure times are likely to desorb the hydrogen in the region illuminated by the laser spot. However, the experiments were carried out on a sample with a specific hydrogen coverage rate, and the laser power limit might change with the hydrogen content, since it should depend on the thermal conductivity. Nonetheless, this result suggests that Raman measurements on hydrogenated graphene should rather be carried out with a relatively low laser power.

Tapping mode AFM was used in some of the hydrogenated and fluorinated samples to investigate the change in the surface topography. For hydrogenated samples, this technique provided clear evidence of an etching mechanism happening simultaneously with hydrogen chemisorption. The formation of circular nanopores was observed for low hydrogen exposure times, and their growth mechanism was deduced from images of samples exposed for extended times. The origin of this etching mechanism was investigated by molecular dynamics calculations performed in our consortium, but remains unclear. Nothing similar was observed on fluorination.

A few TERS measurements were carried out on some hydrogenated and fluorinated graphene layers deposited on ultra-flat gold substrates, with the ambition to detect the C-H and C-F vibrational modes. However, although the Raman scattering was enhanced by the tip, the Raman peaks corresponding to these modes could not be detected. Moreover, fluorine was found to react with the gold substrate, causing serious damage to the sample.

Finally, electrical transport measurements were performed at various temperatures, using a physical property measurement system (PPMS), on several fluorinated graphene devices. The gate voltage (V_g) dependence of the longitudinal conductivity (σ_{xx}) was investigated to determine the mobility (μ) as well as the residual charge carrier concentration ($n_0 + p_0$). In parallel, the V_g dependence of the transverse voltage under an out-of-plane magnetic field was investigated to determine the Hall sensitivity, which is closely related to $n_0 + p_0$ and is independent of μ. The results indicate that the charge carriers' mobility is strongly deteriorated by fluorination, which contributes to decreasing the conductivity. In addition, the evolution of $n_0 + p_0$ with the temperature was fitted with a disorder-induced electron-hole puddle model from the literature, and allowed us to extract the disorder amplitude, thereby confirming that fluorination is inhomogeneous and induces strong spatial doping fluctuations (i.e., electron-hole puddles). Consequently, the temperature dependence of the maximum resistivity is not explained by a thermal activation law nor by Mott's law, suggesting that fluorination may not have induced a bandgap. However, more samples with a larger range of fluorine coverage are needed to go further in this study.

The future extensions are relatively broad and cover all the areas explored in this thesis. Firstly, adapting the presented HFCVD reactor by adding one or two atomic hydrogen guns identical to those used by Liv Hornekaer's group to hydrogenate both sides at once and comparing this to the current method would provide more parameters and better control. During this work, we have positioned a molybdenum (Mo) plate between the filaments and the sample, which greatly reduces the temperature due to radiation. We

have not yet tested resist masking with this cover, which is an interesting possibility for further studies. We have also used a shadow mask for graphene electrodes on polyether ether ketone (PEEK), and this could also be tested with hydrogenation. Finally, the creation of nanodevices is not straightforward because hydrogenation is fragile and, in air at 180°C, there is no longer any hydrogen. Protection is therefore required, for example, with h-BN. However, functionalization reduces carrier mobility, which is not favorable for fast transistors. A gap can also be created with a bilayer [112], so the effort required to create a new device may be too great. Furthermore, hydrogenation is not statistical because the chemisorption of an atomic hydrogen in the ortho and para positions is favored after the chemisorption of the first atom. These heterogeneities are an intrinsic barrier to reproducibility. Finally, we have been able to revisit the works presented in the literature and go further, opening up new perspectives, although this remains very delicate.

References

[1] Chaves, A., Azadani, J. G., Alsalman, H., Da Costa, D. R., Frisenda, R., Chaves, A. J., ... & Low, T. (2020). Bandgap engineering of two-dimensional semiconductor materials. *npj 2D Materials and Applications*, *4*(1), 29.

[2] Painter, G. S., & Ellis, D. E. (1970). Electronic band structure and optical properties of graphite from a variational approach. *Physical Review B*, *1*(12), 4747.

[3] Novoselov, K. S., Geim, A. K., Morozov, S. V., Jiang, D. E., Zhang, Y., Dubonos, S. V., ... & Firsov, A. A. (2004). Electric field effect in atomically thin carbon films. *science*, *306*(5696), 666-669.

[4] Purdie, D. G., Pugno, N. M., Taniguchi, T., Watanabe, K., Ferrari, A. C., & Lombardo, A. (2018). Cleaning interfaces in layered materials heterostructures. *Nature communications*, *9*(1), 5387.

[5] Petit, L., Fournier, T., Ballon, G., Robert, C., Lagarde, D., Puech, P., ... & Lassagne, B. (2024). Performance of graphene Hall effect sensors: Role of bias current, disorder, and Fermi velocity. *Physical Review Applied*, *22*(1), 014071.

[6] Wu, Y., Jenkins, K. A., Valdes-Garcia, A., Farmer, D. B., Zhu, Y., Bol, A. A., ... & Lin, Y. M. (2012). State-of-the-art graphene high-frequency electronics. *Nano letters*, *12*(6), 3062-3067.

[7] Ahmed, S., & Yi, J. (2017). Two-dimensional transition metal dichalcogenides and their charge carrier mobilities in field-effect transistors. *Nano-micro letters*, *9*, 1-23.

[8] Son, Y. W., Cohen, M. L., & Louie, S. G. (2006). Energy gaps in graphene nanoribbons. *Physical review letters*, *97*(21), 216803.

[9] Celis, A., Nair, M. N., Taleb-Ibrahimi, A., Conrad, E. H., Berger, C., De Heer, W. A., & Tejeda, A. (2016). Graphene nanoribbons: fabrication, properties and devices. *Journal of Physics D: Applied Physics*, *49*(14), 143001.

[10] Piazza, F., Cruz, K., Monthioux, M., Puech, P., & Gerber, I. (2020). Raman evidence for the successful synthesis of diamane. *Carbon*, *169*, 129-133.

[11] Balog, R., Jørgensen, B., Wells, J., Lægsgaard, E., Hofmann, P., Besenbacher, F., & Hornekær, L. (2009). Atomic hydrogen adsorbate structures on graphene. *Journal of the American Chemical Society*, *131*(25), 8744-8745.

[12] Elias, D. C., Nair, R. R., Mohiuddin, T. M. G., Morozov, S. V., Blake, P., Halsall, M. P., ... & Novoselov, K. S. (2009). Control of graphene's properties by reversible hydrogenation: evidence for graphane. *Science*, *323*(5914), 610-613.

[13] AlSalem, H., Just-Baringo, X., Larrosa, I., Monteverde, U., Jiang, X., Feng, Y., & Koehler, S. P. (2019). Evidence for site-specific reversible hydrogen adsorption on graphene by sum-frequency generation spectroscopy and density functional theory. *The Journal of Physical Chemistry C*, *123*(42), 25883-25889.

[14] Ryu, S., Han, M. Y., Maultzsch, J., Heinz, T. F., Kim, P., Steigerwald, M. L., & Brus, L. E. (2008). Reversible basal plane hydrogenation of graphene. *Nano letters*, *8*(12), 4597-4602.

[15] Bakharev, P. V., Huang, M., Saxena, M., Lee, S. W., Joo, S. H., Park, S. O., ... & Ruoff, R. S. (2020). Chemically induced transformation of chemical vapour deposition grown bilayer graphene into fluorinated single-layer diamond. *Nature nanotechnology*, *15*(1), 59-66.

[16] Lee, W. H., Suk, J. W., Chou, H., Lee, J., Hao, Y., Wu, Y., ... & Ruoff, R. S. (2012). Selective-area fluorination of graphene with fluoropolymer and laser irradiation. *Nano letters*, *12*(5), 2374-2378.

[17] Dubois, M., Guérin, K., Ahmad, Y., Batisse, N., Mar, M., Frezet, L., ... & Simon, L. (2014). Thermal exfoliation of fluorinated graphite. *Carbon*, *77*, 688-704.

[18] Chernozatonskii, L. A., Sorokin, P. B., Kvashnin, A. G., & Kvashnin, D. G. E. (2009). Diamond-like C_2H nanolayer, diamane: Simulation of the structure and properties. *Jetp Letters*, *90*, 134-138.

[19] Nair, R. R., Ren, W., Jalil, R., Riaz, I., Kravets, V. G., Britnell, L., ... & Geim, A. K. (2010). Fluorographene: a two-dimensional counterpart of Teflon. *small*, *6*(24), 2877-2884.

[20] Balog, R., Jørgensen, B., Nilsson, L., Andersen, M., Rienks, E., Bianchi, M., ... & Hornekær, L. (2010). Bandgap opening in graphene induced by patterned hydrogen adsorption. *Nature materials*, *9*(4), 315-319.

[21] Robinson, J. T., Burgess, J. S., Junkermeier, C. E., Badescu, S. C., Reinecke, T. L., Perkins, F. K., ... & Snow, E. S. (2010). Properties of fluorinated graphene films. *Nano letters*, *10*(8), 3001-3005.

[22] Fournier, T., Cruz, K., Monthioux, M., Lassagne, B., Petit, L., Moyano, S., ... & Piazza, F. (2024). Raman analysis of the dehydrogenation process of hydrogenated monolayer graphene. *Materials Chemistry and Physics*, *321*, 129490.

[23] Hornekær, L., Šljivančanin, Ž., Xu, W., Otero, R., Rauls, E., Stensgaard, I., ... & Besenbacher, F. (2006). Metastable Structures and Recombination Pathways for Atomic Hydrogen on the Graphite (0001) Surface. *Physical review letters*, *96*(15), 156104.

[24] Luo, Z., Yu, T., Ni, Z., Lim, S., Hu, H., Shang, J., ... & Lin, J. (2011). Electronic structures and structural evolution of hydrogenated graphene probed by Raman spectroscopy. *The Journal of Physical Chemistry C*, *115*(5), 1422-1427.

[25] Withers, F., Bointon, T. H., Dubois, M., Russo, S., & Craciun, M. F. (2011). Nanopatterning of fluorinated graphene by electron beam irradiation. *Nano letters*, *11*(9), 3912-3916.

[26] Schwander, M., & Partes, K. (2011). A review of diamond synthesis by CVD processes. *Diamond and related materials*, *20*(9), 1287-1301.

[27] Saslow, W., Bergstresser, T. K., & Cohen, M. L. (1966). Band structure and optical properties of diamond. *Physical Review Letters*, *16*(9), 354.

[28] Pappis, J., & Blum, S. L. (1961). Properties of pyrolytic graphite. *Journal of the American Ceramic Society*, *44*(12), 592-597.

[29] Torche, A., Mauri, F., Charlier, J. C., & Calandra, M. (2017). First-principles determination of the Raman fingerprint of rhombohedral graphite. *Physical Review Materials*, *1*(4), 041001.

[30] Inagaki, M. (Ed.). (2000). *New carbons-control of structure and functions*. Elsevier.

[31] Reich, S., Thomsen, C., & Maultzsch, J. (2004). *Carbon nanotubes: basic concepts and physical properties*. John Wiley & Sons.

[32] Geim, A. K., & Novoselov, K. S. (2007). The rise of graphene. *Nature materials*, *6*(3), 183-191.

[33] A., & Miano, G. (2014). Electrical properties of graphene for interconnect applications. *Applied Sciences*, *4*(2), 305-317.

[34] Cai, M., Thorpe, D., Adamson, D. H., & Schniepp, H. C. (2012). Methods of graphite exfoliation. Journal of Materials Chemistry, 22(48), 24992-25002.

[35] Nagashio, K., Yamashita, T., Nishimura, T., Kita, K., & Toriumi, A. (2011). Electrical transport properties of graphene on SiO2 with specific surface structures. *Journal of Applied Physics*, *110*(2).

[36] Blake, P., Hill, E. W., Castro Neto, A. H., Novoselov, K. S., Jiang, D., Yang, R., ... & Geim, A. K. (2007). Making graphene visible. Applied physics letters, 91(6).

[37] Sheppard, C. J. R. (1995). Approximate calculation of the reflection coefficient from a stratified medium. *Pure and Applied Optics: Journal of the European Optical Society Part A*, *4*(5), 665.

[38] Bajuri, S. N. M., Halim, N. H. A., Nor, M. N. M., & Hashim, U. (2005). PMMA characterization and optimization for nano structure formation. In *Proc. of 1st National Conference on Electronic Design*.

[39] Vieu, C., Carcenac, F., Pepin, A., Chen, Y., Mejias, M., Lebib, A., ... & Launois, H. (2000). Electron beam lithography: resolution limits and applications. *Applied surface science*, *164*(1-4), 111-117.

[40] Beams, R. (2018). Tip-enhanced Raman scattering of graphene. *Journal of Raman Spectroscopy*, *49*(1), 157-167.

[41] Pizzocchero, F., Gammelgaard, L., Jessen, B. S., Caridad, J. M., Wang, L., Hone, J., ... & Booth, T. J. (2016). The hot pick-up technique for batch assembly of van der Waals heterostructures. *Nature communications*, *7*(1), 11894.

[42] Jung, W., Kim, D., Lee, M., Kim, S., Kim, J. H., & Han, C. S. (2014). Ultraconformal contact transfer of monolayer graphene on metal to various substrates. *Advanced Materials (Deerfield Beach, Fla.)*, *26*(37), 6394-6400.

[43] Deokar, G., Avila, J., Razado-Colambo, I., Codron, J. L., Boyaval, C., Galopin, E., ... & Vignaud, D. (2015). Towards high quality CVD graphene growth and transfer. *Carbon*, *89*, 82-92.

[44] Lu, W., Cheng, S., Yan, M., Wang, Y., & Xia, Y. (2019). Selective soluble polymer–assisted electrochemical delamination of chemical vapor deposition graphene. *Journal of Solid State Electrochemistry*, *23*, 943-951.

[45] Leong, W. S., Wang, H., Yeo, J., Martin-Martinez, F. J., Zubair, A., Shen, P. C., ... & Kong, J. (2019). Paraffin-enabled graphene transfer. *Nature communications*, *10*(1), 867.

[46] Wojtaszek, M., Tombros, N., Caretta, A., Van Loosdrecht, P. H. M., & Van Wees, B. J. (2011). A road to hydrogenating graphene by a reactive ion etching plasma. *Journal of Applied Physics*, *110*(6).

[47] Lucchese, M. M., Stavale, F., Ferreira, E. M., Vilani, C., Moutinho, M. D. O., Capaz, R. B., ... & Jorio, A. (2010). Quantifying ion-induced defects and Raman relaxation length in graphene. *Carbon*, *48*(5), 1592-1597.

[48] Piazza, F., Monthioux, M., Puech, P., & Gerber, I. C. (2020). Towards a better understanding of the structure of diamanoïds and diamanoïd/graphene hybrids. *Carbon*, *156*, 234-241.

[49] Piazza, F., Monthioux, M., Puech, P., Gerber, I. C., & Gough, K. (2021). Progress on diamane and diamanoid thin film pressureless synthesis. *C*, *7*(1), 9.

[50] Piazza, F., Gough, K., Monthioux, M., Puech, P., Gerber, I., Wiens, R., ... & Ozoria, C. (2019). Low temperature, pressureless sp2 to sp3 transformation of ultrathin, crystalline carbon films. *Carbon*, *145*, 10-22.

[51] Tong, L., & Shi, Y. J. (2009). Carburization of tungsten filaments in a hot-wire chemical vapor deposition process using 1, 1, 3, 3-Tetramethyl-1, 3-disilacyclobutane. *ACS Applied Materials & Interfaces*, *1*(9), 1919-1926.

[52] Zeiler, E., Schwarz, S., Rosiwal, S. M., & Singer, R. F. (2002). Structural changes of tungsten heating filaments during CVD of diamond. *Materials Science and Engineering: A*, *335*(1-2), 236-245.

[53] Emelin, E. V., Cho, H. D., Korepanov, V. I., Varlamova, L. A., Erohin, S. V., Kim, D. Y., ... & Panin, G. N. (2022). Formation of diamane nanostructures in bilayer graphene on langasite under irradiation with a focused electron beam. *Nanomaterials*, *12*(24), 4408.

[54] Withers, F., Russo, S., Dubois, M., & Craciun, M. F. (2011). Tuning the electronic transport properties of graphene through functionalisation with fluorine. *Nanoscale research letters*, *6*(1), 526.

[55] Raman, C. V. (1928). A new radiation. *Indian Journal of physics*, *2*.

[56] Peter, Y. U., & Cardona, M. (2010). *Fundamentals of semiconductors: physics and materials properties*. Springer Science & Business Media.

[57] Ferraro, J. R. (2003). *Introductory raman spectroscopy*. Elsevier.

[58] Venezuela, P., Lazzeri, M., & Mauri, F. (2011). Theory of double-resonant Raman spectra in graphene: Intensity and line shape of defect-induced and two-phonon bands. *Physical Review B—Condensed Matter and Materials Physics*, *84*(3), 035433.

[59] Nemanich, R. J., Lucovsky, G., & Solin, S. A. (1977). Infrared active optical vibrations of graphite. *Solid State Communications*, *23*(2), 117-120.

[60] Beams, R., Cançado, L. G., & Novotny, L. (2015). Raman characterization of defects and dopants in graphene. *Journal of Physics: Condensed Matter*, *27*(8), 083002.

[61] Das, A., Pisana, S., Chakraborty, B., Piscanec, S., Saha, S. K., Waghmare, U. V., ... & Sood, A. K. (2008). Monitoring dopants by Raman scattering in an electrochemically top-gated graphene transistor. *Nature nanotechnology*, *3*(4), 210-215.

[62] Pisana, S., Lazzeri, M., Casiraghi, C., Novoselov, K. S., Geim, A. K., Ferrari, A. C., & Mauri, F. (2007). Breakdown of the adiabatic Born–Oppenheimer approximation in graphene. *Nature materials*, *6*(3), 198-201.

[63] Milošević, I., Kepčija, N., Dobardžić, E., Damnjanović, M., Mohr, M., Maultzsch, J., & Thomsen, C. (2011). Kohn anomaly in graphene. *Materials Science and Engineering: B*, *176*(6), 510-511.

[64] Kohn, W. (1959). Image of the Fermi Surface in the Vibration Spectrum of a Metal. *Physical Review Letters*, *2*(9), 393.

[65] Ding, F., Ji, H., Chen, Y., Herklotz, A., Dörr, K., Mei, Y., ... & Schmidt, O. G. (2010). Stretchable graphene: a close look at fundamental parameters through biaxial straining. *Nano letters*, *10*(9), 3453-3458.

[66] Ferrari, A. C., & Basko, D. M. (2013). Raman spectroscopy as a versatile tool for studying the properties of graphene. *Nature nanotechnology*, *8*(4), 235-246.

[67] Malard, L. M., Pimenta, M. A., Dresselhaus, G., & Dresselhaus, M. S. (2009). Raman spectroscopy in graphene. *Physics reports*, *473*(5-6), 51-87.

[68] Yan, J., Zhang, Y., Kim, P., & Pinczuk, A. (2007). Electric field effect tuning of electron-phonon coupling in graphene. *Physical review letters*, *98*(16), 166802.

[69] Lee, J. E., Ahn, G., Shim, J., Lee, Y. S., & Ryu, S. (2012). Optical separation of mechanical strain from charge doping in graphene. *Nature communications*, *3*(1), 1024.

[70] Herziger, F., Calandra, M., Gava, P., May, P., Lazzeri, M., Mauri, F., & Maultzsch, J. (2014). Two-dimensional analysis of the double-resonant 2D Raman mode in bilayer graphene. *Physical review letters*, *113*(18), 187401.

[71] Eckmann, A., Felten, A., Mishchenko, A., Britnell, L., Krupke, R., Novoselov, K. S., & Casiraghi, C. (2012). Probing the nature of defects in graphene by Raman spectroscopy. *Nano letters*, *12*(8), 3925-3930.

[72] Wang, Y. Y., Ni, Z. H., Shen, Z. X., Wang, H. M., & Wu, Y. H. (2008). Interference enhancement of

Raman signal of graphene. *Applied Physics Letters*, *92*(4).

[73] Yoon, D., Moon, H., Son, Y. W., Choi, J. S., Park, B. H., Cha, Y. H., ... & Cheong, H. (2009). Interference effect on Raman spectrum of graphene on SiO2/Si. *Physical Review B—Condensed Matter and Materials Physics*, *80*(12), 125422.

[74] Fournier, T., Crespos, C., Arshad, I., Dubois, M., Lassagne, B., Monthioux, M., ... & Puech, P. (2025). Quantifying the sp3/sp2 ratio in functionalized graphene. *Carbon*, 120657.

[75] Alam, A. U., Howlader, M. M. R., & Deen, M. J. (2014). The effects of oxygen plasma and humidity on surface roughness, water contact angle and hardness of silicon, silicon dioxide and glass. *Journal of Micromechanics and Microengineering*, *24*(3), 035010.

[76] Beams, R. (2018). Tip-enhanced Raman scattering of graphene. *Journal of Raman Spectroscopy*, *49*(1), 157-167.

[77] Lee, H., Lee, D. Y., Kang, M. G., Koo, Y., Kim, T., & Park, K. D. (2020). Tip-enhanced photoluminescence nano-spectroscopy and nano-imaging. *Nanophotonics*, *9*(10), 3089-3110.

[78] Li, Q., Hwang, E. H., & Das Sarma, S. (2011). Disorder-induced temperature-dependent transport in graphene: Puddles, impurities, activation, and diffusion. *Physical Review B—Condensed Matter and Materials Physics*, *84*(11), 115442.

[79] Meric, I., Han, M. Y., Young, A. F., Ozyilmaz, B., Kim, P., & Shepard, K. L. (2008). Current saturation in zero-bandgap, top-gated graphene field-effect transistors. *Nature nanotechnology*, *3*(11), 654-659.

[80] Adam, S., Hwang, E. H., & Sarma, S. D. (2008). Scattering mechanisms and Boltzmann transport in graphene. *Physica E: Low-dimensional Systems and Nanostructures*, *40*(5), 1022-1025.

[81] Stauber, T., Peres, N. M. R., & Guinea, F. (2007). Electronic transport in graphene: A semiclassical approach including midgap states. *Physical Review B—Condensed Matter and Materials Physics*, *76*(20), 205423.

[82] Hall, E. H. (1880). On the new action of magnetism on a permanent electric current. *American Journal of Science*, *3*(117), 161-186.

[83] Ando, T. (2006). Screening effect and impurity scattering in monolayer graphene. *Journal of the Physical Society of Japan*, *75*(7), 074716.

[84] Varshni, Y. P. (1967). Temperature dependence of the energy gap in semiconductors. *physica*, *34*(1), 149-154.

[85] Mott, N. F. (1969). Conduction in non-crystalline materials: III. Localized states in a pseudogap and near extremities of conduction and valence bands. *Philosophical Magazine*, *19*(160), 835-852.

[86] Shklovskii, B. I., & Efros, A. L. (2013). *Electronic properties of doped semiconductors* (Vol. 45). Springer Science & Business Media.

[87] Martin, J., Akerman, N., Ulbricht, G., Lohmann, T., Smet, J. V., Von Klitzing, K., & Yacoby, A. (2008). Observation of electron–hole puddles in graphene using a scanning single-electron transistor. *Nature physics*, *4*(2), 144-148.

[88] Ferrari, A. C., & Robertson, J. (2000). Interpretation of Raman spectra of disordered and amorphous carbon. *Physical review B*, *61*(20), 14095.

[89] Cançado, L. G., Jorio, A., Ferreira, E. M., Stavale, F., Achete, C. A., Capaz, R. B., ... & Ferrari, A. C. (2011). Quantifying defects in graphene via Raman spectroscopy at different excitation energies. *Nano letters*, *11*(8), 3190-3196.

[90] Cançado, L. G., Jorio, A., & Pimenta, M. A. (2007). Measuring the absolute Raman cross section of nanographites as a function of laser energy and crystallite size. *Physical Review B—Condensed Matter and Materials Physics*, *76*(6), 064304.

[91] Wang, Q. H., Jin, Z., Kim, K. K., Hilmer, A. J., Paulus, G. L., Shih, C. J., ... & Strano, M. S. (2012). Understanding and controlling the substrate effect on graphene electron-transfer chemistry via reactivity imprint lithography. *Nature chemistry*, *4*(9), 724-732.

[92] Grimme, S., Brandenburg, J. G., Bannwarth, C., & Hansen, A. (2015). Consistent structures and interactions by density functional theory with small atomic orbital basis sets. *The Journal of chemical physics*, *143*(5).

[93] Picheau, E., Impellizzeri, A., Rybkovskiy, D., Bayle, M., Mevellec, J. Y., Hof, F., ... & Pénicaud, A. (2021). Intense Raman D band without disorder in flattened carbon nanotubes. *Acs Nano*, *15*(1), 596-603.

[94] Cheng, L., Jandhyala, S., Mordi, G., Lucero, A. T., Huang, J., Azcatl, A., ... & Kim, J. (2016). Partially fluorinated graphene: structural and electrical characterization. *ACS applied materials & interfaces*, *8*(7), 5002-5008.

[95] Puech, P., Plewa, J. M., Mallet-Ladeira, P., & Monthioux, M. (2016). Spatial confinement model applied to phonons in disordered graphene-based carbons. *Carbon*, *105*, 275-281.

[96] Kathavate, Y. V. (1945, May). The diffraction of light by an assembly of opaque circular disks. In *Proceedings of the Indian Academy of Sciences-Section A* (Vol. 21, No. 5, pp. 233-239). New Delhi: Springer India.

[97] Zecho, T., Güttler, A., Sha, X., Jackson, B., & Küppers, J. (2002). Adsorption of hydrogen and deuterium atoms on the (0001) graphite surface. *The Journal of chemical physics*, *117*(18), 8486-8492.

[98] Luo, Z., Yu, T., Kim, K. J., Ni, Z., You, Y., Lim, S., ... & Lin, J. (2009). Thickness-dependent reversible hydrogenation of graphene layers. *Acs Nano*, *3*(7), 1781-1788.

[99] Pei, Q. X., Sha, Z. D., & Zhang, Y. W. (2011). A theoretical analysis of the thermal conductivity of hydrogenated graphene. *Carbon*, *49*(14), 4752-4759.

[100] Diankov, G., Neumann, M., & Goldhaber-Gordon, D. (2013). Extreme monolayer-selectivity of hydrogen-plasma reactions with graphene. *ACS nano*, *7*(2), 1324-1332.

[101] Fournier, T., El Masaoudi, S., Gerber, I. C., Lassagne, B., Crespos, C., Leyssale, J. M., ... & Piazza, F. (2025). Hydrogenation and etching of single-layer graphene during exposure to atomic hydrogen. *Carbon Trends*, 100553.

[102] Piazza, F., Morell, G., Beltran-Huarac, J., Paredes, G., Ahmadi, M., & Guinel, M. (2014). Carbon nanotubes coated with diamond nanocrystals and silicon carbide by hot-filament chemical vapor deposition below 200 C substrate temperature. *Carbon*, *75*, 113-123.

[103] Harpale, A., Panesi, M., & Chew, H. B. (2016). Plasma-graphene interaction and its effects on nanoscale patterning. *Physical Review B*, *93*(3), 035416.

[104] May, P. W., Harvey, J. N., Smith, J. A., & Mankelevich, Y. A. (2006). Reevaluation of the mechanism for ultrananocrystalline diamond deposition from Ar/CH4/H2 gas mixtures. *Journal of applied physics*, *99*(10).

[105] Jones, J. D., Hoffmann, W. D., Jesseph, A. V., Morris, C. J., Verbeck, G. F., & Pérez, J. M. (2010). On the mechanism for plasma hydrogenation of graphene. *Applied Physics Letters*, *97*(23).

[106] Felten, A., McManus, D., Rice, C., Nittler, L., Pireaux, J. J., & Casiraghi, C. (2014). Insight into hydrogenation of graphene: Effect of hydrogen plasma chemistry. *Applied Physics Letters*, *105*(18).

[107] Ashfold, M. N., May, P. W., Petherbridge, J. R., Rosser, K. N., Smith, J. A., Mankelevich, Y. A., & Suetin, N. V. (2001). Unravelling aspects of the gas phase chemistry involved in diamond chemical vapour deposition. *Physical chemistry chemical physics*, *3*(17), 3471-3485.

[108] Kanai, C., Watanabe, K., & Takakuwa, Y. (2001). Ab initio calculations on etching of graphite and diamond surfaces by atomic hydrogen. *Physical Review B*, *63*(23), 235311.

[109] Aussems, D. U. B., Bal, K. M., Morgan, T. W., Van De Sanden, M. C. M., & Neyts, E. C. (2017). Atomistic simulations of graphite etching at realistic time scales. *Chemical Science*, *8*(10), 7160-7168.

[110] Aussems, D. U. B., Bal, K. M., Morgan, T. W., van de Sanden, M. C. M., & Neyts, E. C. (2018). Mechanisms of elementary hydrogen ion-surface interactions during multilayer graphene etching at high surface temperature as a function of flux. *Carbon*, *137*, 527-532.

[111] Wang, L., Meric, I., Huang, P. Y., Gao, Q., Gao, Y., Tran, H., ... & Dean, C. R. (2013). One-dimensional electrical contact to a two-dimensional material. *Science*, *342*(6158), 614-617.

[112] Lee, S. Y., Duong, D. L., Vu, Q. A., Jin, Y., Kim, P., & Lee, Y. H. (2015). Chemically modulated band gap in bilayer graphene memory transistors with high on/off ratio. *ACS nano*, *9*(9), 9034-9042.

Résumé en français

Introduction & Contexte

La grande famille des matériaux de van der Waals, c'est-à-dire des empilements de couches maintenues ensemble par des interactions de van der Waals, couvre un large éventail de composés cristallins présentant de nombreuses propriétés électroniques différentes. Par exemple, le nitrure de bore hexagonal (h-BN) est un très bon isolant électrique avec une bande interdite dans le domaine de l'ultraviolet [1], tandis que le graphite a des propriétés métalliques en raison de son intervalle d'énergie nul [2]. D'autres composés sont des semi-conducteurs, tels que les dichalcogénures de métaux de transition (TMD), qui couvrent des bandes interdites allant de l'infrarouge au visible. De plus, en raison de leurs faibles interactions intercouches, ces matériaux peuvent être exfoliés pour obtenir des cristaux bidimensionnels (2D), appelés « matériaux 2D », dont les structures de bandes électroniques diffèrent de celles de leurs équivalents massifs. En 2004, deux chercheurs de Manchester, A. K. Geim et K. S. Novoselov, ont été les premiers à mettre en évidence une couche de carbone d'épaisseur atomique, appelée graphène, obtenue par exfoliation mécanique d'un cristal de graphite massif [3]. En plus d'être bidimensionnel, le graphène se distingue du graphite par sa structure de bande électronique, qui présente une dispersion d'énergie linéaire à proximité de certains points spécifiques à haute symétrie de la zone de Brillouin. Par conséquent, les électrons et les trous imitent les fermions de Dirac sans masse. Leur mobilité peut être beaucoup plus importante que dans le graphite, atteignant des valeurs allant jusqu'à 180 000 $cm^2V^{-1}s^{-1}$ [4]. Ces propriétés électroniques peuvent être utilisées dans de nombreuses applications, telles que les capteurs magnétiques hautement sensibles [5] ou les transistors haute fréquence [6]. Cependant, en raison de leur bande interdite nulle, les transistors en graphène ont un rapport passant/non-passant très faible [7], ce qui les rend inadaptés aux applications électroniques numériques. Pour surmonter ce problème, plusieurs approches visant à induire une bande interdite dans le graphène ont été rapportées dans la littérature. Par exemple, il a été démontré que, dans les nanorubans de graphène, les effets de confinement conduisent à une discrétisation du vecteur d'onde, ouvrant une bande interdite réglable par la largeur du ruban [8,9]. Une autre approche consiste à faire passer chimiquement l'hybridation des atomes de carbone de sp^2 à sp^3 par fonctionnalisation. L'hydrogénation [10-14] et la fluoration [15-17] sont les techniques les plus couramment utilisées à cette fin. Dans le cas idéal, où chaque atome de carbone est lié de manière covalente à un atome d'hydrogène ou de fluor, les matériaux respectifs sont appelés graphane ou fluorographène avec des bandes interdites supérieures à 3 eV [18,19]. Pour une hydrogénation ou une fluoration incomplète, la valeur de la bande interdite dépend du taux de couverture en hydrogène ou en fluor. De plus, la réversibilité de ces processus a été démontrée à plusieurs reprises dans la littérature. Par conséquent, un contrôle précis des processus de fonctionnalisation et de défonctionnalisation devrait permettre d'ajuster chimiquement les propriétés électroniques du graphène. Cependant, cela ne peut être réalisé sans utiliser des techniques de caractérisation adaptées, ni en tirant des conclusions hâtives à partir d'expériences. Cela implique de combiner la spectroscopie Raman avec des mesures de transport électrique et des techniques de microscopie, par exemple, ce qui n'est pas toujours fait dans la littérature. Bien que ce doctorat ait été initialement motivé par l'ouverture de la bande interdite dans le graphène via l'hydrogénation afin de fabriquer des hétérostructures planes 2D sp^2/sp^3 pour des applications en nanoélectronique, il s'est orienté vers d'autres horizons lorsque les défis liés à la synthèse et à la caractérisation ont été pris en compte. Ainsi, ce travail expérimental se concentre sur l'hydrogénation

et la fluoration unilatérales de couches de graphène supportées par des plaquettes de Si/SiO2 ou d'or, depuis la fabrication des échantillons jusqu'à leur caractérisation. La préparation des échantillons de graphène, ainsi que leur caractérisation, ont été entièrement réalisées au CEMES et au LPCNO. Les échantillons ont été principalement caractérisés par spectroscopie Raman, mais certains ont également été analysés par microscopie à force atomique (AFM), spectroscopie Raman amplifiée par pointe et mesures de transport électrique. En ce qui concerne l'hydrogénation et la fluoration, ces processus ont été réalisés en collaboration avec deux spécialistes : le professeur Fabrice Piazza de la PUCMM à Santiago de los Caballeros (République dominicaine) et le processeur Marc Dubois de l'université de Clermont-Ferrand (France). J'ai eu l'occasion de passer quelques mois à la PUCMM et quelques jours à l'université de Clermont-Ferrand.

1 Fabrication des échantillons

1.1 Exfoliation mécanique

La méthode utilisée par A. K. Geim et K. S. Novoselov pour obtenir des films minces et des monocouches de graphite est la technique du « scotch », un processus d'exfoliation mécanique consistant à décoller le graphite à l'aide d'un ruban adhésif. La même technique a été utilisée dans le cadre de cette thèse pour extraire des films minces de graphite à partir d'un cristal HOPG acheté auprès de la société HQ graphene.

Deux types de substrats ont été utilisés en fonction de la caractérisation :

(1) Des substrats en silicium recouverts de 285 nm de SiO2 pour effectuer des mesures de transport électrique, ainsi que pour améliorer le contraste optique et le signal Raman par des effets d'interférence.

(2) Des substrats en or ultraplats pour améliorer le signal TERS.

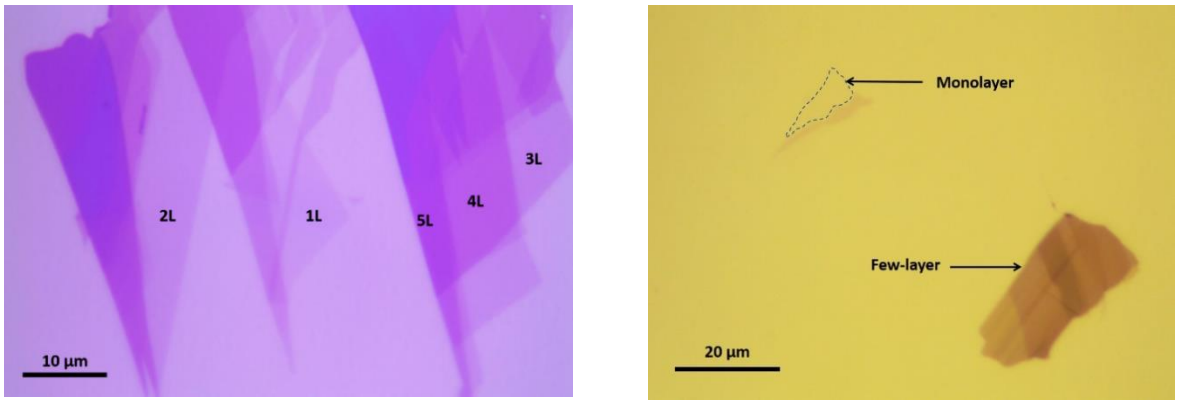


Figure 1: Images optiques de feuillets graphite déposés sur (a) SiO_2 et (b) Or.

Comme le montre la **Figure 1**, le graphène apparaît beaucoup plus contrasté sur le Si/SiO2 que sur le substrat en or. Cela est dû aux effets d'interférence induits par la couche d'oxyde. Le contraste optique dépend du nombre de couches de graphène, de la longueur d'onde de la lumière incidente et de l'épaisseur

de l'oxyde. Pour une monocouche de graphène, une map du contraste en fonction de la longueur d'onde et de l'épaisseur d'oxyde est présentée en **Figure 2**.

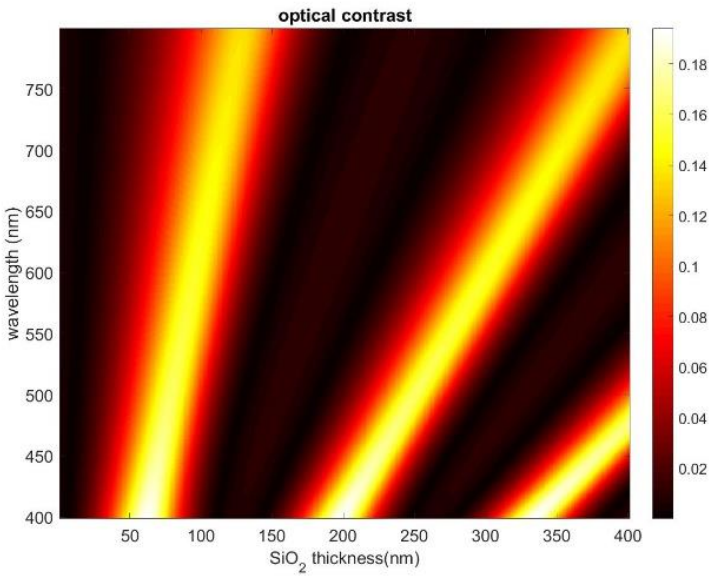


Figure 2 : Carte du contraste optique d'une monocouche de graphene sur SiO_2 en fonction de la longueur d'onde et de l'épaisseur d'oxyde.

1.2 Microfabrication de dispositifs en graphene sur Si/SiO_2

L'étude des propriétés de transport électronique du graphène nécessite plusieurs étapes de microfabrication pour passer d'un feuillet de graphène sur SiO_2 à un échantillon structuré avec des contacts électriques et une géométrie et des dimensions choisies. Dans ce travail, le graphite a été directement exfolié sur des substrats Si/SiO2 avec une épaisseur d'oxyde de 285 nm et structuré avec des marques d'alignement en forme de L en Cr/Au distinguées par des chiffres alphanumériques. Ensuite, comme la résistance dépend des paramètres géométriques de l'échantillon, le feuillet de graphène doit être gravé localement pour définir la géométrie du dispositif et extraire les paramètres intrinsèques tels que la conductivité, la mobilité et la densité résiduelle des porteurs de charge. En général, l'échantillon prend la forme d'une « barre de Hall » qui correspond à un canal longitudinal traversé par plusieurs canaux transversaux. Elle permet d'effectuer des mesures à 4 sondes pour surmonter la résistance de contact et, en particulier, d'effectuer des mesures Hall et de déterminer à la fois la résistance longitudinale et transversale. Enfin, des microélectrodes sont fabriquées pour connecter les différents canaux afin de mesurer les propriétés du dispositif. Dans le cadre de ce doctorat, des barres Hall avec 2 ou 3 canaux transversaux ont été fabriquées, impliquant respectivement 6 ou 8 électrodes par échantillon.

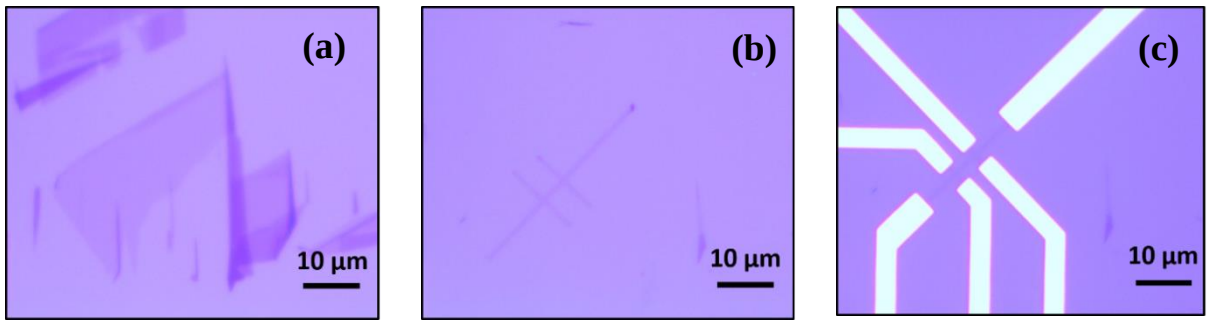


Figure 3: Images d'un morceau de graphène sur SiO_2 (285 nm) (a) tel qu'exfolié, (b) gravé et (c) connecté par des microélectrodes.

1.3 Méthode de transfert humide assistée par polymères

L'or étant un métal, il est difficile d'observer la variation de réflectivité entre le substrat et une couche de graphène, car il n'y a pas d'amplification du champ électrique induite par l'effet d'interférence. Par conséquent, il n'est pas recommandé d'effectuer l'exfoliation directement sur l'or, car il est très difficile de localiser optiquement les feuillets de graphène monocouches transférés (voir figure 1b). Pour surmonter ce problème, le transfert de couches de graphène de grande surface a été réalisé. Des films de graphène polycristallin développés par CVD sur des feuilles de cuivre ont été achetés auprès de Graphenea et transférés du cuivre vers des substrats en or ultra-plats. De nombreux protocoles différents ont été envisagés pour réussir le transfert, mais aucun d'entre eux n'a vraiment abouti à une couche de graphène parfaitement propre et plate sur l'or. La plupart du temps, le graphène transféré était soit déchiré et froissé, soit contaminé par des résidus de polymère. Plusieurs résultats publiés dans la littérature font état d'un transfert de très bonne qualité [42-45], en particulier la méthode de transfert assisté par paraffine [45], mais ils n'ont pas pu être reproduits dans le cadre de cette thèse. Le protocole le plus utilisé dans ce travail est le transfert humide assisté par polymère. Il consiste à utiliser un film mince de polymère (généralement du PMMA) comme couche sacrificielle pour transférer le graphène de sa feuille de cuivre vers un substrat cible (**Figure 2**).

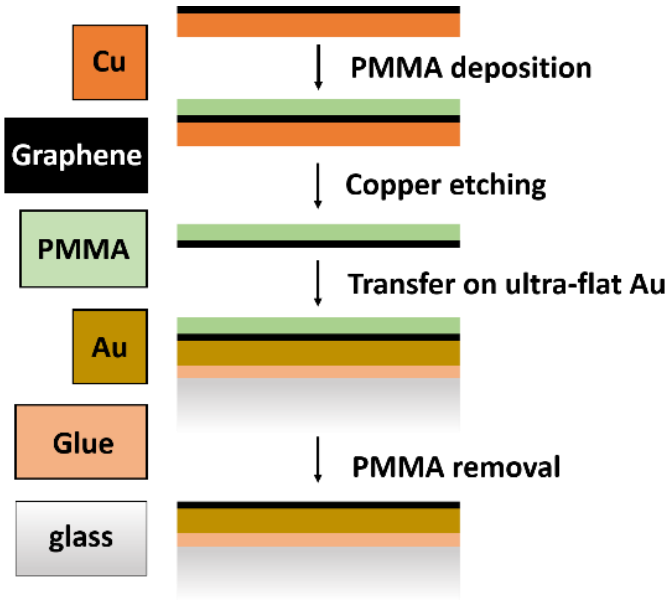


Figure 4: Transfert assisté par PMMA de graphène obtenu par CVD depuis une feuille de cuivre vers un substrat d'or ultraplat.

2 Description des techniques utilisées pour l'hydrogénation et la fluoration

2.1 Hydrogénation

2.1.1 Procédé à filaments chauds

L'hydrogénation par procédé à filaments chauds a été la principale méthode expérimentale utilisée dans cette thèse pour hydrogéner le graphène. Il s'agit d'un procédé CVD couramment utilisé pour la synthèse de matériaux diamantaires 2D [10,48-50], dans lequel la phase gazeuse est chauffée par des filaments chauds. Piazza *et al* [10] ont réussi à transformer une bicouche de graphène en une monocouche de diamane (C_2H de type diamant) à l'aide d'un réacteur à filament chaud disponible dans le commerce (BWI 1000 de Blue Wave Semiconductors), et le même réacteur a été utilisé ici pour hydrogéner le graphène.

À l'instar de l'hydrogénation par plasma, où l'hydrogène moléculaire est converti en hydrogène ionique afin de favoriser la réaction chimique avec le graphène, le procédé à filaments chauds vise à dissocier les molécules d'H_2 en radicaux hydrogène qui sont plus réactifs en raison de leur électron non apparié. La dissociation des molécules d'H_2 est activée thermiquement à haute température. Dans les procédés à filament chaud, l'énergie thermique est fournie par des filaments chauffés par l'effet Joule. Ici, les deux filaments parallèles en W sont chauffés entre 1800 °C et 2300 °C, ce qui correspond à un courant électrique compris entre 40 A et 60 A environ. Afin d'améliorer la stabilité thermique des filaments et d'éviter la sublimation du W pendant le procédé, une étape de carburation est nécessaire avant chaque procédé

d'hydrogénation. La carburation consiste à permettre la diffusion du carbone à l'intérieur du filament, ce qui entraîne un changement de phase du W au W_2C ou WC [51,52]. Le carbone est fourni par des radicaux méthyles provenant de l'activation d'une phase gazeuse de CH_4 à 1800 °C [51]. Afin d'éviter toute contamination du carbone sur l'échantillon, la cémentation des filaments doit être réalisée avant d'introduire les échantillons dans la chambre.

2.1.2 Hydrogénation locale par faisceau d'électrons

Dans le cadre de ce doctorat, certains tests ont été réalisés avec du PMMA et ont donné des résultats intéressants en spectroscopie Raman. Une série de six feuillets de graphène sur un substrat Si/SiO_2 a été préparée par exfoliation. Ensuite, environ 75 nm de PMMA 950 A2 ont été déposés par centrifugation sur le dessus, et, au-dessus de chaque feuillet sélectionné, une zone carrée a été balayée par un faisceau d'électrons contrôlé par un microscope électronique à balayage (MEB) de JEOL. Le PMMA a ensuite été éliminé dans de l'acétone pendant 10 minutes, sauf dans certaines zones balayées où la résine photosensible s'était réticulée et était devenue insoluble dans l'acétone.

2.2 Fluoration

La technique la plus couramment utilisée pour la fluoration consiste en un procédé en phase gazeuse où la chimisorption du fluor est activée thermiquement. Contrairement à l'hydrogénation, qui nécessite de l'hydrogène ionique ou atomique, la fluoration est rendue possible par une réaction chimique entre le graphène et le fluor moléculaire. La réactivité élevée des molécules de F_2 constitue un véritable défi pour l'obtention de graphène fluoré. Le F_2 réagit généralement fortement avec le graphène, formant des fluorocarbures volatils tels que le CF_4 ou le C_2F_6 [17].

Notre approche consistait à utiliser une phase vapeur froide (15 °C à 30 °C) composée de molécules F_2 diluées dans du N_2 (1% à 10%) afin de limiter les dommages causés au réseau cristallin du graphène. Les échantillons de graphène ont été placés dans un réacteur à flux continu commercial (**Figure 7**) évacué à l'aide d'une pompe primaire (10-3 mbar). Le réacteur a ensuite été chauffé et l'échantillon a été exposé à un flux de gaz de 300 ml/min. Lorsque la pression a atteint 1 atm, le réacteur a été ouvert vers un piège à chaux sodée afin d'éviter toute surpression dans le réacteur. À la fin du processus, le flux de gaz F_2 a été arrêté et le réacteur a été rincé avec 300 ml/min de N_2 afin d'éliminer toute trace de molécules de F_2 dans le réacteur et de récupérer l'échantillon en toute sécurité.

3 Techniques de characterisation

3.1 Spectroscopie Raman dans le graphène

La **Figure 5** montre un spectre Raman d'un échantillon de graphène vierge et d'un échantillon de graphène défectueux (défauts introduits par fluoration), confirmant ainsi que, contrairement aux bandes G et 2D, les bandes D et D' ne sont activées qu'en présence de défauts. La bande D+D'' résulte d'un processus de double résonance qui combine un phonon iTO (D) et un phonon acoustique longitudinal (LA) (D''). Pour le graphène défectueux, une large bande est visible, car elle correspond à la bande D+D'. Cette bande provient

d'un processus de triple résonance activé par des défauts.

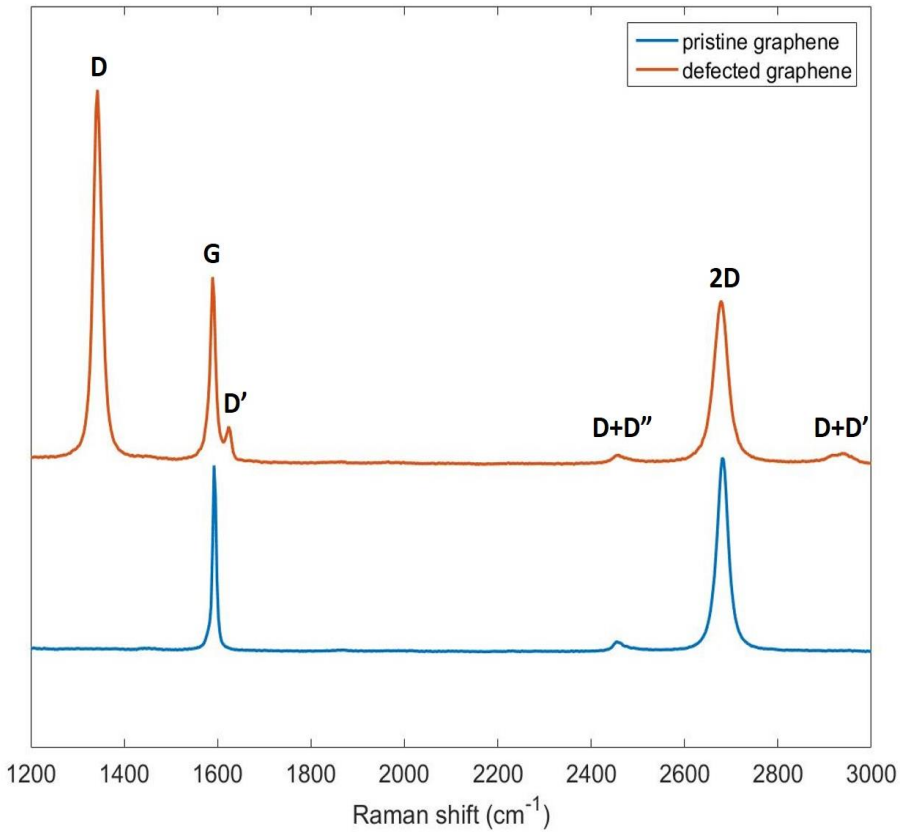


Figure 5: Comparaison des spectres Raman d'un échantillon de graphène parfait et d'un échantillon présentant des défauts.

Les bandes D et 2D sont sensibles à la structure électronique. En particulier, leur position est fortement dispersive avec l'énergie laser [66], et elles sont représentatives du nombre de couches. Dans le graphène bicouche, la bande 2D comporte quatre composantes, alors qu'elle n'en comporte qu'une dans le graphène monocouche, comme le montre la **Figure 6**. Pour plus de deux couches, il y a encore plus de contributions. Dans le cadre de cette thèse, la différence entre une monocouche et une bicouche a été intuitée à partir du contraste optique du graphène sur SiO_2, mais la spectroscopie Raman a été constamment utilisée à des fins de confirmation.

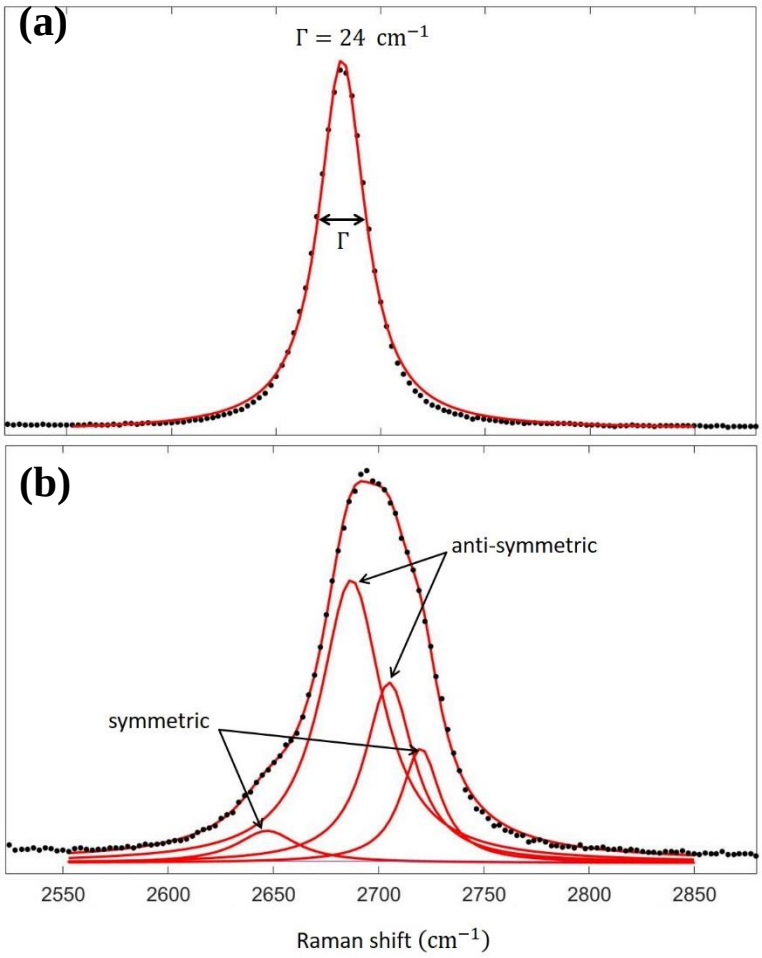


Figure 6: Fit de la bande 2D pour (a) une monocouche et (b) une bicouche de graphène, montrant la différence du nombre de composantes.

3.2 Rôle du substrat interférentiel

Il a été mentionné précédemment que le contraste optique d'une couche de graphène sur Si/SiO_2 peut être amplifié par des effets d'interférence. L'intensité du signal Raman peut être améliorée de manière similaire [72,73]. Le facteur d'amélioration du signal Raman des bandes G, D et 2D est représenté dans la **Figure 7** en fonction de la longueur d'onde du laser pour le graphène sur Si/SiO_2 et le graphène sur or. En ce qui concerne la bande D', sa fréquence est suffisamment proche de celle de la bande G pour considérer que l'amélioration de la bande G constitue une bonne estimation de celle de la bande D'.

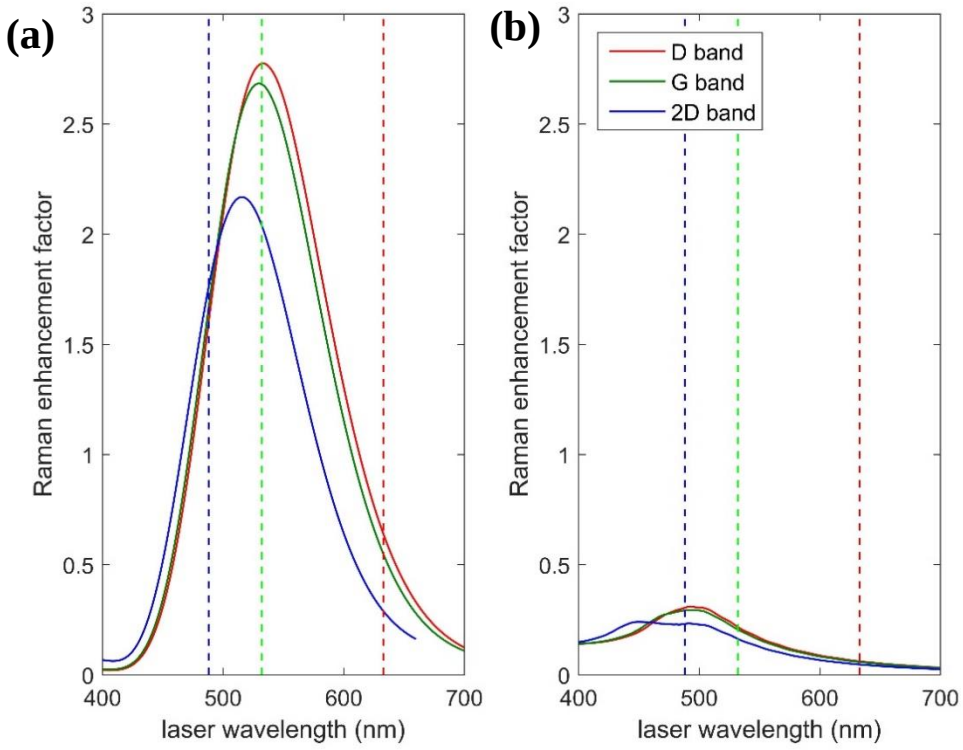


Figure 7 : Facteur d'amplification du signal Raman correspondant aux bandes G, D et 2D, dans le cas de graphène (a) sur SiO_2 et (b) sur Or.

3.3 Setup expérimental

Dans le cadre de ce doctorat, trois spectromètres Raman commerciaux différents ont été utilisés : deux d'entre eux ont été fabriqués par Horiba et le troisième par Renishaw. Pour décrire brièvement ce qu'est un dispositif Raman, celui-ci peut être décomposé en différents éléments : un laser, un microscope confocal, un filtre, un réseau de diffraction et un détecteur CCD.

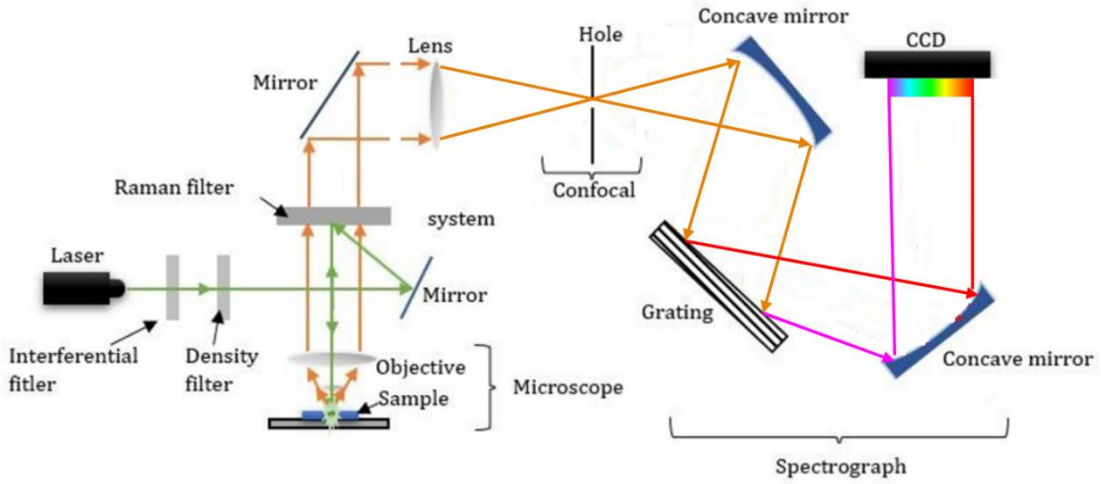


Figure 8: Représentation schématique d'un spectromètre Raman.

3.4 Microscopie à force atomique

Dans ce travail, l'AFM a principalement été utilisée comme technique complémentaire pour confirmer l'origine des défauts détectés par spectroscopie Raman. Bien qu'il ne soit pas possible de détecter les défauts de type sp3 avec l'AFM, d'autres types de déformations structurelles (trous, fissures, plis, etc.) contribuant à la bande D peuvent être résolus avec l'AFM.

La résolution spatiale dépend de différents paramètres tels que le rayon de courbure de la pointe et les paramètres de balayage (vitesse et taille du pas). Le laboratoire achète des sondes AFM auprès de la société App Nano et celles utilisées dans ce travail étaient des sondes SPM à cantilever avec une pointe en silicium caractérisée par un rayon de courbure de 6 nm. Toutes les images AFM de ce travail ont été réalisées en mode tapping. Les constantes de rappel des cantilevers de ces modèles sont comprises entre 0,6 et 3,5 N/m et leurs fréquences de résonance entre 43 et 81 kHz.

3.5 Spectroscopie Raman amplifiée par effet de pointe (TERS)

Dans le cadre de ce doctorat, la technique TERS a été utilisée dans le but de détecter le signal Raman provenant respectivement des liaisons C-H et C-F dans le graphène hydrogéné et fluoré. Les modes vibrationnels associés ont été calculés par Ibrahim Arshad lors de son stage au CEMES. Les résultats sont synthétisés en **Figure 9.**

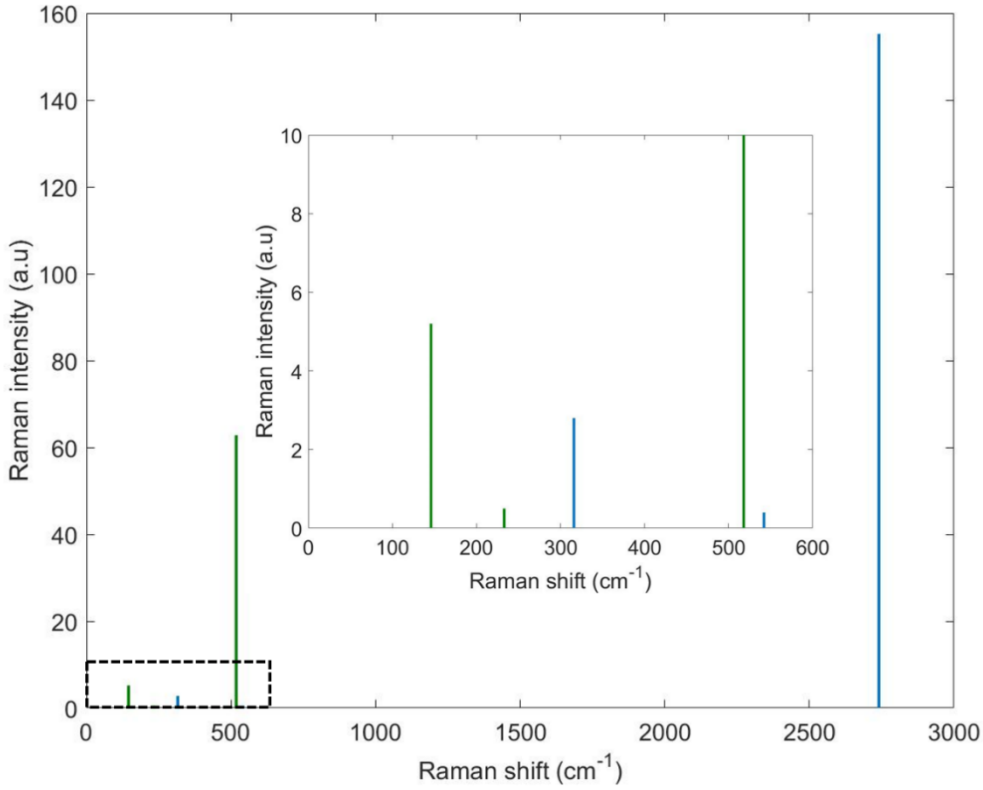


Figure 9: Bandes Raman calculées numériquement pour les liaisons C-H (bleu) et C-F (vert). L'insert représente un zoom sur la zone encadrée en pointillée.

3.6 Mesures de transport électrique

3.6.1 Propriétés électroniques du graphène fonctionnalisé

Bien que les propriétés électroniques du graphène aient été largement étudiées depuis sa découverte par A. K. Geim et K. S. Novoselov, les propriétés induites par la chimisorption des adatomes sont assez complexes à étudier expérimentalement. Certains rapports font état de l'existence d'une bande interdite et d'une transition métal-isolant, mais la caractérisation n'est pas toujours convaincante et souvent mal interprétée. Selon moi, il est important de distinguer deux cas différents :

(1) La proportion d'atomes de carbone hybridés sp^3 est suffisamment importante pour avoir ouvert une bande interdite dans la structure électronique du graphène. la résistivité au point de neutralité de charge suit le comportement thermique bien connu des semi-conducteurs intrinsèques. La bande interdite dépend de la température et peut être approchée par l'équation de Varshni [84].

(2) La proportion d'atomes de carbone hybridés sp^3 est relativement faible ou n'est pas répartie de manière homogène (domaines sp3 parmi de grandes régions sp^2), ce qui induit un désordre et des fluctuations de dopage. Le désordre dans les métaux peut conduire à un « pseudo-écart » où la conduction se produit

par saut [85]. Dans la littérature, la loi de Mott est couramment utilisée pour décrire le comportement de la résistivité au point de neutralité de charge dans un graphène désordonné [12,54]. Un autre modèle proposé par Li *et al* [78] considère que la conductivité du graphène désordonné est déterminée par des flaques d'électrons-trous qui correspondent à des fluctuations spatiales de la densité des porteurs de charge. Dans ce modèle, un paramètre clé pour estimer le degré de désordre est l'écart-type des fluctuations de potentiel responsables de l'apparition des poches d'électrons-trous, qui est représenté par un paramètre s.

3.6.2 Mesures

Une mesure complète est effectuée à l'aide de six sondes : deux sondes pour l'injection de courant, deux sondes pour la mesure de la tension longitudinale et deux sondes pour la mesure de la tension transversale (voir **Figure 10**). Dans cette configuration, la résistance de contact disparaît et la résistivité du graphène peut être directement extraite de la mesure de résistance. La tension de grille est appliquée directement à l'arrière du substrat par contact électrique avec le support de substrat en cuivre.

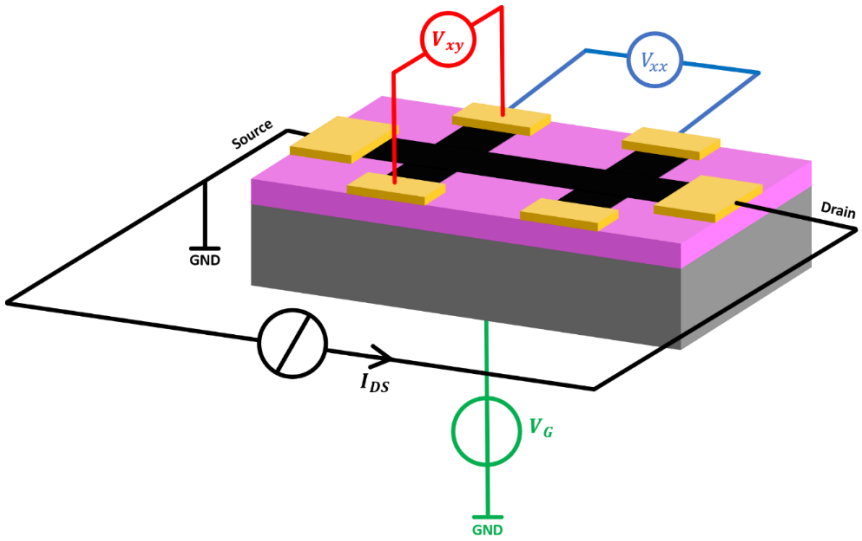


Figure 10: Configuration de mesure des dispositifs type « bar de Hall » en graphène.

4 Modèle Raman pour quantifier le ratio sp^2/sp^3 dans le graphène fonctionnalisé

Ce travail propose un modèle non empirique adapté à la fonctionnalisation covalente du graphène (y compris l'hydrogénation et la fluoration) avec des paramètres d'entrée dérivés de calculs de chimie quantique. L'adsorption atomique ou moléculaire sur une couche de graphène peut être modélisée comme des défauts ponctuels qui perturbent le couplage électron-phonon au sein du réseau de carbone sp^2 environnant. Dans le cadre du présent modèle, trois régions concentriques sont définies autour de chaque site chimisorbé, caractérisées par les rayons r_{sp3}, r_S et r_A (voir **Figure 11**) : région désactivée (sp^3), région

distordue et région activée.

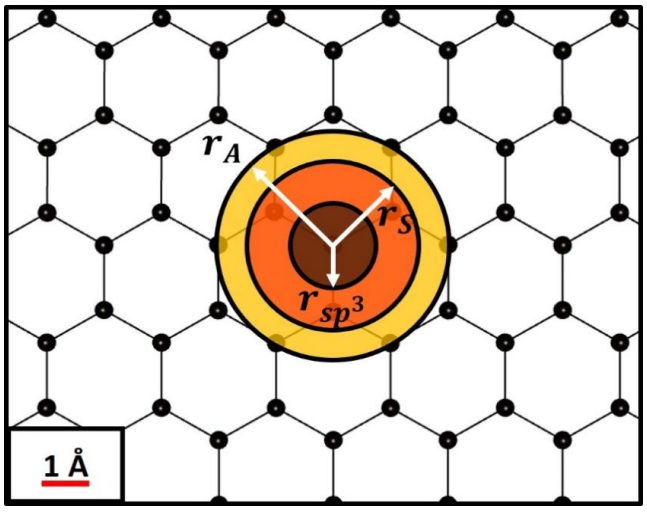


Figure 11: Définition du défaut ponctuel de type sp^3, représentant les régions désactivées (brun), distordues (orange) et activées (jaune).

La **Figure 12** représente le rapport en intensité I_D/I_G entre les bandes D et G en fonction de la distance moyenne entre les sites sp^3 L_D. Les résultats sont comparés aux données expérimentales issues de la littérature et aux deux lois empiriques mentionnées précédemment, démontrant ainsi que le modèle surpasse largement ses prédécesseurs, du moins en ce qui les défauts ponctuels de type sp^3.

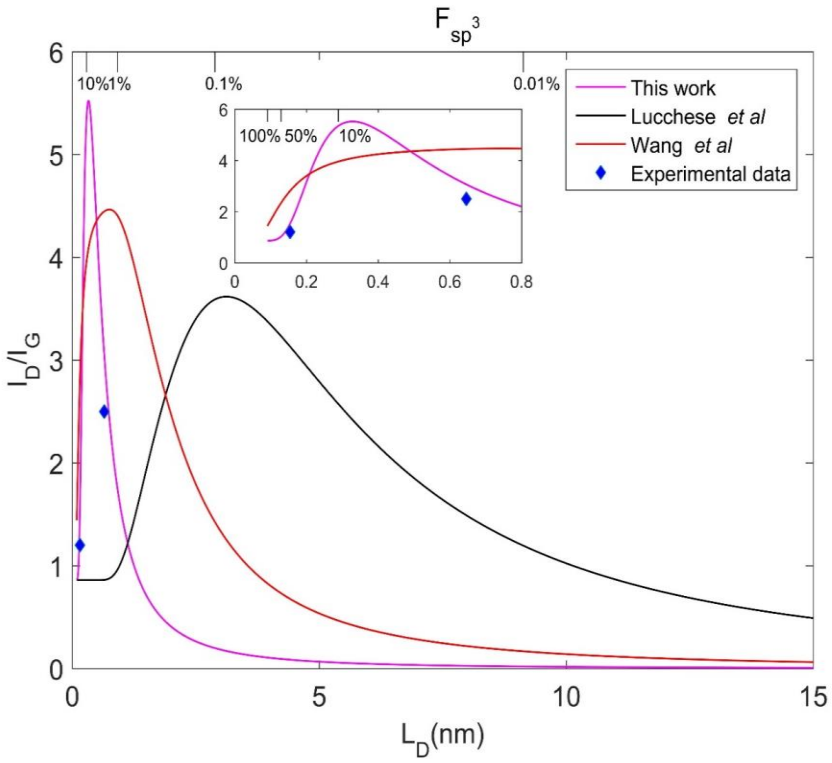


Figure 12: Rapport en intensité I_D/I_G entre les bandes D et G en fonction de L_D pour notre modèle et d'autres modèles dans la littérature. La comparaison avec les points expérimentaux (diamants bleus) montre que notre modèle offre une meilleure estimation.

Comme le montre la **Figure 12**, le rapport I_D/I_G seul ne suffit pas à déterminer la teneur en sp^3, car il peut correspondre à deux valeurs distinctes de L_D. Cependant, les étapes 1 et 2 peuvent être distinguées de manière fiable en analysant la largeur à mi-hauteur de la bande D (Γ_D). Comme le montre la **Figure 13**, deux comportements distincts sont observés. À de faibles taux de couverture, où le chevauchement des disques est minime, Γ_D reste presque constant. Les quelques défauts sp^3 dispersés sur la feuille de graphène donnent la même largeur de bande D ; seul le rapport I_D/I_G reflète le nombre de défauts. À des taux de couverture élevés, où un chevauchement important se produit, le modèle de confinement s'applique en raison de la création de petits domaines : Γ_D augmente à mesure que I_D/I_G diminue.

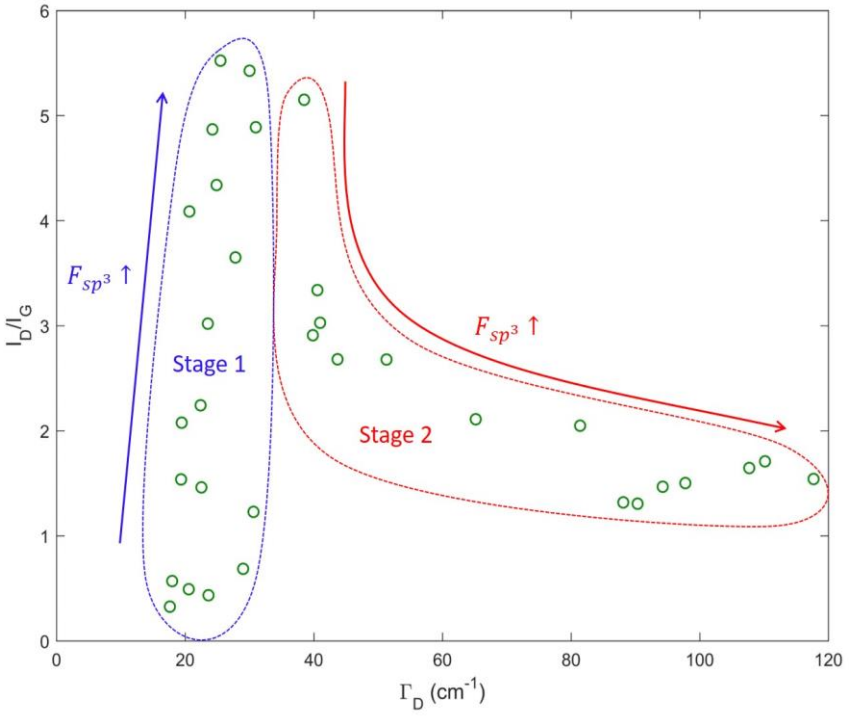


Figure 13: Ratio en fonction de la largeur de la bande D pour plusieurs échantillons de graphene fluorés, mettant en évidence la distinction entre les stades 1 et 2 de désordre.

5 Résultats et analyse du graphène hydrogéné

5.1 Spectroscopie Raman

5.1.1 Caractéristique Raman du graphène hydrogéné

La **Figure 14** montre un ensemble de spectres Raman correspondant à différents taux de couverture en hydrogène. Les bandes D et D' apparaissent toutes deux au taux de couverture le plus bas, soit 0,05 %, mais avec une intensité très faible pour la bande D'. Le rapport maximal I_D/I_G atteint une valeur maximale de 4 à un taux de couverture de 9,26 %, ce qui correspond approximativement à la frontière entre les étapes 1 et 2 (voir chapitre 5), tandis que le rapport $I_{D'}/I_G$ ne dépasse pas 0,5. Il est intéressant de noter que le rapport signal/bruit tend à diminuer fortement avec l'augmentation du taux de couverture, ce qui pourrait être interprété comme une diminution de la fraction de surface sp^2.

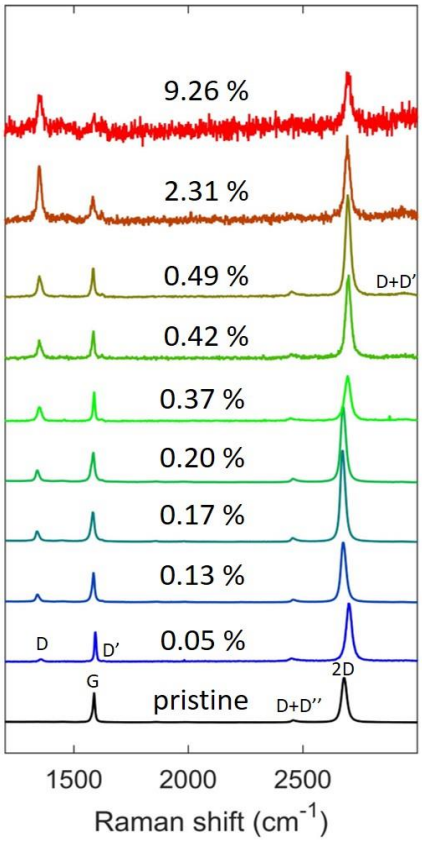


Figure 14: Spectres Raman d'échantillons de graphène hydrogénés en fonction du taux de couverture d'hydrogène.

Pour analyser ces spectres Raman et étudier le lien avec les différentes conditions expérimentales, la **Figure 15** présente le rapport I_D/I_G en fonction de la largeur de raie de la bande D et du rapport $I_{D'}/I_G$ pour plusieurs échantillons exposés à différentes conditions d'hydrogénation.

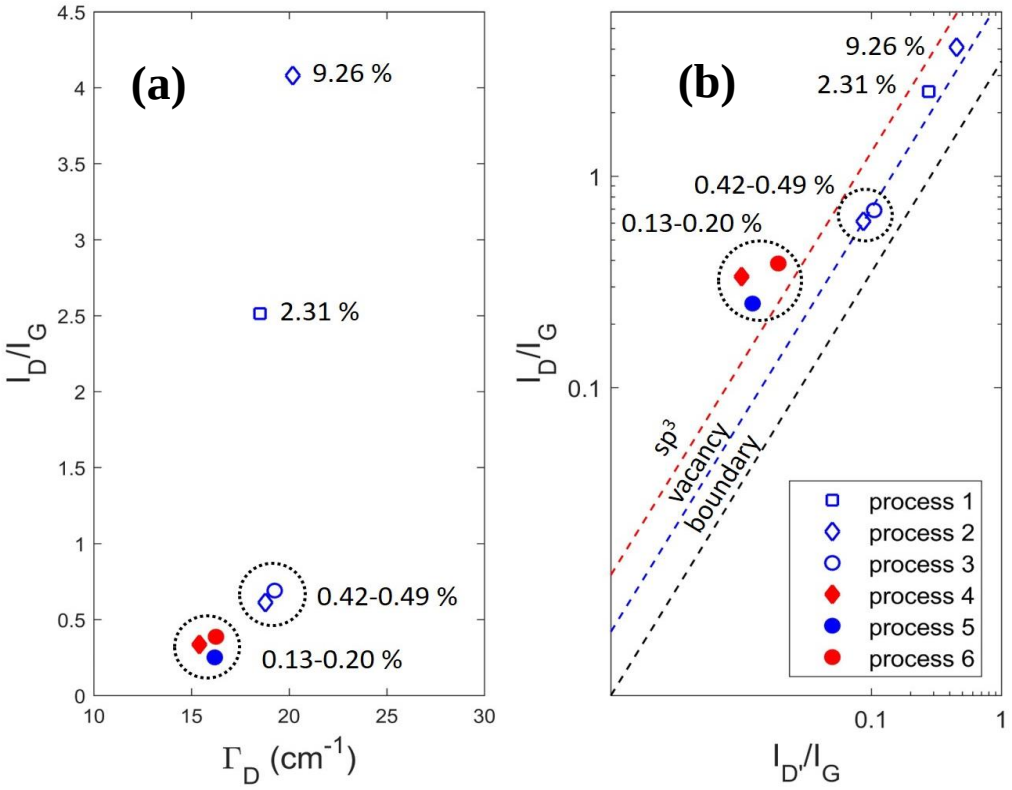


Figure 15: Rapport I_D/I_G en fonction de la largeur de raie de la bande D et du rapport $I_{D'}/I_G$ pour plusieurs échantillons exposés à différentes conditions d'hydrogénation.

5.1.2 Etude Raman de la stabilité thermique de l'hydrogène

5.1.2.1 Déshydrogénation induite par recuit thermique

La grande hétérogénéité des données rapportées dans la littérature ne résout pas le problème de la stabilité thermique de l'hydrogène sur le graphène. Par conséquent, la déshydrogénation thermiquement activée du graphène monocouche a été étudiée par spectroscopie Raman. Pour recuire les échantillons et étudier le processus de déshydrogénation qui s'ensuit, un cryostat/réchauffeur Linkam (-195 à 600 °C) dans de l'azote ultrapur à pression atmosphérique avec refroidissement à l'eau a été utilisé.

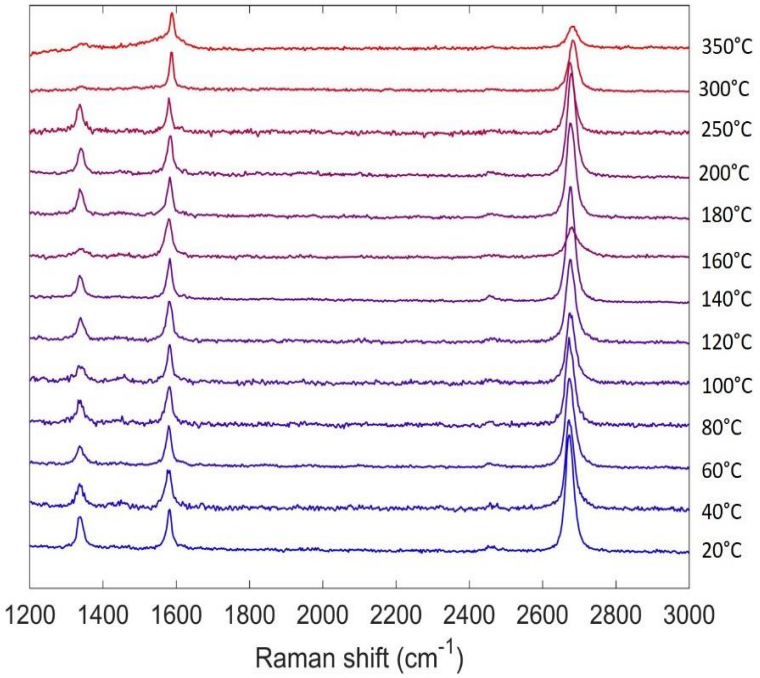


Figure 16: Spectres Raman d'un échantillon de graphene hydrogéné après recuit thermique à plusieurs températures entre 20°C et 350°C.

La **Figure 16** montre les spectres Raman obtenus sur la zone hydrogénée après recuit. Les spectres semblent assez hétérogènes, mais l'intensité relative de la bande D reste assez importante jusqu'à une température de recuit de 250 °C. À partir de 300 °C, l'intensité relative de la bande D devient très faible ou disparaît. Une température de recuit de 350 °C a permis d'obtenir des spectres similaires à ceux obtenus par Elias *et al* [12]. D'après ces observations, il semble que l'hydrogène reste lié au graphène jusqu'à 250 °C. Le recuit de l'échantillon au-dessus de cette température est susceptible de permettre la désorption de l'hydrogène, récupérant ainsi la couche de graphène. Cependant, en raison des hétérogénéités spatiales observées dans le taux de couverture d'hydrogène, une étude statistique à grande échelle serait nécessaire pour confirmer ces observations.

Pour certains échantillons, le graphène n'a pas été complètement récupéré par recuit thermique à plus de 300 °C. C'est le cas, par exemple, d'un échantillon hydrogéné pendant 10 minutes avec une pression de service et un débit de gaz de 4 Torr et 10 sccm, respectivement, et une température de filament de 2100 °C. Un obturateur en molybdène, placé à 3 cm au-dessus de l'échantillon, a protégé l'échantillon de graphène de l'exposition directe au rayonnement thermique du filament, garantissant ainsi que le substrat reste à basse température. Le processus de déshydrogénation a été réalisé par recuit à 400 °C sous une atmosphère d'Ar/H_2 pendant 1 heure. Après hydrogénation, le rapport I_D/I_G était d'environ 0,6 et le rapport I_D/I_D, était de 10,6, ce qui suggère que les défauts induits par l'hydrogénation pourraient être composés d'atomes de carbone sp^3 et de lacunes. Après recuit, les rapports I_D/I_G et I_D/I_D, tombent respectivement à 0,3 et 7, ce qui indique que l'hydrogène a été complètement éliminé et que les défauts restants sont des lacunes.

5.1.2.2 Déshydrogénation induite par irradiation laser

Une autre question importante concerne la stabilité sous irradiation laser. Pour étudier cet effet, la dépendance des caractéristiques du spectre Raman par rapport à la puissance du laser a été étudiée. Une série de spectres Raman a été acquise sur la même zone d'un échantillon hydrogéné toutes les minutes pendant 60 minutes pour une longueur d'onde de 633 nm. La puissance a été démarrée à 0,15 mW pour acquérir les spectres Raman pour la première série temporelle, puis la puissance a été augmentée successivement à 0,5, 2, 4 et 8 mW pour acquérir les spectres pour les autres séries temporelles, respectivement.

À une puissance laser inférieure à 4 mW, aucun effet significatif n'a été observé. La **Figure 17** montre la variation du rapport I_D/I_G en fonction du temps d'irradiation photochimique à 4 mW. L'intensité I_D/I_G diminue avec l'augmentation du temps d'irradiation photochimique, ce qui peut s'expliquer par la désorption d'hydrogène causée par la surchauffe. Après la série d'irradiations à 4 mW, le rapport I_D/I_G est resté constant lors de l'utilisation d'une puissance plus élevée (8 mW), ce qui signifie que le graphène ne pouvait pas être modifié davantage.

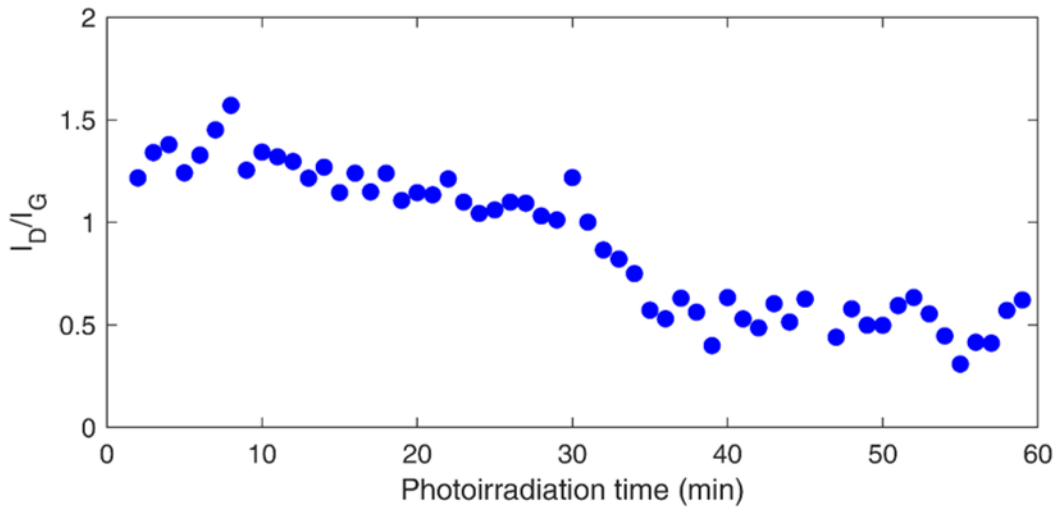


Figure 17: Variation du ratio I_D/I_G en fonction du temps d'exposition à un faisceau laser de 4 mW.

Cette méthode de déshydrogénation a été utilisée sur un graphène hydrogéné pendant 20 minutes avec une pression de fonctionnement et un débit de gaz respectivement de 4 Torr et 10 sccm, et une température de filament de 2100 °C. La figure 6.8 présente les spectres obtenus en exposant l'échantillon à une puissance croissante pendant les mesures Raman. Les spectres sont normalisés par puissance laser pour permettre une comparaison directe de l'intensité. Les données montrent qu'une partie du signal Raman du graphène est progressivement récupérée à partir d'une puissance laser de 1,2 mW, bien que l'intensité relative de la bande 2D reste faible. Cette récupération n'est pas due à un manque de matériau ou à une non-linéarité du détecteur, comme le prouve l'augmentation minimale du signal du support Si (pic 3TO) avec l'augmentation de la puissance du laser, tandis que l'intensité de la bande D augmente de manière significative. Cela suggère

que l'augmentation de la puissance du laser pendant les mesures Raman a permis de récupérer le signal Raman du graphène et a favorisé la déshydrogénation.

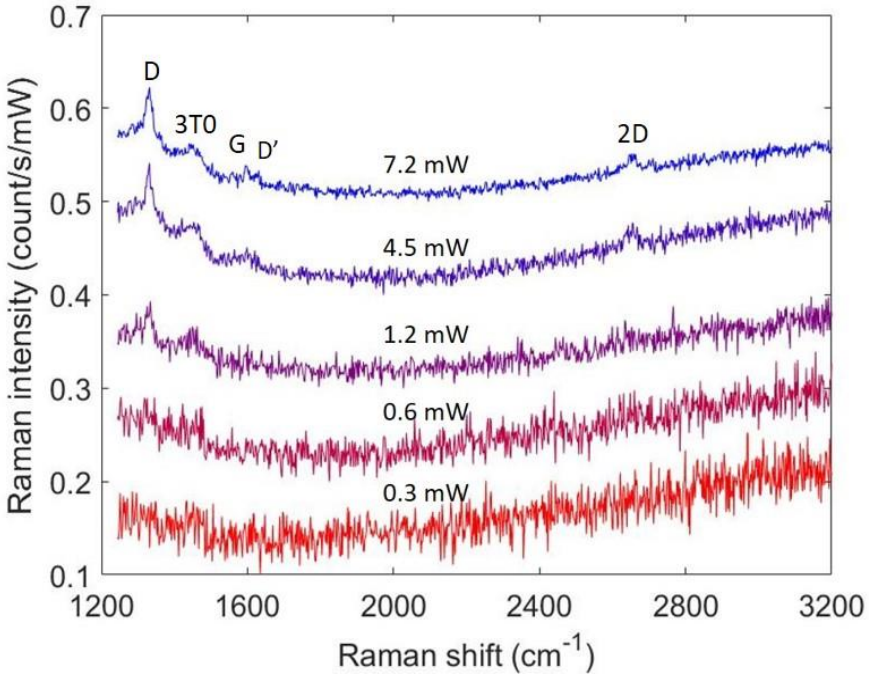


Figure 18: Spectres Raman d'un échantillon hydrogéné pour différentes puissances laser, montrant le procédé de déshydrogénation induit par laser.

5.2 Microscopie à force atomique

Une analyse topographique AFM a été réalisée sur deux échantillons hydrogénés dans des conditions similaires, mais avec des temps d'exposition différents (10 et 20 minutes). Il convient de rappeler qu'un obturateur en molybdène, placé à 3 cm au-dessus des échantillons, protégeait l'échantillon de graphène de l'exposition directe au rayonnement thermique du filament. Dans la suite, ces échantillons sont désignés par « échantillon 1 » (10 minutes) et « échantillon 2 » (20 minutes) pour plus de simplicité. Les images AFM (**Figure 19**) réalisées en mode tapping sous atmosphère N_2 révèlent des changements significatifs dans la topographie des feuillets de graphène exposés à ces conditions d'hydrogénation.

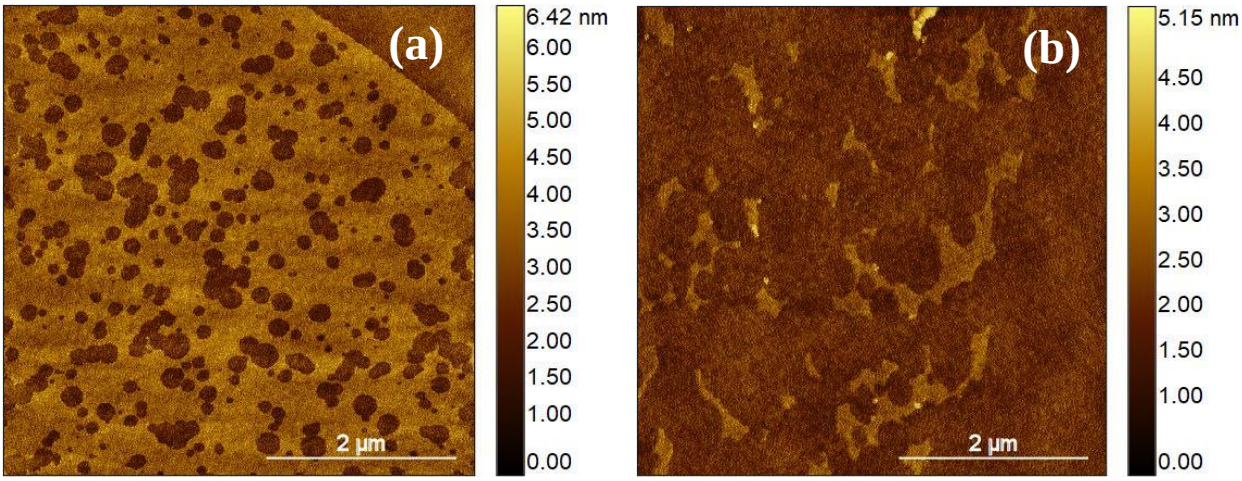


Figure 19: Images AFM de (a) l'échantillon 1 et de (b) l'échantillon 2.

Pour l'échantillon 1, l'image AFM (figure 6.8a) révèle une forte densité de trous de taille submicrométrique à la surface, qui apparaissent sous forme de contrastes circulaires sombres. La distribution de la taille des trous donne un aperçu de la dynamique de formation des trous. La distribution polymodale suggère l'implication de divers mécanismes de formation, ce qui correspond à l'observation de formes de trous variables (grosso modo rondes ou hexagonales) et/ou de différents stades de formation des trous. La nature large de la distribution indique une variation considérable dans le processus de formation, ce qui suggère que certaines configurations locales sont plus propices à la formation de trous que d'autres.

Pour l'échantillon 2, l'image topographique AFM (**Figure 19b**) révèle qu'une grande partie de la couche a été gravée, ne laissant intactes que certaines zones. Étant donné que l'hydrogénation de cet échantillon ne diffère de celle de l'échantillon 1 que par un temps d'exposition plus long, cela suggère que ces grands domaines gravés résultent d'une croissance continue des trous avec le temps d'exposition. D'après la taille des plus grands trous circulaires observés dans la **Figure 19a** (0,27 µm), qui sont vraisemblablement les premiers à avoir été créés à t = 0 min et qui se sont ensuite agrandis sans fusionner avec d'autres, on peut estimer que le rayon des trous a augmenté à un rythme moyen de 13 nm/min pendant les 10 premières minutes. La linéarité de l'expansion des trous, et donc du processus de gravure, s'est maintenue au cours des 10 minutes suivantes, comme le montre la **Figure 19b**. Ceci est corroboré par les résultats d'un modèle linéaire, qui suppose la création aléatoire de creux à un taux de 40 creux/min sur une surface de 5 µm × 5 µm et une vitesse de gravure linéaire de 13 nm/min. Le taux de gravure observé ici à une température de substrat inférieure à 100 °C peut être comparé au taux extrapolé de 10 nm/min à 100 °C pour le graphène monocouche, tel que rapporté dans [100], confirmant ainsi les observations précédentes.

Ces résultats confirment que l'exposition du graphène à un flux de radicaux hydrogène peut avoir deux effets : (i) la chimisorption d'hydrogène et (ii) la gravure.

5.3 Raman amplifié par effet de pointe

Les mesures TERS ont été réalisées à l'aide d'un laser rouge (633 nm) sur du graphène CVD déposé sur un substrat en or ultraplat et hydrogéné. L'objectif principal était de détecter le mode d'étirement C-H à 2740

cm^{-1}. Le graphène CVD a été transféré d'une feuille de cuivre vers un substrat en or à l'aide de la technique de transfert humide. Malheureusement, le mode C-H n'a pas pu être détecté, ce qui suggère que (i) soit l'hydrogène ne pouvait pas se lier au graphène, (ii) soit les spectres ont été acquis dans des régions à faible teneur en hydrogène. Le cas (i) pourrait s'expliquer par des interactions différentes entre le graphène et l'or par rapport au SiO_2, modifiant ainsi l'énergie d'absorption. Cependant, cela reste purement hypothétique. Une autre explication plausible est la présence de résidus de PMMA restant sur le graphène après le processus de transfert. Ces résidus ont été observés à plusieurs reprises en spectroscopie AFM et Raman, et pourraient poser problème pour les interactions entre l'hydrogène et le graphène. Le cas (ii) est possible si la couverture d'hydrogène est faible et n'est pas répartie uniformément sur la surface.

5.4 Perspectives : hydrogénation locale par faisceau d'électrons

Comme mentionné précédemment, l'hydrogénation du graphène peut être réalisée à l'aide d'un faisceau électronique afin de libérer l'hydrogène d'une couche de PMMA appliquée par centrifugation sur l'échantillon. Cette technique a été décrite dans la littérature [53] et reproduite au LPCNO sur des feuillets de graphène exfoliés sur un substrat Si/SiO_2 au cours de cette thèse afin de la comparer au procédé à filament chaud. Les feuillets de graphène ont été caractérisés par spectroscopie Raman avec une excitation laser verte (532 nm) avant et après l'hydrogénation.

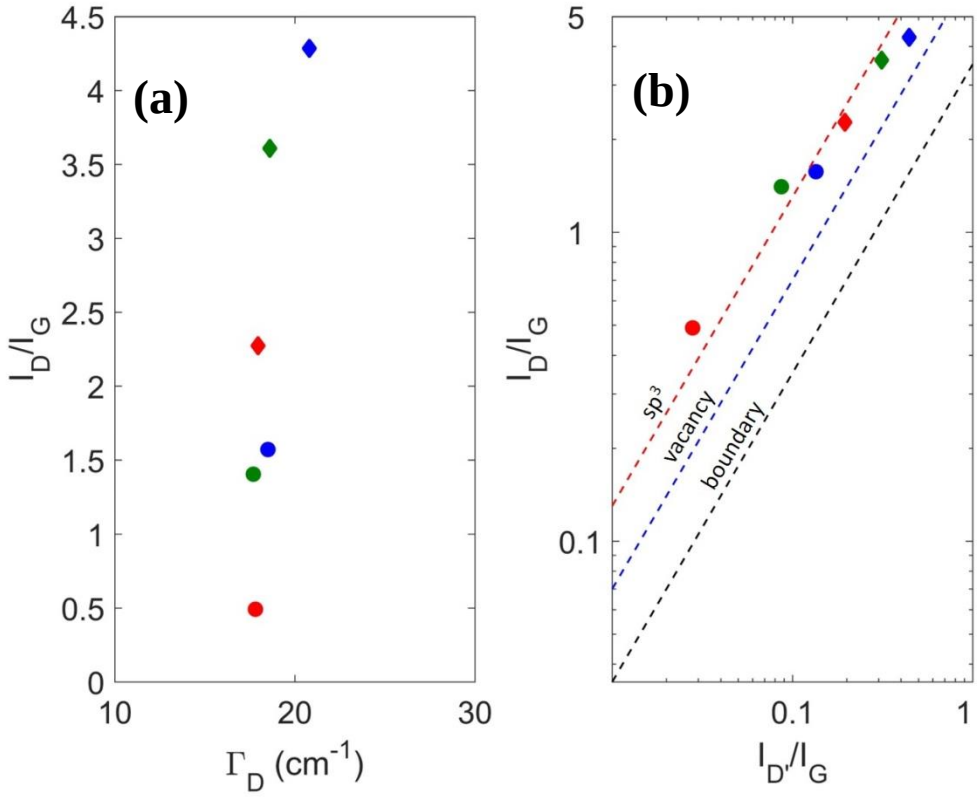


Figure 20: Rapport I_D/I_G en fonction du rapport $I_{D'}/I_G$et de la largeur de raie de la bande D pour plusieurs échantillons exposés à différentes conditions d'hydrogénation.

La **Figure 20** représente le rapport I_D/I_G en fonction du rapport $I_{D'}/I_G$et de la largeur de raie de la bande D. Elle montre que les valeurs Γ_D et $I_D/I_{D'}$ sont à peu près constantes. La largeur de raie de la bande D reste proche de 20 cm^{-1}, tandis que le rapport reste autour de 13 pour chaque échantillon, ce qui indique que des défauts ponctuels de type sp3 ont été induits dans les feuillets de graphène, surpassant la majorité des résultats obtenus avec le HFCVD. De plus, aucun type de trou n'a été observé en AFM. Le rapport I_D/I_G évolue de 0,5 à 4,3, ce qui correspond à des taux de couverture en hydrogène de 0,25 % et 3,3 % respectivement.

6 Résultats et analyse des échantillons fluorés

6.1 Spectroscopie Raman

La spectroscopie Raman a été réalisée avant et après chaque expérience avec une excitation laser verte (532 nm) afin d'étudier les changements induits par la fluoration. La **Figure 21** représente I_D/I_Gpar rapport à $I_{D'}/I_G$ pour plusieurs échantillons au stade 1 après exposition à trois conditions de fluoration différentes. D'après cette figure, comme pour l'hydrogénation, la réaction chimique du fluor avec le graphène peut avoir deux effets : (i) la chimisorption du fluor et (ii) la rupture de la liaison C-C.

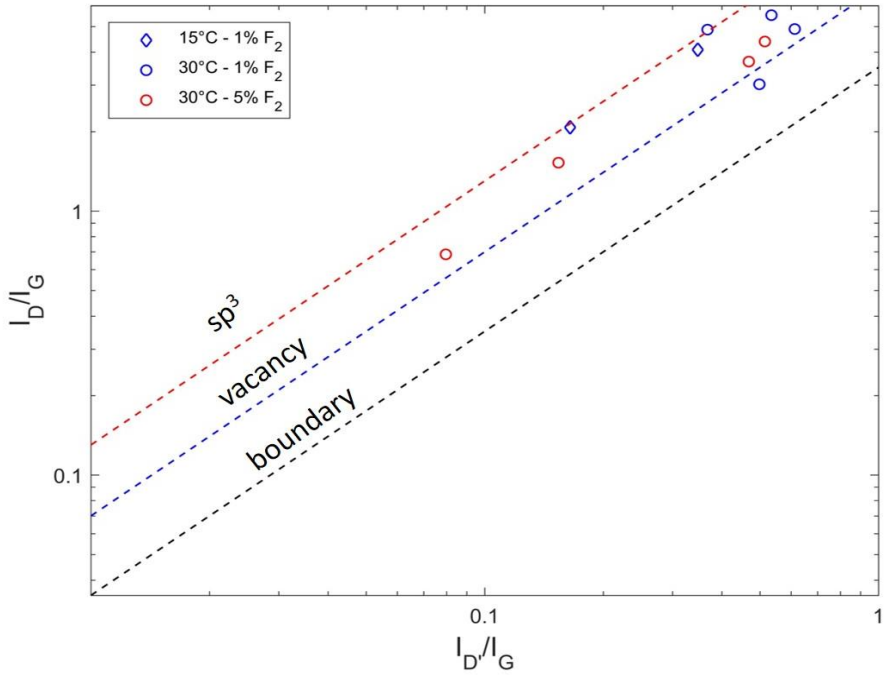


Figure 21: Rapport I_D/I_G en fonction du rapport $I_{D'}/I_G$ pour plusieurs échantillons exposés à différentes conditions de fluoration.

La **Figure 21a** représente I_D/I_Gen fonction de Γ_D pour différents échantillons et indique les conditions de fluoration auxquelles ils ont été exposés, montrant que des conditions similaires peuvent conduire à des taux de couverture en fluor fortement hétérogènes. La fluoration est si hétérogène que les étapes 1 et 2 sont observées dans des conditions similaires. Le taux de couverture en fluor a été déterminé pour chaque

échantillon, et I_D/I_G et Γ_D sont représentés en fonction du taux de couverture dans la **Figure 21b**. Les valeurs de couverture sont fortement dispersées sur une large plage et semblent être totalement indépendantes de la température et de la teneur en fluor dans la phase gazeuse. L'exemple le plus extrême est le cas de la fluoration à 30 °C avec un flux gazeux composé de 5 % de F2. Ces conditions expérimentales ont été appliquées à quelques échantillons, y compris certains feuillets de graphène sur le même substrat, et les taux de couverture en fluor prédits par le modèle variaient entre 0,4 % et 42 %.

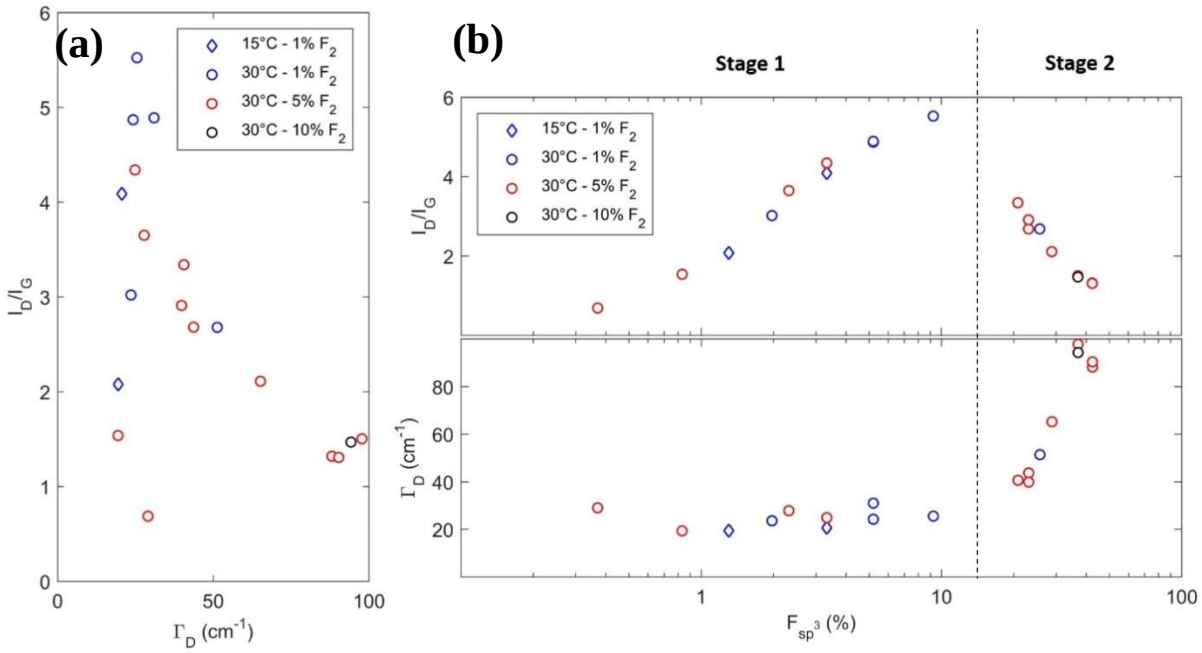


Figure 21: (a) I_D/I_Gen fonction de Γ_D et (b) et I_D/I_G et Γ_D en fonction du taux de couverture pou des échantillons exposés à différentes conditions de fluoration.

Bien qu'il soit impossible d'attribuer une signature Raman typique à chaque condition de fluoration, la **Figure 22a** montre que le spectre Raman semble être assez représentatif du taux de couverture en fluor. Ensuite, des échantillons présentant différentes teneurs en fluor sont représentés ensemble dans la **Figure 22b** afin de montrer l'évolution de la réponse Raman de 0 % (état vierge) à 42,5 %. Selon la **Figure 22b**, la transition du stade au stade 2 se produit entre environ 10 % et 20 %. Les spectres attribués au stade 1 présentent une bande D nette avec une intensité relative croissante avec la concentration en fluor, et une bande D' bien définie, détachée de la bande G. Au stade 2, l'augmentation du taux de fluoration contribue non seulement à diminuer l'intensité relative de la bande D et à augmenter sa largeur de raie, mais elle provoque également la fusion des bandes G et D' pour former une seule bande large. L'intensité relative de la bande 2D diminue continuellement avec l'augmentation de la teneur en fluor (c'est-à-dire l'augmentation du désordre) jusqu'à disparaître presque complètement. Un décalage de fréquence de la bande D peut également être observé, en particulier au stade 2, en raison de la modification de la structure de la bande électronique qui induit un changement dans la condition de résonance.

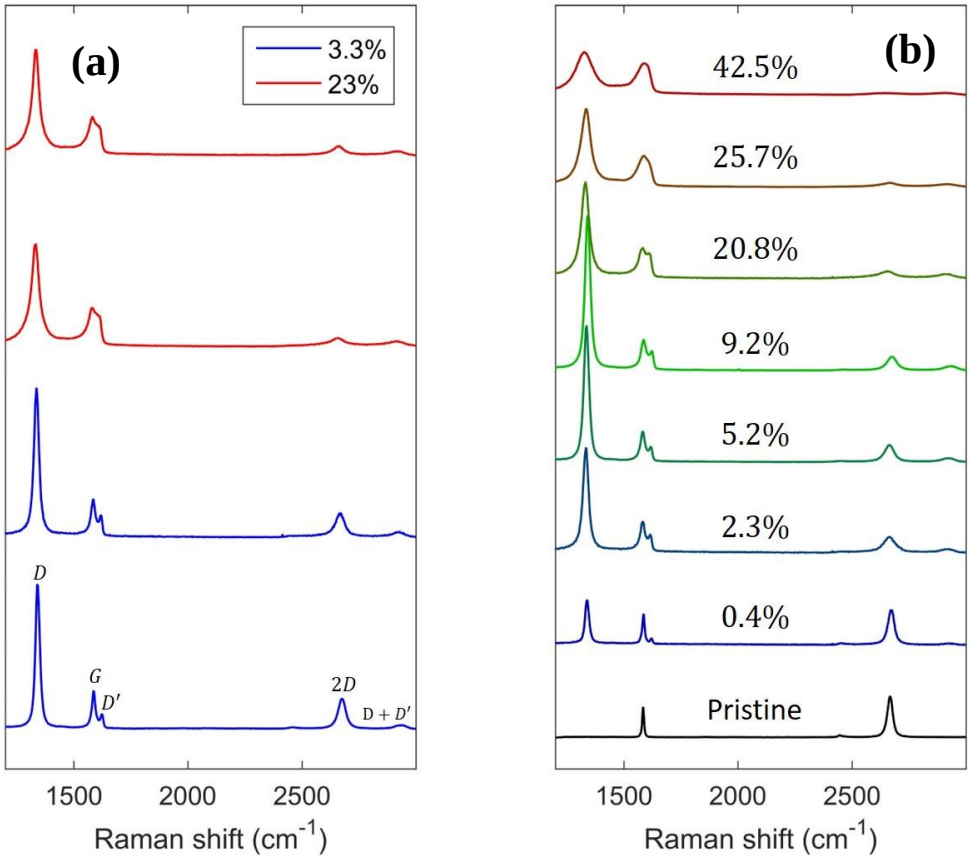


Figure 22: (a) Spectres Raman correspondant à quatre échantillons de graphène avec des taux de couverture en fluor de 3,3 % (bleu) et 23 % (rouge). (b) Spectres Raman de huit échantillons de graphène avec des taux de couverture en fluor distincts allant de 0 % à 42,5 %.

6.2 Microscopie à force atomique

Une imagerie AFM a été réalisée sur un échantillon (**Figure 23**) avec un taux de couverture en fluor de 3,3 % afin d'étudier la topographie de surface des échantillons de graphène après fluoration. L'objectif principal était de valider la présence de trous dans la structure, comme pour le graphène hydrogéné. Les deux scans différents réalisés sur l'échantillon (**Figure 23**) ne révèlent aucun trou ni aucun autre dommage structurel (fissures, plis, etc.). Au lieu de dommages structurels, les images AFM révèlent la présence de résidus.

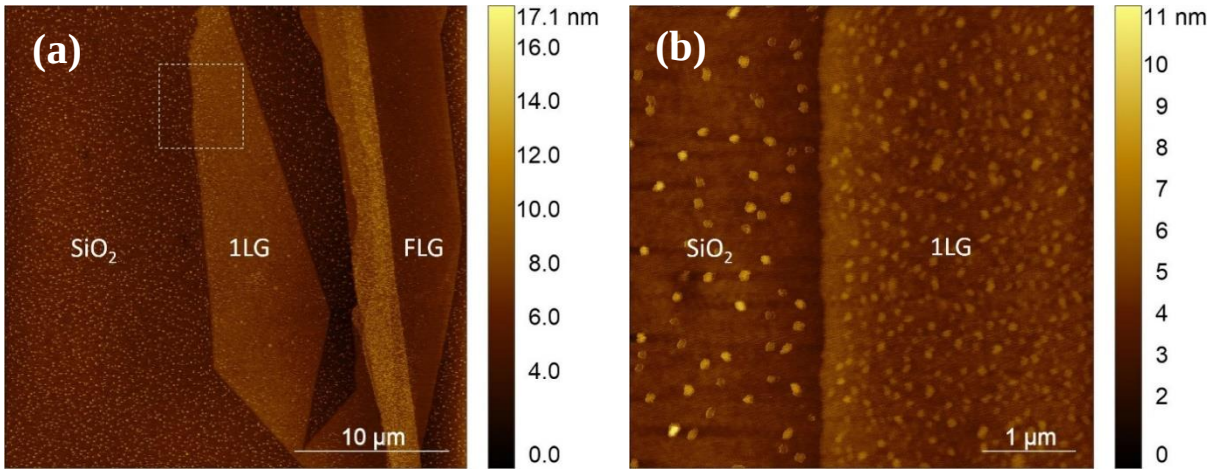


Figure 23: (a) Image AFM 30 × 30 µm d'un feuillet de graphène fluoré sur un substrat Si/SiO_2 avec une teneur en fluor de 3,3 %. (b) Image AFM 5 × 5 µm correspondant à la zone encadrée dans (a).

6.3 Spectroscopie Raman amplifiée par effet de pointe (TERS)

Les mesures TERS ont été réalisées par Ibrahim Arshad pendant son stage au CEMES. Les échantillons ont été préparés par exfoliation mécanique de HOPG sur un substrat en or, et les mesures ont été effectuées à l'aide d'un spectromètre Raman couplé à un laser de 532 nm et d'un AFM avec des pointes recouvertes d'or. Malheureusement, le fluor a réagi chimiquement avec le substrat en or, rendant l'échantillon inutilisable. Une carte linéaire a été réalisée avec les deux configurations : (i) pointe sur la surface et (ii) pointe hors de la surface, montrant une forte exaltation du signal Raman dans la région du champ proche. Cependant, les spectres du champ proche sont hétérogènes et présentent de nombreux pics non identifiés.

6.4 Mesures de transport électrique

Les propriétés électroniques de deux dispositifs à graphène fluoré ont été étudiées à l'aide de mesures électriques sous un champ magnétique hors plan et à différentes températures comprises entre 10 et 300 K à l'aide d'un PPMS.

6.4.1.1 Echantillon 1

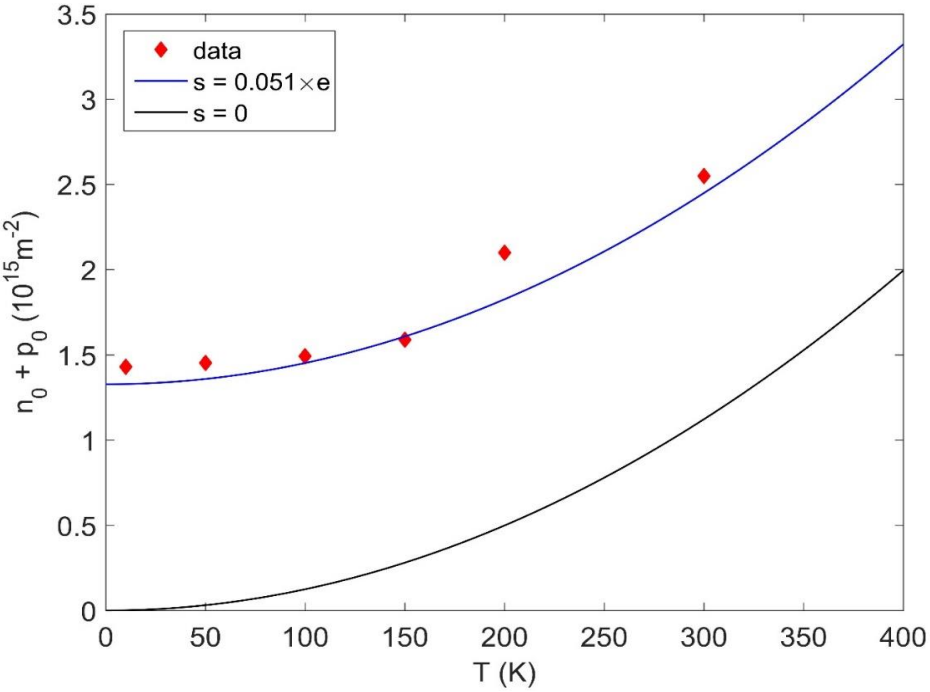


Figure 24: Dépendance à la température de la densité résiduelle des porteurs de charge représentée pour les données expérimentales (losanges) et les valeurs théoriques (lignes) obtenues avec le modèle de Li en utilisant s = 0,051e et s = 0.

La **Figure 24** compare les valeurs expérimentales avec le modèle de Li pour s = 0,051e et s = 0 (graphène vierge). Les points de données correspondent assez bien à la courbe théorique. On peut en conclure que la dépendance de la concentration des porteurs de charge résiduels par rapport à la température est raisonnablement bien décrite par le modèle de Li avec un paramètre de désordre s = 0,051e, ce qui est assez significatif. Ce désordre se traduit par des poches d'électrons-trous et devrait avoir un impact sur la mobilité des porteurs de charge. Comme prévu, la fluoration entraîne une détérioration globale de la mobilité.

6.4.1.2 Echantillon 2

Pour cet échantillon, la dépendance à la température peut être raisonnablement bien reproduite par le modèle de Li avec un paramètre de désordre s = 0,16e, qui est plus de trois fois supérieur à la valeur déterminée pour l'échantillon 1. Tout cela suggère que cet échantillon présente un degré de désordre plus important, c'est-à-dire un taux de fluoration plus élevé, que l'échantillon 1. La **Figure 25** compare les valeurs de dopage résiduelles extraites des données expérimentales avec les courbes théoriques du modèle de Li pour s = 0,16e (cet échantillon), s = 0,051e (échantillon 1) et s = 0 (graphène vierge), montrant une assez bonne concordance entre les mesures et le modèle de Li évaluée à s = 0,16e.

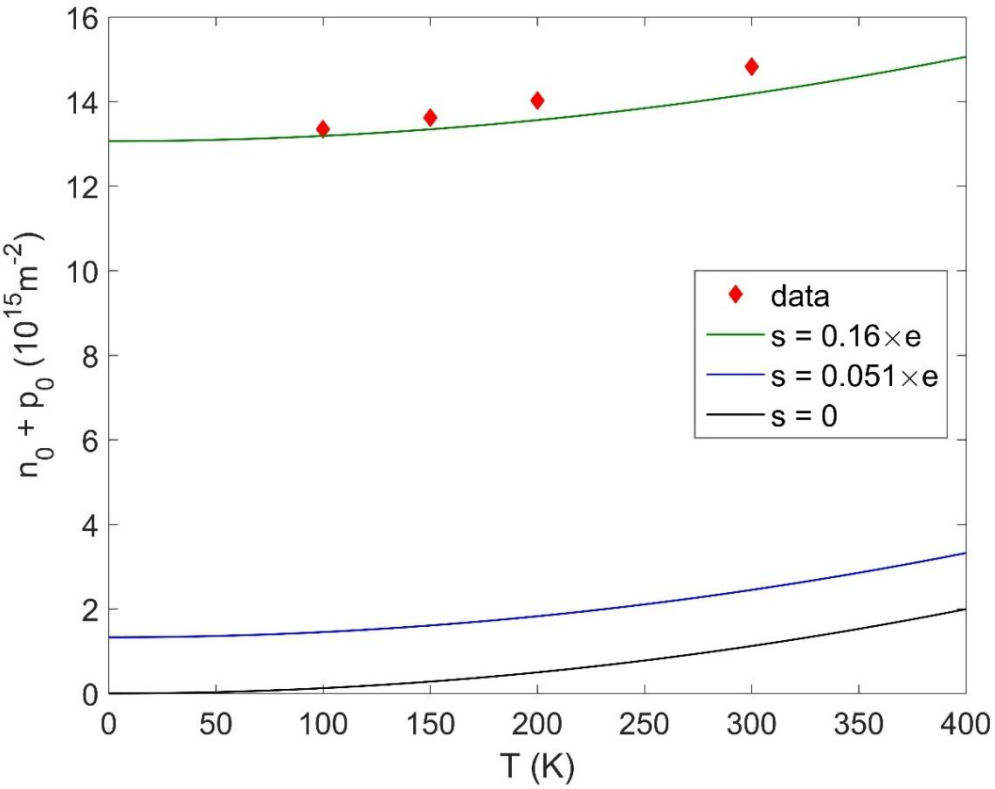


Figure 25 : Dépendance à la température de la densité résiduelle des porteurs de charge représentée pour les données expérimentales (losanges) et les valeurs théoriques (lignes) obtenues avec le modèle de Li en utilisant s = 0,16e, s = 0,051e et s = 0.

Cependant, les valeurs expérimentales de la résistivité maximale (**Figure 26**) ne sont décrites ni par l'activation thermique ni par la loi de Mott. En d'autres termes, ce dispositif en graphène fluoré conserve une nature semi-métallique (absence de bande interdite) et ne présente pas les caractéristiques d'une conduction par saut via des états localisés. Une autre explication possible pourrait être que cet échantillon présente une petite bande interdite masquée par les fortes fluctuations du potentiel électronique données par le paramètre de désordre s.

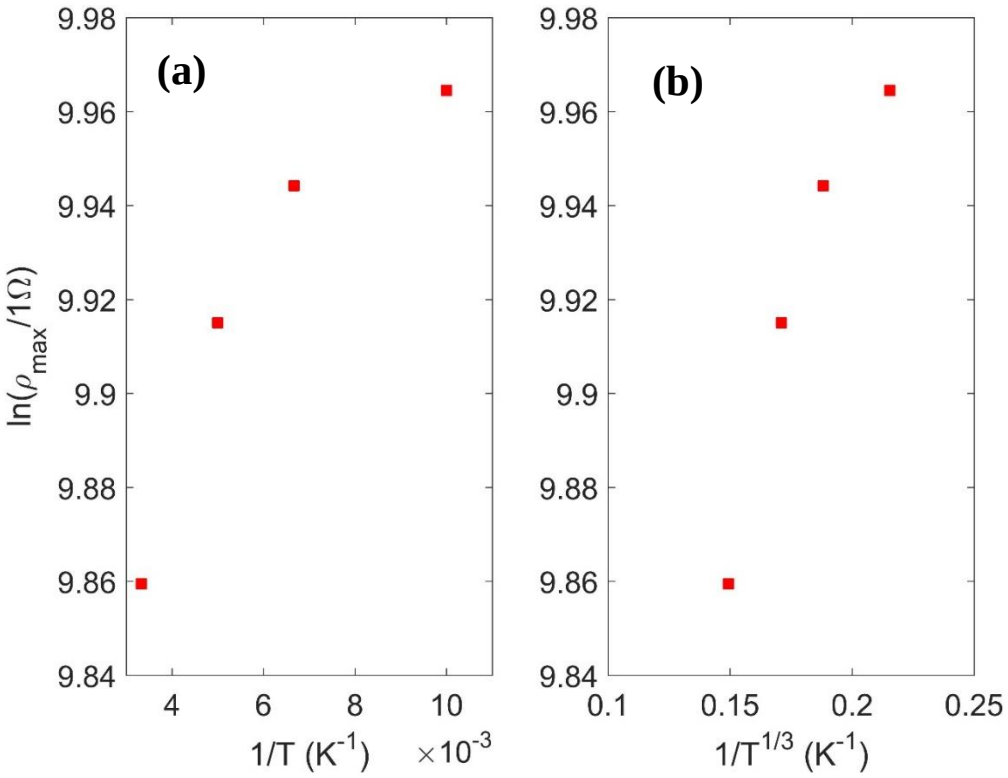


Figure 26: Preuve des comportements non exponentiels des valeurs maximales de résistivité expérimentale, contrairement à (a) la loi d'activation thermique et (b) la loi de Mott. Si l'une de ces lois permettait de reproduire les données, les points rouges seraient alignés sur une ligne droite, ce qui n'est manifestement pas le cas ici.

Ces fluctuations du niveau de Fermi proviennent probablement d'une fluoration non homogène. Certains groupes de fluor pourraient former des zones fortement dopées en p, tandis que d'autres zones caractérisées par une faible teneur en fluor devraient être plus neutres sur le plan électrique.

De plus, des calculs DFT de la structure de bande électronique du graphène fluoré ont été réalisés au sein de notre consortium et comparés à des calculs similaires pour le graphène hydrogéné. Les résultats montrent que, contrairement à l'hydrogénation, la fluoration induit une structure de bande particulière où le niveau de Fermi se trouve dans la bande de conduction. Néanmoins, dans le cas d'un taux de couverture en fluor important et homogène, une barrière d'activation devrait être visible via des mesures de transport électronique à différentes tensions de grille, comme cela a été fait dans cette étude. Cependant, comme les données expérimentales sont interprétées comme un fort désordre induit par une fluoration non homogène, l'absence de barrière d'activation pourrait s'expliquer par certains alignements des niveaux de Fermi provenant de différentes régions dopées lors des balayages de tension de grille.

Conclusion

La chimisorption d'atomes d'hydrogène et de fluor sur une face d'une monocouche de graphène supportée a été étudiée expérimentalement au cours de ce doctorat, avec pour objectif principal d'ouvrir une bande interdite dans la structure électronique du graphène. La préparation des échantillons de graphène, ainsi que leur caractérisation, ont été entièrement réalisées au CEMES et au LPCNO. Les échantillons ont été principalement caractérisés par spectroscopie Raman, mais certains ont également été analysés par microscopie à force atomique (AFM), spectroscopie Raman améliorée par pointe (TERS) et mesures de transport électrique. Deux types de substrats ont été utilisés en fonction de la caractérisation : (i) des substrats en silicium recouverts de 285 nm de SiO_2 pour effectuer des mesures de transport électrique, ainsi que pour améliorer le contraste optique et le signal Raman par des effets d'interférence et (ii) des substrats en or ultraplats pour améliorer le signal TERS.

Le graphène a été transféré sur ces substrats par exfoliation mécanique de graphite pyrolytique hautement orienté (HOPG), à l'aide de la technique du « ruban adhésif ». Pour les substrats en or ultraplats, certains échantillons ont également été préparés à l'aide de techniques de transfert humide assisté par polymère de graphène à grande surface obtenu par dépôt chimique en phase vapeur (CVD). Pour effectuer les mesures de transport électrique, des dispositifs ont été fabriqués à partir de feuillets de graphène sur Si/SiO_2, à l'aide de techniques de microfabrication conventionnelles.

Les processus d'hydrogénation et de fluoration ont été réalisés en collaboration avec deux spécialistes : le professeur Fabrice Piazza de la PUCMM à Santiago de los Caballeros (République dominicaine) et le professeur Marc Dubois de l'université de Clermont-Ferrand (France). J'ai eu l'occasion de passer quelques mois à la PUCMM et quelques jours à l'université de Clermont-Ferrand. Le processus d'hydrogénation consiste en un procédé CVD à filament chaud, dans lequel les molécules d'H_2 sont dissociées par activation thermique à très haute température (>1800 °C) à l'intérieur d'une chambre à vide. Le processus de fluoration se produit à des températures beaucoup plus basses (15-30 °C) en raison de la réactivité élevée du fluor. Il est réalisé à l'intérieur d'un réacteur à flux gazeux et utilise un mélange gazeux composé de 1 à 10 % de F_2 dilué dans du N_2. En parallèle, l'hydrogénation sélective par faisceau électronique, qui consiste à libérer localement de l'hydrogène à partir de zones spécifiques d'un film PMMA recouvrant une couche de graphène à l'aide d'un faisceau électronique, a été testée au LPCNO et les premiers résultats semblent très prometteurs. La spectroscopie Raman a été utilisée pour étudier les modifications des propriétés du graphène induites par l'hydrogénation et la fluoration. Notamment, un modèle a été développé pour déterminer quantitativement le taux de fonctionnalisation dans le graphène à partir d'un spectre Raman. Le Raman a aussi été utilisé pour étudier la stabilité du graphène hydrogéné lors d'un recuit thermique et d'une mesure optique.

L'AFM a été utilisé sur certains échantillons hydrogénés et fluorés afin d'étudier les changements dans la topographie de surface. Pour les échantillons hydrogénés, cette technique a fourni des preuves claires d'un mécanisme de gravure se produisant simultanément avec la chimisorption d'hydrogène. La formation de nanopores circulaires a été observée pour des temps d'exposition à l'hydrogène faibles, et leur mécanisme de croissance a été déduit à partir d'images d'échantillons exposés pendant des durées prolongées. L'origine de ce mécanisme de gravure a été étudiée à l'aide de calculs de dynamique moléculaire effectués par notre consortium, mais reste incertaine. Aucun phénomène similaire n'a été observé lors de la fluoration.

Quelques mesures TERS ont été réalisées sur certaines couches de graphène hydrogénées et fluorées déposées sur des substrats en or ultra-plats, dans le but de détecter les modes vibrationnels C-H et C-F. Cependant, bien que la diffusion Raman ait été renforcée par la pointe, les pics Raman correspondant à ces modes n'ont pas pu être détectés. De plus, il a été constaté que le fluor réagissait avec le substrat en or, causant de graves dommages à l'échantillon.

Enfin, des mesures de transport électrique ont été effectuées à différentes températures, à l'aide d'un système de mesure des propriétés physiques (PPMS), sur quelques dispositifs en graphène fluoré. Les résultats sont caractéristiques d'un graphène désordonné mais n'apportent pas l'évidence d'un gap.

RÉPUBLIQUE FRANÇAISE
Liberté
Égalité
Fraternité

Université de Toulouse

Titre : Aperçu de la fonctionnalisation du graphène pour le développement de nouveaux dispositifs 2D

Mots clés : graphène, hydrogénation, fluoration, Raman

Résumé : Cette thèse intitulée « Aperçu de la fonctionnalisation du graphène pour le développement de nouveaux dispositifs 2D » porte sur l'étude expérimentale de la fonctionnalisation du graphène avec de l'hydrogène atomique (hydrogénation) et du fluor (fluoration) dans le but de modifier les propriétés électroniques en changeant l'hybridation du carbone de sp2 à sp3.
Étant donné que des applications potentielles telles que les dispositifs électroniques 2D sont envisagées, ce travail se concentre sur la fonctionnalisation du graphène sur substrat Si/SiO2. Des échantillons de graphène ont été déposés sur Si/SiO2 par exfoliation mécanique de HOPG. Pour la caractérisation en champ proche (TERS), quelques échantillons ont été préparés par transfert de graphène par croissance CVD sur un substrat d'or ultraplat.
L'hydrogénation a été réalisée à l'aide de différentes techniques, notamment la CVD à filaments chauds (HFCVD), le faisceau d'hydrogène et l'irradiation par faisceau d'électrons du graphène recouvert de PMMA. La technique la plus utilisée a été la HFCVD. La fluoration a été réalisée en phase gazeuse à l'aide d'un réacteur à flux.
La stabilité de l'hydrogène chimisorbé a été étudiée par recuit thermique et irradiation laser. Dans certains cas, le graphène a pu être entièrement récupéré. Certains tests ont également été effectués sur le fluor qui s'est avéré beaucoup plus stable.
Des échantillons de graphène vierge, fonctionnalisé et récupéré ont été analysés par spectroscopie Raman afin d'étudier les modifications de la structure cristalline et de la structure des bandes électroniques. Un modèle a été développé pour déterminer le rapport sp3/sp2 à partir d'un spectre Raman.
La topographie de la surface a été étudiée par microscopie à force atomique et a permis de mettre en évidence que l'hydrogénation est susceptible de graver le graphène dans certaines conditions expérimentales alors que ce n'est pas le cas de la fluoration.
Enfin, des mesures de transport électrique ont été effectuées sur du graphène vierge et fluoré. Les échantillons fluorés se sont révélés plus résistifs en raison du désordre induit par le fluor chimisorbé, mais la présence d'un gap en énergie reste incertaine.

Title: Insight into the functionalization of graphene for the development of novel 2D devices

Key words: graphene, hydrogenation, fluorination, Raman

Abstract: This PhD entitled “Insight into the functionalization of graphene for the development of novel 2D devices” is about the experimental study of graphene functionalization with atomic hydrogen (hydrogenation) and fluorine (fluorination) within the objective of modifying the electronic properties by switching carbon hybridization from sp2 to sp3.
Since potential applications such as 2D electronic devices are considered (logic transistors and micrometric electrodes for biological applications), this work mainly focuses on the functionalization of graphene on a Si/SiO2 substrate. Graphene samples were obtained by mechanical exfoliation of HOPG. For near-field characterization (TERS), some samples were prepared by the transfer of CVD-grown graphene on an ultra-flat gold substrate.
Hydrogenation was performed using different techniques, including hot filament CVD (HFCVD), a hydrogen beam, and electron-beam irradiation of PMMA-coated graphene. The main technique used was HFCVD. Fluorination was performed using a gas flow reactor. Know-how skills during these 3 years were developed to be able to design devices and required adaptation of the routinely clean-room processes to keep the functionalization.
The stability of chemisorbed hydrogen was investigated by thermal annealing and laser irradiation. In some cases, graphene could be entirely recovered, indicating that hydrogenation exhibits low stability. Conversely, similar tests performed on fluorine demonstrated the high stability of fluorination, although it comes with the disadvantage of high reactivity.
Pristine, functionalized, and recovered graphene samples were analyzed using Raman spectroscopy to study the modifications in the crystalline structure and electronic band structure. A model based on physical parameters deduced from first principles and geometrical considerations was developed to determine the sp3/sp2 ratio from a single Raman spectrum. One side coverages as high as 9.3% for hydrogenation and 42.5% for fluorination have been reached.
The topography of the surface was investigated by atomic force microscopy and allowed to evidence that hydrogenation is likely to etch graphene in some experimental conditions, whereas it is not the case with fluorination.
Finally, some electrical transport measurements were performed on pristine and fluorinated graphene. The fluorinated samples were found to be more resistive due to disorder induced by chemisorbed fluorine, but the presence of an energy gap remains unclear.